université de BORDEAUX

THÈSE PRÉSENTÉE POUR OBTENIR LE GRADE DE

DOCTEUR DE

L'UNIVERSITÉ DE BORDEAUX

ÉCOLE DOCTORALE DES SCIENCES CHIMIQUES

SPÉCIALITÉ : Physico-Chimie de la Matière Condensée

Par Arnaud DANDRE

Synthèse, caractérisation et mise en forme de nanoparticules à base de $SrTiO_3$ en tant que matériaux d'anode EHT pour le couplage oxydant du méthane

Synthesis, characterization and shaping of nanoparticles based on $SrTiO_3$ as HTE anode materials for the oxidative coupling of methane

Sous la direction de : Cyril AYMONIER,

Et Jean-Marc BASSAT

Soutenue le 10/04/25

Membres du jury :

Mme. GUILLOUX-VIRY Maryline, Professeure, Université de Rennes	Rapporteure
M. IVERSEN Bo Brummerstedt, Professeur, Aarhus University	Rapporteur
M. AYMONIER Cyril, Directeur de recherche, CNRS-ICMCB	Directeur de thèse
M. BASSAT Jean-Marc, Directeur de recherche, CNRS-ICMCB	Co-directeur de thèse
M. DE SOUZA Roger, Professeur, RWTH Aachen University	Examinateur
M. MAGLIONE Mario, Directeur de recherche, CNRS-ICMCB	Président
M. PHILIPPOT Gilles, Maître de conférences, Université de Bordeaux-ICMCB	Examinateur
M. YOKO Akira, Professeur associé, Tohoku University	Examinateur

Acknowledgements

This PhD research was conducted as part of the ANR 2020 call in the field of “Energy and Material Science,” under the project named CHEEC, which stands for “Coupling Catalysis and High Temperature Electrolysis for Ethylene from CO_2.” The project was a collaboration among several French laboratories, including ICPEES in Strasbourg (Institut de chimie et procédés pour l’énergie, l’environnement et la santé), IC2MP in Poitiers (Institut de chimie des milieux et matériaux de Poitiers), CEA in Grenoble (Commissariat à l’énergie atomique et aux énergies alternatives), and ICMCB in Bordeaux (Institut de chimie de la matière condensée de bordeaux). I extend my gratitude to everyone who contributed to this project.

I would like to express my sincere thanks to the directors of ICMCB for their leadership during the three years of my PhD research and for warmly welcoming me to this outstanding workplace. By a stroke of good fortune, they also became my close advisors on my research. I am particularly grateful to Cyril Aymonier and, previously, Mario Maglione for leading one of the most prestigious french laboratories specializing in materials science.

This work was a collaboration between two research groups at ICMCB: Group 7, “Fluides Supercritiques,” and Group 1, “Chimie et Electroceramique.” I would like to thank the group leaders, Samuel Marre and Cathy Elissalde, as well as all the permanent members of both groups for allowing me access to the advanced equipments, essential for the progress of this thesis.

I would also like to express my heartfelt gratitude to the jury members. First, I extend my sincere thanks to Maryline Guilloux-Viry (Université de Rennes) and Bo Iversen (Aarhus University) for their invaluable role as thesis referees and for their thoughtful assessment of this PhD manuscript. I am equally grateful to Akira Yoko (Tohoku University) and Roger De Souza (RWTH Aachen University) for joining the thesis committee as examiners, demonstrating their genuine interest in this research topic.

On a more personal note, I wish to express my deepest gratitude to all my advisors. Warmest thanks go to Cyril Aymonier (once again!) for taking on the responsibility of directing this thesis work. Your exemplary scientific leadership has been an inspiration, and I am proud to be one of the many PhD students you had under your supervision. I wish you the best in your future endeavours as head of ICMCB. I extend my sincere thanks to Jean-Marc Bassat for co-directing this work; his invaluable scientific advice and warm presence greatly enriched our numerous interactions. I will always cherish the memory of you being the “godfather” of my diving baptism.

I am deeply grateful to Gilles Philippot for his guidance and for introducing me to supercritical synthesis. I consider you as the “precursor” behind my proficiency in this complex synthesis method that merges chemistry and engineering. Your insights throughout this work were priceless. Lastly, I would like to thank Mario Maglione (once again!) for supervising the electronic analysis aspect of this thesis. Your problem-solving skills and the stimulating discussions we shared have left a lasting impression. I regard each of you as inspiring mentors, and I will carry forward the invaluable lessons learned during our time together as a personal legacy.

I would also like to acknowledge the collective support staff at ICMCB, whose expertise and dedication made this thesis possible. Special thanks to Eric Lebraud for the X-ray diffraction measurements, Sonia Buffiere for the transmission electron microscopy and energy-dispersive X-ray spectroscopy characterization, Christine Labrugere Sarroste for the X-ray photoelectron spectroscopy, Alexandre Fargues for the optical measurements, Natalie Daro for the CHNS analysis, U-chan Chung for the spark-plasma sintering, and Rodolphe Decourt for the electronic conductivity measurements.

I would like to extend a special thanks to Dany Carlier-Larregaray, Olivier Toutlemonde, and especially Manuel Gaudon. Although we did not collaborate directly, these individuals played an essential role in encouraging me to continue my studies after earning my bachelor's degree at the University of Bordeaux. Without their influence, achieving a PhD would not have been possible for me. I am forever grateful to you all.

Now, I would like to express my heartfelt gratitude to all the wonderful people I met at ICMCB, who made my time there truly memorable. I am thankful to everyone in the supercritical fluids and electrochemistry and ceramic groups, dividing them into yearly "generations" that made this work environment special. I begin by thanking those I met in my first year who welcomed me into this initially daunting field: Erwan, Brian, Emeline, Antoine, Kameel, Elen, Iulia, Olivier (fondly known as “Olive”), Fatma, and Thomas (the unbeatable badminton champion). To the friends I made during my second year, once I had become more familiar with the environment: Jeanne, Rosa, Maïder, Yu, Paola, Richard, Marion, Théo, Elise, Dorian, Florian, Yohann, Thomas (the tennis master), Axelle, “Baba”, Insaf, Enmanuel, Ebtisam, Lucien, Vadim, Zoé, Marine, Jeanice, and Yoan, many thanks for the camaraderie. Lastly, for my third year, as my adventure came to a close, I am grateful to those who arrived and bonded with me despite the short time we shared: Elisabeth, Emma, Abbey, Laurie, Charlotte, Lucas, Anthony, Enzo, Sylvain Stephanio, Valentin, Clémence, and anyone I may have inadvertently left out. I wish you all the best in the years to come, and for those pursuing a PhD, I hope your experience is as fulfilling as mine has been as I write these words.

I would also like to capture and share more personal moments that I will never forget. Yoan and “Olive” (the best engineer who surely knows the secret of eternal youth), thank you for your dedication during the “reactor update.” I couldn't have managed without you. Yoan, I wish you the best in the coming months as you enter the “writing phase”, I have no doubt that you will excel. Neil, congratulations on your accomplishments over these three years. Starting at almost the same time bonded us, and I want you to know that I consider you a friend (despite you drawing the “colleague” line).

A special shout-out to the “Maribor team,” including Fatma, Dorian, and Ebtisam, sharing that conference with you was a fantastic experience. Dodo, we can be proud of ourselves for safely navigating the “Flow Line” at the Pohorje Bike Park. It was a memorable adventure and probably the best beer I’ve ever had! To Elisabeth and Emma, thank you for being my co-riders on the commute to the lab. What began as mutual aid between neighbours during bad weather turned into a strong bond. I am immensely grateful for your presence and your constructive feedback, which (questionably) improved my driving skills and definitely enhanced my social skills. A slight improvement in my punctuality was even noted toward the end of my contract and no, I was not forced to include this part. Finally, thanks to the “BT” team for sharing good times (though not often enough), especially with the “old school” former PhD students of ICMCB. Baptiste, a.k.a. “Baba,” I aspire to emit the same positive energy as you one day. And Thomas, if you ever let me win a single set of badminton, drinks will be on me. The offer extends to you as well, Cyril Nicard. Speaking of drinks, I want to thank everyone I had the pleasure of meeting: Helies, Matthieu, Fouad, Gaël, Jazer, Laurent, Hugo, and everyone else I shared conversations and drinks with. Meeting all of you has been a joy, and I will forever cherish the memories we made together

I want to express my heartfelt thanks to my close friends who have stood by me up to this day. To my childhood friends, Anthony, Antoine, Loris, Alexis, Jordan, Maxime, Alexandre, Clément, Thomas, Lucille, Sébastien, Anthony (Brossard), Axel, and Gabin, thank you for your unwavering support. I also extend my gratitude to the friends I made during my university years, including Chrislain, Jeremy, Marc, Alexandre (Roméga), Olivier (Ivory) (I hope your rap career takes off), Aina, Nicole, Pablo, and Nathan.

To wrap up these lengthy acknowledgments, and because my eyes are getting misty as I write these lines, I would like to thank my parents, Francine and Pierre; my grandmother, Yvette; my “big” brothers, Maxime and Benjamin; my twin brother, Guillaume; and Emma for their unwavering support.

This journey has been an incredible one, and as I close this chapter of my life, you, the readers, are beginning the chapters of this three-year thesis work. Thank you for taking the time to read my research.

Table of Content:

Introduction 12

Chapter 1: Strontium Titanate in 21st Century: Bridging Energy, Environment and Technology 16

1. Strontium Titanate in the 21st Century 17

2. Crystal Structure and Physical Properties 18

2.1 Crystal structure of strontium titanate 18

2.2 Dielectric and Ferroelectric properties 20

2.3 Thermal properties: 26

2.4 Optical properties: 30

2.5 Catalytic properties: 34

2.5.1 Photocatalysis 34

2.5.2 Oxidative coupling of methane 35

2.6 Substitution/Doping of strontium titanate 38

2.6.1 Doping on A-site 38

2.6.2 Doping on B-site 40

2.6.3 Codoping in A and/or B sites 43

3. Synthesis Methods of Strontium Titanate 44

3.1 Solid-State reaction: 45

3.2 Sol-Gel method: 47

3.3 Synthesis methods-based on high-pressure techniques: 49

3.4.1 Hydrothermal synthesis 49

3.4.2 Solvothermal synthesis 52

3.5 Summary on the synthesis of strontium titanate: 53

4. Supercritical Approach for the Synthesis of Strontium Titanate 54

4.1 Supercritical fluids synthesis: Definition and properties 55

4.2 Nanomaterial synthesis using supercritical fluids 56

4.3 Synthesis of strontium titanate-based nanoparticles in supercritical fluids 57

4.3.1 Late achievements on the strontium titanate synthesis 58

4.3.2 Recent achievements on the strontium titanate synthesis 58

Conclusion of Chapter 1 65

Chapter 2: Preparation of Nanomaterials using the Supercritical Fluid Technology: Processing and Characterization 68

1. Synthesis of High-Quality Nanoparticles in Supercritical Fluids 69

1.1 Original setup for the supercritical solvothermal synthesis of undoped and doped $SrTiO_3$ 69

1.1.1 Setup description 69
1.1.2 Materials and method 71
1.2 Improved setup for the supercritical solvothermal synthesis of undoped and doped $SrTiO_3$ 72
1.1.1 Setup description 72
1.1.2 Materials and Methods 75
1.3 Conclusion on the setups development 76
2. $SrTiO_3$-based nanoparticles characterizations 77
2.1 Structural Investigations 78
2.1.1 Powder X-ray diffraction 78
2.1.2 Spectroscopy investigation 79
2.1.3 Size and morphology characterization and elemental investigation 80
2.2 Conclusion 82
3. Shaping of Catalytic Cells and Ceramics 83
3.1 Development of half-cell 83
3.1.1 Ink preparation 84
3.1.2 Screen printing 84
3.1.3 Thermal treatment 85
3.1.4 Deposit characterization 86
3.2 Electronic conductivity of dense ceramics 87
3.2.1 Ceramics processing 87
3.2.2 Spark Plasma sintering 88
3.2.3 Density measurement 89
3.2.4 Electronic conductivity measurement 90
Conclusion of Chapter 2 93
Chapter 3: New Precursors for the Solvothermal Flow Synthesis of $SrTiO_3$ nanoparticles 94
1. Synthesis of $SrTiO_3$ Nanoparticles 96
1.1 Materials 96
1.2 Method 96
2. $SrTiO_3$ Nanoparticles Characterization 97
2.1 $SrTiO_3$ nanoparticles structure 97
2.2 $SrTiO_3$ nanoparticle chemical homogeneity 102
3. *In situ* Investigation of $SrTiO_3$ Thermal Stability and Optimization of $SrTiO_3$ synthesis 106
3.1 *In situ* exploration of supercritical $SrTiO_3$ thermal stability 106
3.2 Toward an understanding of the origin of the defects 113
3.3 Optimization of supercritical $SrTiO_3$ stoichiometry 116
3.3.1 Excess of strontium acetylacetonate precursors 116

3.3.2 Replacement of the titanium precursor and influence of the excess of strontium acetylacetonate precursors 118
3.3.3 Adaptation of the new reactor 121
Conclusion of the Chapter 3 125
Chapter 4: Synthesis, Characterization and Shaping of Doped $SrTiO_3$ Nanoparticles 126
1. Synthesis of Doped $SrTiO_3$ 128
1.1 Selection of n and p doping elements of $SrTiO_3$ 128
1.2 Proof of concept: Doping A and B sites in $SrTiO_3$ 132
1.3 Development of doped optimized composition of $SrTiO_3$ 137
1.3.1 A-site doped $SrTiO_3$ 138
1.3.2 B-site doped $SrTiO_3$ 143
1.3.3 A/B codoped $SrTiO_3$ 145
1.4 Summary 147
2. Shaping of $SrTiO_3$ powders 148
2.1 Shaping of strontium titanate nanoparticles into dense pellets 148
2.1.1 Materials for pelletization 148
2.1.2 Methodology 148
2.2 Pellet characterization 149
2.2.1 Structural characterization of the pellet 149
2.2.2 Determination of the pellet density 151
2.3 Electronic properties of doped $SrTiO_3$ 151
2.3.1 Electronic properties of commercial $SrTiO_3$ 152
2.3.2 Electronic properties of $SrTiO_3$ synthesized by the supercritical solvothermal method 153
2.3.3 Electronic properties of $SrTiO_3$ substituted with dopants 154
2.3.4 Summary 156
3. Shaping Synthesized $SrTiO_3$ Into Electrodes 157
3.1 Structure evolution of the developed electrodes 158
3.2 $SrTiO_3$ deposit characteristics 159
3.3 Summary 160
Conclusion of Chapter 4 162
General Conclusion 164
Perspectives 168
Appendix 170
List of Abbreviations 178
Scientific contributions 180
List of Figures 181

List of Tables 185

Bibliography 186

Introduction

Climate change is a serious concern that must be considered in order to find solutions to reduce environmental risks. According to a study from the International Energy Agency (IEA) published in March 2024, a new record was set at 37.4 billion tons (Gt) in 2023 for the worldwide emission of CO_2. The production increased by 1.1% in 2023, which is equivalent to 410 million tons (Mt). Also, it is important to consider that out of the total worldwide CO_2 emission, 42% is due to the production of electricity. Here is one important sentence from this report, *"Emissions grew in 2023, but clean energy is limiting the growth."* [1].

In order to reduce the impact of electricity production on the emission of CO_2, many solutions are developed, the most famous one being the use of renewable energies. These energies are based on the use of infinite resources such as solar or wind energies. However, these energies have drawbacks compared to conventional methods and fuel energy for producing electricity, one of them being their "flexibility". Their use for electricity production varies based on the time and the period of the year, which accentuates the issue of the inadequate electrical supply/demand over time. To solve this issue, energy storage is currently investigated. Out of the solutions available for the electricity storage/retrieval routes, the conversion of electrons into chemicals represents one of the most suitable solutions, including water/CO_2 electrolysis and catalytic hydrogenation of CO_2 into methane, called power-to-gas (P2G) or, in this case, power-to-methane.

The main existing technology for water electrolysis is the high-temperature electrolysis units (HTE). It gives access to much higher efficiency than low-temperature technology and includes a valorization of (possibly lost or fatal) heat. In addition to the production of hydrogen by water electrolysis, the HTE unit produces oxygen that is difficult to revalorize.

Co-electrolysis, which involves converting water and carbon dioxide into hydrogen and carbon monoxide, is one way to partly solve this challenge. To go even further, the combination of hydrogen and carbon monoxide can produce methane through a power-to-gas process, which can finally be used to create hydrocarbons through the oxidative coupling of methane (OCM).

In this context, this thesis was part of the "Agence National de Recherche" (ANR) project labelled CHEEC, which stands for "Coupling Catalysis and High Temperature Electrolysis for Ethylene from CO_2." The innovation presented was to consider the following case: in conventional high-temperature electrolysis (HTE) systems, the oxygen produced during electrolysis is typically released. However, the concept behind CHEEC involves the use of this oxygen as a reactant for the anodic catalytic conversion of methane into ethylene. If successful this would allow the upgrade of common HTE units based on

the power-to-gas process to a power-to-chemical process, which represents more value than using methane for electricity production since one of the by-products is CO_2.

For this application, two critical physico-chemical properties are required: high catalytic efficiency for the oxidative coupling of methane (OCM) and robust mixed ionic-electronic conductivities. Oxide compounds with a strong basic character, such as La-based oxides, are known to exhibit both properties. Additionally, because high-temperature electrolysis (HTE) also operates under oxidizing conditions, the material must also offer thermal stability, making oxide compounds promising candidates due to their properties.

Since the catalytic reaction in OCM is surface-dependent, nanostructuring the material has been proposed to maximize the amount of active sites and enhance the reaction efficiency. Regarding mixed conductivity, the material must support electron transport, which is influenced by the "energetic distance", or the "energy gap", being the distance between the conduction band and the valence band in a material, also called the band gap, given its role as the anode in the electrolysis unit. For OCM, it should also facilitate the movement of oxygen anions generated as byproducts of water electrolysis at the cathode. Perovskite oxides with the structure ABO_3, specifically strontium titanate ($SrTiO_3$), have been identified as potential candidates based on recent studies highlighting their suitability for OCM.

Strontium titanate is a material of great interest due to its remarkable electrical, optical, and catalytic properties, as well as its chemical stability. Its perovskite-type crystal structure, which allows for various dopings to easily adjust its properties, is central for this PhD project. This historical material, known since the fifties, has been used for many types of electronic applications, especially as supercapacitors, thanks to its dielectric properties. It is also used today in applications such as energy-related applications, with the recent discovery of doped strontium titanate for Li-ion batteries or environmental remediation such as water purification systems based on its photocatalytic properties. Even in biomedical applications, strontium titanate is used as a substrate for drug-release systems for cancer treatment. Staying in the framework of energy-related applications, strontium titanate has been extensively investigated for electrolysis units in combination with fuel cells.

Beyond its role in these processes, strontium titanate also meets critical catalytic property requirements. It functions as a semiconductor with a large band gap close to that of an insulator, yet its perovskite structure allows for straightforward doping at both A and B sites, enhancing its performances and adaptability in various catalytic and conductive applications. The A site corresponds to the edge of the cubic structure occupied by strontium atoms, and the B site is at the center of the cube occupied by titanium atoms. Doping or substituting involves replacing some of the principal cations, such as strontium or titanium, at a certain atomic rate. This modification of the material

impacts its structure, affecting its dielectric, optical, and electronic properties. The purpose of this PhD project was to tune the electronic properties of strontium titanate to exhibit a mixed ionic-electronic conductivity. To obtain nanosized particles, which improve the catalytic performance of the material, the continuous flow supercritical fluid synthesis was chosen.

Based on the knowledge of the “Supercritical Fluids” group at the “Institut de Chimie de la Matière Condensée de Bordeaux” (ICMCB), the chemical synthesis of highly crystallized perovskite-based nanoparticles was achieved on several materials using the supercritical fluid synthesis in a continuous flow. The first supercritical fluid synthesis of strontium titanate at ICMCB was reported in 2005.

This PhD thesis promotes a new way to synthesize strontium titanate using supercritical fluids in continuous flow, with the possibility to produce extrinsic strontium titanate semiconductors, a method previously unaccomplished in the state-of-the-art of strontium titanate and supercritical fluids research. A particular focus is done on the electronic properties following the doping of the material, as well as the electrode cell preparation by screen printing using the knowledge of the “Chemistry and Electroceramics” group at ICMCB.

The first chapter focuses on a complete state of the art on strontium titanate itself, divided into three main parts. First, a full description of the properties of the material is presented based on its structural, dielectric, optical, thermal, and catalytic properties. The catalytic properties are shared in two parts, the photocatalytic properties on one side and its application to the oxidative coupling of methane on the other side. This section is concluded with a table summarizing most of the extrinsic strontium titanate semiconductors prepared, emphasizing how versatile the doping of strontium titanate is. The second part of the first chapter details the different synthesis methods for the production of strontium titanate, going from microscale size particles with the conventional solid-state route down to nanoscale size of particles using the sol-gel synthesis. Other synthesis methods are also mentioned with a focus on high-pressure synthesis technologies such as hydrothermal and solvothermal ones. A third and last part is focused on the general state of the art on supercritical fluid-based synthesis. A focus is done on the synthesis of strontium titanate compounds using the continuous supercritical fluid technology and the recent discovery around the framework subject is delivered.

The second chapter is named “Materials and Methods”. The first part presents the design of the supercritical reactors developed and used during this PhD work. This thesis started using a historical set-up developed at ICMCB in 2004. This was followed by the full design and development of a new supercritical continuous flow set-up that provides a new platform for powder synthesis for the years to come. The second part regroups all the characterization techniques used to provide a full fingerprint of the synthesized $SrTiO_3$-based nanoparticles. The third part introduces the different techniques used

for shaping the nanopowders into electrode cells and dense pellets for the electronic conductivity characterization by four probes measurement.

The third chapter relates the synthesis of strontium titanate nanoparticles using the supercritical continuous-flow process with a new type of precursors. A full description of the material structural properties is given, coupled with advanced *in-situ* techniques. This part highlights in particular the specificity of the supercritical synthesis, allowing the stabilization of particles with a high A-site deficiency.

The fourth chapter presents the structural studies of extrinsic strontium titanate semiconductors. The synthesis has been adjusted to produce doped strontium titanate-based materials with rare-earth such as yttrium, neodymium and praseodymium and/or metal transition such as iron and niobium with varying atomic rate going from 1% to 10%, exposing the versatility of the synthesis method. The shaping of the nanoparticles is presented, with a first part on the production of dense pellets using the spark plasma sintering method. This shaping has allowed a deep study of the electronic conductivity properties of strontium titanate-based materials. The successful production of electrode cells is also highlighted from a slurry of nanoparticles-based formulation.

A last part concludes on the results presented throughout the whole thesis and the achievements related to the synthesis and shaping of the nanoparticles of strontium titanate for advanced applications. A perspective is presented regarding the different improvements that can be made on the synthesis and the opportunities related to the supercritical solvothermal synthesis of oxide.

Chapter 1: Strontium Titanate in 21st Century:

Bridging Energy, Environment and Technology



Image generated by OpenAI's DALL·E, prompted by Arnaud Dandre on December 22, 2024. The image illustrates renewable energy sources, including wind turbines, solar panels, and hydropower in a minimalist style.

1. Strontium Titanate in the 21st Century

This chapter introduces strontium titanate ($SrTiO_3$), a material that has emerged in the fifties [2], and is still considered nowadays as a material of significant interest due to its exceptional properties, and its applications across various scientific and technological domains. This material has unique combinations of electrical, optical, and catalytic properties, along with a high chemical stability.

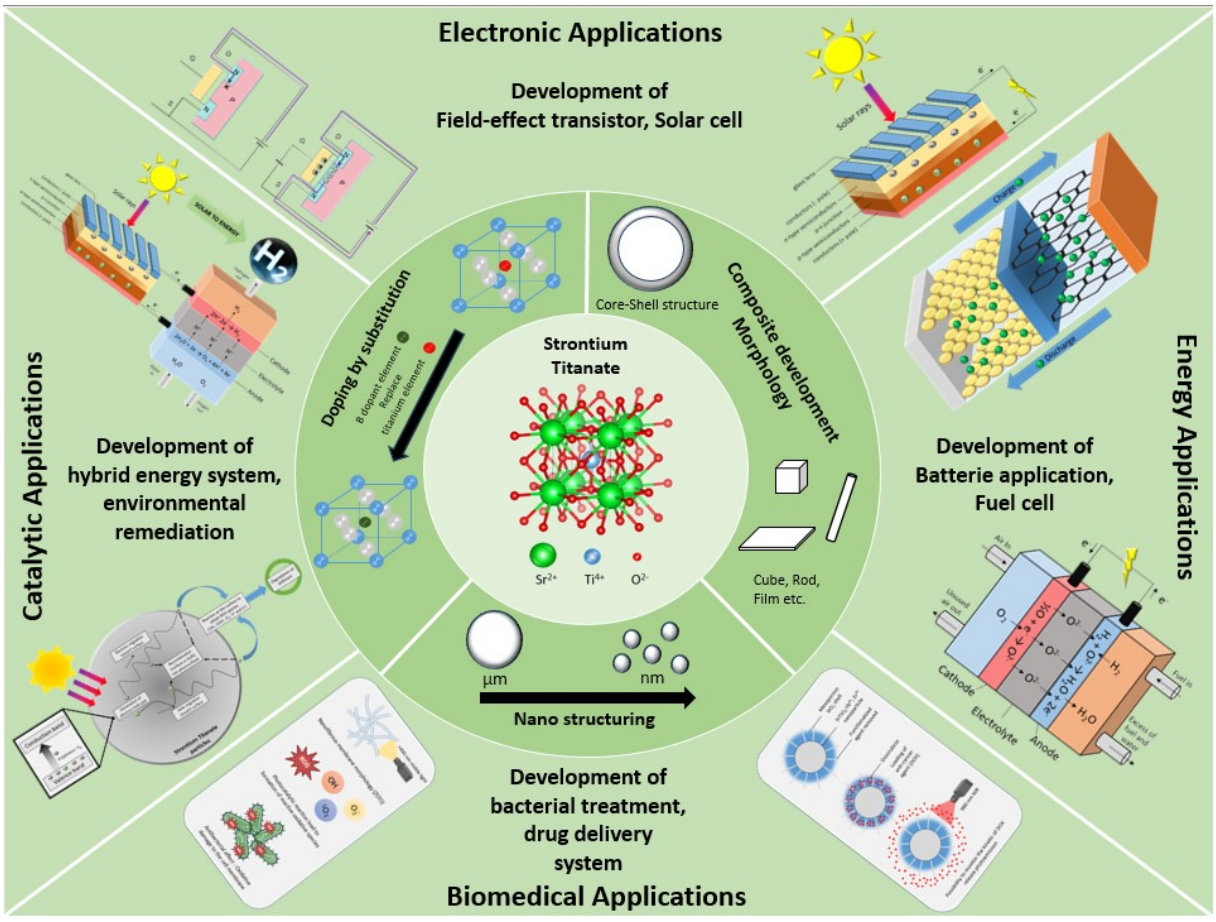

Figure 1.1: Overall summary of strontium titanate possible applications (see Appendix A for details)

One of the key aspects that makes strontium titanate stand out is its crystal structure. It belongs to the perovskite family, characterized by the arrangement of strontium, titanium, and oxygen atoms in a cubic lattice. As described on ***Figure 1.1***, this crystal structure confers to strontium titanate its remarkable physical properties, such as high dielectric constant, incipient ferroelectric combined with excellent stability and chemical compatibility with other materials. In the realm of electronics, strontium titanate has shown promise for various applications. Its high dielectric constant (300 at room temperature) enables miniaturization and increased energy storage capacity. It has been investigated

for the improvement of field-effect transistors (FETs) due to its high dielectric strength which is critical for efficient electronic devices to reduce leakage currents [3–5]. Its use in photovoltaic devices is well known since it could easily convert light into electricity [6–8]. Energy applications are also exploiting the properties of strontium titanate. In the field of solid oxide fuel cells (SOFCs), strontium titanate-based materials have demonstrated satisfying mixed electronic and ionic conductivities, high electrochemical stability, and compatibility with other fuel cell components [9–11]. Similarly, strontium titanate has been recently highlighted as a coating active material for lithium-ion batteries, offering high capacity and improved cycling stability [12–14]. Such developments contribute to the advancement of sustainable energy storage technologies. Catalytic applications represent another important area where strontium titanate has brought significant contributions. The catalytic activity of the material has been leveraged in water splitting reactions for renewable hydrogen production stability [15–17]. Additionally, strontium titanate-based catalysts have shown potential in environmental remediation, facilitating pollutant degradation and water purification [18]. Finally, its potential use for biomedical applications such as drug delivery or bone regeneration proves the versatility of the material [19,20].

The primary objective of this chapter is to provide a comprehensive overview of strontium titanate, encompassing its crystal structure, physical properties and synthesis methods.

2. Crystal Structure and Physical Properties

This section delves into the crystal structure of strontium titanate, highlighting its perovskite structure and the arrangement of strontium, titanium, and oxygen atoms. The impact of the crystal structure on the material properties is discussed in details.

2.1 Crystal structure of strontium titanate

Strontium titanate is a Perovskite crystal structure [21]. The general formula ABO_3 has been described back in 1945 by Helen D. Megaw [2]. In this structure, strontium cations (Sr^{2+}) are located at each edge of a cubic unit cell. These positions are referred to the A sites in the perovskite structure. In this cubic symmetry, each Sr^{2+} cations are surrounded by 12 nearest-neighbor oxygen ions making the coordination number equal to 12. Titanium cations (Ti^{4+}) are found at the center of the cubic unit cell, which is defined as the B sites (***Figure 1.2***). Based on the Shannon table [22], the ionic radius of strontium is equal to 144 pm and the ionic radius of titanium is equal to 60.5 pm. Each Ti^{4+} cations are octahedrally coordinated by 6 oxygen ions (O^{2-}), forming TiO_6 octahedra. Finally, the anions O^{2-} are at the centers of the faces of the cubic unit cell and each anion is shared among two adjacent TiO_6

octahedras [23]. This structure can also be described in terms of coordination and connectivity [24,25]. TiO_6 octahedra shares corners with adjacent octahedra, creating a continuous 3D network [26]. This corner-sharing arrangement is a key feature of the perovskite structure. At room temperature, $SrTiO_3$ adopts a cubic crystal structure with the space group Pm-3m [27]. This contributes to the material unique physical properties, such as its dielectric behavior thanks to a highly symmetrical structure [28–30].

The lattice parameter of cubic strontium titanate is 3.905 Å at room temperature [31–33]. The material also has a symmetry transition feature and can undergo a phase transition at low temperatures [34]. Below near 105 K, it transitions from the cubic phase to a tetragonal one resulting in a slight rotation of the TiO_6 octahedra, leading to a reduction of the symmetry [35]. The features of the perovskite structure led to a rise of several notable properties like its dielectric permittivity, which is due to the high symmetry, and polarizability of its cubic phase. Also its optical transparency, in accordance with a large band gap of 3.2 eV, makes $SrTiO_3$ transparent to visible light [36–38]. It is also interesting to notice that the band gap is temperature-dependent, with a decrease from 3.2 eV at 4 K to 1.8 eV at 1703 K [39]. The wide band gap of strontium titanate is primarily a result of its electronic structure and the nature of the chemical bonds within the material [40]. The highest occupied energy band, which is the valence band of strontium titanate, is mainly composed of electrons associated with the 2p orbitals of oxygen atoms. The conduction band is primarily derived from the titanium 3d orbitals [41,42]. There is a significant energy difference between these orbitals, which contributes to the wide band gap [43]. The bonding nature in strontium titanate involves strong ionic and covalent interactions [44]. The ionic nature of Sr-O and Ti-O bonds lead to a large separation between the valence and conduction bands. The Ti-O bonds, in particular, contribute significantly to the electronic structure. As shown in ***Figure 1.2***, the energy required to excite an electron from the O 2p orbitals is substantial, resulting in a wide band gap. In their study, Kahn *et al.* propose a plot of Madelung potential energies for an electron at various sites of $SrTiO_3$ as a function of the oxygen charge. This one is relatively wide compared to many other semiconductors (e.g. silicon with a band gap of 1.1 eV [45]). The octahedral coordination of Ti^{4+} cations with O^{2-} anions also plays a big part. This coordination affects the splitting of 3d orbitals, contributing to the overall energy difference between the valence band (VB) and the conduction band (CB). Also, the electronegativity differences between oxygen and titanium atoms lead to a larger separation of electronic states, enhancing the band gap [46]. In summary, the wide band gap of strontium titanate arises from its crystal structure, electronic configuration and the nature of its chemical bonds [47]. The significant energy difference between the oxygen 2p orbitals in the valence band and the titanium 3d orbitals in the conduction band results in a band gap of about 3.25 eV [48,49]. Back to ***Figure 1.2***, the energy to excite an electron from an oxygen (2p) state to the closest

cations states is represented by the dotted line considering the gap value mentioned previously. It indicates an ionicity of 85% for the oxygen charge, meaning the effective charge on oxygen is not exactly 2. This suggests that the bonding is not purely ionic. The wide band gap confines strontium titanate light absorption to the UV range, which is a characteristic of its electronic and optical properties.

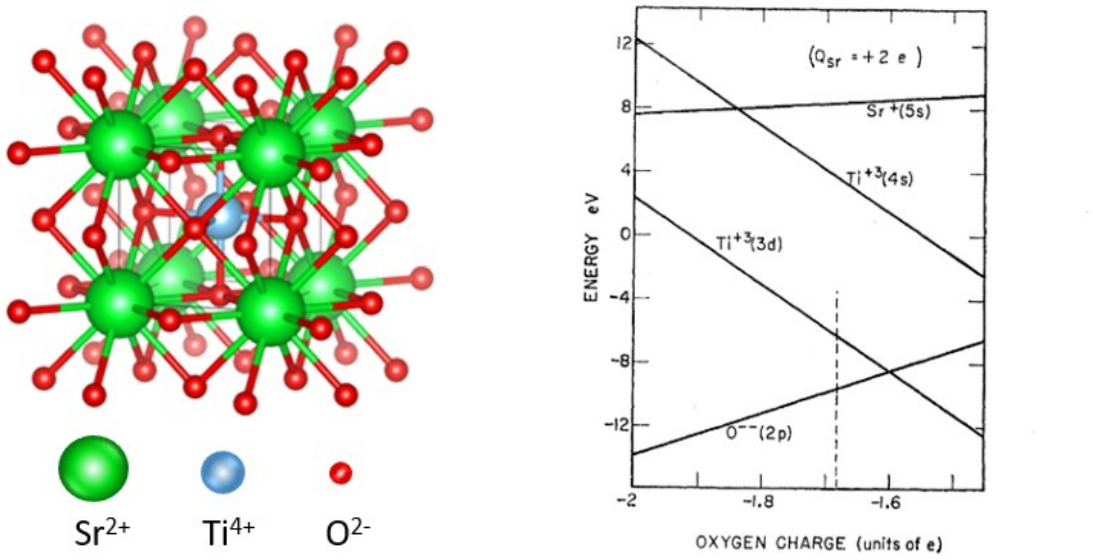

Figure 1.2: Unit cell of the perovskite structured strontium titanate made with the software VESTA (left). Plot of energies on the ionic model as a function of oxygen charge by Kahn *et al.* [49] (right)

It is important to highlight that those properties can be easily modified through doping which, alters its electronic and optical properties. Although $SrTiO_3$ itself is not ferroelectric at room temperature, doping and strain can induce ferroelectricity and piezoelectricity, leveraging the flexibility of the perovskite structure.

2.2 Dielectric and Ferroelectric properties

In this section, strontium titanate dielectric and ferroelectric properties are described, focusing on its high dielectric constant, dielectric loss, polarization behavior, and ferroelectric phase transitions.

The dielectric properties of strontium titanate are primarily characterized by its high dielectric constant, which is significantly influenced by temperature and external electric fields [50]. At room temperature, $SrTiO_3$ exhibits a cubic structure and is paraelectric [51], meaning that it does not have a spontaneous electric polarization but can be polarized by an external electric field. One of the perks of $SrTiO_3$ is its extremely high dielectric constant at low temperatures. At room temperature, the dielectric constant is around 300, but as the temperature decreases, it increases dramatically as shown

on ***Figure 1.3***, reaching values as high as 20000 near liquid helium temperatures (4 K) [52]. A third phase transition was claimed below 51 K where the structure transforms from tetragonal to orthorhombic [53] but there is no consensus about this.

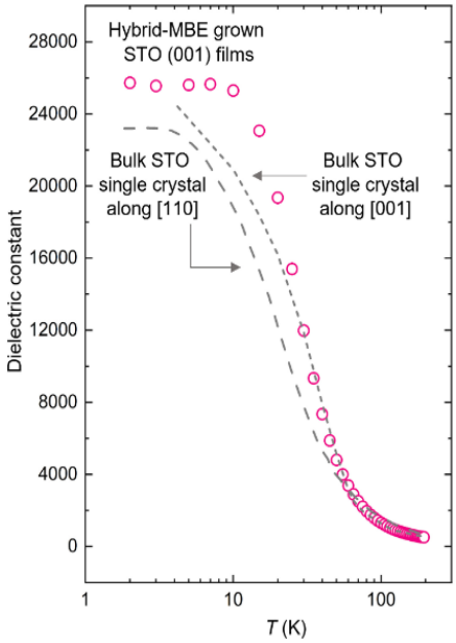

Figure 1.3: Evolution of the dielectric constant along the different crystallographic directions as a function of the temperature by Yang *et al.* [52]

This temperature dependence follows the Curie-Weiss law, leading to a strong link between temperature and electric behavior. The high dielectric constant of $SrTiO_3$ makes it an excellent material for its use in capacitors, where a high capacitance per unit volume is desirable. Additionally, the material low dielectric loss (between 0.0007-0.02 from Wang *et al.* study [54]) makes it suitable for applications in microwave and radio frequency devices, where maintaining signal integrity is critical.

Despite its impressive dielectric properties, pure strontium titanate is not ferroelectric at any temperature, it is called an incipient ferroelectric or quantum paraelectric material, the main outcome being the flattening of the dielectric permittivity versus temperature below 10 K. This means that while it does not exhibit ferroelectricity naturally, it is on the verge of a ferroelectric phase transition and can exhibit ferroelectric properties under certain conditions, such as applying pressure [55], doping [56] or strain engineering [57].

In the classical approach described by Tosatti *et al.* [58] for perovskite ferroelectrics, the ferroelectric transition occurs due to a small permanent displacement of the central cation B towards an off-center position relative to its surrounding oxygen cage. This phenomenon is termed “displacive”. The off-

center displacement of the B cation breaks the octahedral symmetry of the cell which leads to a net dipole moment proportional to the displacement d.

Normally, $SrTiO_3$ remains paraelectric down to very low temperatures due to quantum fluctuations that prevent the establishment of long-range ferroelectric order. However, by ionic substitution into the lattice, ferroelectricity can be induced. For example, with calcium (Ca^{2+}) substitution at low rate such as 4 at.% [59] or/and barium at higher substitution reaching 60 at.% rate (Ba^{2+}) [60,61], the dielectric constant can be drastically boosted (x10 times at room temperature [61]). Even with other rare earth elements (cerium [62], samarium [63], dysprosium [64]) or transition metals (tantalum [65], chromium [66]), a ferroelectric phase can be stabilized resulting from A-site deficiency in the case of cerium doping (1 at.%) or inducing a tetragonal distortion. In the latter, a full solid solution can be obtained in barium strontium titanate (BST). When reaching a threshold, localized lattice distortions resulting from barium substitution can induce a spontaneous polarization. This structure change is explained using the Goldschmidt tolerance factor. The tolerance factor that Goldschmidt proposed for the perovskite structure only accounts to ensure contact between different types of spheres in the structure. Given that the ionic radii are usually well known, it is possible to compute a tolerance factor that represents how "compatible" a particular set of ions is into the ideal cubic perovskite structure. It is considered that the anions act as a separator between the A- and the B-cations.

In the diagonal plane, Goldschmidt tolerance factor is given by equation (1) where r_X corresponds to the radius of the anion (here the oxygen), r_A corresponds to the radius of the A cation (here the strontium) and r_B corresponds to the radius of the B cation (here the titanium).

$$\tau = \frac{r_X + r_A}{\sqrt{2}(r_X + r_B)} \quad (1)$$

It gives information about the preferred crystal structure of perovskite compounds by quantitatively relating the ionic radii of the constituent cations and anions. The tolerance factor provides a tool for predicting whether a particular composition would adopt a cubic, tetragonal, orthorhombic, or rhombohedral perovskite structure by comparing the sum of the ionic radii of the A-site and B-site cations to that of the O anions. By assuming the size of the ions based on the Shannon classification (Sr = 144 pm, Ti = 60.5 pm and O = 140 pm), the τ value is close to 1 predicting a cubic structure for $SrTiO_3$. This relationship is crucial for determining which site within the structure is being substituted by the doping element. It makes sense to use a dopant that has similar ionic radii to the substituted cation to ensure the doping phenomena. Knowing the substitute rate of each element, the values of

r_A or r_B can be calculated, enabling the determination of the tolerance factor. This one should ideally fall between 0.9 and 1, consistently favoring a cubic arrangement as described in **Table 1.1**.

Table 1.1: Perovskite structure at room temperature depending on the tolerance factors (τ) (1998, Carsten Schinzer)

Goldschmidt tolerance factor (τ)	Structure	Example	Cations requirements
> 1	Tetragonal	$BaTiO_3$	Size difference between A and B ions too important
0.9 – 1	Cubic	$SrTiO_3$	A and B ions have « ideal » size
0.71 – 0.9	Orthorhombic	$CaTiO_3$	Size lacking of A ions make them unable to fit into B ions interstices
< 0.71	Hexagonal	$FeTiO_3$	A and B ions have similar ionic radii

Applying a mechanical strain to $SrTiO_3$ can also induce ferroelectricity. When $SrTiO_3$ is grown as a thin film on a substrate with a different lattice parameter, see Tkach *et al.* [67], the resulting strain can distort the crystal structure, leading to a non-centrosymmetric arrangement necessary for promoting a ferroelectric behavior. This strain engineering is a powerful tool in tailoring the ferroelectric properties of $SrTiO_3$ for specific applications but concerns other materials such as $PrVO_3$ [68]. Strain engineering involves the intentional application of mechanical stress to a material to alter its crystal structure and modify its physical properties. This technique is particularly significant in material science.

Those phenomena are due to a lattice mismatch but they can also come from the structure itself like the distortion of TiO_6 octahedra due to pressure as described in ***Figure 1.4***. In the perovskite structure of $SrTiO_3$, the titanium ion is located in the center of each TiO_6 octahedra with oxygen ions at the vertices. Strain alters the distances and angles between these ions and so, for compressive strain, the in-plane Ti-O bounds shorten, the out-of-plane bonds lengthen. In tensile strain, the opposite occurs. It is also important to consider the Ti-O-Ti bond angles. In an ideal perovskite structure, these angles are close to 180 degrees.

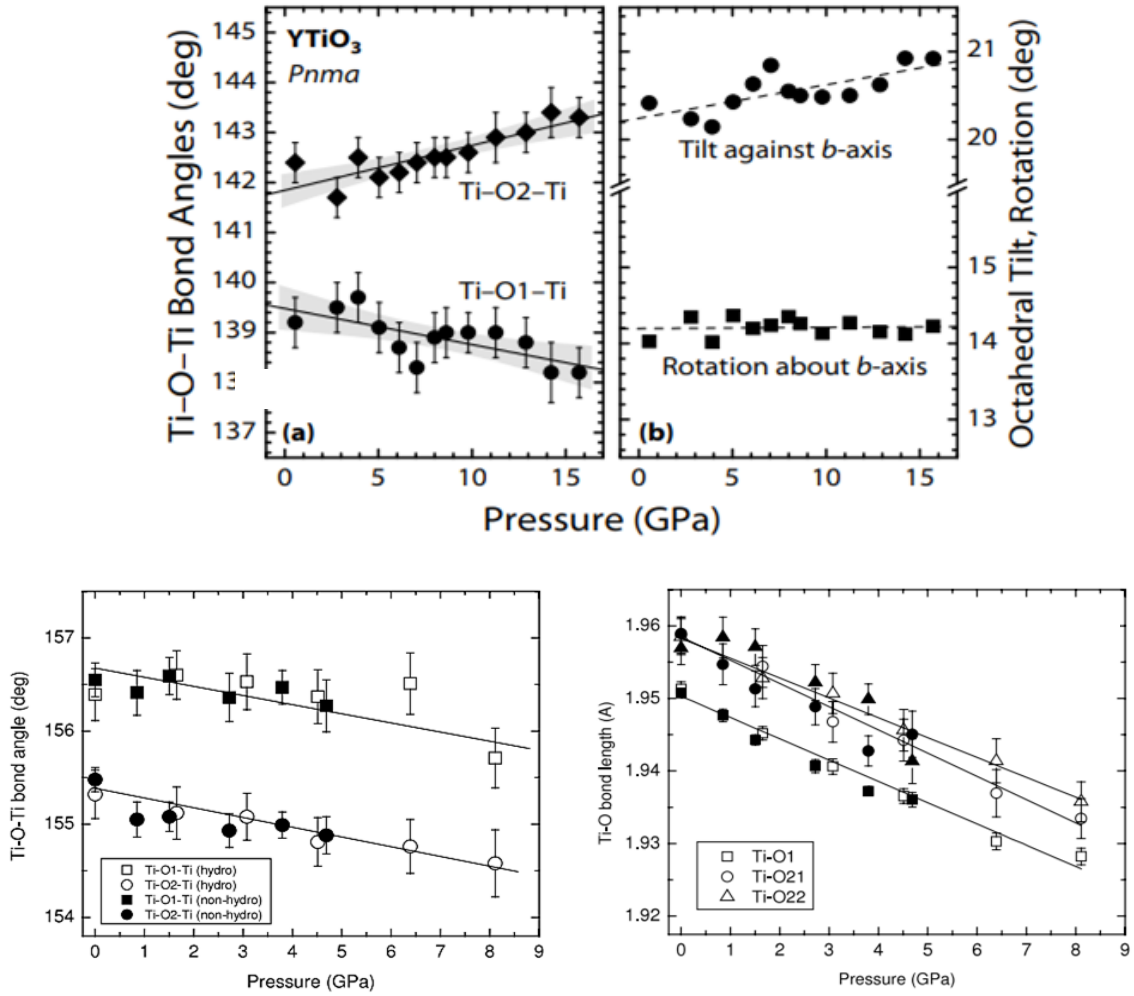

Figure 1.4: Ti-O-Ti bond angles (left) and octahedral tilt and rotation angles (right) in $YTiO_3$ as a function of pressure from Loa *et al.* [69] (top)

Ti-O-Ti bond angles (left) and Ti-O bond distances (right) in $CaTiO_3$ as a function of pressure from Zhao *et al.* [70] (bottom)

Strain can bend these angles away from 180 degrees, distorting the octahedra. These kind of distortions are observable on similar structures such as $YTiO_3$ [69], or $CaTiO_3$ [70].

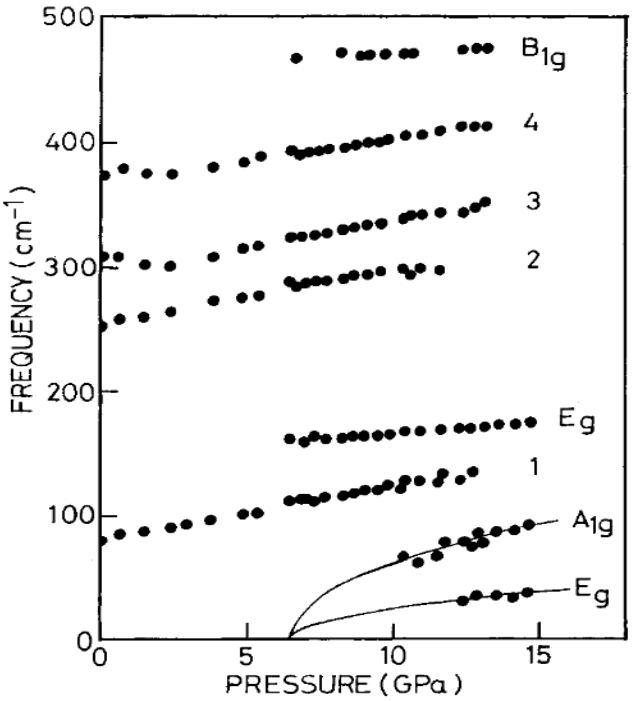

Figure 1.5: Pressure dependence of the second order phonon modes and the first order phonon modes from Ishidate *et al.* [71]

This lattice parameter modification, related to the symmetry of the cubic structure, impacts the overall structure itself by changing its symmetry. It can transform into lower symmetry phases such as tetragonal or orthorhombic under strain, as the apparition of new phonon modes happens as described in ***Figure 1.5***. This transformation occurs because the strain imposes anisotropic forces on the crystal, leading to different lattice parameters along different crystallographic directions. The ferroelectricity induction is done by breaking the symmetry inversion of the crystal, which is a requirement for ferroelectricity. By distorting the TiO_6 octahedral and shifting the position of Ti cations and O anions relative to each other, strain can induce a non-centrosymmetric structure with a spontaneous electric polarization. This induced ferroelectricity can also come from external parameters, such as the hydrostatic pressure. The transition from a non-polar to a polar structure in $SrTiO_3$ can be achieved by applying a pressure of a few gigapascals, as shown by Ishidate *et al.*, applying 6.4 GPa [71].

Figure 1.6 illustrates this through the changes in dielectric properties and the appearance of spontaneous polarization due to structure modification (here from cubic to tetragonal structure) [72].

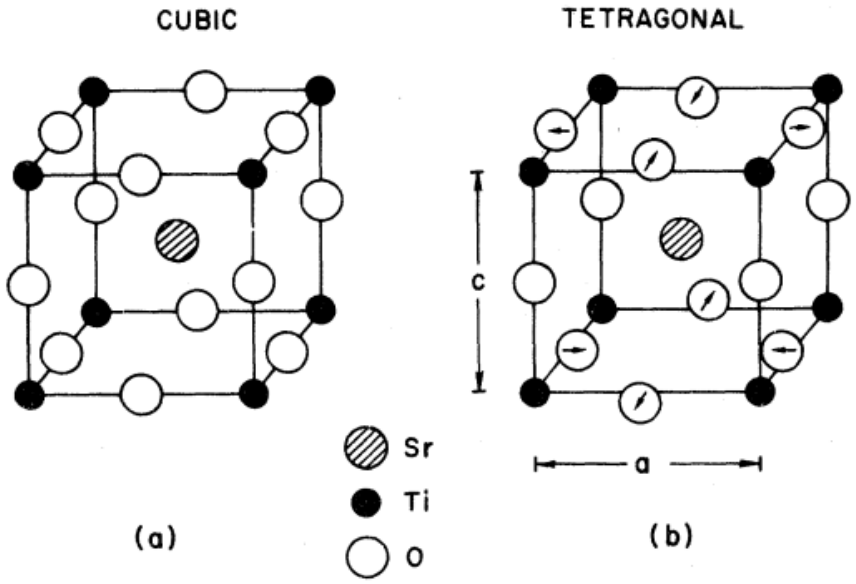

Figure 1.6: Atom positions in cubic $SrTiO_3$ (a) and oxygen atoms displacement indicated by arrow in the tetragonal state (b) from Mattheiss *et al*. [72]

In summary, distorting the crystal structure leads the transformation of the dielectric properties from paraelectric to ferroelectric.

2.3 Thermal properties:

This section details the thermal properties of strontium titanate, encompassing thermal conductivity, thermal expansion coefficient, and the impact of temperature on its properties. The moderate thermal conductivity of strontium titanate (ten times less than Si), depends on many parameters either its morphology such as the grain size [73,74], or the doping [75,76] as described in ***Figure 1.7***. The average value at room temperature is estimated around 12 $W \cdot m^{-1} \cdot K^{-1}$ [74,75,77,78].

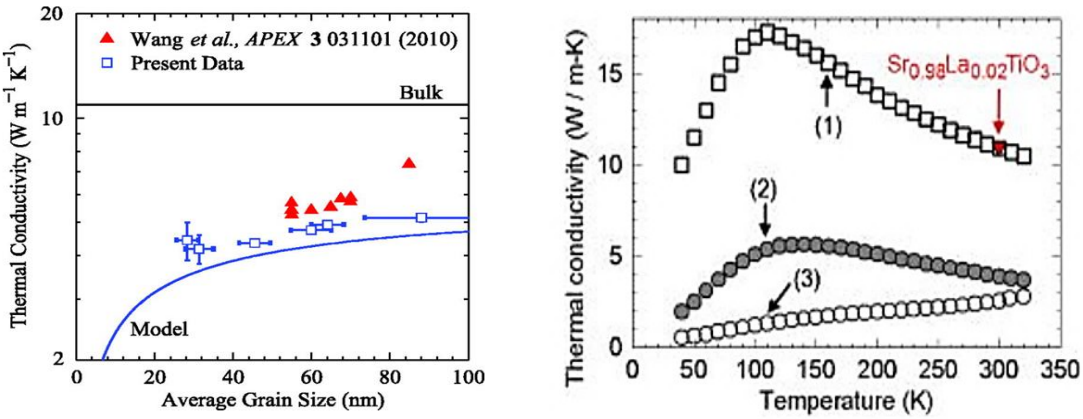

Figure 1.7: Thermal conductivity of strontium titanate as a function of the average grain size from Foley *et al*. [73] (left), the bulk value is represented by the straight line. Thermal conductivity of bulk single crystal strontium titanate as a function of temperature (1), lines (2) and (3) refer to strontium titanate thin film annealed at different temperatures from Yu *et al.* [75] (right)

This property is influenced by the phonon scattering mechanisms which are intrinsic to the crystal structure or composition, as seen previously. Even the atomic density and the nature of atomic bonding (a strong bonding enhances thermal conductivity [79]) are also important to consider. For example, features such as the high density of atoms per unit cell in a material like strontium titanate (5.118 g.cm^{-3}) leads to an increased phonon scattering intercalation due to the increased number of scattering centers, complex lattice dynamics, variations in atomic mass [80], and bonding. In addition, inherent structural disorder, enhanced coupling between vibrational modes, and increased phonon-phonon interactions can increase such scattering. These factors can collectively reduce or increase the mean free path of phonons, resulting in lower or higher thermal conductivity [74,81,82]. Additionally, the presence of dislocations, which can alter the atomic density, influences the phonon scattering and thus the thermal conductivity; high dislocation densities lead to reduced thermal conductivity [83]. This decrease can be explained by more vibrational modes that will increase the phonon-phonon interactions and scattering events. Those complex interactions between vibrational modes can enhance anharmonicity, and so, phonons scattering [84].

In a context of solid-state physics and lattice dynamics, anharmonicity refers to the deviation from the perfect harmonic oscillator model in the potential energy of atoms within a crystal lattice. In a purely harmonic system, atoms in the lattice are assumed to oscillate around their equilibrium positions with forces that are directly proportional to their displacements. This is considered as a parabolic potential energy function. However, real crystals exhibit anharmonicity, where the potential energy function deviates from this ideal parabolic shape, especially at higher amplitudes of atomic displacement. This means that the forces restoring atoms to their equilibrium positions are not perfectly proportional to the displacements, leading to non-linear terms in the potential energy function. The anharmonicity

impacts the way phonon-phonon interactions happen. Phonons are considered as quasiparticles [85] representing the quantized modes of vibrations in a crystal. In a purely harmonic crystal, phonons would not interact with each other because the lattice vibrations would be independent. To delve deeper into details, the anharmonic phonon allows for three-phonon interactions [86], where two phonons can combine to form a third one (absorption process) or a single phonon can divide into two phonons (decay process) as represented in ***Figure 1.8***. These processes are forbidden in a purely harmonic crystal because energy and momentum conservation rules would not permit them without anharmonic terms. This is a direct impact on the phonon lifetime, which is the average time where a phonon can travel before interacting with another one (mean free path). This is because the anharmonic terms in potential energy increase the probability of phonon-phonon interactions. It leads to a decreased mean free path, which corresponds to the average distance for a phonon traveling between interactions. It is reduced due to an increased phonon-phonon scattering. This results in a higher rate of phonon collisions, leading to more frequent energy and momentum exchanges [87].

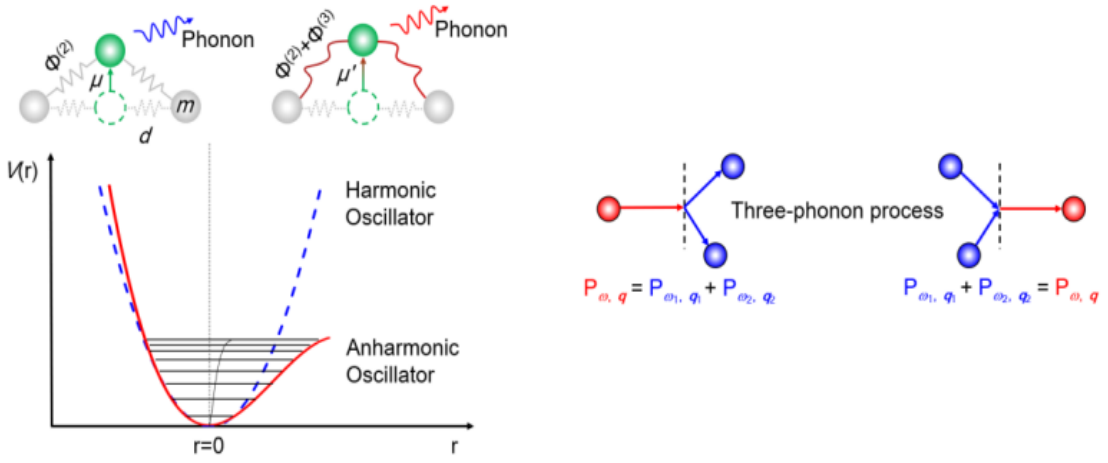

Figure 1.8: Representation of the harmonic and anharmonic phonon with a 1D ball and spring model (left). Sketches of the three phonon scattering processes with decay and absorption respectively (right) from Wei *et al.* [87]

Basically, the thermal conductivity in insulators and semiconductors is primarily due to phonon transport. When anharmonicity increases phonon-phonon interactions, it enhances the scattering of phonons, thus reducing their ability to carry heat efficiently. To summarize, anharmonicity in a crystal lattice introduces non-linear terms in the potential energy, leading to deviations from the ideal harmonic behavior. This anharmonicity facilitates the phonon-phonon interactions by allowing processes where phonons can scatter off each other, merge or split. Increased phonon-phonon interactions due to anharmonicity reduce phonon lifetimes and mean free paths, thereby decreasing the material thermal conductivity. Understanding anharmonicity is crucial for tailoring materials for

specific thermal and electronic applications, especially where thermal management is a key concern [88].

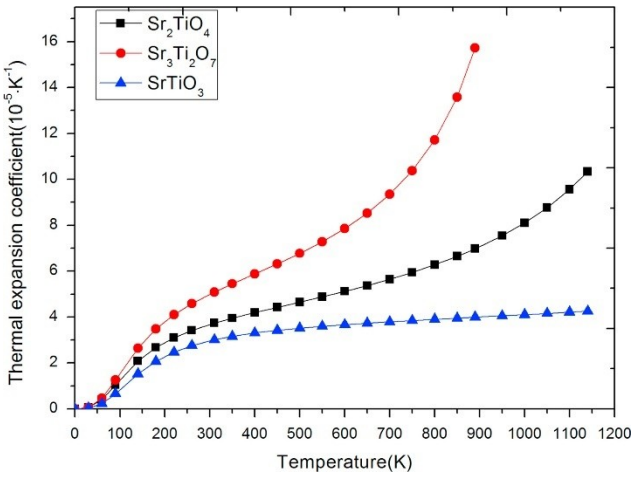

Figure 1.9: Thermal expansion coefficient of cubic perovskite and layered perovskite strontium titanate as a function of temperature from Lu *et al.* [92]

The thermal expansion coefficient (CTE) of $SrTiO_3$ is about 1 x 10^{-5} K^{-1} at room temperature (***Figure 1.9***) [89–92]. This property indicates that strontium titanate expands and contracts at a predictable rate with temperature changes, which is important for maintaining the structural integrity in thermal cycling applications. This involves understanding how the atomic lattice responds to temperature changes at a microscopic level. The physical basis of thermal expansion considers the atomic vibrations. Atoms in a solid are not static, they vibrate around their equilibrium positions. The amplitude of these vibrations increases with temperature due to the increase in thermal energy. It also considers the anharmonic potential, which causes the average distance between atoms to increase as the temperature rises, because the potential energy curve is asymmetric, typically being shallower at higher energies. Finally, it depends on the interatomic forces, because their nature (ionic, covalent or metallic) affects how strongly atoms are bound together, and how the interatomic distances change with temperature. The presence of vacancies can also change the value [93]. In the strontium titanate structure, as the temperature increases, the atoms vibrate more intensely, and the anharmonic potential allows the average atomic separations to increase, leading to the thermal expansion of the lattice parameter [94]. Strontium titanate also exhibits different phases upon temperature such as a cubic phase at temperatures above 105 K, and a tetragonal phase at temperatures under 105 K. This phase transition affects the coefficient of thermal expansion [92]. In the cubic phase, thermal expansion is isotropic in all x, y and z directions [94] while in the tetragonal phase, thermal expansion becomes anisotropic due to the different lattice parameters along the different crystallographic axes

which is observable on other tetragonal structure materials. ***Figure 1.10*** shows the evolution of the *c* and *a* parameters for strontium borate [95].

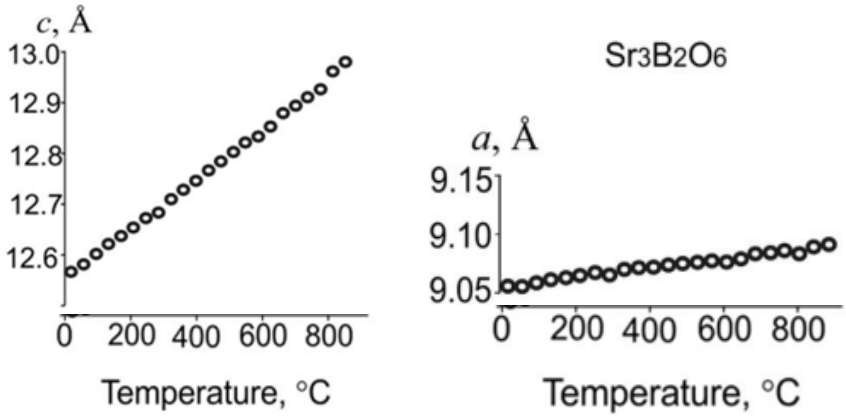

Figure 1.10: Temperature dependencies of unit-cell parameters of strontium borate from Filatov *et al.* [95]

To summarize, the coefficient of thermal expansion in strontium titanate is a result of the anharmonicity in the potential energy of its atoms. The perovskite structure of $SrTiO_3$ responds to thermal vibrations by expanding, and this expansion can vary depending on the crystallographic phase and temperature. The phase transition from cubic to tetragonal near 105 K introduces anisotropy in the thermal expansion properties, demonstrating how temperature-induced lattice dynamics play a crucial role in determining the thermal behavior of strontium titanate.

2.4 Optical properties:

In this section, the optical properties of strontium titanate are discussed, focusing on its transparency in both the visible and infrared regions, its refractive index, and its optical absorption. Additionally, the impact of dopants and defects on these optical properties is also discussed.

Strontium titanate is a material renowned for its exceptional optical properties, which makes it valuable in various applications, including photonics [96], optoelectronics [97], and as a synthetic gemstone [98]. These properties are primarily influenced by its crystal structure and the electronic transitions within the material.

Strontium titanate possesses a wide band gap, which means that $SrTiO_3$ is transparent to visible light, and can absorb ultraviolet light [99,100]. Its large band gap means that its conductivity is rather low ($\sigma \approx 10^{-9}$ S.cm^{-1} at 25 °C [101]), and so its resistivity is high [102,103]. ***Figure 1.11*** shows the optical properties such as its band structure, and its absorption spectra. A direct band gap is described by the

following approach: in a semiconductor with a direct band gap, the minimum of the conduction band, and the maximum of the valence band occur at the same k-vector value in the Brillouin zone. This means that an electron without any change in its momentum can directly have a transition from the valence band to the conduction band, and *vice-versa*. This is a key characteristic regarding the photon absorption and emission. Since it involves no change in momentum, the photon emission/absorption is efficient. Conversely, an indirect band gap is described as the minimum of the conduction band, and the maximum of the valence band occurring at different momentum (k-vector) values. This implies that an electron transitioning from the valence band to the conduction band (or vice versa) must undergo a change in momentum. The impact on the absorption/emission is that the transition of electrons requires a change in momentum facilitated by phonons themselves [104]. The tunable band gap is possible thanks to the use of dopants such as transition metals or strain engineering [97]. Regarding the value of the band gap, it is important to take into account the multiple techniques (such as UV-Vis spectroscopy, Scanning Tunneling Spectroscopy or Electron Energy Loss Spectroscopy) used to determine it, from optical spectroscopy [105] to computational simulation [106], leading to different values.

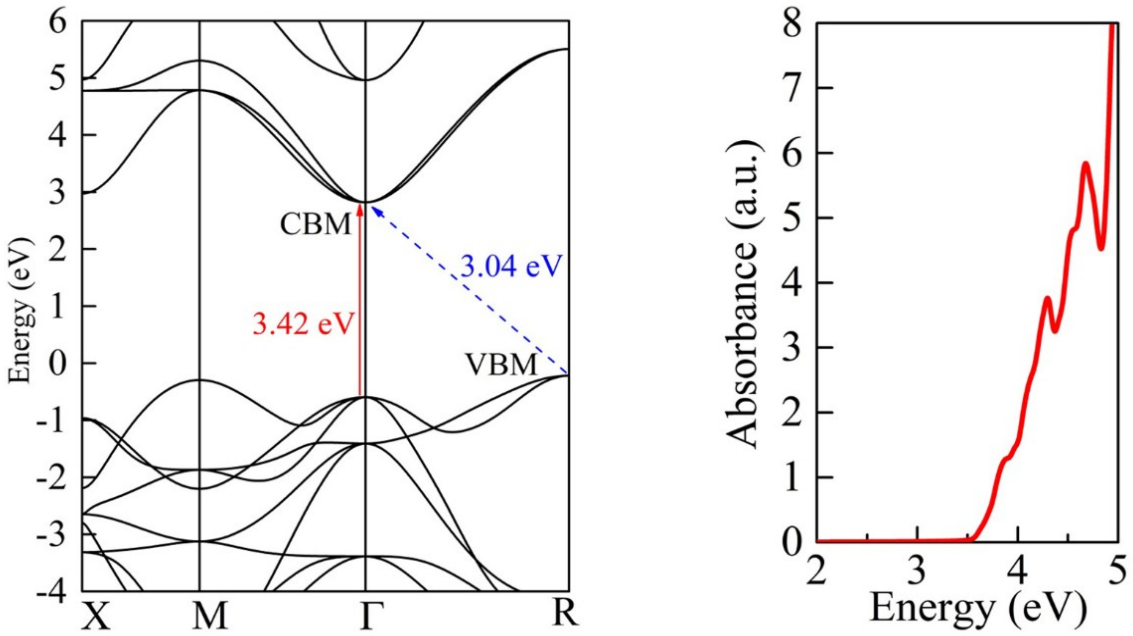

Figure 1.11: Band structure of pristine strontium titanate (left) and optical absorption of pristine strontium titanate (right) from Hou *et al.* [106]

One of the most notable optical properties of $SrTiO_3$ is its high refractive index (diamond being a reference with 2.4 [107]) of 2.38 at room temperature and λ = 600 nm as shown in ***Figure 1.12*** [108,109].

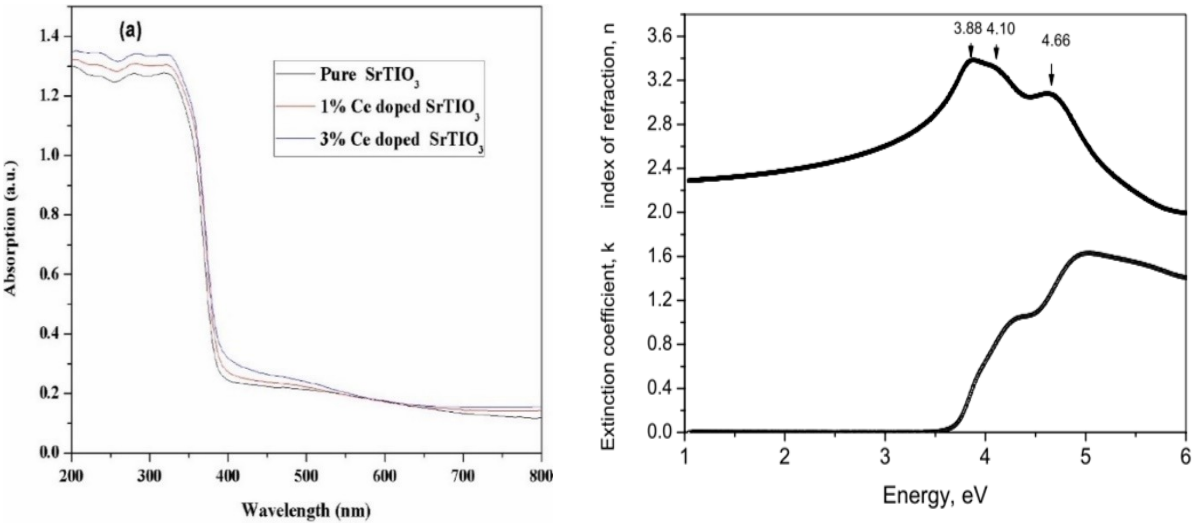

Figure 1.12: UV-Visible spectroscopy of pure strontium titanate and cerium doped strontium titanate (3 at.%) from Saravanan *et al.* [100] (left). Index of refraction of bulk strontium titanate from Trepakov *et al.* [109] (right)

Its high refractive index is explained by many factors such as its polarizability. This microscopic property describes how individual atoms within the material answer to the electric field, and how easily their electrons could be distorted [110]. Indeed, the light interacts with the material electron cloud and leads to oscillations [111,112]. It is also deeply bound to the crystal structure, and contributes to the overall polarizability [26,113]. The bonding characteristics play an important role since the material is mainly made by mixed ionic and covalent bonding [114]. The ionic bonds come from massive differences of electronegativity, leading the electrons to be transferred from one atom to another, creating positive and negative ions. The phenomenon of polarization results from the separation of charges within the material. The positive and negative ions are transferred in opposite directions, which leads to an induced dipole moment. The nature of covalent bonds comes from the sharing of electrons between atoms with similar electronegativity. Here, the interaction between the electric field of the light and the atomic bonding causes a deformation of the electron clouds associated with the shared electrons. This distortion occurs because the electrons are not as tightly bound to anyone in the nucleus as in ionic bonds, making them more susceptible to be modified by the electric field [115–117].

Strontium titanate features a perovskite structure where the bonding is mostly ionic between Sr^{2+} and O^{2-}, and mostly covalent between Ti and O [118,119]. To resume, the ionic component contributes to strong polarization effects, while the covalent component allows for significant electron cloud distortion. This polarizability is also linked to the ionic radius of the strontium ions (Sr^{2+}) and is relatively large; so the ions have loosely bound outer electrons compared to smaller ones [120–122]. The

electron cloud around Sr^{2+} ions is more easily distorted by the electric field of light and so leads to a high polarizability and thus a higher refractive index [123]. ***Figure 1.13*** represents the bonding between the different elements using the maximum entropy method charge density distribution following the different planes.

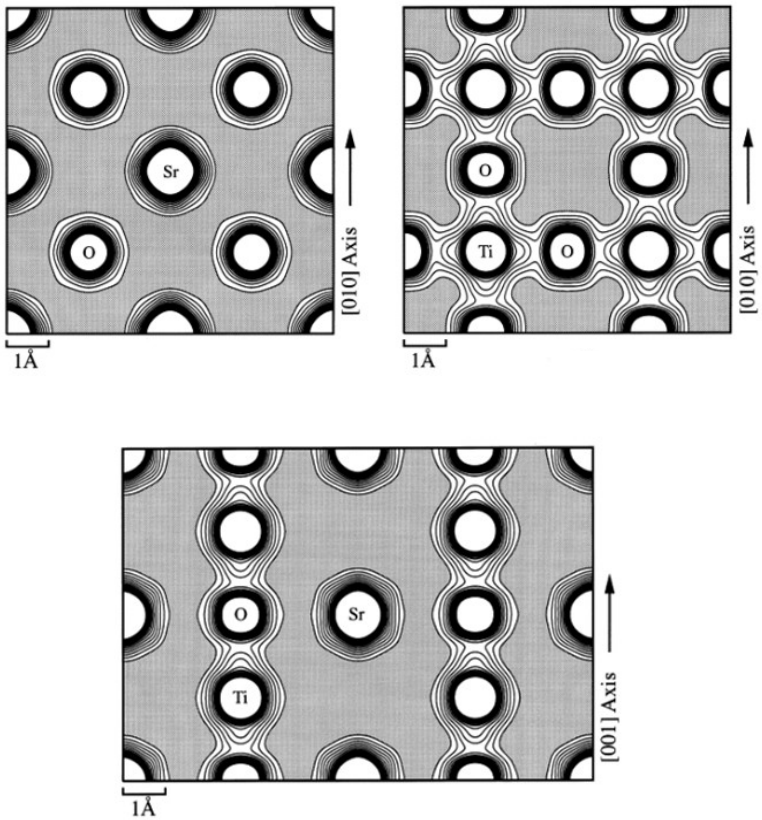

Figure 1.13: The maximum entropy method (MEM) charge density distribution of strontium titanate at room temperature. Plane (001) (left) and plane (002) (right) from Ikeda *et al.* [118] (top)

Maximum entropy method (MEM) charge density distribution of strontium titanate at room temperature. Plane (110) from Ikeda *et al.* [118] (bottom)

A last characteristic worth mentioning is that the refractive index is not constant and depends on the frequency of the incident light. This phenomenon, known as optical dispersion, indicates a rather strong electronic polarizability across different light wavelengths. The strong interaction between light and the material electronic structure at various frequencies leads to a consistently high refractive index. This optical dispersion is strongly linked to the crystal structure. Any modification of the structure alters the dielectric properties, which impact the optical ones of the material such as the refractive or the spectral absorption. Using doping, strain engineering, or morphology, led to this modification [97,124]. It is worth mentioning the versatile tuning of its conductivity. A modification of its band gap spacing will induce a modification of the electronic properties, and increase its conductivity either with n-donor (rare earth on A site) [125–127], or p-donor (transition metal on B

site) [128–131]. The doping can induce a metallic electronic transport [132] or even enhance the mixed-ionic electronic conductivity type [133].

To summarize, its high refractive index is primarily due to its significant electronic polarizability, and its perovskite crystal structure. Its ability to be easily polarized in response to an electric field, combined with the strong interaction between its electronic structure and the incident light, results in a higher refractive index. The mixed ionic-covalent bonding and large Sr^{2+} ions further enhance this property. The electronic properties which result from its band gap can also be tuned by principally doping to fulfill the different requirements for applications.

2.5 Catalytic properties:

In recent years, $SrTiO_3$ has been studied for its potential applications in catalysis and photocatalysis for water splitting, and, notably, for the oxidative coupling of methane (OCM). In the framework of the present project, a focus on the oxidative coupling of methane is evidenced.

2.5.1 Photocatalysis

Strontium titanate can be used in water purification, leveraging its photocatalytic properties [134]. The mechanism of water purification implies a first step of photocatalysis where the material acts as a photocatalyst under UV light [18]. The degradation of contaminants uses the reactive oxygen species (ROS) generated in the photocatalytic processes, which are highly reactive and are effective on various organic pollutants, such as dye, pesticides, and pharmaceuticals, into harmless byproducts like carbon dioxide and water. The ROS generated during the photocatalytic process can also attack and destroy bacterial cell walls and other microorganisms, leading to the disinfection of water [135].

The main advantage of strontium titanate is the possibility to tune the composition by doping with transition metals such as copper [136], nickel, aluminum [137], and cobalt, consequently the band gap is narrowed, allowing strontium titanate to absorb visible light and enhancing its photocatalytic efficiency under solar illumination. Defect engineering can thus improve the photocatalytic performance [138]. It is possible to produce nanostructured strontium titanate with increased surface area, providing more active sites for photocatalytic reactions, thereby enhancing the degradation rate of pollutants. Improved morphology can also contribute to more efficient absorption and charge transfer [139]. It can be coupled with the formation of composites such as graphene and carbon quantum dots [140], or other semiconductors (*e.g.* TiO_2 [141]), which improve the charge separation and enhance the photocatalytic activity. These composites can create heterojunctions that facilitate

the transfer of photogenerated electrons and holes to different materials, reducing the recombination and enhancing overall efficiency [142].

2.5.2 Oxidative coupling of methane

Strontium titanate offers several advantages as a catalyst for the oxidative coupling of methane (OCM) reaction. Methane (CH_4) is the primary component for natural gas and represents an opportunity as an underrated resource. For example, the storage of the excess of electric energy produced by renewable energy led to its waste if it is not used. Thanks to a power to gas reaction (P2G), this excess of electricity can be converted into methane, which is much more easily storable, and can be converted back into electricity when needed. This could be achieved by the use of an electrolysis unit as shown in ***Figure 1.14***.

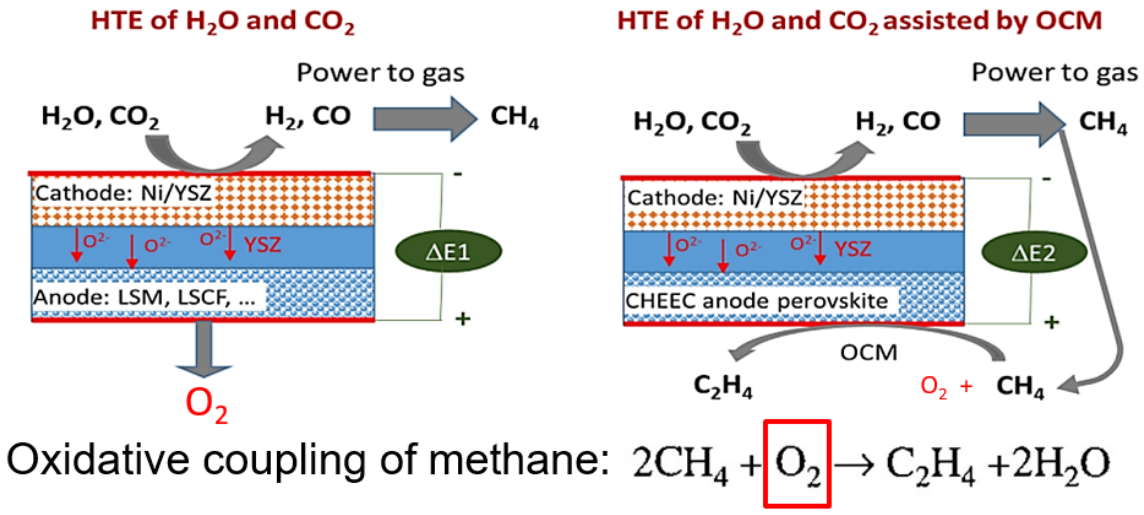

Figure 1.14: Scheme of the potential upgrade of high temperature electrolysis unit from a power to gas process to a power to chemical achieving the conversion of methane into ethylene by OCM

The oxidative coupling of methane offers a direct and potentially lower-emission reaction to produce C_2 hydrocarbons like ethylene (C_2H_4), which is an essential feedstock in the petrochemical industry. However, the main challenge to develop efficient catalysts is to control reaction pathways to maximize the production of desired C_2 products while minimizing complete oxidation to CO_2.

This is where strontium titanate represents a major candidate as a potential catalyst. The perovskite ABO_3 catalysts have been previously studied, including La-based ones, where it was demonstrated that surface lattice oxygen species are capital for the selective conversion of methane as it is described in ***Figure 1.15*** [143].

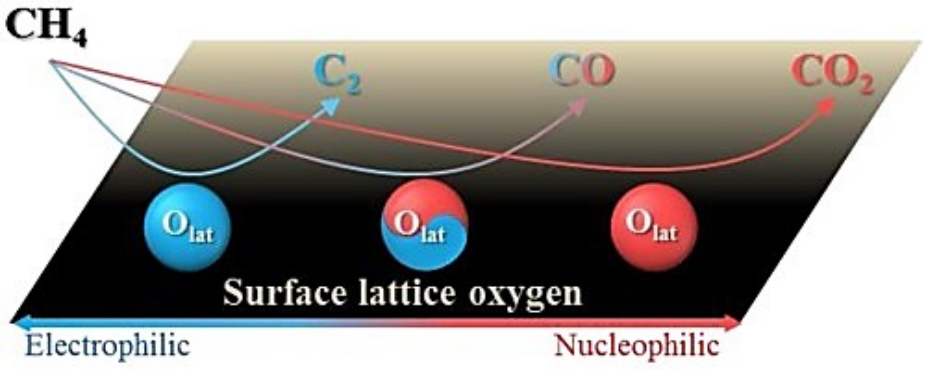

Figure 1.15: Graphical abstract of Kim *et al.* [143] in a paper showing the different CH_4 conversion route based on the different selective oxygen species

Thanks to its thermal stability, strontium titanate can increase the efficiency of OCM operating under high temperature (up to 800 °C) [144], favouring C_2 production while maintaining moderate methane production. In 2022, Thanh *et al.* [145] showed that $SrTiO_3$ achieves a methane conversion rate of approximately 35% at 850 °C. However, they reported a low ethylene yield reaching 0.12% at 800 °C. Also, the catalytic performance is influenced by surface composition, where a higher surface density of strontium enhances CH_4 conversion and C_2 selectivity [146]. In 2022, Pavlova *et al.* [147] showed that the layered perovskite Sr_2TiO_4, with different surface Sr concentrations and active surface oxygen species such as oxygen vacancies could be optimized and lead to a CH_4 conversion and C_2 yield reaching 25.6 and 15.5% respectively, at 900 °C. Conversely, it is important to consider that the presence of defects such as oxygen vacancies also promotes the high selectivity of C_2 conversion [148,149]. One way to tune electronic surface structure and oxygen species of strontium titanate is its doping. In 2019, Lim *et al.* [150] presented a deep insight on the effect of partial substitution on the catalytic properties of $SrTiO_3$ perovskite. By tuning the electrophilic character, the OCM can be promoted. This study also highlighted, using density functional theory (DFT), the impact of oxygen vacancy formation energy (E_f(vac)) between 2 and 4 eV specific to each substituted composition. ***Figure 1.16*** shows the suggested surface reaction in the case of high E_f(vac).

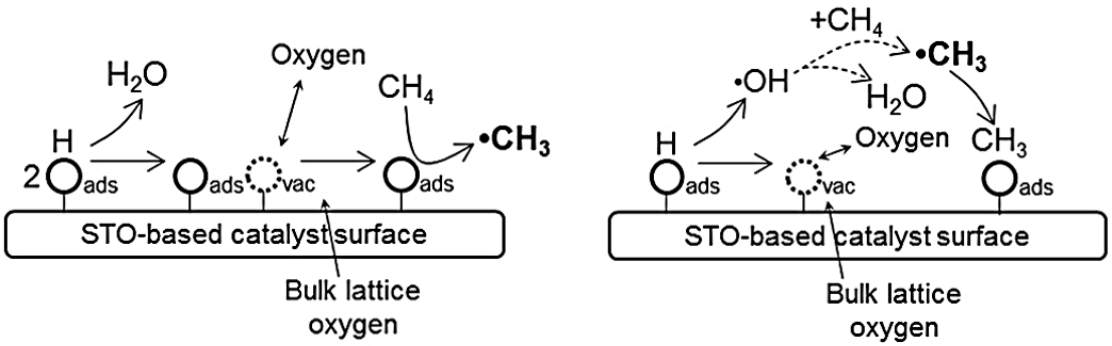

Figure 1.16: Suggested surface reactions as depicted by Lim *et al.* [150]

It is stated that a high E_f(vac) leads to an increase of $\cdot CH_3$ radical formation which induces the production of more CO and CO_2 species, and limits the production of C_{2+} hydrocarbons. The study concludes that the best dopants are neodymium and praseodymium, located in the B-site of the perovskite. However, no lattice parameter study confirms the successful doping of the elements in this study.

Overall, the introduction of dopants into $SrTiO_3$ allows to tune its key properties that play an important role for the OCM process. By altering the material properties, these changes increase its efficiency and broaden its functional applications, addressing issues such as low reactivity and limited performance seen in the pure, undoped form as shown by the increase of C_{2+} selectivity for certain doping elements.

Within the framework of the project CHEEC, previous studies emphasizing the potential of strontium titanate, and its doped variants, formed the basis for exploring its use as a catalyst in the oxidative coupling of methane reaction. As noted earlier, doping can modify the electronic properties of inherently highly resistive strontium titanate, converting it into a material with mixed ionic and electronic conductivity, suitable for advanced HTE units. This thesis focused on producing nanoparticles of both undoped and doped strontium titanate with the supercritical continuous flow synthesis method.

The next section will discuss how various dopants affect the structural, electronic, optical and dielectric properties of strontium titanate.

2.6 Substitution/Doping of strontium titanate

In the previous part, we mentioned the application of strontium titanate related to its photocatalytic properties for energy applications. However, the bare material itself is not concerned. One of the major benefits of strontium titanate lies in its versatile perovskite structure. It allows intentional introduction of dopant atoms into the strontium titanate structure.

The synthesis of extrinsic strontium titanate semiconductor has been thoroughly investigated up to now. This part presents a summary of all the elements used for the tuning of bare strontium titanate.

2.6.1 Doping on A-site

This part presents the research works concerning A-site doping. The replaced atom is the strontium ion, which has an ionic radius of 144 pm with a coordination number of twelve (CN=12), which is two times bigger compared to the ionic radius of titanium (60.5 pm with CN=6). ***Table 1.2*** presents a state of the art of existing compositions with the ionic configuration, the synthesis way, one of the targeted properties to be tuned, and the associated reference.

Based on this summary, the main type of dopant elements reported are rare-earth elements thanks to their ionic radius being two times bigger than B-site dopants. It is important to consider that the Shannon table does not give a defined value for most of the rare earth with a coordination number of twelve. However, we supposed that as CN increases, the ionic radius also increases slightly accordingly. The ionic radius of the mentioned dopant is hypothetically smaller than the ionic radius of strontium. They also all possess a valence of 3+, which, in 100% of the case, lead to a n-semiconductor, except for calcium. The dielectric properties are modified even in A-site doping, which is linked to the decrease of the lattice parameter. Based on the reference found, there is a balance between the solid state and the sol-gel reactions, perhaps based on the viability of the precursors depending on the synthesis method. This large panel still allows modification of either the electronic, optical, dielectric and thermal properties.

Table 1.2: Summarized A-site doped strontium titanate

Dopant	Ionic configuration	Ionic radius for CN=12 (pm)	Substitution rate	Synthesis	Tuned property	Reference
Calcium	Ca^{2+}	134	x = 0.40	-	Dielectric	[151]
Yttrium	Y^{3+}	122	0 < x < 0.10	Sol gel	Electronic	[152]
Cadmium	Cd^{2+}	131	0 < x < 0.05	Solid-state	Optical	[153]
Bismuth	Bi^{3+}	117 (CN=8)	x = 0.053	Solid-state	Dielectric	[154]
Lanthanum	La^{3+}	136	0 < x < 0.09	Sol-gel	Electronic	[155]
Cerium	Ce^{3+}	134	0.005 < x < 0.04	Solid-state	Dielectric	[62]
Praseodymium	Pr^{3+}	130	0.05 < x < 0.30	Solid-state	Electronic	[125]
Neodymium	Nd^{3+}	127	-	Solvothermal	Optical	[156]
Samarium	Sm^{3+}	124	0 < x < 0.05	Solid-state	Optical	[157]
Europium	Eu^{3+}	112 (CN=9)	0.01 < x < 0.07	Sol-gel	Optical	[158]
Gadolinium	Gd^{3+}	111 (CN=9)	0 < x < 0.20	Solid-state	Electronic	[126]
Terbium	Tb^{3+}	88 (CN=8)	x = 0.02	Sol-gel	Optical	[159]
Dysprosium	Dy^{3+}	109 (CN=9)	0 < x < 0.05	Solid-state	Dielectric	[64]
Holmium	Ho^{3+}	112 (CN=10)	x = 0.025	Sol-gel	Electronic	[127]
Erbium	Er^{3+}	106 (CN=9)	-	Solid-state	Optical	[160]
Thulium	Tm^{3+}	105 (CN=9)	x = 0.005	Sol-gel	Electronic	[161]
Ytterbium	Yb^{3+}	104 (CN=9)	0 < x < 0.075	Sol-gel	Optical	[162]
Lutetium	Lu^{3+}	103 (CN=9)	x = 0.02	Sol-gel	Optical	[163]

It is interesting to mention that the doping through A-site in strontium titanate significantly influences the mentioned properties also because of the introduction of cationic defects. For instance, A-site vacancies are introduced by doping with n-dopant (donor), i.e. a cation with a higher valence. Meanwhile, substituting with p-dopant (acceptor), i.e. a cation with a lower valence could lead to the creation of oxygen vacancies in a compound ABO_3 if the B-site valence remains unchanged. Verbraeken *et al.* published a complete study on the exploitation of defect chemistry in strontium titanate for the application of SOFC anode [164]. In the framework of boosting the electronic conductivity, the impact of donor substituted is attested by stating that their introduction is compensated by the creation of strontium vacancies. The elements studied are lanthanum and yttrium which as we saw previously, substitute the strontium element, and are considered as A-site doping. The niobium, due to the size

difference, substitute in B site titanium. However, it is stated that the defect chemistry is equivalent. It is also important to consider the range of defect content that can be inserted inside the material. Chen *et al.* managed through a sol-gel reaction, to introduce 10 at.% of A-site defect in $La_{0.4}Sr_{0.5}Ti_{0.94}Ni_{0.06}O_{3-\delta}$ and enhanced ammonia conversion for catalytic applications [165]. Meanwhile, Li *et al.* achieved the production of thulium (114 pm, CN=12) doped strontium titanate ceramic exhibiting colossal permittivity (~$3 \cdot 10^6$) for a substitution content of 1 at.% leading to a content of A-site defect 0.5 at.% (based on the defined composition $Sr_{1-3x/2}Tm_xTiO_3$) [166]. As mentioned previously, the A site defect can also come from B site doping. For instance Gao *et al.*, using a solid state reaction, synthesized with 20 at.% A-site vacancy strontium titanate doped with 10 at.% of nickel promoting also the creation of oxygen vacancies [131].

It is important to mention also the possibility to induce B-site vacancies meaning a deficiency in titanium. As it was stated by Shen *et al.*, strontium vacancies are thermodynamically favorable compensating defects in comparison with titanium defects in doped strontium titanate with trivalent ions. The study attests the successful synthesis of $Dy_xSr_{1-x}Ti_{1-x/4}O_3$ by solid state reaction with an improvement of the dielectric properties by 10 times except for the composition with 1 at. % of titanium defects [167]. Other studies relate with the preparation of rare-earth doped strontium titanate with light amount of B-site vacancies [168,169].

The following part presents the different elements used for B site doping. One of the main highlighted differences is the presence of acceptors (p-dopant) which impact the defect chemistry.

2.6.2 Doping on B-site

In order to successfully insert a dopant or substitute an original element of the lattice, the ionic radius has to be considered. This part presents the work on B-site doping. The replaced atom is the titanium atom which has an ionic radius of 60.5 pm with a coordination number equal to 6 (CN=6). ***Table 1.3*** presents the state of the art of existing compositions with the ionic configuration, the synthesis way, the targeted properties to be tuned and the reference.

From the ***Table 1.3***, we can conclude that the main elements used for B-site doping are transition metals. This is based on the ionic radius being more or less similar. However, the properties of strontium titanate are modified.

Table 1.3: Summarized B-site doped strontium titanate

Dopant	Ionic Configuration	Ionic radius for CN=6 (pm)	Substitution rate	Synthesis route	Tuned property	Reference
Niobium	Nb^{5+}	64	$0 < x < 0.08$	Solid-state	Electronic	[170]
Indium	In^{3+}	80	$0 < x < 0.50$	Solid-state	Electronic	[171]
Iron	Fe^{3+}	64	$0 < x < 0.80$	Sol-gel	Electronic	[172]
Tantalum	Ta^{5+}	64	$0 < x < 0.006$	Solid-state	Dielectric	[65]
Zirconium	Zr^{4+}	72	$0 < x < 0.20$	Sol-gel	Optical	[173]
Tungsten	W^{5+}	62	$0 < x < 0.10$	Solid-state	Thermal	[174]
Vanadium	V^{3+}	64	$0 < x < 0.10$	Solid-state	Optical	[175]
Manganese	Mn^{4+}	53	$0.40 < x < 0.60$	Solid-state	Optical	[176]
Cobalt	Co^{3+}	54	$0 < x < 0.50$	Solid-state	Optical	[177]
Nickel	Ni^{2+}	69	$0 < x < 0.10$	Solid-state	Electronic	[131]
Copper	Cu^{2+}	73	$0 < x < 0.10$	Hydrothermal	Optical	[178]
Zinc	Zn^{2+}	74	$0.01 < x < 0.10$	Solid-state	Electronic	[179]
Molybdenum	Mo^{6+}	59	$10^{-3} < x < 0.01$	Molten salt	Optical	[180]
Magnesium	Mg^{2+}	72	$x = 0.05$	Solid-state	Electronic	[128]
Gallium	Ga^{3+}	62	$x = 0.045$	Sputtering	Electronic	[130]
Aluminum	Al^{3+}	53	$0 < x < 0.4$	Solid-state	Electronic	[129]
Ruthenium	Ru^{4+}	62	$x = 0.028$	Solid State	Optical	[181]
Chromium	Cr^{3+}	61	$0 < x < 0.06$	Sol-gel	Electrical	[182]
Rhodium	Rh^{3+}	66	-	Hydrothermal	Optical	[183]
Palladium	Pd^{4+}	61	$x = 0.01$	Hydrothermal	Optical	[184]
Hafnium	Hf^{4+}	71	$x = 0.5$	Solid-state	Dielectric	[185]
Iridium	Ir^{4+}	62	$0 < x < 0.10$	Hydrothermal	Optical	[186]
Platinum	Pt^{4+}	62	$x = 0.50$	Solid-state	Optical	[187]
Silver	Ag^{3+}	75	$0 < x < 0.04$	Sol-gel	Optical	[188]

The dielectric properties of the material are tuned thanks to the modification of the lattice parameters and symmetry. Doping with bigger or smaller cations will induce microstructural modification such as the tilting or rotation of octahedra. This loss of symmetry will lead to a ferroelectric state of the

material. In the case of hafnium, we observed that the valence of both elements (Ti and Hf) is the same meaning that the modification of the dielectric properties is mainly due to its size and the proportion of element inserted. In the referenced study, the ionic radius of hafnium is 0.71 pm for CN = 6, and the substitution rate is 50% to disrupt the cubic structure and induce spontaneous polarization, leading to a drastic increase in the dielectric properties. Still, using an atom with a different valence can have an effect on the dielectric properties but moreover on the electronic properties.

For example, the electron conductivity is tuned thanks to the valence of the doping element. Doping with niobium 5^+ will add a free electron in the semiconductor that will become n-type. Conversely, doping with an element with a lower (such as indium 3^+) induces formations of holes. The semiconductor is then p-type. Both of the mentioned charges increase the charge carriers' concentration leading to enhanced electronic transport and, consequently, higher conductivity.

The electronic transport being tightly linked to the band gap and mostly a decrease of the band gap energy, the doping has also an effect on the optical properties, being the absorption spectra. However, in the case of elements with the same valence, the improvement of optical properties could be questioned. Indeed, in the case of supposed doping with palladium and platinum (noble metals), the element did not insert inside the lattice leading to the synthesis of a composite and not a doped material.

A large number of transition metals has already been used for the synthesis of doped strontium titanate. This highlights the possibility to either use a n-doped element or a p-doped element and highlights the tunability of the material. Based on the reference used, a large majority of the syntheses have been performed using the solid-state route which is the conventional method.

Large niobium substitutions, being donor dopant, provides an upper limit for the concentration of compensating strontium vacancies in A-site deficient $Sr_{0.97}Ti_{0.9}Nb_{0.1}O_{3\pm\delta}$ and $Sr_{0.93}Ti_{0.9}Nb_{0.1}O_{3\pm\delta}$. However, some slight TiO_2 are detected for the highest A-site deficiency by electron dispersive spectroscopy suggesting the excess of A-site deficiency can lead to the formation of impurities. From this results and under reducing conditions, the perovskite lattice is able to fit 5% of A-site deficiency throughout the solid-state synthesis in this case [189]. A patent published in 2019 relates on the preparation of B-site vacancy Fe-doped strontium titanate using a sol gel method with an iron substitution rate of 40 at.% and B-site deficiency rate going 0.04 to 0.07 at.% [190].

The following part presents a third option related to the production of co-doped in A and B-sites strontium titanate.

2.6.3 Codoping in A and/or B sites

The previous parts presented single component doping with a brief explanation on their impact on the properties of intrinsic strontium titanate.

Table 1.4: Summarized codoped strontium titanate

Co-Dopants	Doping Site(s)	Ionic configuration	Substitution rate	Synthesis	Tuned property	Reference
Niobium/Nickel	B	Nb^{5+}/Ni^{2+}	$x_{Nb} = 0.05$ $0 < x_{Ni} < 0.1$	Solid-state	Optical	[191]
Lanthanum /Nickel	A/B	La^{3+}/Ni^{2+}	-	Sol-gel	Electronic	[192]
Lanthanum/ Neodymium	A	La^{3+}/Nd^{3+}	$x_{La} = 0.10$ $0.05 < x_{Nd} < 0.11$	Solid-state	Dielectric	[193]
Yttrium/Iron	A/B	Y^{3+}/Fe^{3+}	$x_{Y} = 0.08$ $x_{Fe} = 0.40$	Sol-gel	Electronic	[194]
Niobium/Zinc	B	Nb^{5+}/Zn^{2+}	$x_{Nb} = 0.10$ $x_{Zn} = 0.05$	Solid-state	Dielectric	[195]
Praseodymium /Nickel	A/B	Pr^{3+}/Ni^{2+}	$x_{Pr} = 0.30$ $0.06 < x_{Ni} < 0.1$	Solid-state	Electronic	[196]
Vanadium/ Molybdenum	B	V^{5+}/Mo^{6+}	$x_{Mo} = 0.05$ $x_{v} = 0.05$	Sol-gel	Optical	[197]
Niobium/Nickel	B	Nb^{5+}/Ni^{2+}	$x_{Nb} = 0.05$ $x_{Ni} = 0.05$	Sol-gel	Electronic	[198]
Rhodium /Antimony	B	Rh^{3+}/Sb^{3+}	$x_{Rh} = 0.01$ $x_{Sb} = 0.01$	Solid-state	Optical	[199]
Niobium /Aluminum	B	Nb^{5+}/Al^{3+}	$10^{-2} < x_{Nb}, x_{Al} < 0.03$	Solid-state	Dielectric	[200]
Ytterbium /Holmium	A	Yb^{3+}/Ho^{3+}	$x_{Yb} = 0.17$ $x_{Ho} = 0.03$	Sol-gel	Optical	[19]
Bismuth /Chromium	A/B	Bi^{3+}/Cr^{3+}	$x_{Bi} = 0.20$ $x_{Cr} = 0.20$	Solid-state	Optical	[201]
Lanthanum /Niobium	A/B	La^{3+}/Nb^{5+}	$0 < x_{La} < 0.02$ $x_{Nb} = 0.10$	Solid-state	Electronic	[202]
Lanthanum/ Calcium	A	La^{3+}/Ca^{2+}	$x_{La} = 0.20$ $x_{Ca} = 0.45$	-	Electronic	[203]
Yttrium/Iron	A/B	Y^{3+}/Fe^{3+}	$x_{Y} = 0.08$ $0.2 < x_{Fe} < 0.40$	Sol-gel	Electronic	[204]

They are usually linked to the deformation they brought to the lattice or the modification of the band gap energy. However, it is possible to have a synergistic effect if more than two elements are inserted into the lattice.

Different combinations of co-doping whether one or two site of the perovskite structure (A and B) are concerned as shown in ***Table 1.4***. For example, in the case of co-doping in B site with niobium and nickel, the purpose is obtaining a donor-type perovskite material codoped with catalytically active and reducible metals to fit the requirement of the metal exsolution concept as described by Weber *et al.* [191]. In the case of A/B codoping, the purpose is usually to use A site dopant to promote electronic conductivity by adding new charges in the material and B site dopant to promote ionic conductivity by the creation of oxygen vacancies (case of Y and Fe). This allows the development of exclusive properties such as a mixed ionic-electronic conductivity. It is also highlighted that the main synthesis route is the solid state showing the limit of synthesis option to synthesize complex oxide. This thesis work focuses on achieving mixed ionic-electronic conductivity, demonstrating that this property can be obtained by incorporating two elements instead of one.

The defects engineering can also be used to tune even more the properties of strontium titanate in order to reach the desired application. Lu *et al.* present a codoped strontium titanate with lanthanum (20 at.%) and calcium (45 at.%) with an A-site deficiency of 10 at.% without giving the method of synthesis [203]. In 2024, Sharma *et al.* added a B-site doping with nickel (5 at.%) using the same composition for electrolysis cells [205]. No study on combining codoping and B-site vacancy has been published yet.

This concludes this part of the existing composition of the perovskite strontium titanate. The elements used were listed and classified. Many cases showed some problems regarding the successful development of doped strontium titanate, for instance with the use of noble metal usually leading to a composite formation with precipitation of the metals at the surface of the strontium titanate particles. The solid-state route is the most common technique used which, despite being the less complicated technique, limits the shaping of the material. The next part will present the existing route for the chemical synthesis of strontium titanate.

3. Synthesis Methods of Strontium Titanate

As aforementioned in Chapter 1, the material properties are linked to its crystal composition and structure which strongly depends on the synthesis method. Each synthesis route promotes distinct

features characteristics such as the size or the shape of the particles which can enhance the different properties of the material.

This section presents different methods reported to synthesize strontium titanate at different size scales and morphologies. The different experimental parameters and their impact on the properties of the material is highlighted.

3.1 Solid-State reaction:

The solid-state reaction method is a traditional and widely used approach to synthesize ceramic materials. This method involves mixing solid reactant powders and bringing them to high temperatures to induce a solid-state reaction that forms the desired product.

Regarding the selection of precursors, the typical precursors are strontium carbonate ($SrCO_3$) and titanium dioxide (TiO_2) [206]. The precursors are accurately weighed in order to reach correct stoichiometric amounts of strontium and titanium. This is followed by a calcination step where the mixed powders are placed in a furnace and heated to a high temperature (typically between 1100-1400 °C) for several hours [207]. This high-temperature treatment facilitates the solid-state diffusion and reaction between $SrCO_3$ and TiO_2 to form $SrTiO_3$. The mechanisms of the solid-state reaction start with the thermal decomposition of strontium carbonate into strontium oxide and carbon dioxide. This occurs at temperatures above 1000 °C [208]. It is followed with a reaction between strontium oxide and titanium dioxide (Sr^{2+} and Ti^{4+} ions through the solid matrix), improved by high temperatures [209]. It can also be influenced by the type of mixing and the precursor sizes; a decreased size leads to enhanced surface reaction. This phenomenon is called solid-state diffusion and it is linked to the mobility of ions toward the interface of the particles enabled by the high temperature that led to a reaction [210]. Depending on the targeted application, features such as grain sizes or high crystallinity are important. The purity of the phase itself is an important parameter to consider as a secondary phase could decrease the performance searched for a specific application. The product may be ground again to break up any large agglomerates and to increase the reaction surface area, followed by a re-sintering to improve the purity and crystallinity of the desired product [211]. The solid-state reaction is straightforward and does not require complex equipment or chemicals and is easily scalable for industrial production. Nonetheless, the need for high temperatures can lead to increased energy consumption and costs. The process is also time-consuming leading to reactions that can take several hours. Also, achieving uniform mixing and reaction can be challenging and usually lead to inhomogeneous products or impurities [212]. Research indicates that the solid-state route typically

results in the formation of microcrystalline particles, which are less homogeneous and exhibit larger particle sizes than those produced via sol-gel methods. It is also important to consider the research on the defect engineering and more precisely on the incorporation of A site vacancies and B site vacancies has been studied. Combined with n-doping, strontium titanate synthesized using solid-state reaction enhance the electronic conductivity and more especially the ionic conductivity [211,213–216]. Based on the mentioned references, the characteristics of the solid-state synthesis can be resumed as a long synthesis implying post synthesis step such as milling and mixing steps. Relying on high temperature going up to 1400 °C make it energy-consuming. However, it is easily adaptable to the targeted composition since it relies on the use of oxide precursor which was highlighted in the part related to the doping.

Table 1.5: Summary of strontium titanate properties synthesized using the solid-state reaction.

Property	Solid-state reaction
Precursors	Carbonate, Oxide
Crystallite Size	Micrometers
Morphology	Grains, Polycrystalline
Post/Pre treatment	Yes
Duration	Long
A/B Dopant Substitution	Yes, Large (Cf part 2.6)
A Vacancies	Yes, max 10 at.%
B Vacancies	Yes, max 4 at.%

Table 1.5 highlights the principal properties of strontium titanate based on the state of the art, synthesized using the solid-state reaction method. Additionally, this method allows for large dopant substitutions at A and B lattice sites, with low levels of A and B site vacancies limited to 10 at.% (involve secondary phase) and 4 at.%, respectively. This method enables the synthesis of various strontium titanate compositions, incorporating dopants (foreign atoms to modify properties) or cationic defects (vacancies within the lattice). However, its versatility is limited by substitution ranges (e.g., 8 at.% for yttrium, 6 at.% for A-site vacancies) and defect engineering, which can thermodynamically favor secondary phase formation.

3.2 Sol-Gel method:

The sol-gel method is a widely employed technique for synthesizing strontium titanate [217,218]. Commonly used precursors are strontium nitrate ($Sr(NO_3)_2$) [219] or strontium acetate ($Sr(CH_3COO)_2$), and titanium isopropoxide ($Ti[OCH(CH_3)_2]_4$) [219]. Alcohols, such as ethanol [219] or isopropanol [220], are often used as solvents to solubilized the metal precursors. The addition of water then initiates hydrolysis and condensation reactions to form a colloidal suspension (sol) [221]. The reaction mechanisms are described by the following equations where M represents the metal alkoxide and R is an organic group:

Hydrolysis: $M(OR)_n + H_2O \rightarrow M(OH)(OR)_{n-1} + ROH$ (2)

The initial step involves the reaction of the metal alkoxide with water to form hydroxyl groups (-OH) by the replacement of alkoxy groups (-OR) based on equation (2).

Alcohol condensation: $M(OH) + M(OR) \rightarrow M\text{-}O\text{-}M + ROH$ (3)

Water condensation: $M(OH) + M(OH) \rightarrow M\text{-}O\text{-}M + H_2O$ (4)

It is then followed by two different kinds of condensation reactions between hydroxyl groups and remaining alkoxy groups. The alcohol condensation is described by equation (3) with alkoxy group reacting with hydroxyl group to produce metal-oxygen-metal (M-O-M) bonds and releasing alcohol molecules. The water condensation correspond to equation (4) and consider the reaction between two hydroxyl groups to form M-O-M bonds as well but with the release of water [222]. Visuttipitukul *et al.* describe the reaction as follow using strontium nitrate and titanium tetrabutoxide [220].

$Ti(OC_4H_9)_4 + 4H_2O \rightarrow Ti(OH)_4 + 4C_4H_9OH$ (5)

As described by equation (5), the titanium tetrabutoxide reacts with water and is hydrolyzed to form hydroxyl groups ($M(OH)_4$ and ROH).

$Ti(OH)_4 + Sr^{2+} + NO_3^- \rightarrow (NO_3)\text{-}O\text{-}Sr\text{-}O\text{-}Ti\text{-}(OH)_3 + H^+ + H_2O$ (6)

The equation (6) described the supposed water condensation mechanism with $Ti(OH)_4$ and Sr^{2+} cation. It is stated in the study that the nitrate compound is confined in the network or reacts with a proton to form nitric acid.

The next step is the gelation where the sol undergoes further condensation reactions, leading to the formation of a three-dimensional network to form a gel. This gel is then aged, with time, the network structure strengthens and syneresis (shrinkage of the gel) occurs, expelling some of the solvent. Depending on the post-treatment, the sol can be adapted into different types of shape from dense film to nanoparticles. For example, drying in air to remove the solvent, results in a xerogel. The

temperature is limited in order to avoid any cracking. It can be completed by a calcination step where the xerogel is subjected to heat treatment typically between 700-900 °C. This process removes any remaining organic material and leads to mostly crystallized phase.

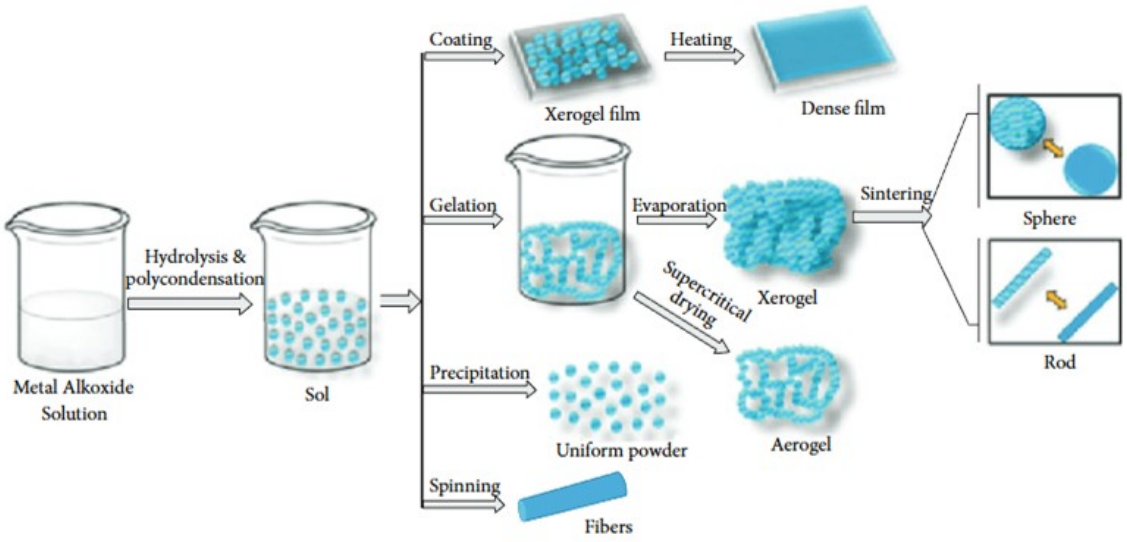

Figure 1.17: Overview of the types of process and morphology that can be obtained with the sol gel method from Bokov *et al.* [223]

As shown in ***Figure 1.17***, the sol-gel synthesis allows a control over the composition and homogeneity. It means a precise control over the stoichiometry and homogenous mixing of components at the molecular level. It also possesses a good versatility and adaptability to produce various forms of undoped/doped materials at different atomic rates (iron [172], silver [188], lanthanum [155] or europium [158]) and particle shape [223]. By understanding and optimizing the sol-gel synthesis process, high-quality strontium titanate with desired properties can be produced.

Table 1.6: Summary of strontium titanate properties synthesized using the sol gel method

Property	Sol gel reaction
Precursors	Metallic, Carbonate, Oxide
Solvent	Water, Ethanol, Ethylene glycol
Crystallite Size	Nanometer
Morphology	Variable, Monocrystalline
Post/Pre treatment	Yes
Duration	Long
A/B Dopant Substitution	Yes, Large (Cf part 2.6)
A Vacancies	Yes, max 14 at.%
B Vacancies	Yes, max 7 at.%

In ***Table 1.6*** summarizes the properties of strontium titanate synthesized using the sol-gel reaction method. The precursors for this process include metallic compounds, carbonates, and oxides, and the solvents used are water, ethanol, and ethylene glycol. The resulting crystallite size is in the nanometer range, and the morphology can vary and includes monocrystalline structures. Both pre- and post-treatment steps are required which makes the process duration long. The method supports large dopant substitutions at A and B lattice sites, with vacancy levels of A sites (up to 14 at.% and B sites (up to 7 at.%). However, the research on the incorporation of cationic defects is low compared to solid-state reaction and relates to a potential use for fuel cell applications [190,224,225].

In summary, the sol-gel reaction relies on much more complex precursors compare to solid-state route. It also implies a lot of post synthesis step (drying + annealing) implying the need of post-treatment synthesis. It is important to consider that the annealing step can remove the secondary phases from the synthesized powder such as strontium carbonate but can imply an increase of the crystallite size. However, this process allows to obtain nanosized crystallites making it more suitable for application that rely on surface action. Additionally, the synthesis can be adapted based on the morphology aimed by adding a surfactant which will favors the crystal growth of certain atomic plan.

3.3 Synthesis methods-based on high-pressure techniques:

3.4.1 Hydrothermal synthesis

Hydrothermal synthesis, which offers unique advantages for controlling the morphology and crystallinity of materials, is explored in this section. The influence of experimental conditions on the synthesis is discussed.

The hydrothermal synthesis is a versatile method to produce strontium titanate ($SrTiO_3$) nanoparticles, leveraging temperature around 100 °C to 300 °C and pressure conditions in aqueous solution to facilitate the reaction and crystallization of the desired product. The main difference with the sol-gel technic is the reaction condition such as the temperature and the pressure that lead to chemical mechanism such as dissolution-precipitation mechanism and involve nucleation and crystal growth. It exists different types of nucleation pathways which depend on the type of precursors used. The chemical key steps are summarized by:

Dissolution of the Metal Precursor Salt: $MX_y(solid) \rightarrow M^{n+} + yX^-$ (7)

The equation (7) refers to dissociation of the metal precursor, dividing into metal cations M and anions X (for instance Cl^- or NO_3^- based on the type of salt), and y is the stoichiometric coefficients for the number of anions. At the same moment, the water dissociates into proton that will combine with anions produced during the dissolution and hydroxide ions (OH^-) that will react with metal cation to form a solid metal hydroxide as shown in equation (8) below.

Formation of Hydroxide Intermediates: $M^{n+} + yOH^- \rightarrow M(OH)_y(solid)$ (8)

The reaction is then concluded by the precipitation and nucleation of the oxide described by equation (9) where the $M(OH)_y$ is dehydrated which led to a water loss of the solid metal hydroxide and the formation of the metal oxide.

Precipitation and Nucleation: $M(OH)_y(solid) \rightarrow MO_x + yH_2O$ (9)

Generally, we also consider that the solution becomes supersaturated, the solubilized ions recombine and precipitate as crystalline product. This is also linked to the dielectric constant of water, which once it reaches the boiling point, drop and force the recrystallization of the compounds.

The usual precursors include strontium hydroxide ($Sr(OH)_2$) [226,227] or strontium nitrate ($Sr(NO_3)_2$) [228], and titanium dioxide (TiO_2) [219,229] or titanium hydroxide ($Ti(OH)_4$) [230]. These precursors are solubilized or dispersed in distilled water. The precursors are then mixed to form a homogeneous solution or suspension. The pH of the solution is usually adjusted to have a basic environment in order to facilitate the hydrothermal reaction since a pH above 7 promote the release of strontium cations making the $SrTiO_3$ unstable [228]. Then, the mixture is transferred to a PTFE Teflon-lined stainless-steel autoclave, which is a pressure-resistant, high- temperature vessel. The autoclave is sealed to create a closed environment, preventing the loss of the aqueous phase and allowing an increased pressure as the temperature increases. The hydrothermal treatment starts when the autoclave is heated to the desired temperature, typically between 150 °C and 300 °C [231], from several hours to a few days. The filling rate of the autoclave coupled with the temperature are the factors which will define the pressure inside the system. The combination of temperature and pressure facilitates the dissolution of the

precursors and promotes the nucleation and growth of $SrTiO_3$ crystals occurring when the solution becomes supersaturated with Sr^{2+} and Ti^{4+} ions. Finally, after the reaction, the autoclave is cooled down to room temperature, either naturally or by controlled cooling ramp. The resulting $SrTiO_3$ particles are collected by filtration or centrifugation, washed with distilled water or ethanol to remove any residual reactants and dried. Once the nucleation starts, the $SrTiO_3$ crystals grow as more ions diffuse to the nucleation sites and incorporate into the growing lattice [232]. In the ***Figure 1.18***, Zhang *et al*. describe the reaction between titanium dioxide (TiO_2) and strontium hydroxide octahydrate ($Sr(OH)_2{\cdot}8H_2O$) where the strontium precursor is producing strontium cation and a hydroxyl group (OH^-) that going to react with TiO_2 to form soluble complex $[Ti(OH)_6]^{2-}$. The both soluble reactants combine into $SrTiO_3$. As the dissolution-precipitation reaction continues, the titanium dioxide powders are dissolved as the more strontium titanate forms until it gets completely depleted. Those synthesis parameters regarding the pressure and the temperature conditions in the autoclave allow for the formation of well-defined and uniform crystals.

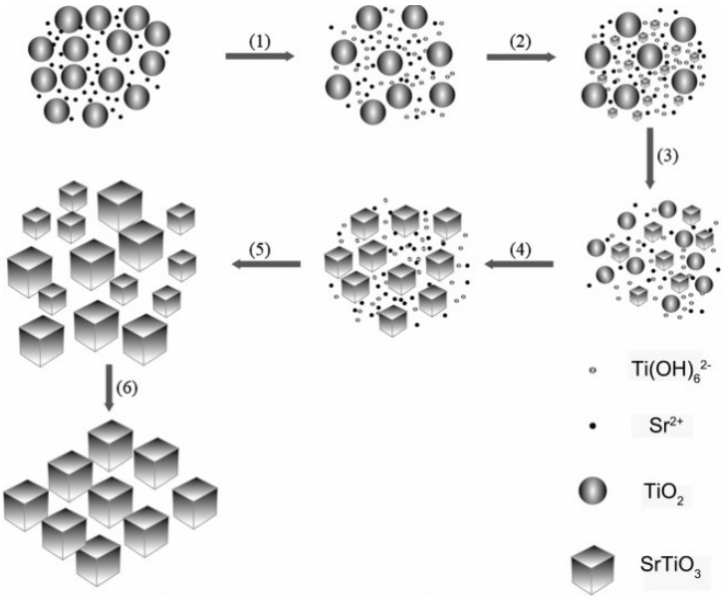

Figure 1.18: Scheme of the hydrothermal synthesis mechanism for strontium titanate from Zhang *et al.* [232]

The hydrothermal synthesis enables a precise control over the size (from 20 nm to 200 nm), shape and crystallinity of the particles. It also promotes uniform mixing at the molecular level, leading to homogenous material with no impurities. Its versatility allows producing a wide range of nanostructures, including nanoparticles [229], nanorods [227] and nanowires [233]. It is also well adapted to the incorporation of doping elements [178]. The synthesis also allows it to work with lower

temperature compared to other synthesis processes. Nonetheless, the need for pressure resistant autoclaves and precise temperature control equipment can increase the costs. Its scalability is also challenging due to the limitations of pressure vessels and the need for uniform heating.

3.4.2 Solvothermal synthesis

The solvothermal synthesis possesses the same parameters as hydrothermal synthesis, the main difference being that it does not use water only as solvent but non-aqueous solvent in combination with or without water. This implies synthesis conditions that vary depending on the solvent used; it involves as well the tight control on temperature and pressure. The use of an organic solvent will have a certain effect on parameters such as the solubility and the reactivity.

It has been recently discovered that the coating of NMC811 with strontium titanate and niobium doped strontium titanate improved the electrical conductivity and strengthened the structure [12,234]. In this work the strontium titanate was produced using the solvothermal method implying the use of triethylene glycol. The solvothermal synthesis in ethylene glycol allows the production of an exclusive morphology such as the flower-like architecture that promotes photocatalytic properties [235]. The ratio of ethylene glycol/water, under solvothermal condition, allows to tune the morphology of the nanoparticles of strontium titanate doped with niobium [236]. The adaptability of the solvothermal synthesis allows to use lot of precursor types, not compatible with water media, and still produces high quality material without involving further steps [237].

Table 1.7: Summary of strontium titanate properties synthesized using the hydrothermal/solvothermal method

Property	Hydrothermal/Solvothermal
Precursors	Metallic, Hydroxide, Chlorine
Solvent	Water, Isopropanol, Ethanol
Crystallite Size	Nanometer
Morphology	Variable, Monocrystalline
Post/Pre treatment	No
Duration	Moderate
A/B Dopant Substitution	Yes, Low (Cf part 2.6)
A Vacancies	Yes, max 20 at.%
B Vacancies	No

Table 1.7 summarizes the properties of strontium titanate synthesized using the hydrothermal/solvothermal method. The precursors employed include metallic compounds,

hydroxides, and chlorides, with solvents such as water, isopropanol, and ethanol. The resulting crystallite sizes are in the nanometer range, and the morphology varies, including monocrystalline structures. Unlike other methods, this approach does not require pre- or post- treatment. The process has a moderate duration and allows for low dopant substitution at both A and B lattice sites. Additionally, A-site vacancies can reach up to 20 at.%, though this may result in the formation of secondary phases [238]), while B site vacancies are not observed. They are relatively few studies addressing the potential to induce A-site cationic defects. However, compared to solid-state or sol-gel reactions, the rate of A-site defects is significantly higher. Additionally, the thermal treatment required is more favorable due to its lower temperature. Fu *et al.* [239] reported the possibility to produce nanopowder at 180 °C with large amount of A site vacancy. However, this led to the creation of secondary phase TiO_2.

To summarize, the high pressure techniques such as the hydrothermal and solvothermal methods lie in enable the synthesis of both pure and doped strontium titanate and allow a large type of morphology (from cubes to rods) thanks to varying some physical and chemical parameters, such as temperature, precursors, pH and surfactant such as oleic acid [228].

One of the key parameters is linked to the behavior of a solvent based on the temperature and pressure. It has been defined that going further towards the critical point leads to the supercritical region with unique properties.

3.5 Summary on the synthesis of strontium titanate:

This section summarizes the various synthesis methods discussed earlier, highlighting their key points. An important question to consider when aiming to synthesize strontium titanate is: “What tools do I have available, and what features are required?”. The ***Table 1.8*** outlines the advantages and disadvantages of each technique presented in this section.

Table 1.8: Overview of the many ways to synthesized strontium titanate undoped and doped

	Solid-state	Sol gel	Hydro/Solvothermal
Precursors			
Solvent			
Morphology			
Size			
Thermal treatment			
Duration			
Doping			
A Vacancy			
B Vacancy			

: Favorable : Moderate : Unfavorable

To organize this table, the approach is to evaluate whether the method is favorable or not based on the accessibility and simplicity of its features. For instance, the "precursor" row is marked as "favorable" if the precursor is easily accessible. In the case of the solid-state reaction, the precursors are primarily carbonates and oxides, which are more accessible and cost-effective compared to complex precursors.

Another consideration is the use of additional chemicals, such as solvents or acids/bases, which the solid-state reaction does not rely on. However, if a specific morphology or nanoscale size is required, this technique becomes unfavorable. For doping, the "favorable" status depends on studies demonstrating the successful synthesis of doped compounds. The rows for "A vacancy" and "B vacancy" reflect the achievable rates for these features.

The time required is also a crucial factor. Most techniques involve high-temperature pre- and post-treatments, which is not the case for hydrothermal/solvothermal synthesis. In the context of this project, the goal is to produce undoped and doped strontium titanate nanoparticles using the smallest possible amount of chemicals while still achieving high crystallinity. Drawing inspiration from the advantages of hydrothermal and solvothermal synthesis, and leveraging the expertise of the ICMCB in oxide synthesis, we have chosen to explore the supercritical approach.

4. Supercritical Approach for the Synthesis of Strontium Titanate

This part will present the supercritical fluids synthesis by a description of this very particular domain in a phase diagram and the opportunity that it represents in the field of nanoparticle synthesis

4.1 Supercritical fluids synthesis: Definition and properties

Synthesis in supercritical fluid (SCF) media are unique. The supercritical fluid process enables the synthesis of nanoparticles with high crystallinity and a well-controlled particle size distribution.

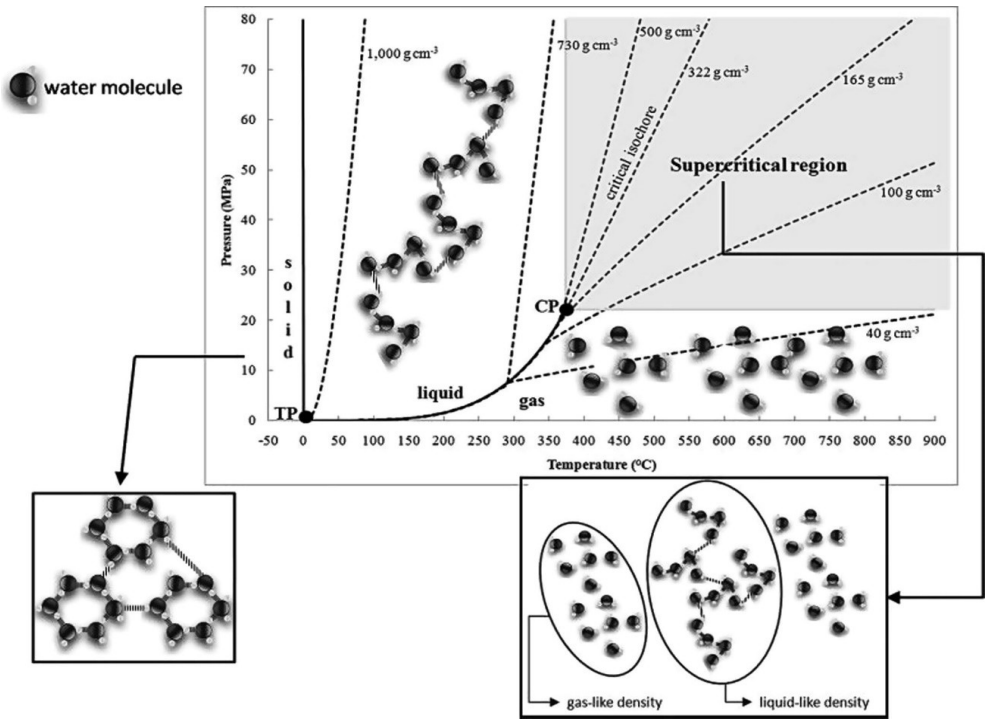

Figure 1.19: Phase diagram of pure water with the information of its critical point (Tc= 374 °C and Pc= 22.1 MPa) from Serani *et al.* [240]

A supercritical fluid is a domain appearing after reaching higher than the critical pressure and temperature of the chosen fluid as represented with water in ***Figure 1.19*** [240]. To go into further the detail, ***Figure 1.19*** shows the three possible states of matter with the solid phase, the liquid phase and the gas phase. All of these "domains" are delimited by different conditions of temperature and pressure where it is possible for matter to be shared between two different states if, for instance, the external condition allow a placement on the boiling line or the vapor-liquid equilibrium (VLE). However, going further, the previously mentioned critical pressure and temperature lead to the supercritical fluid domain. The supercritical domain is more like a dynamic area that can contain sub-domains depending on the pressure and temperature which possess different density. As shown previously, progressing toward the liquid domain increases the density and it is considering as liquid-like SCF. It possesses a high density and viscosity, and low diffusivity. When going toward the gas phase, the density decreases as well as the viscosity but the diffusivity is higher and comparable to a gas like. It makes the transport properties dependent to the critical parameter of the fluid. Usually, lower pressure (on y-axis) means the SCF behave more like a gas (more diffuse) and higher-pressure lead to liquid-like properties. The liquid-like SCFs, due to high solvating properties (density dependent), are

dedicated for application such as extraction. However, the gas-like SCFs which favor higher diffusivity are fitted for material synthesis. This features association is indeed really interesting for synthesis since we can perform gas-only synthesis in a pseudo-liquid media and reciprocally. Those properties are exclusive to this specific feature of SCF.

To summarize, the reaction kinetics are enhanced thanks to the mass and heat transfers of the precursors which are due to liquid like viscosity and gas like diffusivity. The solubility of the precursor can be easily tuned since it is linked to the density of the solvent. It can be modified by adjusting parameters such as the pressure and temperature. This technology can also integrate the feature of a continuous process to synthesize in a single step nanomaterial since we enabled the access to very fast kinetic reaction that take place under a continuous flow [241]. Such synthesis allows a control on the residence time of particles itself in the supercritical system. An aspect of this synthesis is the nucleation which is favored compared to the growth. The mechanisms linked to the supercritical fluid synthesis are based firstly on the precursors solubilized homogeneously in the supercritical fluid, facilitating uniform mixing at the molecular level. The mass transfer is promoted by the solvent properties [242,243]. The nucleation step is the part where the supersaturation is reached in the supercritical phase leading to a rapid nucleation of particles. Thanks to the high solubility and diffusivity in the system, a high density of nucleation sites is obtained which produces small and uniform nanoparticles [244,245]. The narrow size distribution is enabled by the low viscosity and high diffusivity in the supercritical fluids [246]. The advantage of the supercritical fluid synthesis is mainly based on the tight control on the particle size and its morphology due to the precise control of the reaction environment. Finally, it is environmentally friendly depending on the kind of fluid used, for example, supercritical CO_2 is non-toxic and can be easily recycled, making the process environmentally benign [247]. The disadvantage lies in the high-pressure requirements; it induces complexity and cost of the process since it needs advanced equipment.

4.2 Nanomaterial synthesis using supercritical fluids

In the framework of chemical synthesis, supercritical fluids or SFCs are largely developed for the production of nanoparticles, metal oxides and other advanced materials due to the tunability of the solvents. It is used in many applications including the recycling. This part presents a more focused look at chemical reactions used in supercritical fluid synthesis targeting nanosized metal oxides:

- Supercritical Hydrothermal Synthesis (SHS)

This synthesis is based on using supercritical water (T_c = 374 °C and p_c = 22.1 MPa) as a reaction environment. Above the critical point, it becomes a low-dielectric media which enables the possibility to solubilize nonpolar species. The reaction mechanism is mainly based on hydrolysis and dehydration steps [248]. It has been described by Adschiri *et al*.

$$M(NO_3)_x + xH_2O \rightarrow M(OH)_x + xHNO_3 \quad (10)$$

$$M(OH)_x \rightarrow MO_{x/2} + \frac{x}{2}H_2O \quad (11)$$

As it is stated, the lower solubility of ionic species, due to the decreased dielectric constant, favored the equation (10) while the increased temperature shifts the equilibrium of equation (11) toward oxide compound. The precursors used are metal salts such as chlorides [249]. The metal precursors are hydrolyzed to form hydroxides and then precipitate as nanoparticles. The first reported synthesis of metal oxide nanoparticles in scH_2O was the synthesis of cerium oxide by Adschiri *et al.* [250]. It has then being developed for other types of metal oxides [251] such as zinc oxide [252,253], zirconium oxide [254,255], barium titanate, strontium titanate [256,257], etc.

- Supercritical Solvothermal Synthesis

The principle is the same than the supercritical hydrothermal synthesis except the media used which is partially or totally composed of organic solvent such as ethanol or methanol. This method allows a larger panel of material production and also the use of sensitive water reactants [258,259]. Adding a water line allows a sol gel like reaction and to enable the step of hydrolysis followed by the condensation. This leads to the production of highly crystallized nanoparticles [241]. This method was used for the synthesis of strontium titanate nanoparticles using a supercritical continuous flow synthesis [260].

4.3 Synthesis of strontium titanate-based nanoparticles in supercritical fluids

Most of the research on the synthesis of perovskite using supercritical fluids technology is mainly focused on the preparation of solid solutions such as barium strontium titanate which is well known for its ferroelectric properties. The first proclaimed synthesis of strontium titanate using supercritical conditions was back in 2002 by Choi *et al.* [261] with a single phase of $SrTiO_3 : Pr^{3+}$ using supercritical ethanol.

In 2014, Philippot *et al.* [241] reported deep-insight studies on the supercritical fluid technology for the synthesis of barium strontium titanate nanoparticles. The study described the different methods such as supercritical hydrothermal synthesis and the supercritical sol-gel like synthesis.

This part will describe the advancement of the supercritical synthesis reaction of strontium titanate and the work regarding the *in-situ* reaction mechanisms of the supercritical synthesis.

4.3.1 Late achievements on the strontium titanate synthesis

One of the main game-changers for the supercritical fluids technology is the type of precursor used. The first mentioned synthesis involved the use of strontium hydroxide octahydrate ($Sr(OH)_2{\cdot}8H_2O$) and titanium oxide (TiO_2) in an ethanol media as a batch reaction at 270 °C, 7.2 MPa and 2 hours. Three years later, Reverón *et al*. [262] performed the synthesis of barium strontium titanate ($Ba_{0.6}Sr_{0.4}TiO_3$) using the archival strontium isopropoxide ($Sr(OCH(CH_3)_2)_2$) and titanium isopropoxide ($Ti(OCH(CH_3)_2)_4$) combined with continuous flow synthesis in a water ethanol mixture at 380 °C and 26 MPa. One year later, Reverón *et al.* [263] achieved the solid solution of barium strontium titanate (BST) from barium titanate to strontium titanate using the same material and method making it the first achieved strontium titanate material synthesis by continuous flow synthesis with fully crystallized nanoparticles of 19 nm. In 2014, the solid solution of $Ca_{1-x}Sr_xTiO_3$ was achieved using supercritical hydrothermal continuous flow synthesis at 400 °C and 30 MPa [264]. The precursor used for the synthesis were strontium nitrate ($Sr(NO_3)_2$), titanium dioxide sol (TiO_2) and calcium nitrate tetrahydrate ($Ca(NO_3)_2{\cdot}4H_2O$). The setup used a second feed injection line of sodium hydroxide (NaOH) which allows a better solubility of TiO_2 in basic aqueous media which help to increase the dissolved Ti ion species and impact the growth of the nanoparticles as well as the ratio of Ca/Ti and Sr/Ti. We will see later that this notion of A sites deficiency plays an important part in the understanding of the formation mechanism. In the same year Philippot *et al.* published a complete work on the use of supercritical continuous flow synthesis on barium titanate nanoparticles synthesis highlighting the different known mechanisms for the hydrothermal synthesis under supercritical conditions and the supercritical sol-gel like synthesis of barium strontium titanate [241]. One of the main highlights was the relevancy of structural –OH defects which had an impact on the growth of particles.

The following part will focus on the supercritical synthesis progress in understanding mechanisms achieved after 2014.

4.3.2 Recent achievements on the strontium titanate synthesis

This section will cover the advancement on the synthesis of strontium titanate nanoparticles from 2014 to 2024. A deep-insight on the formation mechanism is presented related to similar compounds of the perovskite family on hydrothermal and solvothermal media in a continuous flow set-up.

In 2015, a patent was deposited by Fujifilm corporation [265] for the manufacture of strontium titanate fine particles. The combination of strontium nitrate and titanium chloride ($TiCl_4$) associated with

potassium hydroxide (KOH) and supercritical hydrothermal synthesis allows the production of fine particles in a high yield. This research of industrial scale up was followed in 2016 by the synthesis of barium strontium titanate ($Ba_{(1-x)}Sr_xTiO_3$) using hydrothermal continuous-flow system [257]. The whole solid solution of barium strontium titanate was synthesized using metal nitrate salts such as $Ba(NO_3)_2$ and $Sr(NO_3)_2$ combined with titanium bis(ammonium lactato) dihydroxide. An additional injection feed of sodium hydroxide was added since it has been proven valuable for the hydrothermal supercritical synthesis. The ratio of Sr/Ti has a value equal to 0.81 showing a high deficiency ratio characteristic of the hydrothermal supercritical synthesis of this oxide. In the same year, strontium titanate was synthesized using supercritical water and used three different precursors of titanium dioxide which emphasized the effect of the precursor reactant size in a batch reaction using hydrothermal supercritical synthesis [266].

The formation mechanisms have been thoroughly investigated regarding the perovskite using supercritical hydrothermal synthesis and continuous flow reactor. In 2014, the plausible mechanism of formation of $BaZrO_3$ was proposed into three defined steps:

- At ~0.1 s, the early stage of crystallization of the concerned composition, the cubic perovskite $BaZrO_3$ presents many defects such as Ba site and oxygen defects as well as hydroxyl group (OH^-),
- At ~1 s, the coalescence step implies particles with no defined shape and low crystallinity becoming larger and more crystallized due to an increased residence time,
- After ~10 s, the size became constant. The defect ratio is completed as the increase is controlled by the uptake of Ba ions on the nuclei.

A first proposition represented on ***Figure 1.20*** of the uptake phenomena implies a core-shell structure where the early stage of nucleation is the association of a $BaZrO_3$ core and a $ZrO_{1+x}(OH)_{2-2x}$ shell.

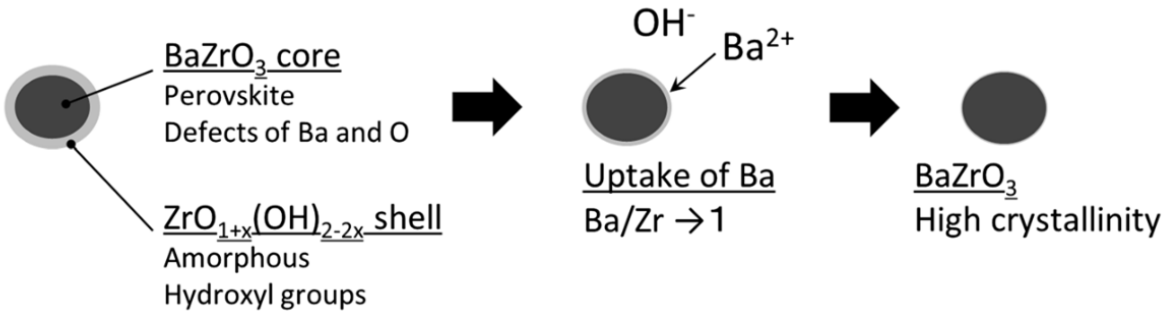

Figure 1.20: Proposition of the uptake phenomena and core-shell structure from the study of Yoko *et al.* [267]

The core is made of early crystallized perovskite composed of perovskite with A-site defect and, by electroneutrality, oxygen vacancies. The shell is made of amorphous zircon oxide and hydroxyl groups.

The barium ion then takes over the defects presence by filling them which lead to a fully crystallized particle [267].

Their research followed in 2016 with the study of the growth of $Ba_{1-x}Sr_xZrO_3$ ($0 \leq x \leq 1$) nanoparticles in supercritical water [268]. They showed that B-site Zr in perovskite structure are responsible for the high nucleation under supercritical conditions compared to A-site on here being barium and strontium ions. The authors explain that the Zr precipitates faster, becoming the adhesive center after their nucleation. This study showed that the A-site elements influence three important parameters: the particle size, the A-site deficiency and the surface –OH density. As concluded, the A-site composition affects the crystal structure, the particle size, the vacancy concentration and the surface state. The high concentrations of A-sites deficiency (almost 70%) for Ba rich compounds prevents the particle growth by increasing the amount of –OH groups located at the surface as shown in ***Figure 1.21***. It was then later explained by the diffusion of A-site cations in A-site deficient perovskite oxides [269]. The theoretical work showed the energy barrier for strontium diffusion being lower at the surface and in the bulk compared to barium diffusion. The diffusivity of A-site ions determines the whole defect composition of the material. The particle growth is controlled by ripening or coalescence.

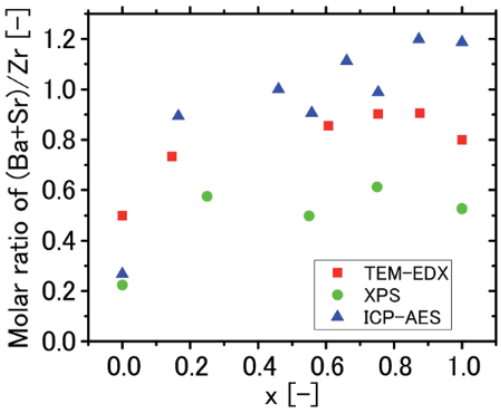

Figure 1.21: Molar ratio of A-site ions (Ba+Sr) per B-site ion (Zr), obtained using different elements quantification analysis from Yoko *et al.* [268]

It is supposed that the A-site deficiency and surface –OH prevent the collision limiting the particle growth.

It is interesting to compare this with the study of Philippot *et al.* [260] that states –OH surface supposedly helps the growth of the particles. We have to consider that both studies use different media where one uses a hydrothermal method and the other a solvothermal method as well as different reactants. To describe the approach given by Philippot *et al.*, the origin of –OH defects was explained by the dissolution of barium and strontium ions under aqueous conditions. Indeed, as

mentioned in ***Figure 1.13***, the chemical bond between Sr-O and Ba-O is ionic. Their dissolution leads to the apparition of –OH defects. Also, in the case of Sr-O bonding, they are more stable than Ba-O so it explained why has the strontium content increase, the surface –OH decrease. Considering the reaction, it takes place in a solvothermal media; we suppose the growth depend of a sol-gel mechanism where a reduction of the surface –OH amount means less active site at the surface of the crystallites for the precursor to react. This explains why in the case of Philippot *et al.*, the particles decrease as the strontium content increase.

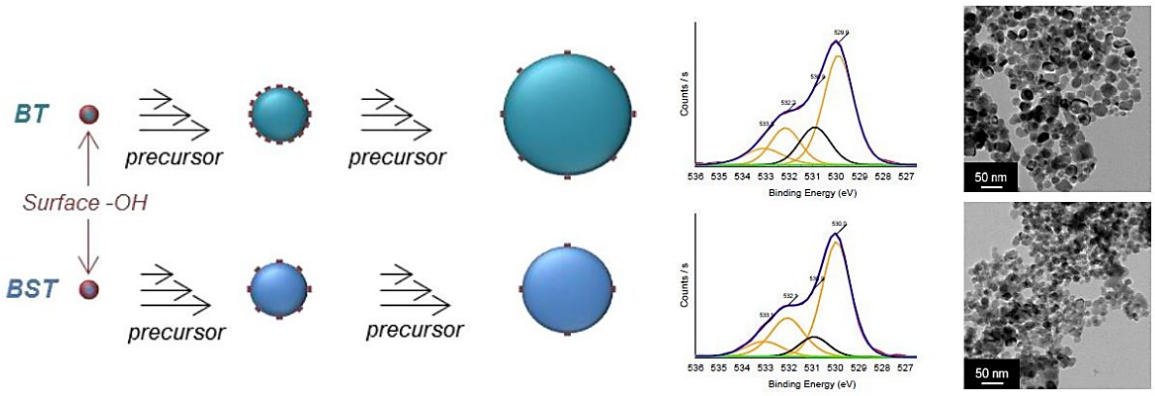

Figure 1.22: Sketch illustrating the particles growth $BaTiO_3$ and $Ba_{0.4}Sr_{0.6}TiO_3$ highlighting the effect of -OH defects amount using isopropoxide precursors in water/ethanol mixture from Philippot *et al.* [280]

Figure 1.22 gives a visual representation as well as O 1s X-ray photoelectron (XPS) response and high-resolution transmission electron microscopy (HRTEM) for the both compositions mentioned earlier. The black curve on the XPS at 530.9 eV for barium titanate (BT) and 531.1 eV for barium strontium titanate (BST) represent the surface –OH defects. In the case of BST, the intensity of the curve decreases compared to BT which led to a smaller size (16 nm for 20 nm with BT particles).

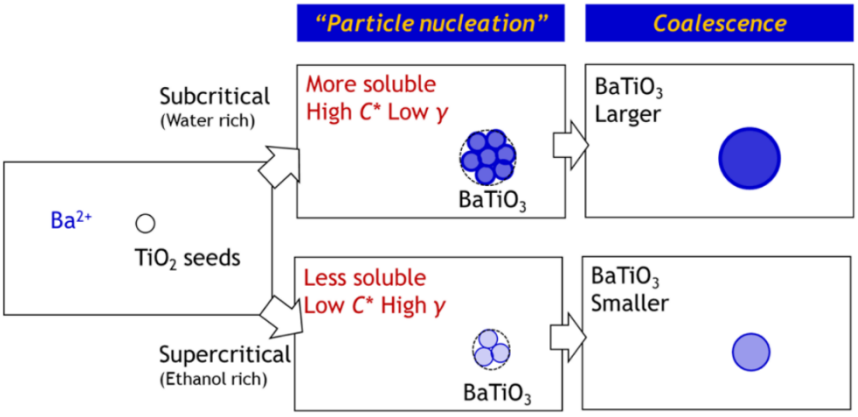

Figure 1.23: Barium titanate nucleation and growth of TiO_2 seeds depending on the solvent properties based on the solubility of barium titanate (C*) and its energy interface (γ) from Yoko *et al.* [270]

In 2021, the barium titanate formation was studied using continuous flow reactor and water ethanol mixed solvents. The purpose of this study was to present the variation on the crystallites due to the media properties. It emphasized the impact of the solubility and interface energy of particles. Again, the idea of coalescence growth is mentioned due to the impact of higher concentrations which lead to more collisions and more growth. Here in this study, the coalescence growth is prevented under ethanol-rich conditions and was explained by its adsorption to particles which prevent the Ba^{2+} uptake or the "adhesivity" of barium titanate particles as shown in ***Figure 1.23***.

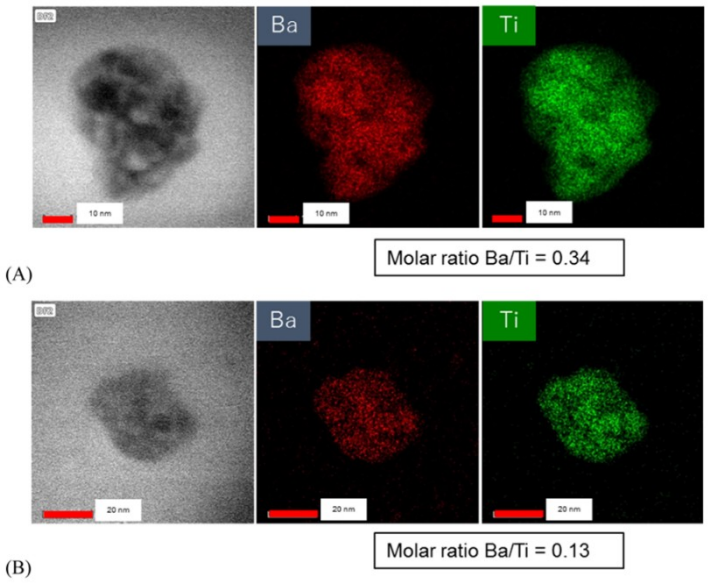

Figure 1.24: TEM images and EDS mapping of $BaTiO_3$ particles with the molar ratio of A and B sites depending on their EtOH mol% media (A: 25% and B: 90%) from Yoko *et al.* [270]

Figure 1.24 shows the impact of the media on the particles size, but also on its A-site deficiency with almost 90% of A-site vacancies for the particles for barium titanate particle synthesized with a media at 90% in volume of ethanol/water ratio despite their XRD signal shows crystallized peaks [270]. This highlights the (exclusive) possibility with supercritical fluid to produce crystallized particles with a huge A-site deficiency. This property could be relevant for its impact on mixed electronic ionic conductivity [271].

Regarding the work on doped strontium titanate, only one paper from 2018 relates to the synthesis of praseodymium-doped calcium strontium titanate nanoparticles ($(Ca_{0.6}Sr_{0.4})_{0.997}Pr_{0.002}TiO_3$ or PCSTO) using hydrothermal supercritical synthesis and flow type reactor. They propose the successful synthesis of calcium strontium titanate with 2 mol.% of praseodymium nanoparticles around 12 nm using nitrate precursor and titanium sols. A-sites deficiency is measured at 15% and ***Figure 1.25*** shows the XRD signal. The intensity of the peaks increases and its width decreases as the temperature increases meaning that the annealing sinters the particles by making them more crystallized and bigger. The doping was assumed by red emission associated with the luminescence of the praseodymium ions and Induced couplet plasma (ICP) measurements. However, no indexation of the phase is presented and no lattice parameter value is given and no ratio of the praseodymium elements was given by the ICP [272].

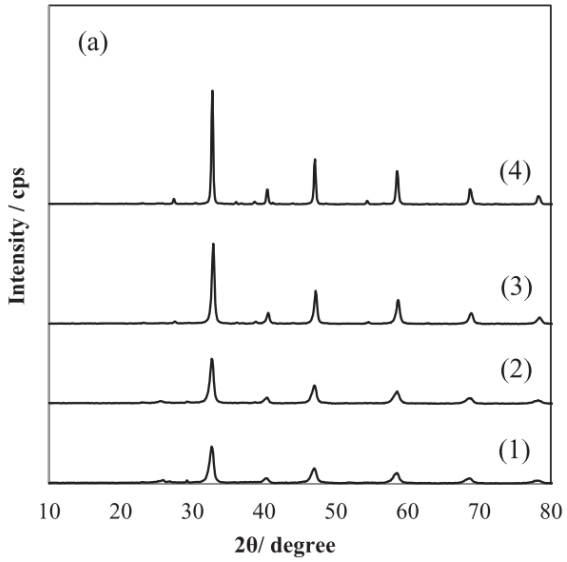

Figure 1.25: XRD profiles of the PCSTO nanoparticles synthesized using hydrothermal synthesis at 400 °C with Ca+Sr/Ti = 0.85 annealed at (2) 600 °C, (3) 800 °C and (4) 1000 °C. from Hakuta *et al.* [272].

Overall, the state of art on the supercritical synthesis of strontium titanate and doped strontium titanate is not extensive with only one patent for industrial production and one paper on the slight insertion of rare earth element in calcium strontium titanate.

We can divide two different approaches on the formation mechanism in a mixture of water/ethanol between the approaches of:

- Philippot *et al.* where the use of alkoxides precursors lead to favorable $Ba_{1-x}Sr_xTiO_3$ ($0 \leq x \leq 1$) particles growth related to the amount of hydroxyl group surface being a point of reaction for alkoxides. The use of alkoxide precursors combined with a mixture of water/ethanol lead to consider this reaction as "supercritical sol-gel like synthesis". The crystals growth is mainly dependent of the amount of surface –OH defects. The barium titanate obtained with this method presented A-sites deficiency rate of 15% and the strontium titanate presented A-site deficiency rate of 10%. The origin of the A-sites defects was explained by the stability of the ionic Ba-O bonding. The difference of A-sites deficiency with strontium titanate is explained by a better stability.
- Yoko *et al.* where the use of salt precursors such as hydroxide for the synthesis of $BaTiO_3$ with an increasing amount of EtOH mol% lead to more –OH surface that disables the growth step by limiting the coalescence phenomena due to energy interface. The use of salts in combination with an aqueous media lead to a "supercritical hydrothermal synthesis". The mechanisms, different from a sol gel reaction, rely on a dissolution and precipitation which is different from the condensation reactions obtained with alkoxides. In this particular case, adding ethanol decrease the solubility of the barium ion which has an effect on the precipitation step during the particle nucleation.

These two approaches underscore the strong interconnection between the chemistry of the precursors and the choice of media used for synthesis under supercritical conditions.

This thesis work will extend the possible synthesis of strontium titanate nanoparticles using the supercritical continuous flow technology in a water ethanol media. The promotion of new organometallic precursors will allow them to produce different extrinsic strontium titanate semiconductors and extend the synthesis possibility via the supercritical fluid technology.

Conclusion of Chapter 1

"Historical" strontium titanate has gained significant attention in various fields due to its properties, such as high dielectric constant, photocatalytic activity, and excellent stability. However, several limitations and challenges need to be addressed to fully exploit its potential in practical applications. Emerging trends and research directions for strontium titanate focus on enhancing its properties mainly for photocatalytic properties to expand its applications through advanced synthesis techniques, doping, nanostructuring and composite developments. The band gap engineering represents an important axis where doping with various elements and the creation of defects plays a huge role on the properties. The nanosize and morphology control are also a major axis, the development of designed structures with nanoparticles/wires or porous structures providing interesting effects on the material physical properties. The last material science axis is the development of composites and hybrid materials where the heterojunction research represents a major part of charge separation optimization. Its versatility allows the material to be a part of many diverse applications from coating layers for lithium-ion batteries, environmental application with water purification, renewable energy application with solar to hydrogen processes and potential use for solid oxide fuel cell.

In this chapter, we first focused on the intrinsic properties of strontium titanate. The discussion began with its dielectric properties, particularly emphasizing the dielectric constant of the material. We highlighted the importance of the atomic structure, which can be tuned through various methods to enhance the dielectric constant. This was followed by an exploration of the thermal properties, with particular attention to the thermal conductivity and the thermal expansion coefficient, where the influence of the atomic structure was once again emphasized. The thermal properties were shown to be strongly linked to the electronic properties of the material, especially in the context of thermoelectric applications. Given that the electronic properties are closely tied to the material band structure, we also examined its optical properties. This included a focus on the refractive index and the nature of the atomic bonding within the material

These properties are closely linked to the material structure. Consequently, doping with new elements into the compound was thoroughly studied within the perovskite structure. A comprehensive table of A-dopants and B-dopants was provided, highlighting how doping can be used to tailor the material to achieve desired properties. The concept of codoping was also discussed, as it allows the combination of different elements for advanced applications. The methods used to synthesize these compounds were also covered, including a discussion of defects that can occur on both the A and B sites. By varying the doping rates, we highlighted the compositional limits that can be reached. Next, we presented the

catalytic properties of the material, focusing first on its global photocatalytic properties and then on the oxidative coupling of methane.

We also reviewed various methods for synthesizing strontium titanate, starting with the most conventional one, the solid-state synthesis. This method allows for a wide range of compositions and accessible precursors but involves high energy costs. Furthermore, defect chemistry, particularly the insertion of defects or n- and p-dopants, is limited by the rate of doping, as higher rates can lead to impurities. Focusing on catalytic applications, we introduced synthesis methods that enable nanosizing of the material, such as the sol-gel and high-pressure techniques like hydrothermal and solvothermal synthesis. We also explored the use of high-pressure technology for nanoparticle synthesis, dedicating a section to supercritical synthesis. An overview of the principles and advantages of supercritical synthesis for nanoparticles was presented, with particular attention to the evolution of strontium titanate synthesis using supercritical hydrothermal and solvothermal methods. A discussion on the role of the -OH defect in nanoparticle growth was included, along with the potential to produce strontium titanate with high A-site vacancies using the supercritical method. These A-site vacancies could be used to tune properties such as ionic conductivity.

In this context, the objectives of this PhD thesis were:

- The synthesis of nanoparticles of strontium titanate and doped strontium titanate using the supercritical fluid technology, with new precursors, and with a deep characterization of the material composition, structure and properties,
- The shaping of nanoparticles into an electrode cell related to the HTE anode application using the screen-printing method and the characterization of the electronic properties such as the electronic conductivity from dense pellet of “supercritical” nanoparticles of strontium titanate obtained by Spark-Plasma Sintering (SPS).

This tuning will allow us to produce a special strontium titanate with modified electronic properties that enable its use for the development of innovative applications. Here, within the framework of this project, the development of an anode for high temperature electrolysis units that present electronic ionic mixed conductivity and oxidative coupling of methane catalytic properties. The electrode development, thanks to ICMCB experience, will be achieved using screen printing process which implies the preparation of a slurry. The electrodes, once finished, will be sent to partners for further characterizations.

Chapter 2: Preparation of Nanomaterials using the Supercritical Fluid Technology: Processing and Characterization

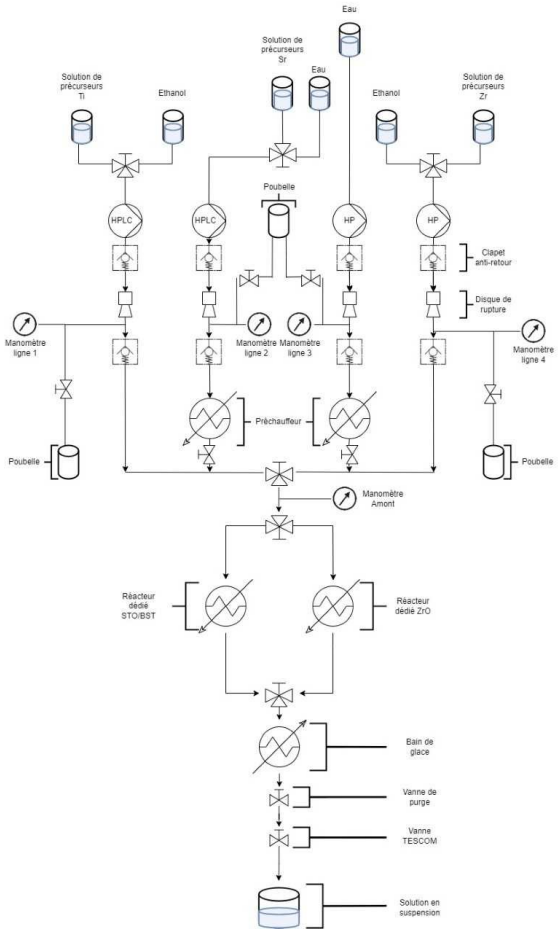

Scheme of the designed supercritical reactor for the synthesis in continuous flow during the PhD

In this chapter, an overview is proposed on the techniques and principles used for the production of pure and doped strontium titanate nanoparticles, with a focus on the characterization methods, from structural to elemental analyses. The processing of nanopowders, including screen-printing for the production of an electrode and the fabrication of dense ceramics, is discussed, along with the tools used for their characterizations.

1. Synthesis of High-Quality Nanoparticles in Supercritical Fluids

For the experimental setup, the nanoparticle synthesis was carried out using a reactor that operates in continuous mode under supercritical conditions. This setup allows for accurate control of key process parameters, such as temperature and pressure, which are critical for synthesizing crystalline nanoparticles. These parameters are essential for working in the supercritical domain, enabling rapid reaction kinetics, short residence times, and ensuring the production in a reproducible way of the synthesized material. The process yields a sufficient material quantity for the various characterizations by producing between 1.2 and 1.5 grams per hour. Two different setups, each one with distinct features, were used in this work. The following section describes these two setups and their operation.

1.1 Original setup for the supercritical solvothermal synthesis of undoped and doped $SrTiO_3$

1.1.1 Setup description

The setup used in this PhD was adapted from a previous design developed by the "Fluides Supercritiques" group at ICMCB; it is featured in ***Figure 2.1***. This setup is highly effective for synthesizing a range of materials, including monocrystalline particles of simple oxides such as titanium dioxide [247] and zirconium oxide [246], complex oxides like barium titanate [273], and controlled solid solutions such as barium strontium titanate [260,263,274] and yttria-zirconium oxide [258]. In this work, it was used to synthesize both pure and doped strontium titanate. A key advantage of this setup is its flexibility, allowing extended tuning towards targeted compositions.

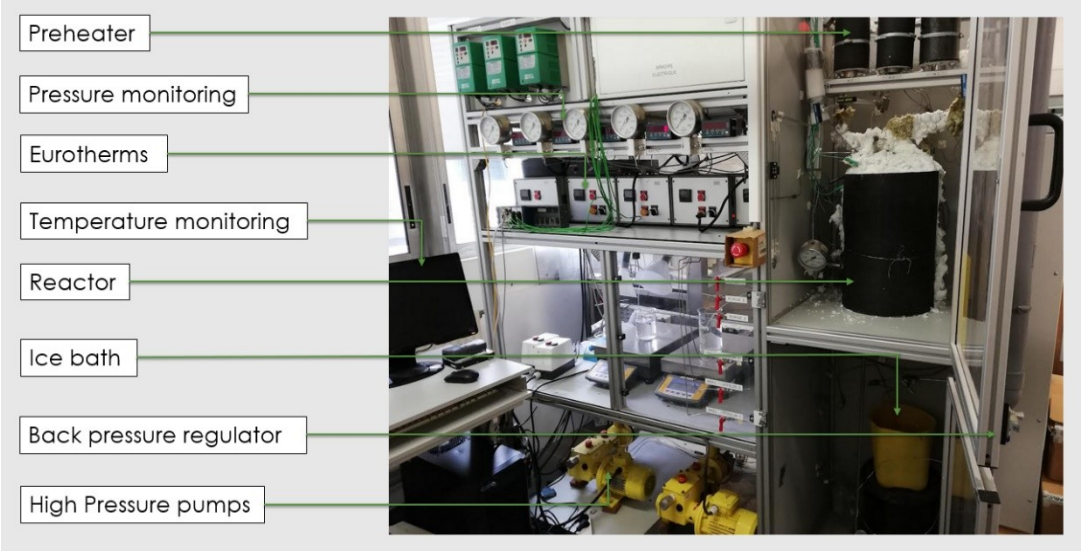

Figure 2.1: Picture of the original reactor built in 2004 with a side description of the different parts. The last project which was based on the use of this setup was about the synthesis of barium titanate

It features two injection lines for different media (water and ethanol), each one fed with precursor solutions *via* high-performance liquid chromatography (HPLC) pumps (JASCO PU-2080 PLUS). Unlike previous pumps, these ones offer accurate flow rate control, a significant improvement over earlier designs. This key difference will be discussed further in Chapter 3. Each HPLC pump can deliver the solution at a speed up to 10 $mL.min^{-1}$ and it allows a pressure limitation that automatically stops the system at 30 MPa.

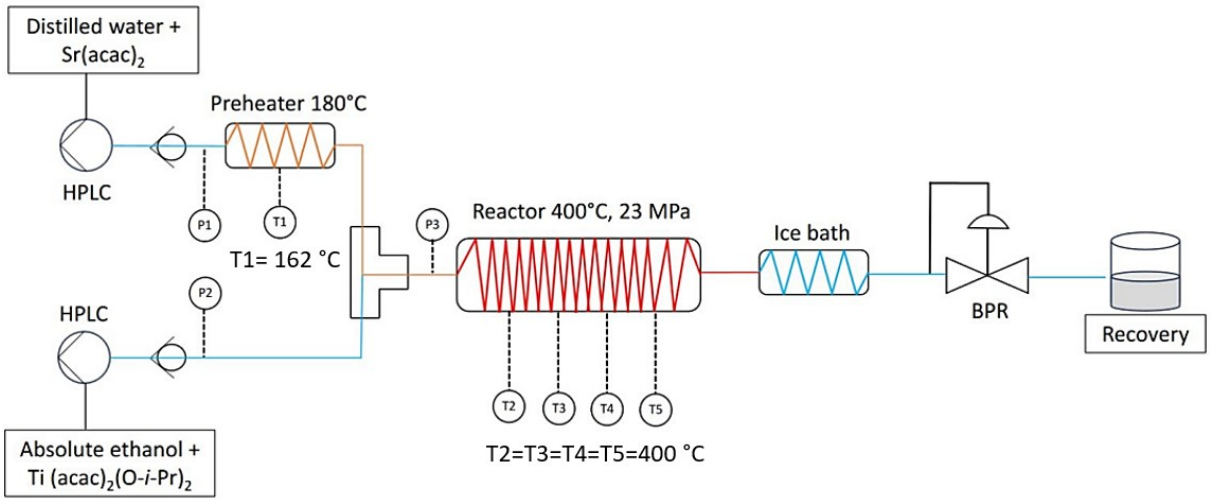

Figure 2.2: Scheme of the supercritical continuous solvothermal synthesis setup for the production of strontium titanate nanoparticles

As described in ***Figure 2.1*** for nanoparticle synthesis, one line injects water with a dissolved acetylacetonate hydrate precursor(s), while the other injects absolute ethanol with diisopropoxide bis(acetylacetonate) precursor. One line is equipped with a preheater, allowing independent temperature control of the solutions before they reach the mixing zone. Once combined, the flows pass through a hot zone composed of a stainless-steel coil (type 316L, inner diameter 1.57 mm) with a total length of 24 m, divided into four sections of 6 meters each. The temperature is regulated by four heating resistors (Thermocoax) and monitored by K-type thermocouples placed at each section of the reactor on its side. The thermocouples are ferruled in a 1/8-inch tube creating a secure, leak-proof seal for precise temperature measurement, keeping the sensor stable for optimal accuracy. The entire reactor is insulated to minimize heat losses, and a Plexiglas cover is installed over the high-pressure/high-temperature zone for safety.

In this setup a uniform pressure is maintained throughout the system, controlled by a back-pressure regulator (Tescom). To prevent overpressure, in addition to the automatic stop mechanism of the HPLC pumps, rupture discs rated at 40 MPa are installed just after the pumps. Nanoparticles are collected directly after the back-pressure regulator. To protect the regulator from thermal stresses, part of the circuit is immersed in ice water immediately after the supercritical reactor zone. It also quenches the nanoparticles growth which is a key factor to retain a uniform structure and small particle sizes [275]. Key reaction parameters, such as pressure and temperature, are monitored in real-time *via* computer using *Labprof* software.

1.1.2 Materials and method

Strontium (II) acetylacetonate hydrate (Sigma-Aldrich), Titanium (IV) bis(acetylacetonate) diisopropoxide in 75 wt% dissolved in 2-propanol (Sigma-Aldrich), absolute ethanol (Scharlau, ≥99 wt%) and deionized water were used to synthesize the nanoparticles of $SrTiO_3$ with the supercritical continuous solvothermal technology.

The supercritical ethanol/water mixture with 0.29 mol% of ethanol was controlled with the pumps flow rate. The critical point of such a mixture for the supercritical solvothermal continuous synthesis has been calculated using the NIST software *Refprop* which gives p_c= 13.1 MPa and T_c= 297 °C. The temperature (400 °C) and pressure (23 MPa) are set higher than this critical point of the mixture. As sketched previously, the top injection line is the water line, where the strontium precursor is solubilized, injected, and preheated at a temperature of 180 °C at which the strontium precursor is still stable. The bottom line is the ethanol line where the titanium precursor is solubilized and injected in the system. The precursor concentrations of Sr^{2+} and Ti^{4+} were fixed at $2x10^{-4}$ M at the mixing point in

order to optimize the production yield and to avoid any clogging in the reactor. The obtained solutions were then centrifuged at 12,000 rotations per minute to recover the nanoparticles which were dried in an oven at 80 °C for 4 h.

The following part describes the characterization of the newly synthesized strontium titanate using acetylacetonate precursors. A first part is a complete structure analysis of the strontium titanate nanoparticles. We associate it with *in-situ* study of the material due to an exclusive characteristic based on its thermal stability and growth phenomenon which has been observed in real time.

In conclusion, the reactor setups employed in this PhD offer accurate control over key parameters such as flow rate, temperature and pressure. The flexibility of the parameters, combined with advanced monitoring and safety features, ensures consistent and repeatable production of high-quality materials. These adaptations, especially the use of improved HPLC pumps and preheater, allow for greater versatility in synthesizing complex oxide nanoparticles under supercritical conditions.

1.2 Improved setup for the supercritical solvothermal synthesis of undoped and doped $SrTiO_3$

1.1.1 Setup description

The previous section outlined the first setup used for the synthesis of strontium titanate. However, this system, built 20 years ago, had been used for various reactions with different compounds. Long-term use of components, such as the heating resistors, also increased the likelihood of malfunction.

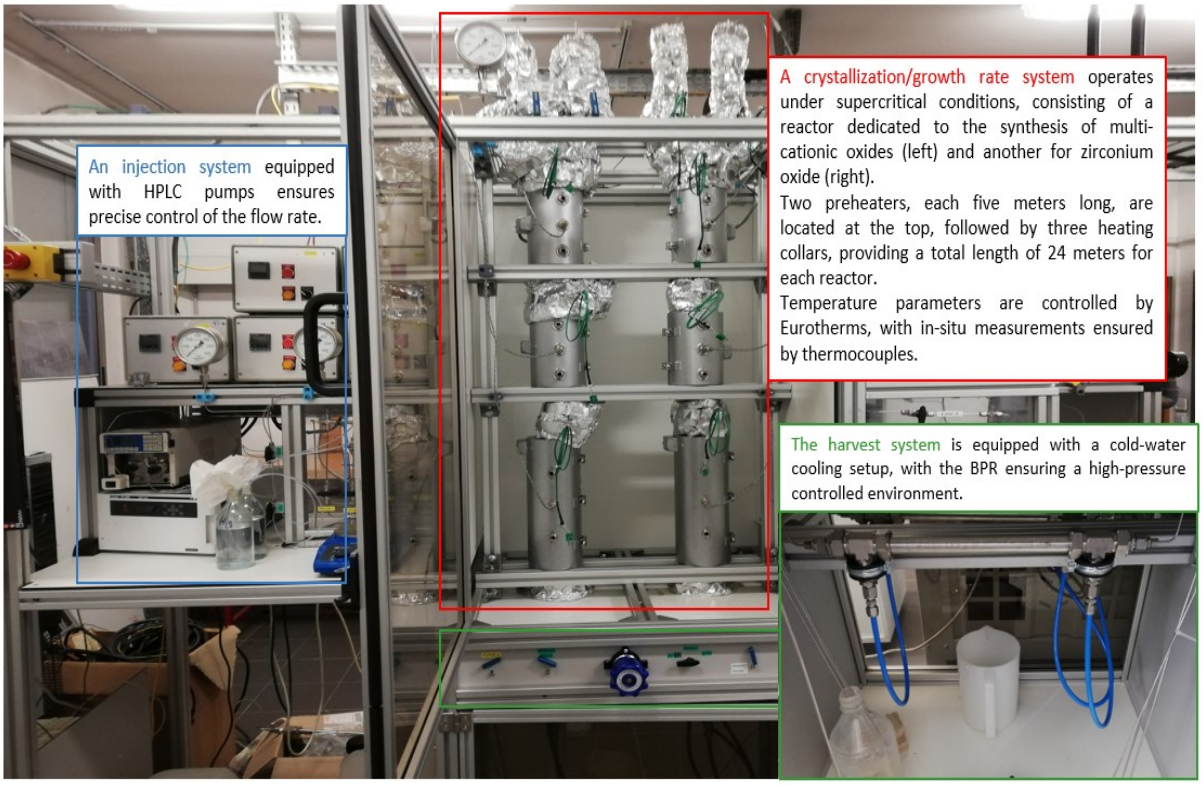

Figure 2.3: Picture of the newly constructed twin reactors setup symbolized by two separated reactors connected to each pumping site located on the side of the setup

A twin reactor setup was developed (***Figure 2.3***) offering the flexibility to isolate one side of the reactor to minimize the risk of contamination from previous syntheses. The heating mechanism was upgraded to a more efficient system, and the recovery process was improved to eliminate exposure to hot tubbing.

The second setup keeps key features from the original one, such as the use of HPLC pumps with two separate injection lines equipped with preheaters, and a 24-m coil reactor made of SS-316 stainless steel tubing (1.58 mm inner diameter). It is described in ***Figure 2.4***.

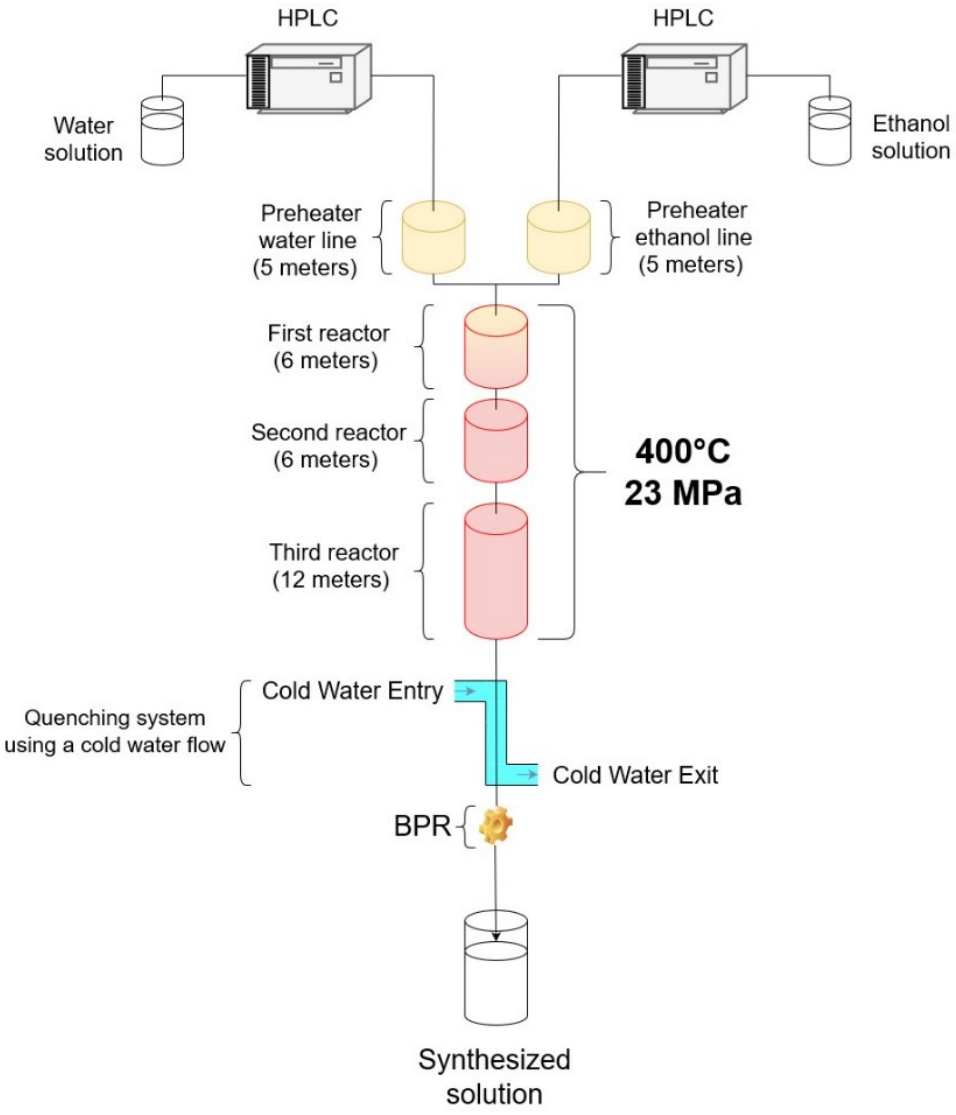

Figure 2.4: Scheme of the newly and improved set-up for the synthesis of doped and undoped strontium titanate nanoparticles

From this previous design, several improvements were achieved. The reactor was divided into three sections: a two 6 meters' sections followed by one 12 meters' section. These sections were placed inside heating clamps to maintain the reaction temperature at 400 °C in order to reach the pressure and temperature of the supercritical domain of the mixture. To optimize the thermal efficiency, the mixing area and all intermediate sections were insulated with glass wool and aluminum foil. Each heating clamp was connected to a Eurotherm controller, with temperature regulation via K-type thermocouples. A significant improvement in this setup was the location of K-type thermocouples directly within the flow system at the outlet of each the reactor section, using T-unions. This allowed for a real-time, *in-situ* temperature monitoring, which is a key improvement compared to the first

setup, where thermocouples were placed externally, leaving the actual internal temperature poorly known.

Strategically positioned purging valves, located before the hot zone and the back-pressure regulator, allowed for targeted purging of specific tubing zones in the heated or injection areas. The quenching system was also upgraded: instead of immersing the reactor outlet in an iced bath, the tubing now passed through an inner ¼-inch stainless steel tube connected to a cold-water line; this is a heat exchanger. This change provided better control and adaptability over the cooling process without sacrificing quenching efficiency. This upgrade allowed a clear control over the cooling part, eliminating the need to refill ice, as required in the previous setup, and avoiding any heat damage to the back-pressure regulator.

1.1.2 Materials and Methods

The STO nanocrystals were synthesized using typical precursors such as organometallics: Strontium (II) acetylacetonate hydrate, 99% (STREM), Titanium (IV) isopropoxide (Sigma-Aldrich), 97%, absolute ethanol (Scharlau, ≥99 %) and deionized water. The dopants used were taken from the same family of compounds, such as Yttrium (III) acetylacetonate hydrate, 99.95% (Sigma-Aldrich), Niobium(V) isopropoxide, 99% in 10 wt% in isopropanol/hexane in a 50:50 ratios (Thermo Scientific Chemicals), Neodymium (III) acetylacetonate hydrate (Sigma-Aldrich), Praseodymium (III) acetylacetonate hydrate (Apollo Scientific) and Iron (III) acetylacetonate, ≥99.9% (Sigma-Aldrich).

The doped nanoparticles of strontium titanate were synthesized using n-doping and p-doping elements. The codoping of was also tested. The acetylacetonate hydrate of strontium was mixed with de-ionized water solution and the isopropoxide of titanium was solubilized in absolute ethanol solution. The titanium and the niobium solution were prepared in an inert atmosphere in order to avoid any contamination of the isopropoxide precursor. The dopants were then added and solubilized in the adapted media and the precursor solutions placed in the setup for injection. For the purpose of creating $SrTiO_3$ doped nanoparticles using the sol-gel reaction the newly built set-up was used. As a reminder, the arrangement is divided into three sections, the first being the injection set-up. Precursor solutions were supplied to the injection lines *via* a solvent delivery system (JASCO PU-2080 PLUS). The primary and secondary lines are used to convey the various precursors while fixing a flow rate for both injection lines regulated at 6 $g.min^{-1}$, allowing the adjustment of water and ethanol ratio at x_{EtOH}=0.29. This provides a mixture system where the critical pressure (13.1 MPa) and temperature (297 °C) are easier to attain. As demonstrated in Chapter 3, the preheating system was not used to avoid any degradation of the acetylacetonate precursor before reaching the mixing area. The “crystallization and

growth system" is the second component of the setup. It consists of a hot zone reactor built from a 24-meter-long coil of SS-316 stainless steel tubing with an inner diameter of 1.58 mm divided into a reactor of 12-meter-long coil and two reactors of 6-meter-long coil each. The coil was put inside the heating collar to adjust the reaction temperature to 400 °C. A TESCOM back pressure regulator (BPR) allowed for the steady pressure of 23 MPa to be maintained when the supercritical conditions are met. The third step is the "harvesting set-up" which involves moving the nanoparticle suspension downstream from the reactor through SS-316 stainless steel tubing inside a secondary system where a cooled water is flowing. This makes the reaction medium return to the liquid domain due to a fast drop in temperature. Because of the proliferation of quenched nanoparticles, this enables powder recovery.

1.3 Conclusion on the setups development

To summarize, this section introduced two reactor setups. The original one, built in 2004, served as a prototype for synthesizing various compounds, with for instance barium titanate. It enabled the mastering of the synthesis of strontium titanate nanoparticles and the production of different doped compositions. However, over time, the setup experienced mechanical failures and contamination issues due to the increasing number of side projects, highlighting the need for an upgrade.

In response, a new, improved setup was built from scratch during the first semester of the second year of this PhD and has been in use since. While it retains some features from the original system such as the total reactor length, dual-pump system, and preheaters, significant improvements were made. These include upgraded heating and cooling system, and a twin reactors setup, with each reactor specialized for specific compounds. A key improvement is the addition of *in-situ* thermocouples that directly measure the temperature of the flow within the three reactor sections, providing more accurate temperature readings than the original setup.

These advancements provide greater flexibility, safety, and efficiency in the synthesis process, ensuring high-quality, reproducible results and allowing it to move to the next synthesis of doped composition.

2. $SrTiO_3$-based Nanoparticles Characterizations

A major objective of this PhD in synthesizing strontium titanate-based nanopowders was to prepare well-controlled compositions and microstructures using the supercritical flow synthesis method. This requires thorough characterization of both the nanopowder structures and compositions, as well as the processed (shaped) powders, whether in the form of cells or ceramics.

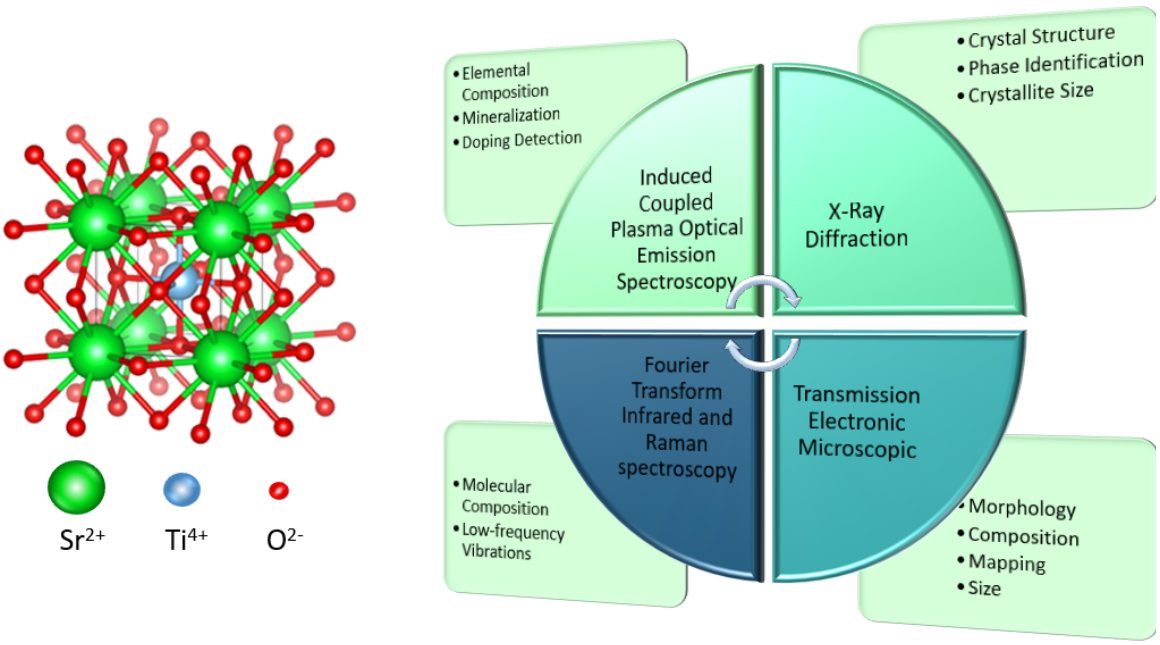

Figure 2.5: Summary of all the characterizations performed on the strontium titanate compound and their purpose

To undertake a comprehensive characterization, various techniques were used as represented in ***Figure 2.5***. This included X-ray diffraction (XRD) at ICMCB platform and Transmission Electron Microscopy (TEM) at PLACAMAT ("Plateforme Aquitaine de Caractérisation des Matériaux") for structural investigation. Spectroscopic analyses, such as Raman and Fourier Transform Infrared (FTIR), were also performed at ICMCB, while X-ray photoelectron spectroscopy (XPS) was carried out at PLACAMAT. For compositional analysis, energy-dispersive spectroscopy (EDS) and inductively coupled plasma (ICP) were used. The material thermal stability was explored through *in-situ* characterization, including high-temperature powder X-ray diffraction and high-temperature transmission electron microscopy, in collaboration with ICPMS in Strasbourg in the frame of the METSA network.

2.1 Structural Investigations

2.1.1 Powder X-ray diffraction

Throughout this work, X-ray diffraction played a crucial role. Conventional powder X-ray diffraction (PXRD) measurements provided essential information on phase purity, crystallinity, and doping success. Additionally, *in-situ* high-temperature X-ray diffraction measurements were performed. This section describes the equipment used for these analyses.

-Conventional X-ray diffraction

Depending on the data required, different X-ray diffractometers were used, each offering varying levels of resolution. The equipment choice and acquisition time affected the signal quality, which in turn enabled more precise analysis of the material cells parameters. Samples were prepared on stainless-steel holders with a razor blade to prevent preferential orientation.

- **PANalytical X'pert MPD-PRO Diffractometer:** XRD patterns were collected using a PANalytical X'pert MPD-PRO Bragg-Brentano θ-θ geometry diffractometer, equipped with a secondary monochromator, a 3X15 position sample changer, and an X'celerator detector. Measurements were taken over an angular range of 2θ = 8-80°, with each acquisition lasting 1 hour. The Cu-Kα radiation was generated at 45 kV and 40 mA (λ = 0.15418 nm).
- **Malvern-PANalytical Empyrean Diffractometer:** XRD patterns were also collected using a Malvern-PANalytical Empyrean diffractometer, featuring a Bragg-Brentano θ-θ geometry, a 3X15 position sample changer, and a 1Der detector. Measurements covered an angular range of 2θ = 8-130°, with an acquisition time of 11 h and 22 min. Recently, an equipment upgrade enabled high-quality acquisitions with a smooth signal using only 30 min of acquisition time. Data was collected over an angular range of 2θ = 6-100°.

The choice of the apparatus to be used depends on the desired information. The rapid XRD acquisition method was used for quick phase identification, crystallinity assessment, and crystallite size estimation. The extended acquisition time provided a smoother signal, allowing for a more accurate determination of the lattice parameters and crystallite sizes once synthesis repeatability was confirmed.

-*In-situ* X-ray diffraction

Due to the targeted high temperature use of our materials, additional tests were conducted to assess its thermal stability. This required monitoring the XRD signal as a function of temperature.

- **PANalytical X'pert MPD-PRO Diffractometer:** Temperature-dependent PXRD patterns were collected using a PANalytical X'pert MPD Bragg-Brentano θ-θ geometry diffractometer, equipped with an Anton Paar HTK16 oven and a secondary monochromator. Measurements were performed over an angular range of 2θ = 10–80°, with each acquisition lasting about 3 h. The Cu-Kα radiation was generated at 45 kV and 40 mA (λ = 0.15418 nm). The sample was mounted on a platinum heating filament holder and flattened with a glass slide, with data acquired at intervals of 100 °C, ranging from 100 °C to 1200 °C.

-Interpretation of the XRD data

For XRD data processing, the phase identification was performed using the ICDD PDF-2 database with EVA software. All powder X-ray (PXRD) patterns were refined using *FullProf* software, with the peak profiles fitted using the Thompson-Cox-Hastings pseudo-Voigt function. Key refined parameters included lattice parameters and crystallite sizes. Crystallite sizes were determined using the detailed MIC file within the same software.

2.1.2 Spectroscopy investigation

-**Fourier transform infrared spectroscopy**

Fourier Transform Infrared (FTIR) spectroscopy was used to investigate the vibrational modes and the possible organics compounds remaining in the nanopowders using a Bruker Equinox 55 spectrophotometer. To perform the measurements, a small quantity of strontium titanate nanoparticles was ground and mixed with KBr powder. The infrared (IR) spectra were collected over a range of 400 to 4000 cm^{-1} with a resolution of 4 cm^{-1}, providing a broad spectral absorption profile of the sample.

Given that this synthesis follows a similar approach to that of a previously studied barium titanate [276] the aim of this study was to determine whether the new material exhibited the same surface properties as the earlier one.

-Raman spectroscopy

Raman spectra were recorded at room temperature using a HORIBA HR Evolution spectrometer with a gas laser with λ = 633 nm. The system spatial resolution includes a confocal microscope with submicron lateral resolution and an axial confocal performance better than 2 micrometers. Raman signal data were collected and analyzed using Labspec6 software over a range of 150 to 800 cm^{-1}.

Raman spectroscopy was crucial for this study because, although the strontium titanate maintains a cubic structure at room temperature, it exhibits both longitudinal (LO) and transverse optical (TO) phonon modes. This provided a complementary analysis to FTIR characterization, as FTIR and Raman spectroscopy are sensitive to different types of lattice vibrations. FTIR is more responsive to polar bonds, while Raman spectroscopy is active in non-centrosymmetric lattices or is activated by defects.

2.1.3 Size and morphology characterization and elemental investigation

-Transmission electron microscopy (TEM)

This characterization was carried out at the PLACAMAT platform, with assistance from Mrs. BUFFIERE, who prepared the samples and conducted the high-resolution analyses. Transmission Electron Microscopy (TEM) was employed to observe the microstructure, size, and morphology of the strontium titanate (nano)particles.

The instruments were a TEM-JEOL 2100 with a filament LABO, providing a resolution of 2.5 Å, and the HRTEM-FEG JEOL 2200FS with field emission, offering a resolution of 1.5 Å. TEM images were acquired and analyzed using Digital Micrograph software. Samples were dispersed in ethanol before being deposited onto copper-carbon grids.

Given the nanoparticle size determined from XRD, it was indeed essential to correlate this with direct morphological characterizations. TEM relies on the interaction between the electron beam and the sample to generate images, allowing for detailed observation of particle size and morphology. In high-resolution mode (HRTEM), it also provides insight into atomic arrangements, enabling comparison with XRD-calculated crystallite sizes to assess whether the nanoparticles are monocrystalline.

Energy-Dispersive X-ray Spectroscopy (EDS) was used as a complementary technique to check the elemental composition of localized areas of the sample. Strontium was quantified using the line located at 14.140 keV, and located at 4.508 keV for titanium, ensuring clear separation and accurate quantification of the spectra.

This characterization enabled us to quantify the elemental composition and assess the homogeneity of the doping elements, confirming a uniform distribution or identifying potential clustering.

***-In-situ* transmission electron microscopy**

To delve deeper into the observations from the *in-situ* high-temperature PXRD, an advanced characterization technique was employed using Transmission Electron Microscopy (TEM) to directly

image the nanoparticles evolutions as the temperature increased. This characterization was conducted at IPCMS in collaboration with Pr. ERSEN and Dr. BAAZIZ in the frame of a METSA application.

In situ TEM experiments were performed using a JEOL JEM-2100F microscope operating at 200 kV. The microscope was equipped with a spherical aberration probe corrector (Cs from CEOS), a high-resolution objective lens pole piece, an UltraScan 1000 CCD array detector (GATAN), and a Centurio EDX detector (JEOL). Prior to analysis, the samples were sonicated in a dichloromethane solution. For *in-situ* observations, a Protochips Atmosphere system was used, where samples were placed between two micro-electro-mechanical systems (MEMS)-based closed cells made of transparent SiNx (for observation) and SiC (for heating).

The *in-situ* analysis followed several steps: first, the sample was heated to 100 °C under vacuum, then air was introduced to reach atmospheric pressure. Next, the temperature was gradually increased to 800 °C at a rate of 10 °C per minute. TEM images were recorded for selected fragments within the temperature range of 500 °C to 800 °C. To minimize electron beam effects, such as contamination and sample damage, observations were conducted to determine the maximum electron beam dose that the sample could tolerate in each gaseous environment. Additionally, the *in-situ* observation areas were not continuously exposed to the electron beam, and regions outside the observation zones were systematically analyzed for comparison to identify any potential artifacts caused by electron irradiation.

-Inductive Coupled Plasma Optical Emission Spectroscopy (ICP-OES)

The previously discussed techniques provided semi-quantitative information regarding elemental composition. To achieve a more accurate stoichiometry investigation, Inductively Coupled Plasma Optical Emission Spectroscopy (ICP-OES) was used.

ICP-OES experiments were conducted using an Agilent 5800 ICP-OES instrument, renowned for its capability in chemical analysis. This instrument operates with a working coil at 1500 V RMS and approximately 27 MHz, generating a plasma temperature around 10000 °C. The data obtained from these experiments were analyzed using Expert software to ensure accuracy and reliability.

For the ICP-OES analysis, the mineralization process followed a specific protocol. First, 10 mg of strontium titanate nanoparticles were precisely weighed and combined with a digestion solution consisting of 10 mL of hydrochloric acid (37 wt.%, Scharlau), 3 mL of nitric acid (69.5 wt.%, Scharlau), and 1 mL of hydrogen peroxide solution (30 wt.%, Scharlau). This mixture was then heated for 4 h at 80 °C using the Environmental Express HotBlock SC154 Digestion System.

After the digestion process, the solution was diluted to a final volume of 100 mL with ultrapure water. This diluted solution was then injected into the ICP-OES device. The quantification of elements was performed by measuring the intensity of specific spectral lines, for example, strontium was detected at 215.283 nm, and titanium at 324.199 nm.

This technique provided a highly accurate determination of the elemental composition of the synthesized strontium titanate and ensured the accuracy of the doping mechanism.

2.2 Conclusion

The goal of using these various characterization techniques was to provide a comprehensive analysis of strontium titanate nanoparticles and their doped variants, with a focus on controlling the dopant percentage. Each technique played a specific role in validating and detailing different aspects of the material synthesis.

X-ray diffraction (XRD) was initially employed to confirm the viability of the supercritical fluid synthesis method using metallic precursors. Once the synthesis process and setup were validated, high-quality XRD data provided precise information about the lattice parameters and crystallite sizes, ensuring the accuracy of the synthesis process.

Spectroscopy techniques, including FTIR and Raman, were used to further investigate the bonding characteristics of the material. FTIR confirmed that the surface groups were consistent with those found in similar materials synthesized using supercritical methods. Raman spectroscopy revealed distinctive features of the material, particularly the presence of defect-induced lattice vibrations, which were not detectable by FTIR.

To assess the nanoparticle morphology and verify their size, Transmission Electron Microscopy (TEM) was used. TEM not only confirmed the nanosize but also validated the monocrystalline nature of the compound. Complementary to TEM, Electron Dispersive Spectroscopy (EDS) provided additional elemental quantification and supported the macroscopic assessment of the uniformity of the nanoparticle composition.

Inductively Coupled Plasma Optical Emission Spectroscopy (ICP-OES) was used for its superior precision in determining the elemental composition, particularly for quantifying very low levels of dopant elements. This technique was essential for confirming the successful incorporation of doping elements.

The powders synthesized in this work exhibited unprecedented thermal stability. To investigate this further, *in-situ* high-temperature XRD was performed to observe how temperature affects the XRD

patterns of the nanoparticles. Following these observations, advanced *in-situ* Transmission Electron Microscopy provided detailed images on how temperature impacts the nanocrystallites, offering deeper insights into the material thermal behavior.

3. Shaping of Catalytic Cells and Ceramics

This section focuses on the formulation of the synthesized nanoparticles. The primary goal of the ANR CHEEC project, in which this PhD was integrated, was to fabricate an anode for fuel cells by depositing $SrTiO_3$-based materials onto a commercial Ni-YSZ/YSZ half-cell. To characterize the electronic conductivity of the deposited $SrTiO_3$-based compositions, a four-probe measurement technique was employed, necessitating the development of dense pellets. The central objective was to demonstrate that doping significantly affects the electronic conductivity of $SrTiO_3$.

3.1 Development of half-cell

Once the $SrTiO_3$ nanoparticles have been synthesized, they are processed into an ink for deposition onto yttria-stabilized zirconia (YSZ) half-cells. Screen printing is the preferred method for shaping the anodes, as it has been successfully employed for electrode developments at ICMCB. Leveraging ICMCB extensive experience with Terpineol-based slurries, we optimized the screen-printing paste and its sintering temperature to enhance the electrochemical properties of the electrodes. The shaping of these electrodes was a crucial aspect of this thesis. The different steps are shown on ***Figure 2.6*** and described further.

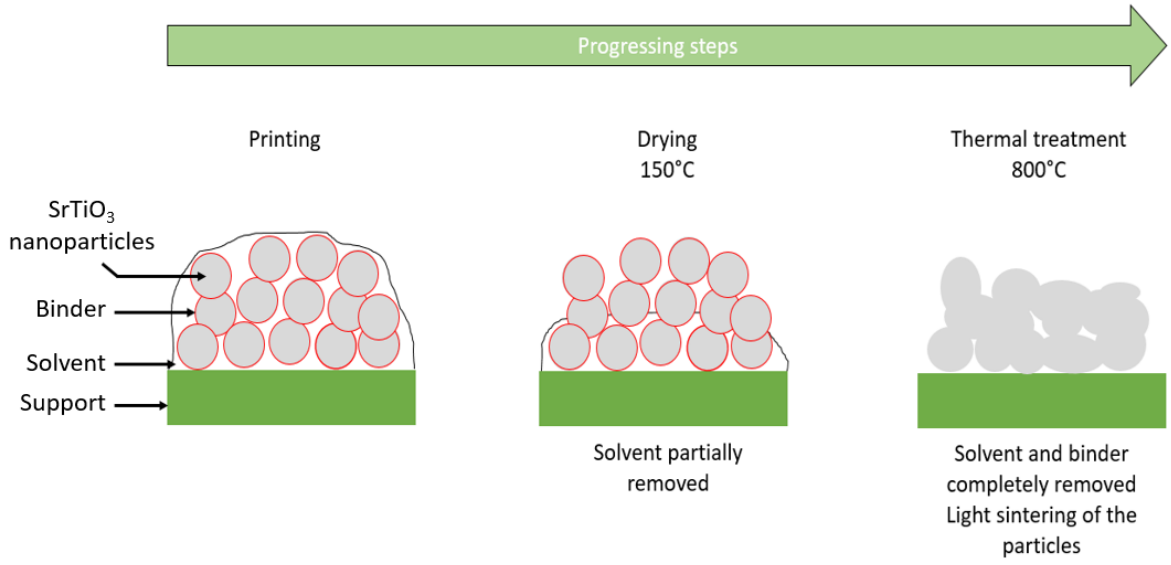

Figure 2.6: Scheme of the evolution of the processing of the nanomaterials throughout the different steps of deposition through screen-printing

3.1.1 Ink preparation

The formulation of the ink involves several key components. The primary material to be deposited is the nanopowder of strontium titanate, synthesized in supercritical water-ethanol. The binder, typically a polymer, ensures cohesion among the nanoparticles and provides mechanical strength once the solvent evaporates during the initial drying phase. The solvent acts as a medium for mixing and greatly influences the ink quality and viscosity, which should ideally be compared to the texture of honey.

The choice of the solvent is crucial; terpineol, for example, is used because it evaporates slowly, preventing the ink from drying or changing its viscosity too quickly. If the solvent quantity is insufficient, the ink becomes too viscous, leading to thicker and inhomogeneous deposits. Conversely, an excess of solvent results in a thinner deposit with a lower powder concentration and can cause the ink to spread uncontrollably, distorting the wanted pattern.

Additionally, a dispersant may be added to ensure a uniform powder concentration, though only in small amounts relative to the binder and solvent. After the ink is applied through screen printing, the solvent is evaporated at low temperature (100 °C). The binder then plays a critical role in maintaining the integrity of the deposit, allowing for the addition of further layers if needed and ensuring that the deposit can withstand high-temperature treatments. The amount of binder is carefully controlled to achieve a uniform deposit while avoiding residual porosity.

3.1.2 Screen printing

Once the ink has been processed to achieve the correct viscosity, the next step is to apply it using screen-printing. This technique is commonly used in the development of fuel cell electrodes, mainly oxygen electrodes. As illustrated in ***Figure 2.7***, the process involves several key steps.

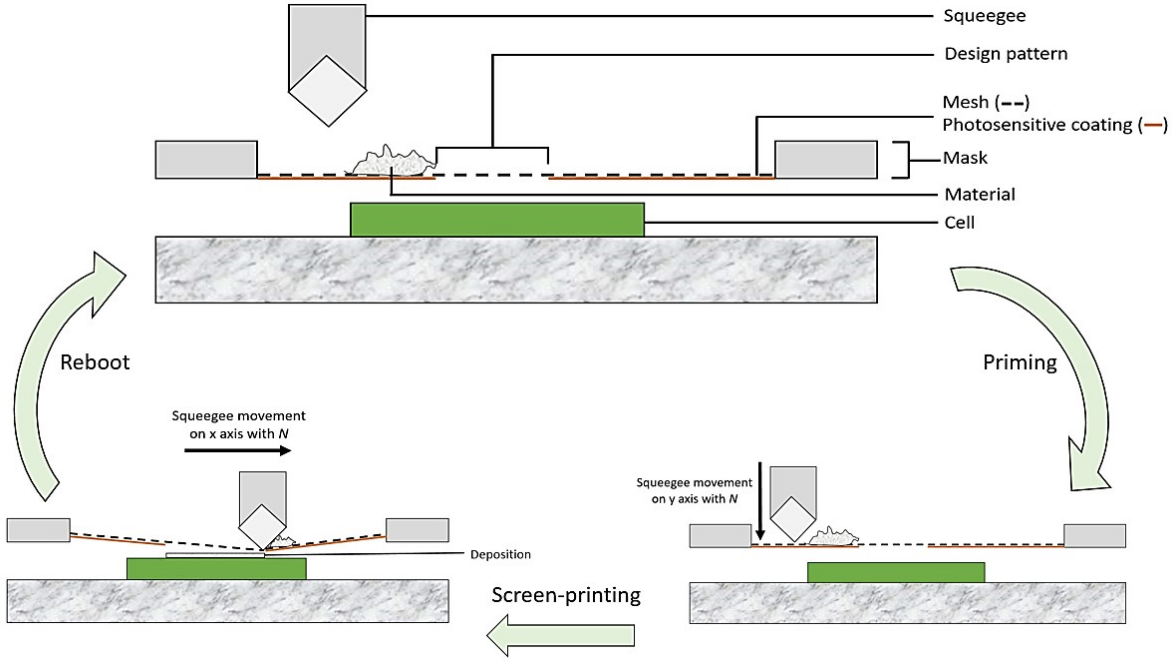

Figure 2.7: Scheme of the overall functioning mechanism of the screen-printing device

The ink was applied on the support using a mechanical arm equipped with a squeegee. Several parameters can be adjusted during this process, including the total distance traveled by the squeegee depending on the targeted pattern. The uniaxial force applied by the squeegee helps ensuring that the ink passes through the mask, especially checking if the ink is stuck in the mask openings due to a high viscosity. Also, the distance between the initial position of the squeegee and its downward movement is adjustable. However, it is important to carefully control both the force and the elongation to avoid damaging the mask, such as tearing it down.

The mask itself is an important piece of the deposition process. It is positioned and fixed between the cell and the deposited ink. It possesses a fine mesh coated with a photosensitive polymer that blocks the ink from passing through unwanted areas. By selectively removing parts of the polymer through light treatment, openings are created in the mask. The researched pattern is obtained thanks to the designed opening area that allows the ink to go. As the squeegee moves across the mask, it pushes the ink through these openings, thereby reproducing the pattern onto the cell with precision.

3.1.3 Thermal treatment

For ceramic electrodes used in Solid Oxide Fuel Cells (SOFCs), the entire cell must undergo high-temperature thermal treatment. This process is essential for removing organic components like binders and solvents and for promoting sintering, which strengthens the mechanical structure of the electrode. This strengthening is critical for the electrode overall performance.

The thermal treatment ensures the removal of organic materials, leaving only the desired ceramic phase. It also facilitates the sintering process, where grains are fused together, enhancing the electrode structural integrity and the formation of the long side network which is mandatory for ensuring the transport of electrons and ions in the ceramic. Sintering relies on thermal diffusion, which requires high temperatures. For nanoparticle powders, the treatment must be carefully controlled. The primary goal of the sintering is to reduce the surface energy, which increases as the particle size decreases. Therefore, the temperature treatment must be optimized to balance between increasing crystallite size, which potentially reduces catalytic properties and ensuring mechanical stability.

Moreover, the thermal treatment needs to be managed to avoid the formation of unwanted reactions at the interface between the electrode and the electrolyte support (YSZ or gadolinium-doped ceria (GDC)). These reactions are considered a double-edged sword since they can either improve the bonding efficiency between the electrolyte and the electrode or create insulating phases that impair the electrode electronic properties.

After the high-temperature treatment, evaluating the adhesion of the deposited material is crucial to confirm the effectiveness of the thermal treatment. One commonly used and straightforward adhesion test is the “Scotch tape test”. In this test, a piece of adhesive tape is applied to the surface of the screen-printed layer and then pulled away. This method, as described in the Handbook of Semiconductor Interconnection Technology *(2006 by Taylor & Francis Group, LLC),* provides a basic indication of adhesion quality. If the top layer peels off more or less completely, it generally signifies (very) poor adhesion, indicating that further adjustments to the thermal treatment are necessary.

3.1.4 Deposit characterization

At ICMCB, we are using the Aurel C890 screen printing apparatus for processing the electrodes. These electrodes were applied to various YSZ cells, including i) commercial 20 mm diameter, 150 µm thick YSZ cells from Neyco, cells added with a 15 µm thick layer of GDC screen-printed by Neyco, and ii) Ni-YSZ cermet cells from Elcogen with a 15 µm thick GDC layer.

The microstructure of these electrodes was analyzed using X-ray diffraction (XRD), as previously described, while thickness measurements were performed using scanning electron microscopy (SEM). The SEM analysis was conducted with a JEOL 6360A, operated by Mrs BUFFIERE at ICMCB, featuring an accelerating voltage range of 0.5 to 30 kV and magnification capabilities up to 30,000x. This technique leverages various electron/material interactions:

- Secondary electrons are used to assess the overall deposition of $SrTiO_3$-based nanoparticles, including their thickness and morphology.
- Backscattered electrons provide chemical contrast, revealing the homogeneity of the composition. This method is particularly useful for detecting any diffusion of species post-thermal treatment, with lighter elements producing less signal and appearing darker on the images, indicating areas of lower interaction.

3.2 Electronic conductivity of dense ceramics

3.2.1 Ceramics processing

To determine the electronic conductivity of doped strontium titanate nanoparticles synthesized using supercritical fluids, it is as a first step mandatory to process the nanoparticles into dense pellets. Densification leads to an increase in the crystallite size due to interdiffusion between grains. Then, since catalytic applications rely on high surface area, linked to small particle size, it is crucial to limit this growth. Additionally, maintaining the nanoscale of the material may enhance conductivity in oxide [277,278].

At ICMCB, we have extensively studied the impact of the sintering on material properties such as zirconium oxide or perovskite such as barium strontium titanate, investigating key parameters such as porosity [279], grain size [280], grain boundary quality [281,282], and the presence of defects [283] in the material. These factors significantly alter the intrinsic properties of the material. Sintering parameters such as heating and cooling rates, dwell temperature, and atmosphere are critical, as they govern the diffusion processes during the thermal treatment.

For compact pellet production, Spark Plasma Sintering (SPS) was used. This technique, mastered by ICMCB, has been applied to a wide range of compounds and is particularly advantageous for sintering nanomaterials while limiting grain growth [284,285]. SPS combines the Joule effect together with uniaxial pressure, enabling rapid heating and sintering, which reduces the time available for grain enlargement.

Dr. U-Chan Chung performed the SPS process, successfully producing dense pellets of both pure and doped strontium titanate nanoparticles. These pellets were characterized by X-ray diffraction to assess any impact of the SPS process on the phase stability, and further analysis was conducted to determine post-treatment crystallite sizes. The density of the pellets was measured using the Archimedes method, and four-probe measurements were conducted to determine the electronic conductivity of the material.

3.2.2 Spark Plasma sintering

This part describes the principle of SPS and how to prepare a dense pellet from the use of $SrTiO_3$ based-nanopowders.

At ICMCB, the Dr. Sinter 515S machine, manufactured by SPS Syntex Inc., is operated by Dr. U-Chan Chung. This equipment delivers a pulsed current output of 1500 A, works at a voltage range of 2 to 20 V, and is able to apply a pressure up to 200 MPa. The process is described on ***Figure 2.8***.

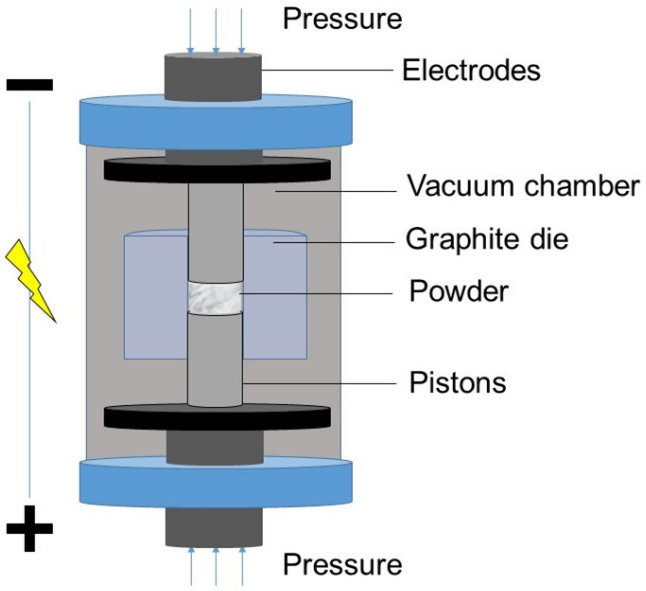

Figure 2.8: Scheme of the principles and the different parts composing the SPS equipment

The $SrTiO_3$-based nanopowder was loaded into a cylindrical carbon die with an inner diameter of 8 mm, without the use of any binder. To ensure optimal conductivity and uniform heating, the powder was wrapped in graphite foil. A pulsed electrical current was passed through the electrodes *via* the die, generating heat through the Joule effect. Uniaxial pressure was applied to enhance the chemical diffusion. Before applying pressure and the pulsed current, the chamber was evacuated resulting in a low oxygen partial pressure. After the SPS process, each pellet was polished and thermally treated at a selected temperature in an air atmosphere to counteract the reducing conditions, such as the formation of oxygen vacancies, and to remove carbon contamination from the die and graphite foil.

The primary advantage of this method, compared to conventional sintering, lies in its rapid sintering kinetics, driven by the enhanced thermal diffusion. The pulsed electric current, converted into heat, allows for a fast-heating ramp (100 °C per minute) combined with high pressure (100 MPa). This

synergy enabled the production of a compact pellet up to 100 times faster compared to conventional sintering, which typically involves a uniaxial pressure step followed by sintering in a tubular reactor.

3.2.3 Density measurement

Prior to the conductivity measurements, Archimedes measurements were performed to determine the density of the pellets produced by SPS. The objective was to reach a density higher than 90% of the theoretical density.

The Archimedes principle is to measure the buoyant force of a solid when submerged in a fluid either water or ethanol. The principle is based on the theory that any object submerged in a fluid experience an upward buoyant force equal to the weight of the fluid displaced by the object. With a hydrostatic balance which enables to weight of a solid in air as in water, it is possible to determine the specific density of a solid if the density of the liquid causing buoyancy is known. The density of a solid can be calculated with the following formula:

$$\rho = \frac{W(a).\rho(fl)}{W(a) - W(fl)} \quad (12)$$

Where *ρ* is the specific density of the solid, *W(a)* is the weight of the solid in air, *W(fl)* is the weight of the solid in liquid and *ρ(fl)* is the density of the liquid.

The following assumptions for the characterization are that i) the solid is fully submerged and does not absorb the liquid; ii) the fluid used has the density assumed at 25 °C; iii) Lastly, the air bubbles are removed from the surface of the solid to avoid errors.

The apparatus used is a YDK03 density kit. The relative density of the pellet was then determined thanks to the following relation:

$$d(\%) = \frac{\rho(experimental)}{\rho(theoretical)} \times 100 \quad (13)$$

Where *ρ(experimental)* is the density determined previously and *ρ(theoretical)* is the value given in the JCPS file 00-035-0734 and is equal to 5.118 $g.cm^{-3}$.

Thanks to the reliability of this method, the density of the pellet processed with $SrTiO_3$-based nanopowder doped and undoped was achieved and implied the successful action of the SPS process to produce dense samples.

3.2.4 Electronic conductivity measurement

The goal of this characterization is to determine the electronic conductivity of the $SrTiO_3$-based nanoparticles synthesized using supercritical fluids and to study the effect of doping with n-donor and p-donor elements. Dr. Rodolphe Decourt carried out these measurements at ICMCB, using a setup he designed himself.

The four-probe method is commonly used for the accurate measurement of electrical resistivity (conductivity) in materials like semiconductors or metals [286–288]. Essentially, it is a major improved version of the two-probe method, which helps eliminating errors caused by contact resistances. In this method, four metallic probes made of tungsten are positioned at equal distances on the material surface. The paste used for the interface probes/sample is made of gold. A current is passed through the outer two probes, while the inner two probes measure the resulting voltage. This setup allows for the calculation of the material resistivity by separating the current-carrying circuit from the voltage measurement one, which greatly reduces the influence of contact resistances on the final result (not the case of two probes measurements).

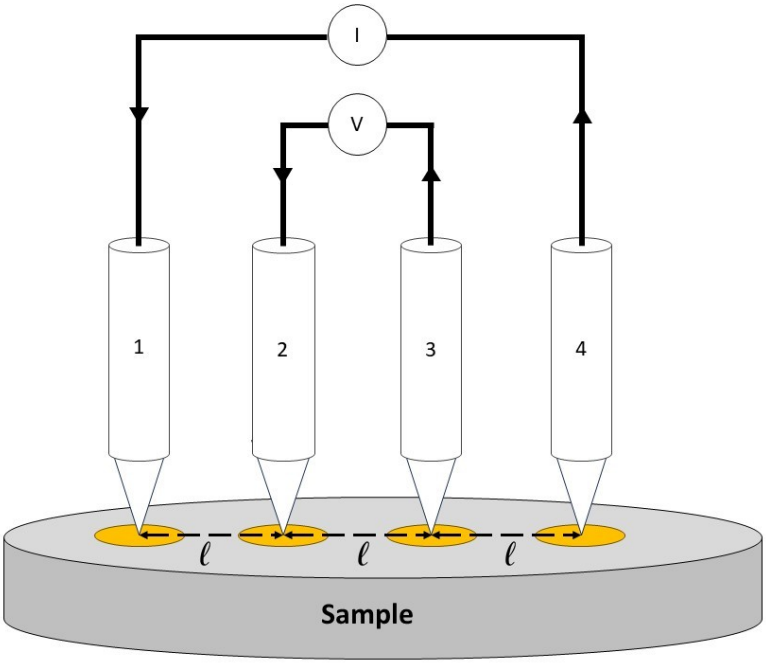

Figure 2.9: Scheme of the electrical resistivity measurement by four-point probe method with the inner probes (2&3) and outer probes (1&4)

Figure 2.9 describes the whole scheme, the contact is made with gold paste and is arranged in a linear configuration and spaced equally apart on the pellet. These are the link with the electrical circuit and are in direct contact with the surface of the material. The current is then applied by connecting a source

to the outer probes (1 and 4). Then a voltmeter is connected to the inner probes (2 and 3), which measures the voltage drop V across the section of the material that the current flows through. The resistance R can be calculated based on the measured voltage V and the applied current I using the Ohm's Law:

$$R = \frac{V}{I} \tag{14}$$

Each pellet was measured between 25 °C and 700 °C under air or argon, a semiconductor conduction type was evidenced in all cases. The resistance is defined as a value representing how much a material opposes the flow of electric current through it. The unit is the ohm (Ω) defined by the formula:

$$R = \rho \frac{L}{A} \tag{15}$$

Where R is the resistance (Ω), ρ is the resistivity of the material (Ω·cm), L is the length of the conductor (cm) and A its cross-sectional area (cm^2). The resistivity, however, is described as an intrinsic property of a material that quantifies how strongly it resists the flow of electric current, independent of its shape or size.

The resistivity is the inverse of conductivity; it can be written as:

$$\rho = \frac{1}{\sigma} \tag{16}$$

Where σ is the conductivity ($S \cdot cm^{-1}$).

The conductivity evolution vs T° can be expressed as an Arrhenius equation since it is used to describe the temperature dependence of physical and chemical processes which include electronic conductivity by considering the following equation:

$$\sigma(T) = \sigma_0 \, exp\left(-\frac{E_A}{k_B T}\right) \tag{17}$$

Where σ_0 is considered as the constant that represents the material conductivity at very high temperatures, E_A is the activation energy, k_B is the Boltzmann constant and T is the temperature. The equation can be expressed as:

$$Ln(\sigma(T)) = Ln(\sigma_0) - \frac{E_A}{k_B T} \tag{18}$$

This allows us to find the activation energy of each characterized sample, E_A being in Joule, the value is then converted into eV. Knowing the activation energy allows to determine the band gap of the material and attest any effect of the doping and/or the synthesis process. σ is also linked to density of carrier n and to their mobility μ and e being the electrical field:

$$\sigma = n \times \mu \times e \tag{19}$$

The range of temperature going from 25 °C to 700 °C and the atmosphere being either oxygen or argon in the cell during the measurement, we consider that the experimental conditions have no impact on the number of charge carriers. Then, we consider that n does not depend on the temperature parameter.

Conclusion of Chapter 2

This chapter presented the supercritical setups for synthesizing strontium titanate nanoparticles. Two designs were discussed: the original, which was foundational for synthesizing these nanoparticles and validating the chemistry with new precursors, and an improved version, developed through collaboration between PhD students and engineers at ICMCB. This updated design introduced enhancements for a more ergonomic system, particularly improving the heating and cooling processes. Being part of this project gave us valuable insight into designing a setup specifically for nanoparticle synthesis at a laboratory scale.

The second section focused on the various characterization methods used for the strontium titanate nanoparticles. Techniques like XRD, Raman spectroscopy, FTIR, TEM, and XPS were employed to thoroughly analyze the material. Advanced *in-situ* characterizations were also performed

The final part of the chapter covered the processing of the synthesized powder into electrode cells and dense pellets. Electrode fabrication involved multiple steps, including ink formulation, screen printing, and thermal treatment, leading to the successful deposition of strontium titanate nanoparticles. These electrodes will be further characterized by collaborating laboratories. Additionally, the nanoparticles were processed into dense pellets using spark plasma sintering. The electronic properties of various strontium titanate compositions were measured using the four-probe method, with the goal to demonstrate the influence of the doping process and its impact on conductivity.

Chapter 3: New Precursors for the Solvothermal Flow Synthesis of $SrTiO_3$ Nanoparticles

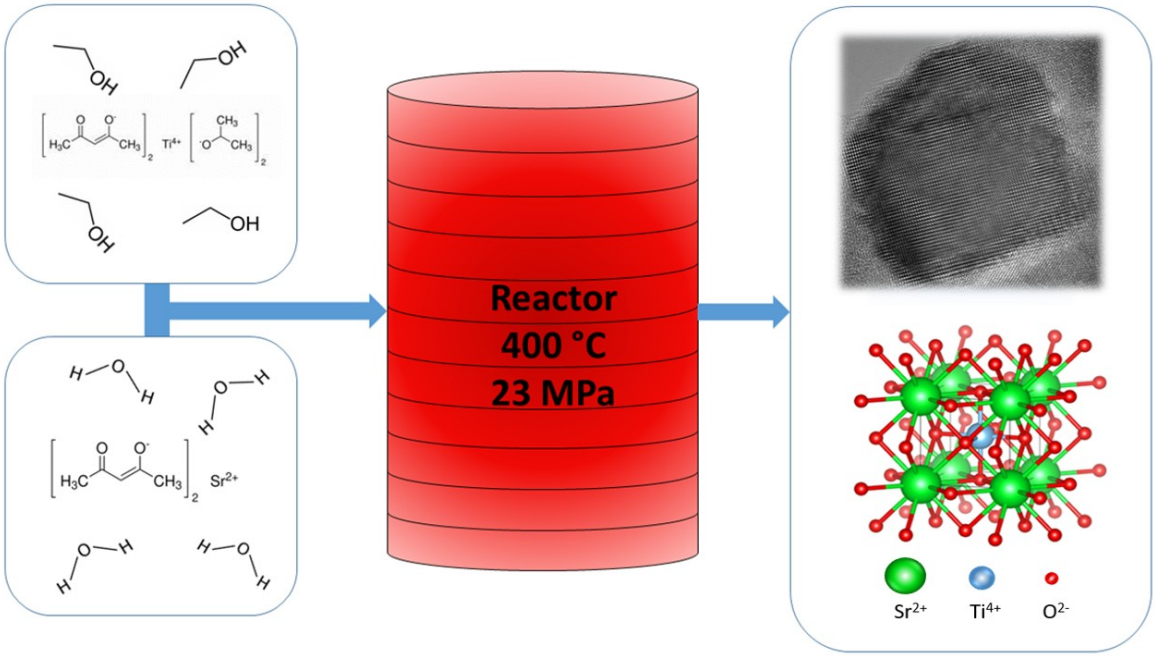

Graphical abstract of the scientific article "New solvothermal flow synthesis of strontium titanate nanoparticles based on the use of acetylacetonate precursors in water/ethanol mixture"

The objective this chapter, is to present a new way to synthesize $SrTiO_3$ nanoparticles using the supercritical continuous flow synthesis route.

As presented in Chapter 1, this material is not new to the research group, it even has a long-standing history starting back in 2005 were they demonstrated the supercritical sol gel like synthesis of $SrTiO_3$ nanocrystal starting with strontium-based alkoxide precursors. Since, the control and understanding of the synthesis has been further producing solutions $BaTiO_3$–$SrTiO_3$ and $BaTiO_3$–$BaZrO_3$ solid. Unfortunately, this approach comes to a dead end since it is not anymore possible to purchase barium and strontium-based alkoxide precursors of good quality. This pushed us to find a new way to produce these particles, adapting the existing procedure to new precursors. The objective was to stand to a sol gel like synthesis, maintaining as much as possible the established experimental parameters. Based on this, we decided to investigate the reactivity of acetylacetonate precursors, including strontium acetylacetonate and titanium acetylacetonate discussed in this chapter, as well as doping agents like yttrium acetylacetonate, which is mentioned later in Chapter 4. As described in Chapter 2, the material characterization has to provide capital information on the physicochemical properties of the produced nanoparticles. This will permit us to evaluate the quality of the synthesized material.

For the first time in the state of art of supercritical synthesis, acetylacetonate precursors of titanium and strontium were used to synthesize strontium titanate. The physicochemical properties of the produced particles with a focus on their thermal stability are discussed using complementary characterization techniques such as powder X-ray diffraction (PXRD), Fourier-Transform Infrared (FTIR) and Raman spectroscopies, Inductively Coupled Plasma-Optical Emission Spectrometry (ICP-OES) and Transmission Electron Microscopy (TEM). Using acetylacetonate precursors give access to materials with unprecedented physicochemical properties.

1. Synthesis of $SrTiO_3$ Nanoparticles

1.1 Materials

Nanoparticles of $SrTiO_3$ were synthesized using the supercritical solvothermal technology, a method known for its efficiency in producing high-quality nanomaterials. The synthesis process employed carefully selected chemical precursors to ensure the formation of pure and well defined $SrTiO_3$ nanoparticles. These included strontium (II) acetylacetonate hydrate, sourced from Sigma-Aldrich, and titanium (IV) bis(acetylacetonate) diisopropoxide, also supplied by Sigma-Aldrich, in a 75 wt.% solution in 2-propanol. Absolute ethanol (Scharlau, ≥99 wt.%) was used as a solvent, while deionized water acted as a reaction medium to facilitate the hydrolysis and condensation steps, critical for the nanoparticle formation. This combination of reagents and technology provided a controlled environment for the synthesis.

1.2 Method

As we mentioned previously, the works and optimization of the alkoxide precursor use allowed us to obtain high-quality nanoparticles but has come to a dead-end due shortfall of strontium alkoxide.

An important aspect of the alkoxide synthesis was that both precursors were solubilized in an ethanol solution, ensuring compatibility between the strontium and titanium precursors. The choice of precursors was constrained due to the limited availability of strontium organometallic compounds that are soluble in ethanol. Such precursors are either scarce or expensive, making strontium salts a more accessible option, though they are not soluble in ethanol. Conversely, titanium salts are also challenging to obtain, making it difficult to combine both elements in a single solvent.

To address this challenge, we considered using the water line as a carrier for transporting also precursors to the mixing point in the setup. Acetylacetonate-based precursors were prioritized because they support the sol-gel mechanism under supercritical conditions, and are soluble in aqueous media. However, the thermal stability of the precursors needed to be carefully examined to set the preheater temperature around 300 °C (see Appendix B) to prevent any side reactions before reaching the mixing zone. Additionally, precise control of the flow rates for both injection lines was essential to ensure stoichiometric balance at the mixing point, further emphasizing the need for meticulous optimization of the synthesis parameters. The optimization regarding the flowrate was one of most important parameters to keep. Indeed, it serves at the access to a tubular flow type model that allows obtaining a narrow size distribution but also the molar fraction of water and ethanol.

$SrTiO_3$ (STO) was synthesized from strontium acetylacetonate and titanium diisopropoxide bis(acetylacetonate) precursors in a supercritical ethanol/water mixture with 0.29 mol.% of ethanol (controlled with the pumps flow rate). The critical point of such a mixture for the supercritical solvothermal continuous synthesis were calculated using the NIST software *Refprop* which gives p_c= 13.1 MPa and T_c= 297 °C. The temperature (400 °C) and pressure (23 MPa) are set higher than this critical point of the mixture. As sketched in ***Figure 2.2***, the top injection line is the water line, where the strontium precursor is solubilized, injected, and preheated at a temperature of 180 °C at which the strontium precursor is still stable. The bottom line is the ethanol line where the titanium precursor is solubilized and injected in the system. The concentrations of Sr^{2+} and Ti^{4+} were fixed at 2×10^{-4} M at the mixing point in order to optimize the production yield and to avoid any clogging in the reactor. The obtained solutions were then centrifuged at 12,000 rotations per minute to recover the nanoparticles which were dried in an oven at 80 °C for 4 h.

The following part describes the characterization of the newly synthesized strontium titanate using acetylacetonate precursor. The first part is a complete structure analysis of the strontium titanate nanoparticles. The application aimed being the high temperature electrolysis, the system itself works at temperature around 600 °C. The thermal stability of the material had to be investigated in order to ensure a right functionality.

2. $SrTiO_3$ Nanoparticles Characterization

2.1 $SrTiO_3$ nanoparticles structure

The newly synthesized strontium titanate has been characterized in order to confirm its cubic perovskite structure. A representative PXRD pattern recorded on a $SrTiO_3$ powder synthesized using the supercritical solvothermal synthesis process is shown on ***Figure 3.1***. The indexation confirms a crystalline phase of $SrTiO_3$ through the ICDD code 00-035-0734. From the Rietveld refinement, a lattice parameter of 3.911 Å, larger than the reference one of 3.905 Å for bulk, was determined. This lattice expansion could be due to a size effect of titanate oxides, well documented in the literature with $BaTiO_3$ or $SrTiO_3$ particles [289,290]. Also, a crystallite size of 20 nm was calculated from the Scherrer equation. No other secondary crystalline phases are observed, which confirms the purity of the powder.

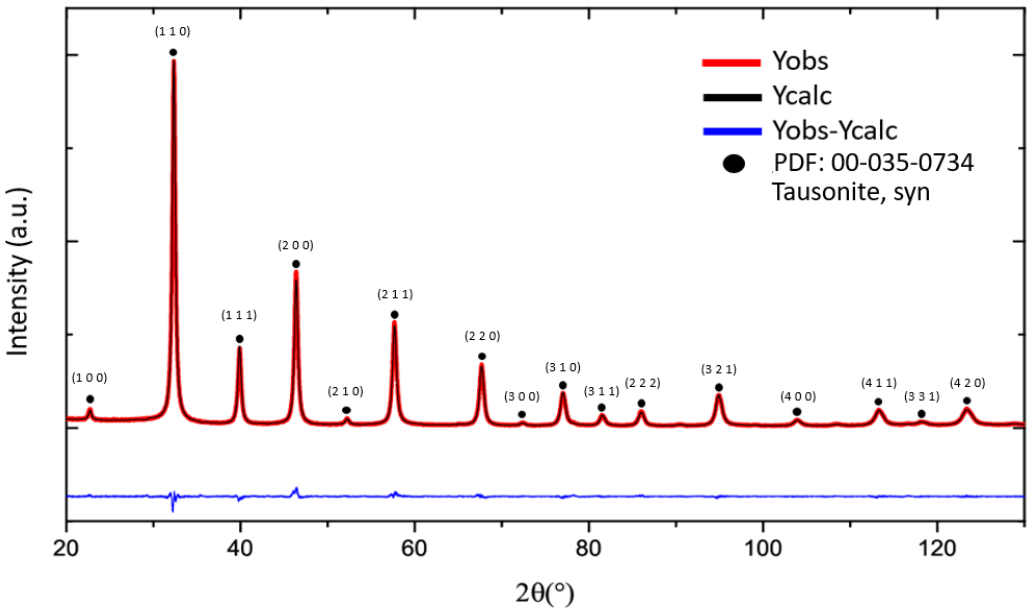

Figure 3.1: *FullProf* profile matching of $SrTiO_3$ (STO) PXRD pattern in the 20° to 130° 2Θ range confirming a lattice parameter of 3.911 Å and a mean crystallite size of 20 nm

Figure 3.1 is also in good agreement with the previous synthesis in supercritical conditions on $SrTiO_3$ obtained from alkoxides as described by ***Figure 3.2***. In comparison with the alkoxides way, the lattice parameter decreases slightly from 3.913 to 3.911 Å as conversely the crystallite size increases from 13 nm to 20 nm. This has been explained by the mentioned size effect since the size is smaller therefore more constrained therefore a larger lattice parameter. This is a first observation showing a similarity between using alkoxides precursors and the acetylacetonate ones. We also confirm from this PXRD acquisition the production of a nanocrystalline material which was the main reason for using the supercritical fluid technology.

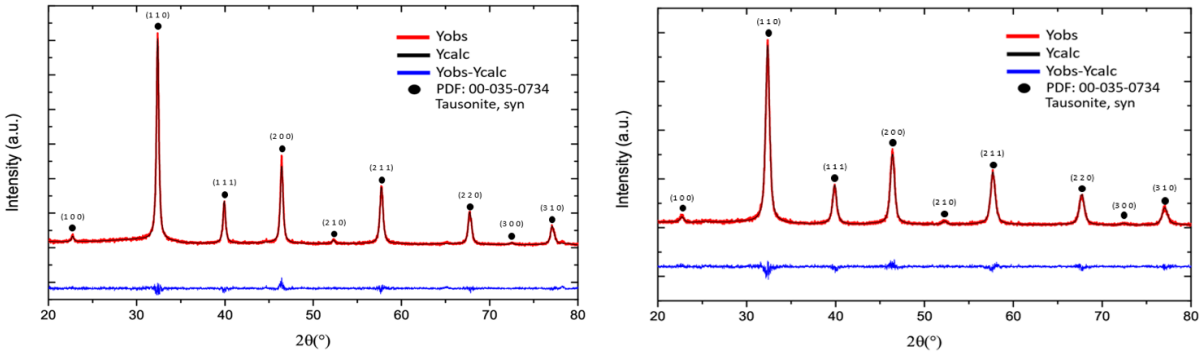

Alkoxide	Parameters	Acetylacetonate
P m -3 m	Space group	P m -3 m
3.91343	**Cell parameter (Å)**	**3.91098**
0.00011	$\sigma_{Cell\ parameter}$ (Å)	0.00007
0.34983	Y	0.24497
0.00489	σ_Y	0.00289
0.06497	I_G	0.00466
0.00194	σ_{I_G}	0.00074
2.45	Bragg R- factor	2.02
1.47	Rf –factor	1.80
1.44	Chi2	1.85
13	**Cristallite size**	**20**

Figure 3.2: PXRD acquisitions of strontium titanate synthesized by alkoxide (left) and acetylacetonate (right), comparative table of the results obtained from the pattern refinement.

Nevertheless, PXRD measurements only give a broad and average view of the crystalline structure. It can be considered as the global structural properties of the synthesized nanoparticles. Indeed, the small size of the crystallites widen even more the peaks. It is also important to mention that PXRD measurement does not allow to detect secondary phase under about 5 wt.%.

After completing the XRD analysis, which provided insights into the crystalline structure, phase composition, and crystallite size of the material, the characterization was extended to Raman spectroscopy.

Raman analysis complements XRD by offering information on vibrational modes, local structural distortions, and chemical bonding within the material, thereby providing a more comprehensive understanding of its structural and compositional properties. Raman spectra were recorded in order to study the local structure and the defect presence by indexing the longitudinal (LO) and transverse optical phonon (TO) modes in $SrTiO_3$. It is important to notice that the perovskite strontium titanate structure is cubic, so the first order Raman modes are not allowed at room temperature. However, point defects like oxygen vacancies and lattice distortion linked to the nanosize of the grains both can

lead to the activation of the transversal and longitudinal modes. The modes observed in ***Figure 3.3*** are thus supposed to result from a local symmetry lowering because of lattice distortion resulting from the supercritical synthesis. Many studies have reported such an indexation on $SrTiO_3$, where the different phonon modes are attributed to different symmetries in the lattice. The modes are attributed to TO_2 (O-Sr-O) and TO_4 (Ti-O-Ti), whose bands are located at 171 cm^{-1} and 545 cm^{-1}, respectively. Other modes are attributed to TO_3 (O-Sr-O) and LO_4 (Ti-O), these bands being located at 268 cm^{-1} and 794 cm^{-1}. More precisely, the TO_2 modes arise from a displacement of Sr versus the TiO_6 octahedron and the TO_4 modes are due to the bending of the octahedron following a polar axe mode. [291–293] To summarize, the Raman spectrum of STO shows a pure strontium titanate in which the presence of defects induces polar instability and leads to the activation of phonon modes despite the cubic structure.

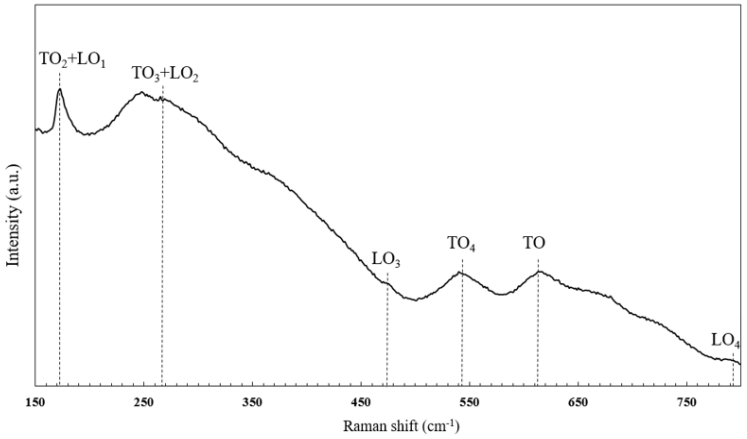

Modes	Ref [*]	Theor [**]	Exp
TO2+LO1	175	207	171
TO3+LO2	266	264	268
LO3	474	-	476
TO4	545	510	545
TO	-	635	615
LO4	795	777	794

[*] Rabuffetti et al. Chem. Mater. **2008**, *20*, 5628–5635
[**] Moreira et al. J. Phys. Chem. C **2012**, *116*, 24792−24808

Figure 3.3*:* Indexed Raman spectrum of obtained $SrTiO_3$ nanoparticles

This observation is very important because it implies the presence of defects in the material. It can also be due to a size effect as seen by Wang *et al.* [294] where the intensity of the different modes increases as the size decreases. Following the origin of this signal enhancement, we can also consider the possible presence of defects such as A-site deficiency characteristic of the compound synthesized using the continuous flow reactor with water ethanol mixed solvent [270].

The PXRD giving information on the global structure of the bulk and the Raman characterization on the local structure, we can correlate them with HRTEM where will be observe the structure and organization at the atomic scale but also the size/morphology of the nanoparticles.

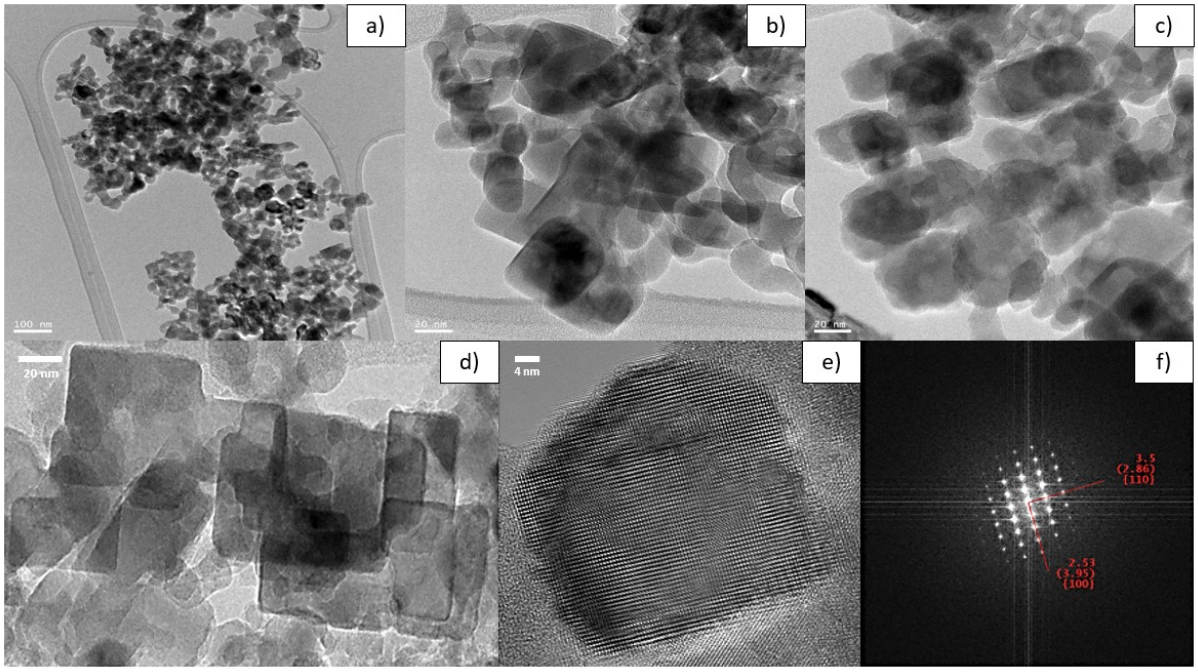

Figure 3.4: HRTEM analysis of the $SrTiO_3$ nanoparticles. a) Unzoomed TEM image of several particles, b) c) Close look on $SrTiO_3$ crystallites aggregation. d) Typical TEM image of several particles, e) high resolution image of a unique crystallite of $SrTiO_3$, f) Fast Fourrier Transform pattern of the image of the $SrTiO_3$ crystallite shown in e)

Figure 3.4 shows a compilation of TEM images of the synthesized strontium titanate nanoparticles. ***Figure 3.4***.a) shows an aggregation of nanoparticles with varying sizes and shapes. They are dispersed unevenly and form dense clusters. Based on the scale bar, the particles are in the nanometer range. ***Figure 3.4***.b) and ***Figure 3.4***.c) shows a closer picture of the cluster observed in image ***Figure 3.4***.a) where the nanoparticles population can be divided in two types. The faceted population characterized by a bigger size (between 15 nm and 30 nm) and a faceted morphology and the spherical population characterized by a smaller size (less than 10 nm) and a different morphology. Moreover, the aggregate aspect is still observable and due to this, it is very hard to determine the boundary of a single crystallite. ***Figure 3.4***.d) reveals a large-scale view of the particles; ***Figure 3.4***.e) shows a focus on one crystallite; and ***Figure 3.4***.f) conveys a fast Fourier transform (FFT) of the image corresponding to the previous particle. ***Figure 3.4***.d) mainly shows the average size and morphology of the crystallites, where two populations of nanoparticles mentioned before are evidenced: i) one includes monocrystalline particles with a faceted morphology (with an average size of 20 nm, in good agreement with the crystallite size determined from Rietveld refinement), ii) the second population is less defined geometrically and smaller in size. ***Figure 3.4***.e) is a focus on one of the faceted particles with single crystal characteristics (another TEM picture is given in Appendix C where the ordered atoms of the crystallites are observed) while the pattern on ***Figure 3.4***.f) corresponds to its indexed fast Fourier transform which confirms the single crystalline nature of the particle. Two of the distances extracted from the FFT (3.50 Å and 2.53 Å, respectively) were used to determine the lattice parameters, *i.e.* 2.86

Å and 3.95 Å respectively, in good agreement with the similar parameters determined by Rietveld refinement from the PXRD of strontium titanate. However, and to complete the TEM investigation, even with images showing faceted monocrystalline crystallites, it is really hard to characterize the particle-size distribution. In this study the size-distribution would not be mentioned.

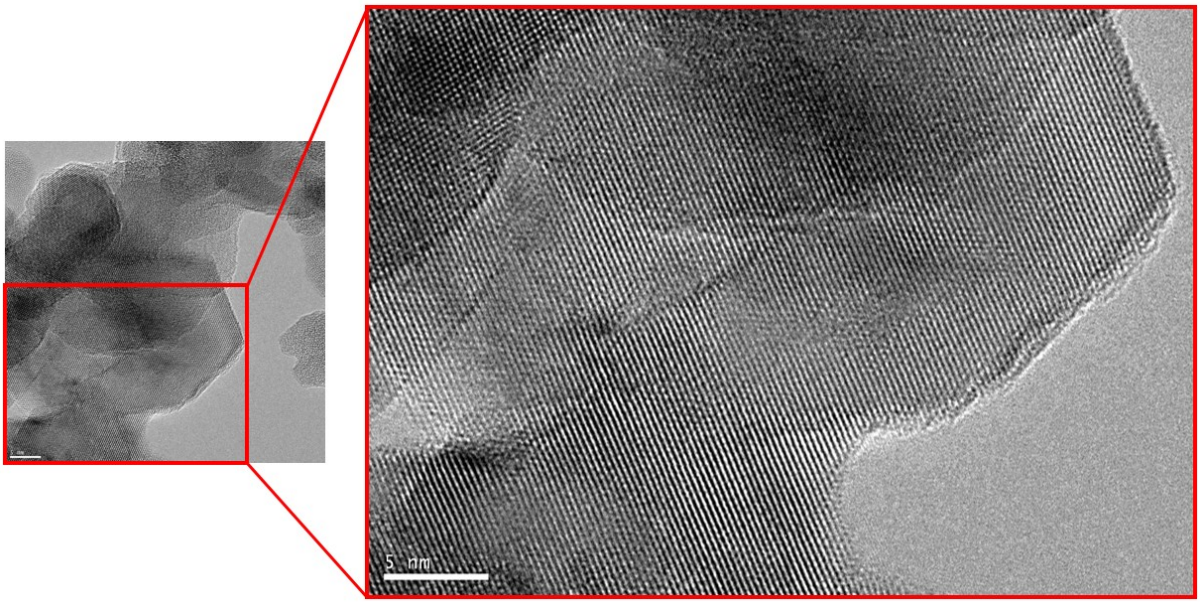

Figure 3.5: High-Resolution TEM Image showing crystalline structure of nanoparticles

Another feature connected to agglomerate structure is shown on ***Figure 3.5***. This image shows a zoom on an aggregate of strontium titanate particles. We can observe their monocrystalline nature thanks to the presence of a continuous atomic plane going from one whole particle to the other which is quite unusual.

This concludes the structural characterization section of strontium titanate nanoparticles synthesized by supercritical solvothermal synthesis. One of the perks of HRTEM is the ability to switch to EDS characterization and obtain information on the chemical homogeneity of the particles. The next part present chemical composition characterization and is completed by ICP-OES and FTIR to combine the bulk composition with the surface state properties.

2.2 $SrTiO_3$ nanoparticle chemical homogeneity

As mentioned previously, EDS measurements were performed in scanning TEM to determine locally the relative amount of strontium and titanium and provide a mapping of the different areas as shown in ***Figure 3.6*** to characterize the chemical homogeneity. On the top left, the STEM image is presented with a grayscale and represents the strontium titanate nanoparticles. This gives an overview of their size and shape. The elemental maps are divided between the Sr/Ti relative map which shows the

relative distribution of strontium (Sr) and titanium (Ti) across the sample. This helps to visualize where each element is concentrated on the previous picture. The maps with green and red spots highlight solely the presence of Sr and Ti, respectively. On the bottom left, the EDS spectrum shows the characteristic peaks corresponding to Sr and Ti and their corresponding peaks highlighted in green are labeled with their energy levels K. The intensity of the peaks indicates each element. Lastly, the quantification table provides the semiquantitative analysis of the elements. The peak energies, the mass percentage and atomic percentage for both strontium and titanium are given.

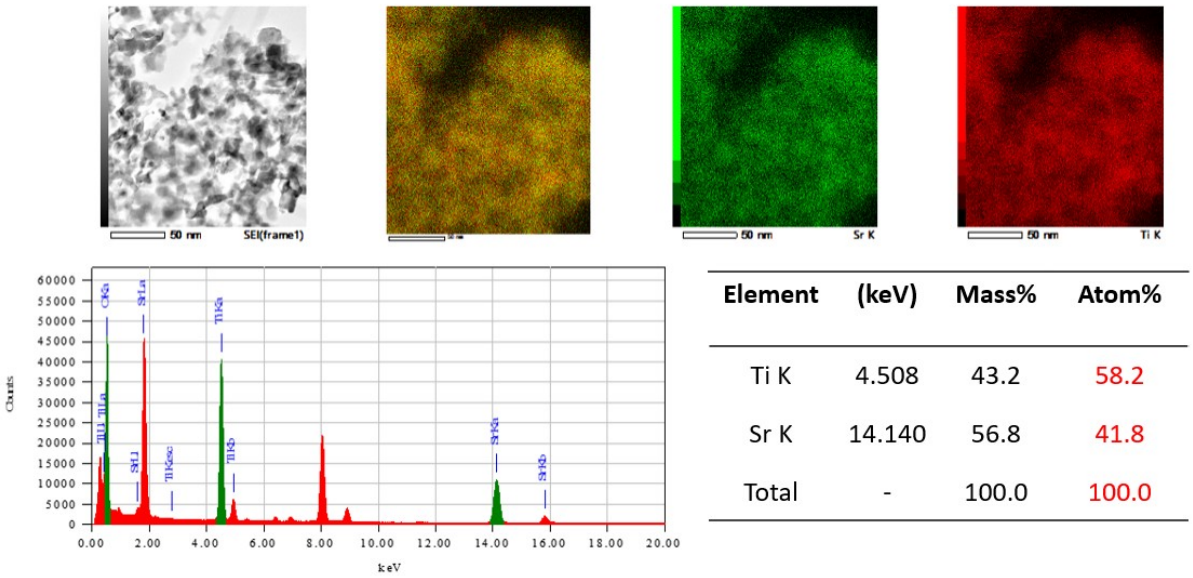

Element	(keV)	Mass%	Atom%
Ti K	4.508	43.2	58.2
Sr K	14.140	56.8	41.8
Total	-	100.0	100.0

Figure 3.6: EDS spectrum (bottom left) recorded in scanning TEM mode on several STO nanoparticles (image on top left) with corresponding elemental maps (top right: Sr/Ti relative map, Sr and Ti elemental maps) and the results of the quantification analysis (bottom right)

In this sample, Sr has a higher mass percentage (56.80%) compared to Ti (43.20%), but Ti has a higher atomic percentage since it is lighter than strontium. For the studied area, the molar contents of strontium and titanium are of 42 and 58 at.%, respectively, confirming thus the strontium deficiency, also at the nanoparticle level. The value of the Sr/Ti ratio is equal to ~0.7 making the nanoparticles of strontium titanate, synthesized by this solvothermal supercritical method, as A-site deficient. However, the chemical homogeneity is verified.

This confirms in a first case, that the material produced by the solvothermal supercritical synthesis possibly got a large amount of A-site deficiency which is very unusual. Indeed, stabilizing this kind of highly A-site deficient material is rarely achieved and this huge amount of defect could possibly have an impact on the material properties. Knowing the semi-quantitative nature of the EDS technic giving the chemical composition of a local area, the chemical composition of the bulk was obtained using the ICP-OES technics. This technic is much more representative in order to characterize the chemical composition.

ICP-OES measurements were performed to quantify the chemical content of strontium and titanium in the studied powders. The strontium titanate was mineralized as well as a commercial nanopowder SIGMA (<100 nm particle size) which was used as a reference. The experiments were duplicated three times per sample to have a coherent average value as well as to confirm the total mineralization of the powder. The ratio Sr/Ti found for the commercial powder is equal to 1, as expected, confirming thus the viability of the mineralization process. The ratio found for the powder synthesized in this work is equal to 0.64, evidencing a large deficiency of strontium in the powder. Compared to value of the EDS, the value is lower but more representative of the real chemical composition which would be written as $Sr_{0.64}TiO_{3-\delta}$. This result is quite unusual considering the amount of A rate inside the material based on the composition strontium titanate synthesized using conventional technics such as solid-state synthesis or sol gel synthesis as it was observed in Chapter 1 (cf 3. Synthesis Methods of Strontium Titanate). The missing strontium element could come from different origins such as strontium element reacting with organic part of the precursor to form strontium carbonate which stay inside the reactor (this has been verified later in the chapter). The second hypothesis would be to consider that strontium element located at the surface solubilized due to the combination of aqueous media and ionic nature of Sr-O bond. We could also consider a special architecture of crystallites itself being either a distinct core-shell structure with a core of n_{Sr}/n_{Ti} equal to 1 and a shell of $n_{Sr}/n_{Ti} < 1$ or a whole particle with a composition gradient of $n_{Sr}/n_{Ti} = 1$ decreasing as it progresses toward the surface of the particles.

From the elemental and structural analysis, we proved the synthesis of crystallized particles with a supposed highly A-site deficiency. The ratio between strontium and titanium shows a strong strontium imbalance. This means the material includes a lot of defects categorized as A-site vacancies. As discussed previously, this type of highly deficient material synthesized in supercritical condition has been observed before. Only the supercritical synthesis relates the possibility to obtain this kind of highly deficient particle. However, we consider the possibility of the existence of amorphous phase rich in titanium content that could create this imbalance between the strontium and titanium content.

Following the ICP-OES analysis, which quantified the elemental composition of the bulk, FTIR spectroscopy was employed to gain further insights into the molecular structure and bonding environment, especially at the surface of the particles. This complementary technique provides information on functional groups and chemical interaction completing the chemical characterization of the particles.

The functions located at the $SrTiO_3$ nanoparticle surface were investigated using Fourier Transform Infrared Red spectroscopy shown on ***Figure 3.7***. The IR signal is decomposed over different wavenumber ranges and is constituted of one main large peak located between 3750 cm^{-1} and 3000

cm^{-1} corresponding to surface hydroxyl groups and a small domain at 1600 cm^{-1} corresponding to lattice hydroxyl groups. These surface and bulk –OH groups are typical of "wet" processes of which the sol gel reaction is a part of. The domain between 3000 cm^{-1} and 2800 cm^{-1} corresponds to organic compounds, which could result from the precursor transformation. A narrow peak located around 1400 cm^{-1} corresponds to strontium carbonate arising from a possible side reaction of the strontium precursor inside the system. All of the above surface groups are identical to those evidenced in a previous study performed on barium titanate using isopropoxide precursors. We can conclude that using this new set of precursors in an adjusted setup has no effect on the nature of the surface groups related to the "wet" processes and more specifically identical to the surface properties found with the previous supercritical continuous flow using alkoxides precursor. This also proved the similarity of the acetylacetonate synthesis with the previous alkoxides synthesis regarding their properties.

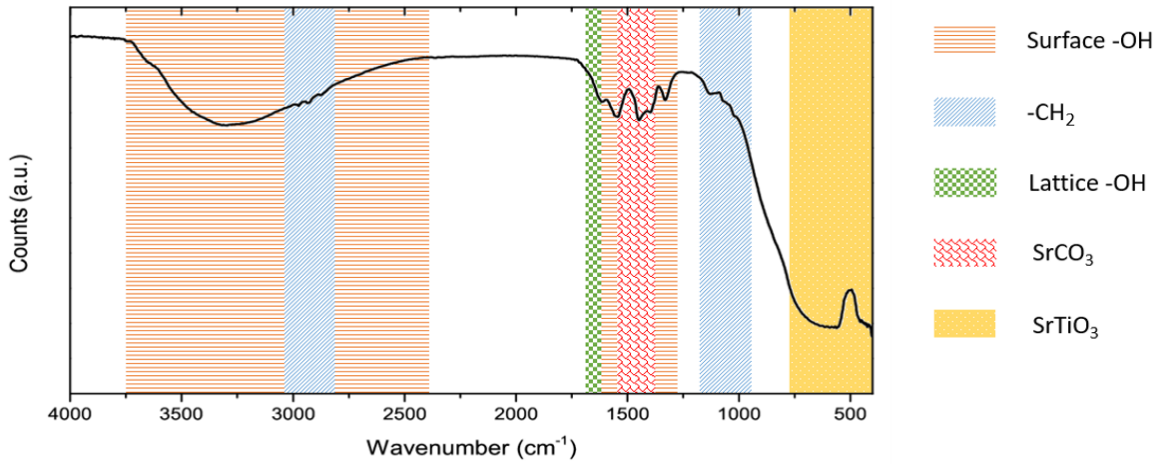

Figure 3.7: IR spectrum of strontium titanate nanosized powder synthesized in the continuous supercritical solvothermal process

To summarize, the structural analysis characterizes the particles as pure, monocrystalline, nanosized (20 nm) with a cubic shape and a lattice parameter slightly bigger than the one of the reference materials. The chemical homogeneity was also investigated and revealed A-site deficiency intrinsic to the material.

This type of highly A-site deficient composition formed during the solvothermal and hydrothermal synthesis has been previously investigated for perovskite material such as $BaTiO_3$, $Ba_{1-x}Sr_xZrO_3$ with x value between 0 and 1 and was explained by the possible link between the diffusivity of A-site ions in the solid and its transport from the bulk to the surface. Also, A-site vacancies charges being compensated by protons lead to the increases in the concentration of bulk and surface –OH, the late one which could be responsible for the growth of the particles by collision and has been studied by Dr. PHILIPPOT and Pr. YOKO [267–269].

The structural characteristic such as the morphology, the size and surface state are indeed important to consider because of the deposit characteristic. Also, the A-site deficiency determined from the chemical investigation imply the possibility of the existence of amorphous phase rich in titanium content that could create this imbalance between the strontium and titanium content. In order to check this hypothesis, we anticipated that this phase could be crystallized by heating the sample at high temperature. In order to check this hypothesis, we anticipated that this phase could be crystallized by heating the sample at high temperature. Thanks to the use of *in-situ* technics in temperature, the thermal stability and the explanation of the imbalance is studied thoroughly in the next part.

3. *In situ* Investigation of $SrTiO_3$ Thermal Stability and Optimization of $SrTiO_3$ Synthesis

3.1 *In situ* exploration of supercritical $SrTiO_3$ thermal stability

The purpose of this part is to study the impact of the material stoichiometry on the thermal stability of the nanoparticles of strontium titanate synthesized using the supercritical solvothermal synthesis.

The first *in-situ* experiment was PXRD in temperature in order to follow the evolution of the strontium titanate structure at a global scale and observe the possible crystallization of the titanium dioxide phase as the temperature increases. The second *in-situ* experiment was HRTEM in temperature in order to have a more local observation at the particle scale.

In situ PXRD experiments were performed from 100 °C to 1200 °C every 100 °C in air with a heating ramp of 2 °C·min^{-1}. From each PXRD pattern as shown in ***Figure 3.8***, the lattice parameter and the crystallite size were determined using Rietveld refinements.

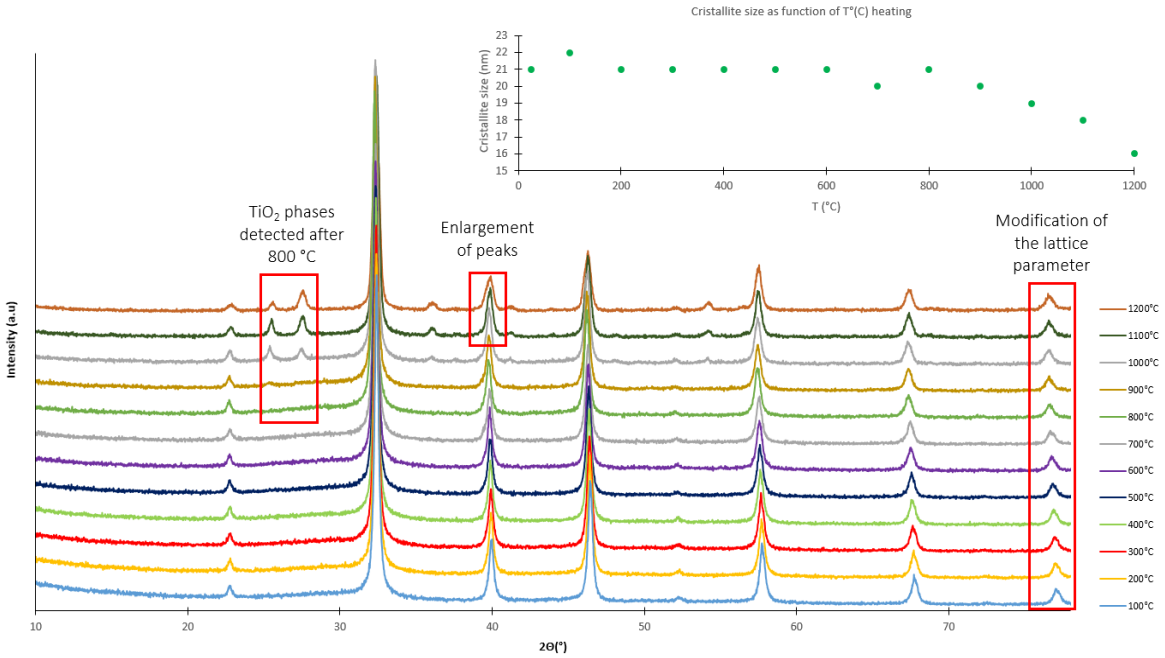

Figure 3.8: *In situ* high temperature X-ray diffraction of $SrTiO_3$ with the evolution of the crystallites size on upper corner as a function of temperature

The main trend stems from an expansion of the lattice parameter resulting in a shift of the peaks to smaller angles upon heating. For T > 800 °C, a second crystallized phase is observed at angles between 20° and 30°. Those phases, after indexation, correspond to a TiO_2 anatase (peak located at 25.58°) and a TiO_2 rutile phase (peak at 27.59°). It is interesting to note the decrease in the TiO_2 anatase peak (thus the phase proportion) and, conversely, the increase in the intensity of the TiO_2 rutile peak as the temperature further increases. This phenomenon is due to the anatase phase being unstable at temperatures exceeding 800 °C. An increase of the anatase peak intensity is observed from 800 °C to 1100 °C followed by a decrease at 1200 °C. An increase in the intensity of the rutile peak is observed from 800 °C to 1200 °C. Another feature is the relative increase of the width of strontium titanate peaks in the same temperature range from 800 °C to 1200 °C showing a decrease in the crystallite size. This correlates with the decrease of the intensity of the strontium titanate peaks signal due to the loss of strontium titanate crystallites. On the inset of **Figure 3.8**, the evolution of the crystallite size as a function of temperature from 25 °C to 1200 °C is plotted. Two distinct behaviors are observed, the first from 25 °C to 700 °C with no clear size modification, and the second from 800 °C to 1200 °C where a decrease of the crystallite size is observed from 21 down to 16 nm. This is connected to the previous observations with decrease of the intensity and the widening of the peaks. The starting value correlates with those deduced previously by PXRD and HRTEM, the differences being due to the accuracy and the sensitivity of each technique.

Figure 3.9 shows the evolution of the lattice parameter of the strontium titanate phase as a function of temperature from 25 °C to 1200 °C during the heating (red square and diamond) and the cooling (blue triangle) steps.

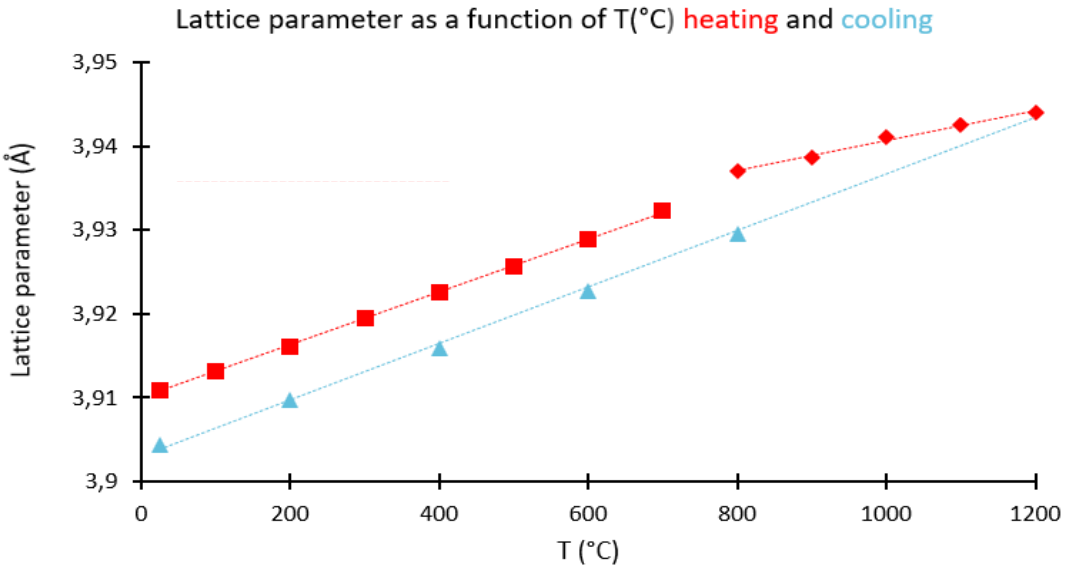

Figure 3.9: Evolution of the lattice parameter of $SrTiO_3$ as a function of the temperature during the heating (red) and cooling (blue) steps

During the heating stage, a two-step behavior of the evolution of the lattice parameter is observed and correlates with the evolution of the crystallite size. From 25 °C to 700 °C, we observe a linear evolution of the lattice parameter as the temperature increase. For T > 800 °C, where a TiO_2 phase starts crystallizing the slope of the linear equation decrease. The $SrTiO_3$ lattice is destabilized at the same time as the crystallite size decreases. This observation fully agrees with the overall diffraction peaks of the $SrTiO_3$ phase where a secondary phase TiO_2 appears. During the cooling, the atom network contracts and the lattice parameter decreases compared to the initial value observed before the crystallization of the secondary TiO_2 phase. It is possible to determine the linear thermal expansion coefficient α_l from the lattice parameter a according to the following equation:

$$\alpha_l = \frac{1}{a_0}\frac{\partial a}{\partial T} \qquad (20)$$

By plotting $(a - a_0) / a_0$ against *T*, with a_0 equal to the value of the lattice parameter at room temperature (25 °C), then performing a linear fit give access to the linear thermal expansion coefficient α_l referring to the slope of the curve.

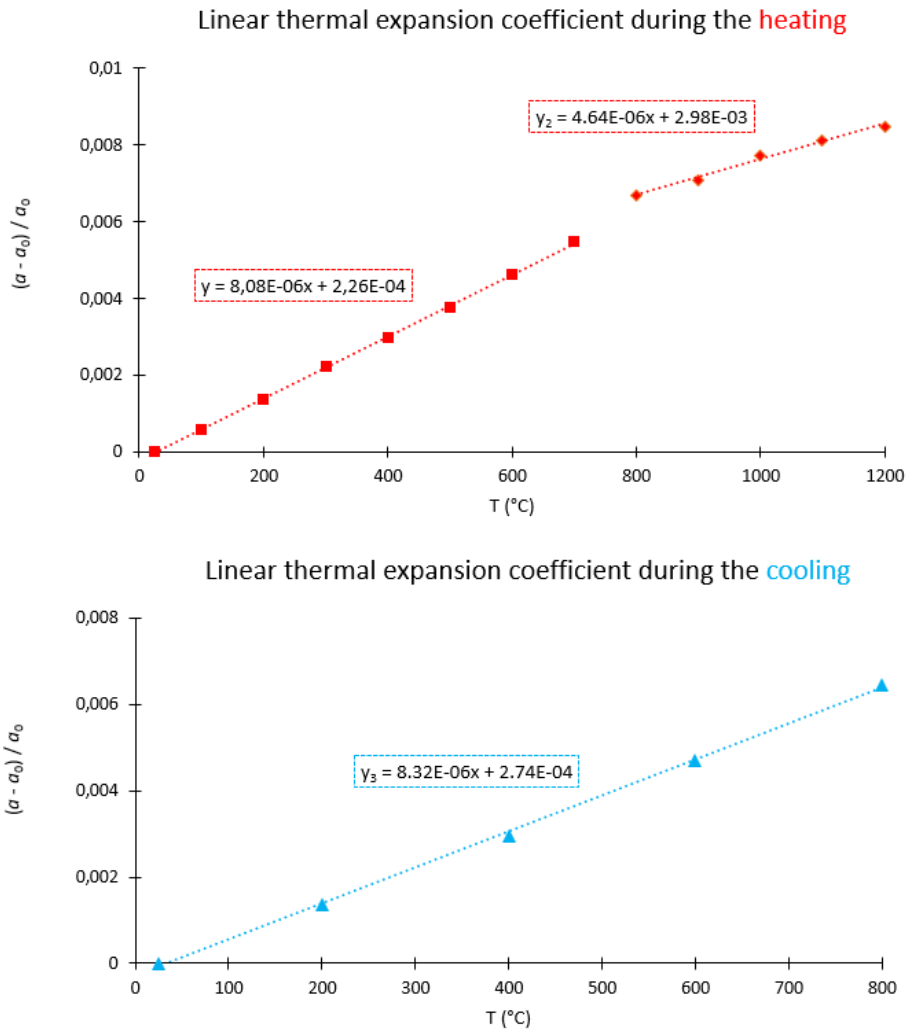

Figure 3.10: Evolution of the linear thermal expansion of $SrTiO_3$ during the heating phase (top) and cooling (bottom) from the lattice parameter a where α_0 is the value at room temperature.

Figure 3.10 represents two graphs illustrating the linear thermal expansion behavior of strontium titanate during the heating from 25 °C to 1200 °C (in red) and the cooling part from 800 °C to 25 °C (in blue). The top graph related to the heating phase is divided into two linear regions with corresponding linear fits indicating a change in the expansion behavior with temperature. In the first region (up to 700 °C), the linear fit shows a thermal expansion coefficient of 8.08×10^{-6} K^{-1}, while in the higher temperature range (from 800 °C and above), the coefficient decreases by nearly half to 4.64×10^{-6} K^{-1}. This reduction in slope suggests a possible structural change in the material's expansion behavior at elevated temperatures, which coincides with the appearance of the TiO_2 phase. The bottom graph presents the thermal expansion coefficient of the same material during the cooling phase. Unlike the heating curve, the cooling data follows a single linear trend throughout the measured range (from 800 °C to 25 °C). The fitted equation gives a thermal expansion coefficient of 8.32×10^{-6} K^{-1} closely

matching the previous value found during the heating from 25 °C to 700 °C. This suggests a reversible expansion behavior at lower temperatures.

There is a slight difference between the thermal expansion coefficient (TEC) of the measured sample and the reference value which is slightly higher (~10×10^{-6} K^{-1} [89]). An increase in the TEC is also observed after restructuring, bringing it even closer to the reference value. The deficiency parameter affects the TEC, but it is not clearly established whether it causes an increase or a decrease. For example, Yang *et al*. [295] showed that a slight A-site deficiency in perovskite material $Sr_2Fe_{1.5}Mo_{0.5}O_{6-\delta}$ (SFM) could change the TEC by decreasing it (from 14.9×10^{-6} K^{-1} to 14.5×10^{-6} K^{-1} for Sr_x= 1.950) and then increase (TEC = 15.1×10^{-6} K^{-1} for Sr_x=1.900). Another investigation by Kharton *et al*. [296] showed for the Ruddlesden-Popper-type material $Sr_3Fe_{2-x}Mo_xO_{7-\delta}$ the oxygen deficiency led to a decrease of the TEC (from 19.9×10^{-6} K^{-1} to 14.2×10^{-6} K^{-1}). Regarding the value, we did observe a slight difference in the TEC during heating (8.08×10^{-6} K^{-1}) from 25 °C to 800 °C and the TEC during cooling (8.32×10^{-6} K^{-1}). Also, if we compare our value to other articles, we can conclude that the linear thermal expansion coefficient value measured is similar to the values from those quoted references [89,90,297].

Moreover, the initial lattice parameter (3.911 Å) decreases after the thermal treatment to 3.904 Å, a value close to the reference one (3.905 Å). Those values, closer to the bulk lattice parameter as well as the thermal expansion coefficient obtained after the thermal treatment, is probably the consequence of a reorganization of the structure and a disappearance of part of the defects in the lattice even if the size of the crystallite decreases. We can thus exclude the presence of an amorphous TiO_2 phase at the initial stage which would crystallize. The evolution of the lattice parameter after annealing rather indicates the transformation of a highly Sr-deficient metastable phase towards a more stoichiometric $SrTiO_3$ phase.

From this characterization, we cannot explain the TiO_2 origin. We supposed it could come from a possible amorphous phase of TiO_2 or $SrTiO_3$ nanoparticles that decompose into TiO_2. To complement the PXRD findings and obtain more detailed information on the phenomenon at atomic level, high temperature *in situ* TEM was achieved to observe at an atomic scale this phase transition.

Working in collaboration with Prof. O. ERSEN and Dr. W. Baaziz from the IPCMS in Strasbourg through the METSA network “Microscopie Electronique et Sonde Atomique”, advanced TEM experiments could be performed on the nanoparticles of strontium titanate.

The high temperature *in-situ* HRTEM analysis gives an explicit interpretation of what is happening at the particle scale. As mentioned before, two types of nanoparticles can be observed on the TEM images. By following the same nanoparticle populations between 500 °C and 800 °C under air, the main phenomena observed are the sintering and the restructuring of the smallest nanoparticles (images c

and e). We can consider this population being amorphous TiO_2 in agreement with the structural evolution observed by *in-situ* PXRD at 800 °C. Another important observation is the stability of the biggest particles regarding their size and morphology from 150 °C to 800 °C.

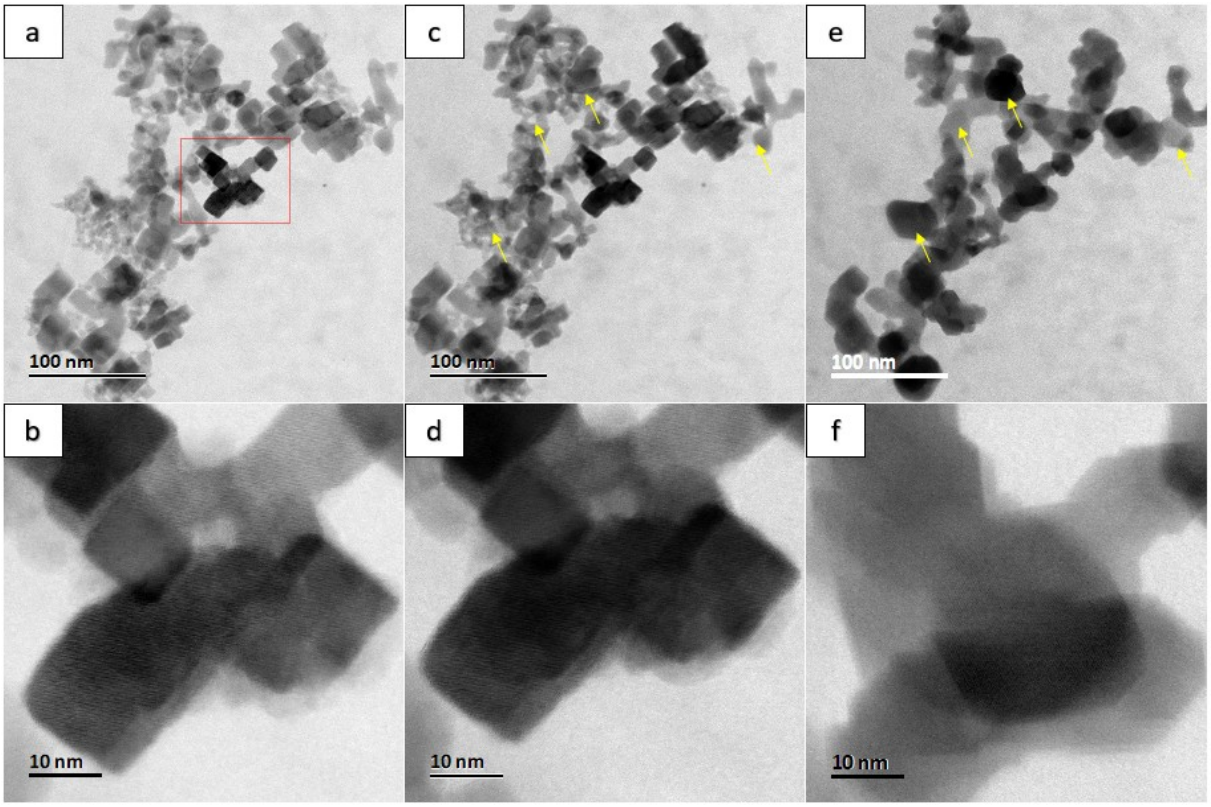

Figure 3.11: *In-situ* high temperature TEM monitoring of an aggregate of STO nanoparticles. Images acquired at 150 °C under vacuum (a and b which corresponds to the red square), at 500 °C under air (c and d) and at 800 °C under air (e and f)

Figure 3.11 shows faceted particles of 20 nm (images b and d). At 800 °C, the monocrystalline nature seems impacted since the shape of the particles becomes considerably less defined than before. We supposed that, due to the defects present in the strontium titanate nanoparticles, the stability of the crystallite is affected at 800 °C. In order to exclude a possible influence of the electron beam during the thermal treatment, an image of an area not exposed to the electron beam during the *in-situ* monitoring has been taken before and after on ***Figure 3.12***. The aggregates show the same type of behavior, meaning the vanishing or sintering of the small particles.

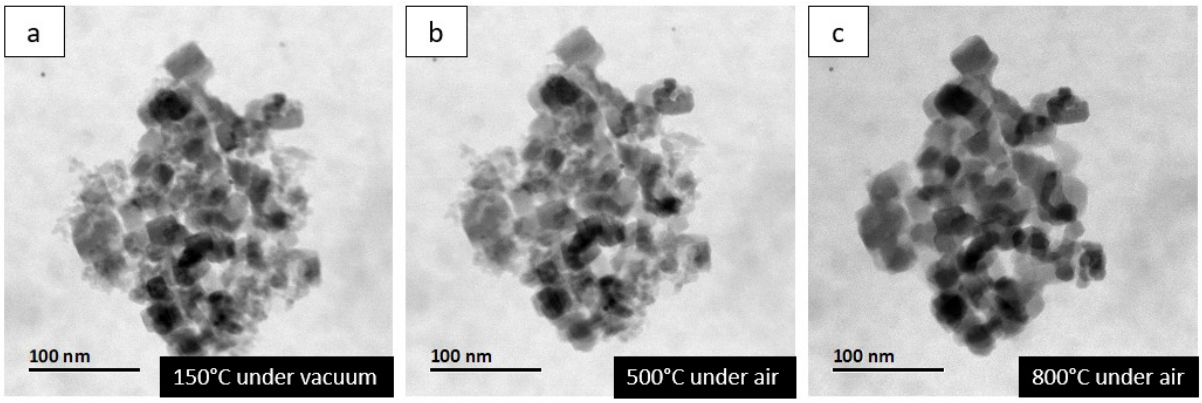

Figure 3.12: *In-situ* high temperature TEM monitoring of an aggregate of STO nanoparticles. Images acquired at 150 °C under vacuum (a), at 500 °C under air (b) and at 800 °C under air (c)

The panel (a) represents the state of the particles at 150 °C under vacuum, the scale bar is 100 nm, indicating that the nanoparticles are still fairly small with some level of agglomeration. The two populations observed are still present and show an overall shape not well defined, possibly indicating incomplete crystallization. The panel (b) shows the evolution of the nanoparticles at 500 °C under the air atmosphere where no changes of the morphology seem to happen. Conversely, panel (c) shows a drastic modification at 800 °C under air atmosphere. The particles are larger and more crystalline, with clear and well-defined shapes. The population of small particles disappeared completely and promoted the grain growth of more faceted nanoparticles. To summarize, as the temperature increases to 800 °C, the smallest particles become more defined and more crystalline due to increased thermal energy driving growth and sintering of the smaller population. The opposite effect is observed on the PXRD at 1000 °C. This phenomenon is pinpointed by ***Figure 3.13***.

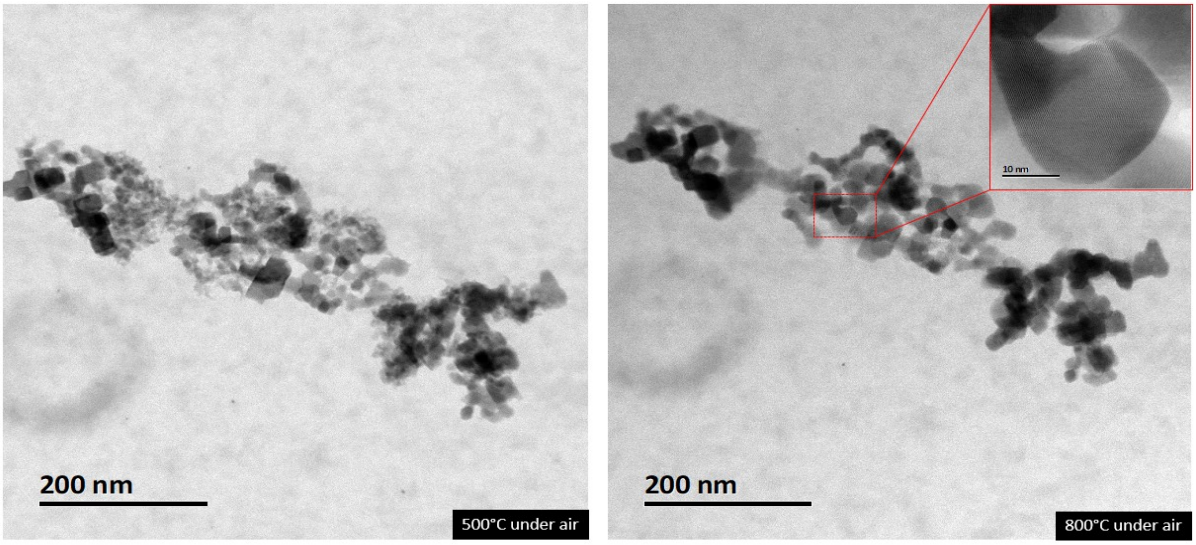

Figure 3.13: *In-situ* high temperature TEM monitoring of an aggregate of STO nanoparticles. The evolution shows the sintering of the smallest population into crystallized nanoparticles

To conclude, we highlighted the presence of two populations of nanoparticles of strontium titanate. Upon increasing temperature, the smallest particles sintered leading to crystallized nanoparticles. We also observed as well an impact of the temperature on the bigger particles where some of them lose their crystalline feature.

3.2 Toward an understanding of the origin of the defects

Those TEM observations correlate with the previous observation of *in situ* high temperature PXRD. The loss of intensity of the $SrTiO_3$ diffraction lines relates to the different effects of temperature on the strontium titanate nanoparticles observed in ***Figure 3.11*** and ***Figure 3.13***. The next question is related to the TiO_2 content. Indeed, by Rietveld refinement, the TiO_2 content is estimated at 13 wt.% which are not observable on the PXRD signal before thermal annealing. Raman spectroscopy should also release intense TiO_2 peaks thanks to its tetragonal structure which was also not observed. To get a better insight into the TiO_2 content supposedly being the smaller particles observed on high temperature *in-situ* HRTEM, we next present local EDS mapping of particles before thermal annealing at 800 °C.

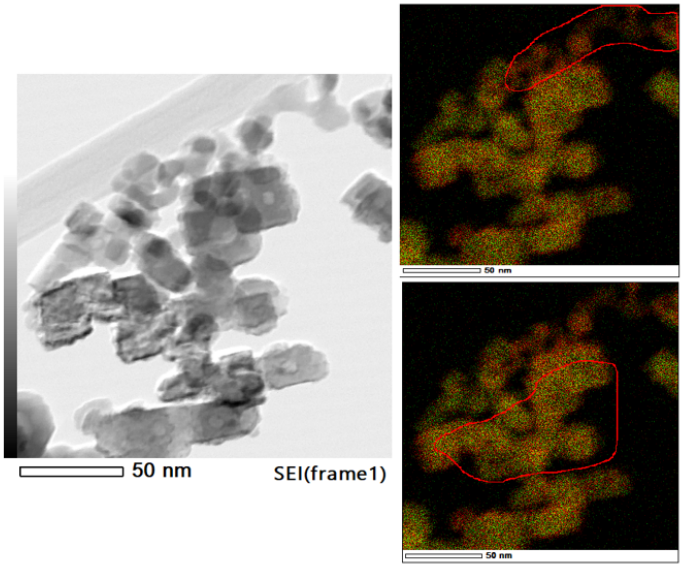

Element	(keV)	Mass%	Atom%
Ti K	4.508	60.6	73.8
Sr K	14.140	39.4	26.2
Total	-	100.0	100.0

Element	(keV)	Mass%	Atom%
Ti K	4.508	46.2	61.1
Sr K	14.140	53.8	38.9
Total	-	100.0	100.0

Figure 3.14: TEM-EDS on the two populations of strontium titanate nanoparticles. The EDS result shows two different ratios of Sr/Ti

Figure 3.14 displays TEM-EDS on the strontium titanate nanoparticles with a TEM picture on the left. The middle pictures are EDS characterization of the relative mapping of Sr/Ti on the chosen area highlighted by the red circle. Lastly, the right table is the quantification of strontium and titanium for each area. This highlights two different Sr/Ti ratios. In the case of the bigger faceted particles, we found a ratio close to the previous value of ~0.64. Conversely, the value found for the smallest particle population area which exhibits an amplified red contrast, gives an even smaller ratio of Sr/Ti of half less ~0.36 which is very important for the understanding of the effect of the thermal mechanism. ***Figure 3.15*** shows the same observation as the previous picture. The main difference is the comparison of the areas. The smallest nanoparticles exhibit the same ratio observed previously; however, if we compare their contribution to the whole area, we can conclude that they are a minority and do not influence the global value of the EDS characterization.

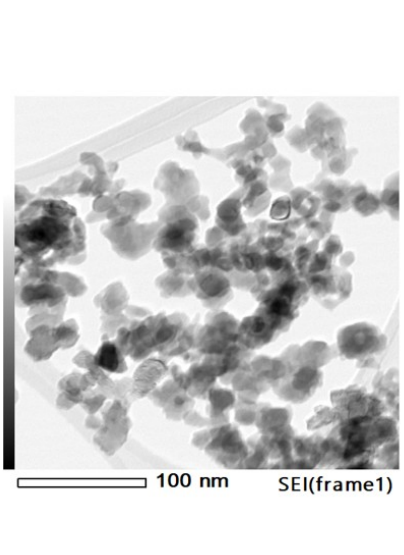

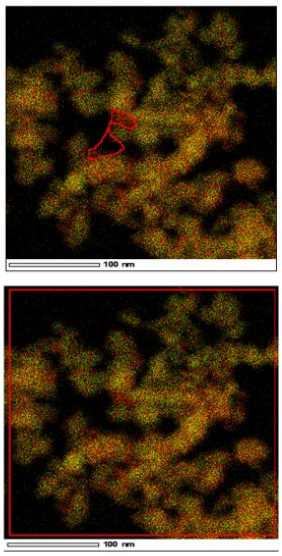

Element	(keV)	Mass%	Atom%
Ti K	4.508	60.1	73.3
Sr K	14.140	39.9	26.7
Total	-	100.0	100.0

Element	(keV)	Mass%	Atom%
Ti K	4.508	46.5	61.4
Sr K	14.140	53.5	38.6
Total	-	100.0	100.0

Figure 3.15: TEM-EDS on the two populations of strontium titanate nanoparticles. Same observations are verified

Following the explanation on the origin of TiO_2, we can refute the hypothesis on the existence of amorphous dioxide titanium since the local elemental analysis of those reactive nanoparticles reveal a content of strontium. However, the hypothesis regarding the decomposition of strontium titanate into TiO_2 still stand. Therefore, the two populations of nanoparticles are indeed strontium titanate presenting A-site vacancies, the deficiency being twice for the smaller particles. As mentioned previously no PXRD signature (nor Raman) corresponding to the presence of titanium dioxide was detected, the amorphous population could be attributed to small metastable particles of highly deficient strontium titanate.

This second population may have been synthesized thanks to the fast reaction in the supercritical conditions leading to the stabilization of the particles with a lower ratio of Sr/Ti. This could explain the evolution of the material above 800 °C (supposed to be stable at 1500 °C) where there is a crystallization of titanium dioxide. In fact, this stoichiometry could cause a “transformation” of the nanocrystalline strontium titanate due to the release of titanium, which occurs easily for T > 800 °C, with a lower Sr/Ti ratio.

Based on those observations, we hypothesized that on what could become the strontium element from the highly strontium deficient nanoparticles. Knowing that the global lattice parameter of strontium titanate becomes closer to reference, we supposed that the “unstable” strontium element migrated toward the bigger particles and balance the whole stoichiometry of the compound. We do not exclude the opposite case where the bigger particles release titanium element leading to the formation of TiO_2.

This concludes the explanation on the possible origin of the TiO_2 formation and thus the thermal stability of the strontium titanate nanoparticles due to the imbalanced ratio between strontium and titanium. The lack of strontium can be explained by side reactions happening with the strontium precursor where strontium can react in the system by decomposition of the organic part forming strontium carbonate, which were identified by FTIR earlier. This highlights the link and the possible origin of the thermal instability of the nanoparticles of strontium titanate.

3.3 Optimization of supercritical $SrTiO_3$ stoichiometry

This part will present the optimization performed on the synthesis to increase the stability of the nanoparticles of strontium titanate synthesized via the continuous-flow supercritical solvothermal method. The main goal is to reduce the Sr deficiency. Three approaches have been tested leading to an overall improvement of the thermal stability of the strontium titanate nanoparticles:

- The kinetic parameters of the reaction, including the concentration of the reactant such as strontium acetylacetonate, were adjusted by varying mol.% excess,
- The titanium reactant, originally titanium bis(acetylacetonate) diisopropoxide, was replaced with titanium isopropoxide, alongside the addition of different mol.% excess of strontium acetylacetonate,
- The new reactor setup was adapted to enhance temperature control and improve overall efficiency.

It is important to consider that this study was conducted on the previous set-up described in Chapter 2 where the control of temperature is not optimal. This upgrade of the thermal stability was crucial in order to produce a material that could sustain the upcoming thermal treatment related to the processing and the shaping.

3.3.1 Excess of strontium acetylacetonate precursors

One of the first assumed hypotheses was to consider the lack of stoichiometry regarding the strontium content as responsible for the lack of stability from the material.

To try to optimize the Sr/Ti ratio, the concentration of the strontium precursor was increased following a molar excess of 1%, 5%, 10%, 15%, and 20% compared to the titanium precursor. The harvested powder was then thermally treated at 850 °C to induce the transformation of the crystallites in order to determine the molar percentage of the TiO_2 and $SrTiO_3$ phases; a subsequent decrease of the titanium dioxide amount upon increasing the excess strontium precursor is expected.

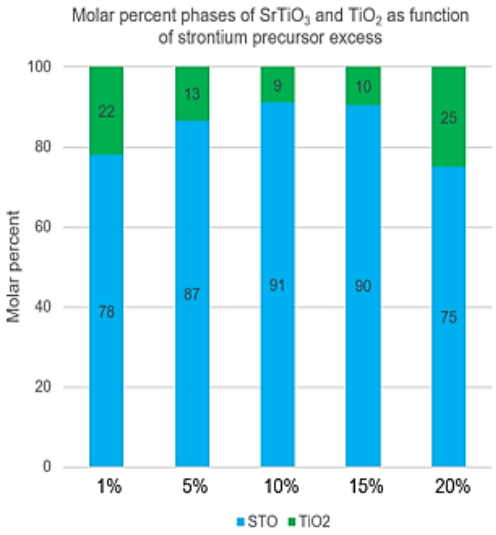

Sr excess (%at.)	1%	5%	10%	15%	20%
a (Å)	3.911	3.911	3.911	3.911	3.911
a after (Å)	3.909	3.909	3.909	3.909	3.909
Size (nm)	21	23	22	22	20
Size after (nm)	25	24	23	23	22
Sr/Ti (ICP-OES)	0.61	0.55	0.68	0.61	0.62

Figure 3.16: Molar percent of the $SrTiO_3$ and TiO_2 after thermal treatment of STO nanoparticles at 850 °C (left), the results were obtained from the PXRD pattern refinement and by ICP-OES (right)

Figure 3.16 shows the molar percentage of TiO_2 and $SrTiO_3$ of the synthesized powder after the thermal treatment. The table on the right focuses on the nanostructural properties of each powder before and after the thermal treatment. In each case (various molar contents), the formation of TiO_2 is evidenced after the thermal treatment performed at 850 °C. The molar percent of TiO_2 was calculated from its weight percent determined from the Rietveld refinement using the PXRD data.

No clear trend connecting the amount of titanium dioxide and the excess of strontium acetylacetonate can be determined. Regarding the lattice parameter, there is no modification of the lattice parameter for all tested compositions and the crystallite sizes are relatively similar. The ICP-OES measurements were performed on each sample, and the average value of the Sr/Ti ratio is equal to 0.6, again meaning that the strontium titanate particles keep their Sr-deficiency. It is difficult to establish a clear trend between the ICP-OES ratio and the amount of TiO_2 obtained after the thermal treatment of each powder. The PXRD data performed before the thermal treatment do not show the presence of an amorphous phase, the only phase existing before is indeed strontium titanate. Those results show that the molar excess of strontium does not influence the structural properties of the material. The difference in molar percentage of titanium dioxide formed after thermal treatment between the different samples could be explained by the possible inhomogeneous composition of the strontium titanate nanoparticles. It could also be explained by a lack of reactivity from the associated reactants. As the opposite case of strontium isopropoxide, titanium isopropoxide is available and this isopropoxide structure makes it a much more reactive precursor than acetylacetonate.

From this experiment, the conclusion toward the improvement of the stability of the nanoparticles is not related to the addition of excess precursors. Consequently, we consider this could be linked to the type of precursor. Conversely to the case of strontium, the isopropoxide of titanium is still available and was used as a replacement to see the impact of a supposed more reactive precursor.

3.3.2 Replacement of the titanium precursor and influence of the excess of strontium acetylacetonate precursors

The purpose of this part was to investigate the impact of using titanium isopropoxide instead of titanium diisopropoxide bis(acetylacetonate) precursor with identical synthesis parameters as described with the first reactor.

Thanks to their structural and electrical properties, isopropoxide molecules are more reactive than acetylacetonates. This feature is attributed to several key factor such as:

- Structural characteristics since metallic isopropoxide have higher ability to form M-O-M bridges which lead to faster hydrolysis and condensation compared to acetylacetonate being more stable [298]. On the other hand, the acetylacetonate structure leads to stable chelate complexes that lead to a limitation of their reactivity [299],
- The thermal stability also differs. Indeed, Krunks *et al.* [300] showed that acetylacetonate-modified titanium isopropoxide has a distinct thermal degradation feature highlighting the stabilization of the precursor due to the presence of acetylacetonate. This leads to a reduction of the reactivity.

The thermal stability was investigated using the *in situ* high temperature PXRD. ***Figure 3.17*** shows the characterization of the nanoparticles of strontium titanate synthesized using continuous-flow supercritical solvothermal method using titanium isopropoxide. A PXRD acquisition was performed at 25 °C and every 100 °C till 1300 °C. Each pattern was treated using Rietveld refinement in order to determine structural parameters of the material such as the lattice and crystallite size.

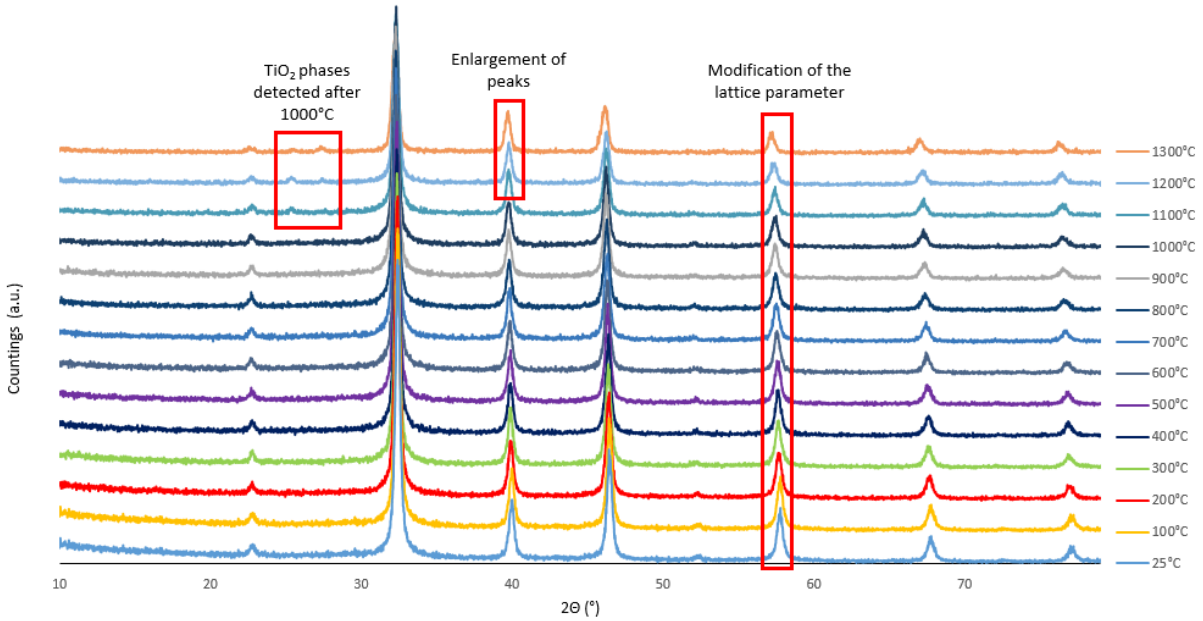

Figure 3.17: High temperature *in-situ* XRD measurement of strontium titanate nanoparticles prepared using titanium isopropoxide precursor

We can compare this panel with ***Figure 3.8*** and see the impact of a titanium isopropoxide precursor on thermal stability. The same modification of the structure observed previously is found here. The effect of temperature on the material leads to a shift of the peaks toward a smaller angle signaling the expansion of the lattice parameter. The broadening of the peak and loss of intensity are observed when reaching higher temperature. Most importantly, the two main points regarding the TiO_2 phase detection are the first detection which is located at much higher temperature (1100 °C instead of 900 °C) and the TiO_2 peak intensity is much lower.

The structural parameters are indicated in ***Figure 3.18***. The lattice parameter increases from 3.911 to 3.915 Å and the crystallite size decreases from 22 to 19 nm. The evolution of the lattice parameter has been plotted as a function of the temperature. Once a temperature above 1100 °C is reached, the evolution is not linear anymore and the lattice parameter drastically increases going from 3.954 to 3.961 Å and the crystallite size decreases from 19 down to 16 nm.

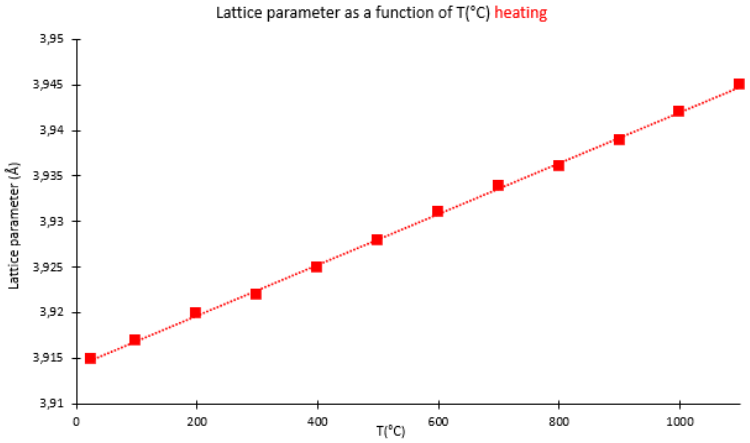

Temperature (°C)	25	100	200	300	400	500	600	700	800	900	1000	1100	1200	1300
Lattice parameter (Å)	3.915	3.917	3.920	3.922	3.925	3.928	3.931	3.934	3.936	3.939	3.942	3.945	3.950	3.961
Crystallite size (nm)	19	19	19	19	19	19	19	18	18	18	18	18	16	16

Figure 3.18: Evolution of lattice parameter as a function of the annealing temperature of strontium titanate synthesized with a titanium precursor and table summarizing the data

From this *in situ* PXRD investigation, we can conclude that the use of titanium isopropoxide precursor has drastically reduced the amount of TiO_2 which appeared much more later compared to the titanium acetylacetonate precursor. The structural parameters are also impacted with a slightly bigger lattice and smaller crystallite size. Overall, the stability is improved and allows further processing of the nanopowder of strontium titanate implying thermal treatment not going over 1000 °C. We supposed that this is indeed due to the reactivity of the isopropoxide precursor which reacts more efficiently with the acetylacetonate of strontium than the previous precursors. The proportion of TiO_2 detected being also lower, we presumed that the ratio of Sr/Ti also increased. This reaction being more effective, we presupposed that it could react more skillfully with the excess of strontium acetylacetonate.

In order to complete the study of the isopropoxide precursor in combination with strontium acetylacetonate precursor, the same molar excess was performed on powder synthesized using this method. The concentration of the strontium precursor was progressively increased by 1%, 5%, 10%, 15%, and 20% molar excess relative to the titanium precursor. The resulting powder was subsequently subjected to thermal treatment at 850 °C to promote crystallite transformation, allowing for the determination of the molar percentages of the TiO_2 and $SrTiO_3$ phases. ***Figure 3.19*** describes the different powder related to a Sr excess. The graph on the left shows the different molar percent of the strontium titanate and titanium dioxide after a thermal treatment of 850 °C on the different samples. The right table gives values related to the evolution of the lattice parameter and the crystallite size which evolve according to the effect of annealing temperature. Moreover, an ICP-OES characterization

has been performed on each powder and the results show an increase of the Sr/Ti ratio going from 0.55 to 0.77 so 20% percent more just by using titanium isopropoxide as a Ti precursor.

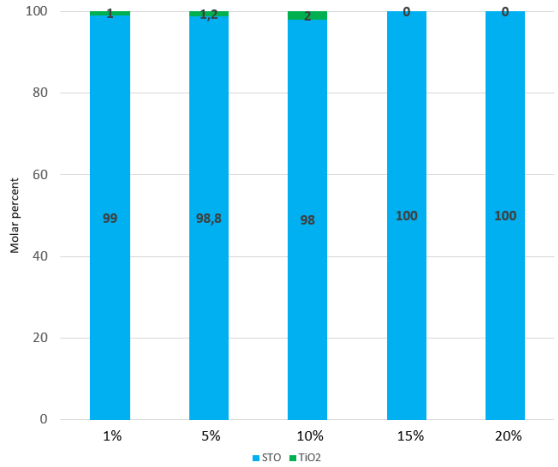

Sr excess (%at.)	1%	5%	10%	15%	20%
a (Å)	3.916	3.915	3.914	3.915	3.915
a after (Å)	3.912	3.912	3.911	3.912	3.912
Size (nm)	15	17	16	15	15
Size after (nm)	16	18	17	16	16
Sr/Ti (ICP-OES)	0.76	0.70	0.73	0.77	0.75

Figure 3.19: Molar percent of the $SrTiO_3$ and TiO_2 after thermal treatment of STO nanoparticles synthesized using titanium precursor at 850 °C (left), the results were obtained from the XRD pattern refinement and by ICP-OES (right)

However, adding an excess of strontium titanate does not produce a positive nor negative effect on ratio of Sr/Ti.

The following part will present the small change brought thanks to the new set-up build and the modification detected on the nanopowder of strontium titanate.

3.3.3 Adaptation of the new reactor

This quick part presents two modifications this time related to the setup itself and not the chemical environment as seen previously. Indeed, the previous part presented were done using the first reactor. When the second reactor was achieved, we considered that the system was different compared to the first reactor. Two studies were performed to understand and pinpoint the intrinsic mechanism inside the reactor.

The first study was related to the use of a preheater. For reminder, the use of a preheater in the alkoxides way to synthesize strontium titanate was to inject heated water to reach a temperature of 150 °C at the mixing point. The mixing point is the localization in the setup where water flow encounters ethanol flow before combining into a mixture and going into the reactor under supercritical conditions. The preheater was programmed in order to reach 150 °C at the mixing point. Moreover, it could also help thermodynamically the system to reach the 400 °C needed and improve the first step of the sol-gel reaction implying the hydrolysis step.

For the acetylacetonate precursors, the temperature was limited since the water media was also carrier of the strontium precursor. The effect of temperature could have an effect on the degradation of the acetylacetonate precursor. A thermogravimetric analysis showed the beginning of the degradation of the organic part around 200 °C (see Appendix B). To avoid any complication, the preheater was programmed at 180 °C but this led to a longer time needed to reach the temperature wanted in the reactor area and lower reactivity at the mixing area. It is also important to consider that the thermocouples of regulation were located outside the reactor which make it difficult to have accurate information of the temperature inside the reactor.

One major improvement brought by the new set-up built was the presence of a thermocouple inserted inside the T junction between each heating collar. This allowed an *in-situ* reading of the flow temperature. Additionally, the heating system was improved from heating resistor to heating collar providing homogeneous heating in the coil system. From there, we studied the impact of the preheater use on the developed materials. ***Figure 3.20*** shows the PXRD acquisition of the different strontium titanate powders synthesized using the preheater on the water line. Each acquisition has its own temperature going, supposedly, 25 °C (no use) to 300 °C.

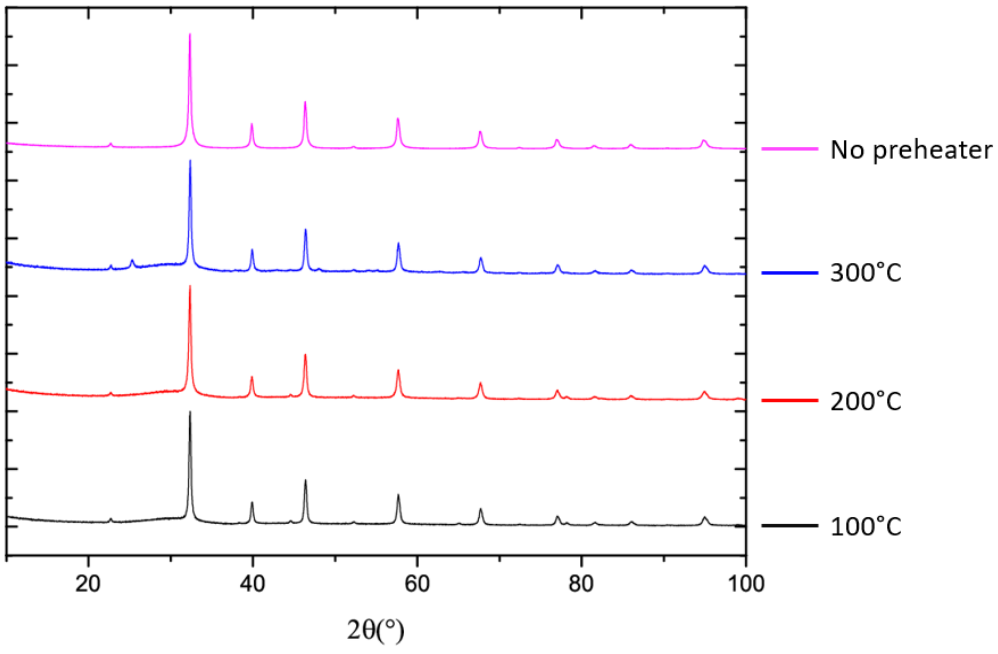

Figure 3.20: PXRD acquisition of the different powders synthesized using the new reactor as a function of the preheater temperature

The black, red and blue X Ray diffraction patterns have a similarity. Each of them has this bump between the peak (1 0 0) and the peak (1 1 0) that can be due to the presence of an amorphous phase.

The blue X Ray diffraction pattern exhibits a secondary phase corresponding to titanium dioxide with a characteristic peak at 25.41° when the temperature of the preheater was 300 °C. Also, concerning the black and red X Ray diffraction patterns, a peak at 44.62° can be indexed and corresponds to the aluminum phase which refer to the support used for the PXRD acquisition. The pink X Ray diffraction pattern, where the preheater, was inactive shows a very smooth line with no sign of amorphous phase.

From these experiments, we can conclude that the use of a preheater is not needed with this set-up in order to produce nanoparticles of strontium titanate. The use even seems to counter the production of "clean" nanoparticles by inducing an amorphous phase and even in the case of 300 °C, a phase of titanium dioxide. This is related to the thermal stability of the acetylacetonate precursor. The new system is very effective on the heating compared to the old reactor and allows the use of a preheater. ICP-OES were conducted on this powder and the ratio Sr/Ti found increased and reached ~0.8 thanks to the heat system being much more effective.

A last study related to the influence of the flow rate was conducted in order to see the impact of decreasing or increasing the concentration of strontium content in the water media. ***Figure 3.21*** shows the PXRD pattern of each synthesized powder depending on the flow rate. This study was performed with the new reactor and without a preheater.

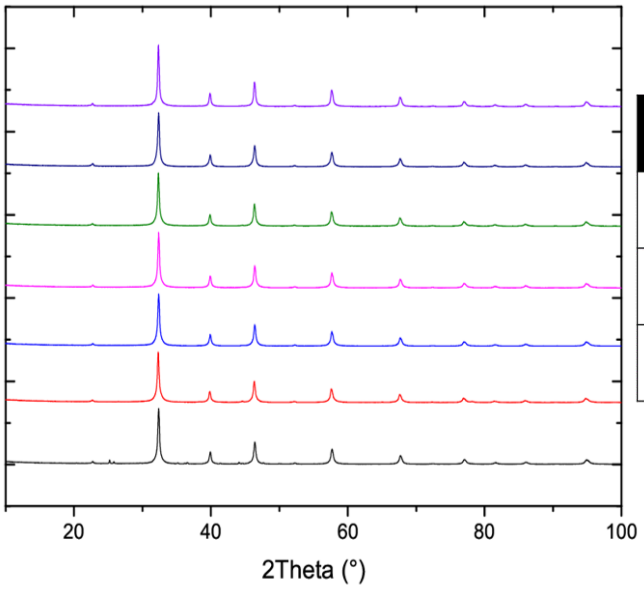

	Black	Red	Blue	Pink	Green	Dark Blue	Purple
Flow rate (mL*min^{-1})	5.8	5.9	6.0	6.2	6.4	6.5	6.6
Lattice (Å)	3.912	3.914	3.913	3.914	3.916	3.915	3.914
C.S. (nm)	18	17	17	17	17	17	17

Figure 3.21: PXRD pattern of synthesized strontium titanate using a different flow rate for the water, 6.4 mL.min^{-1} being the reference, the table on the right summarized the lattice parameter value and the crystallite size (c.s)

Regarding the synthesis method developed, the reference value of the flow rate for the water injection line is 6.4 mL.min^{-1}. No important change is noticed regarding the structural parameter of the nanoparticles of strontium titanate. However, on the black X-ray diffraction pattern, which

corresponds to a flow rate of 5.8 $mL.min^{-1}$, two distinct peaks localized between the strontium titanate peaks (1 0 0) and (1 1 0) correspond to strontium carbonate with a proportion calculated of 5% atomic.

This observation is indeed very interesting and confirms the main hypothesis mentioned in this chapter regarding the origin of the imbalance between strontium element and titanium element. The action of reducing the flow rate will lead to an increase of strontium element concentration. Correlating with the ICP-OES value found for the nanoparticles synthesized with the new reactor, we still have 20% of A-site vacancies (after thermal and chemical optimization). Instead of decreasing the A-site vacancies in the nanoparticles of strontium titanate, the added strontium element reacts with the organic part to form strontium carbonate. This hypothesis was mentioned previously when the imbalance of elements was verified due to FTIR observation and the hypothesis of strontium carbonate being stuck to the wall of the reactor. This study highlights this characteristic of the synthesis: a part of the strontium content reacts to form strontium carbonate and so explains why there are A site vacancies inherent to the nanoparticles.

Conclusion of the Chapter 3

This chapter presented the work achieved on the continuous-flow supercritical solvothermal method for the synthesis of strontium titanate nanoparticles using acetylacetonate precursors. The insight of the strontium titanate structure was investigated at different scales. This chapter presented an optimization of the strontium titanate stoichiometry. Lastly, the different improvements made regarding the chemical used or the synthesis parameter related to reactor set-up limited drastically the formation of pollution at high temperature.

- $SrTiO_3$ nanoparticles with a crystallite size of roughly 20 nm were successfully synthesized. In addition to the cubic structure of $SrTiO_3$, FTIR revealed surface functions that are typical of "wet" processes, while Raman spectroscopy showed the activation of non-centrosymmetric modes brought on by non-linear contributions,
- According to *in-situ* high temperature PXRD measurements, the nanoparticles show a faceted shape and are stable at elevated temperatures. However, due to a chemical deficiency in strontium, titanium dioxide phases are formed at higher temperatures. *In-situ* high temperature HRTEM investigations showed the existence of two populations of particles, with a better stability for the bigger-sized particles after thermal treatment as well as the sintering and restructuring of the smallest ones,
- Also, the microscopy results suggest the possibility of a chemical inhomogeneity within the crystallites by TEM-EDS,
- The influence of external parameters such as the flow rate, the temperature or the titanium precursor used allowed an improvement of the stability of the material and a reduction of the atomic percent of TiO_2.

From this point, both undoped and doped strontium titanate, discussed in the next chapter, are synthesized under optimized conditions. This involves using titanium isopropoxide instead of titanium bis(acetylacetonate) diisopropoxide, eliminating the need for a preheater as the new setup achieves the optimal reaction temperature. The synthesis is carried out in the same water/ethanol mixture without an excess of strontium precursor.

The following step is the preparation of substituted composition of strontium titanate, meaning the insertion of new elements at different atomic percents. The goal is to modify the properties of strontium titanate in order to make it available for the aimed application.

Chapter 4: Synthesis, Characterization and Shaping of Doped $SrTiO_3$ Nanoparticles

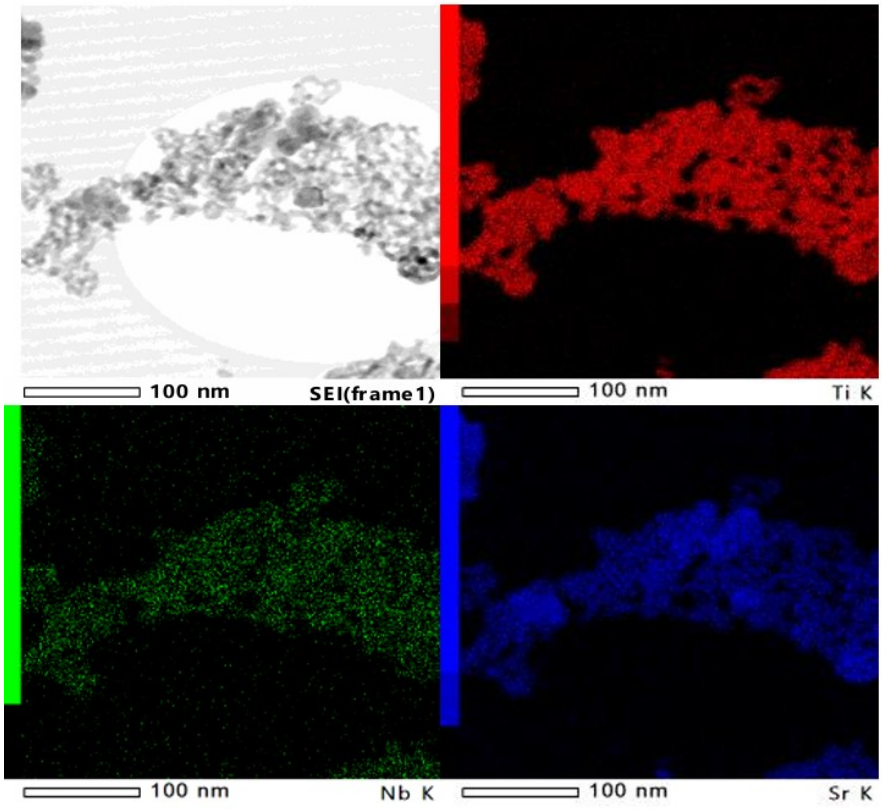

EDS picture of $SrTiO_3$ doped with Niobium with the Sr element in red, Ti element in blue and Nb element in green from the abstract named "Innovative and flexible synthesis of Strontium Titanate nanoparticles with new composition in supercritical water/ethanol mixture" of the 20th European Meetings on Supercritical Fluids

As mentioned previously, strontium titanate is defined as a semiconductor with a large band gap. It means the energy needed by the electron to be excited from the valence band to the conduction band is quite large and leads to dielectric behavior. The use as an electrode for high temperature electrolysis would be impossible since the material exhibit too large resistivity even at high temperature, knowing that for high temperature electrolysis, the working temperature is around 600 °C. However, strontium titanate electronic properties can be tuned thanks to the band gap engineering. It means that the energy gap between the valence band and the conduction band can be decreased, which facilitates electron transfer. This led to an increase of the electronic conductivity. The band-gap engineering can be achieved using many ways and the most used method is doping by substitution. Thanks to this doping, the electronic properties of strontium titanate can be increased by using a slight amount of heterovalent elements during the synthesis to produce a n-doped or p-doped semiconductor.

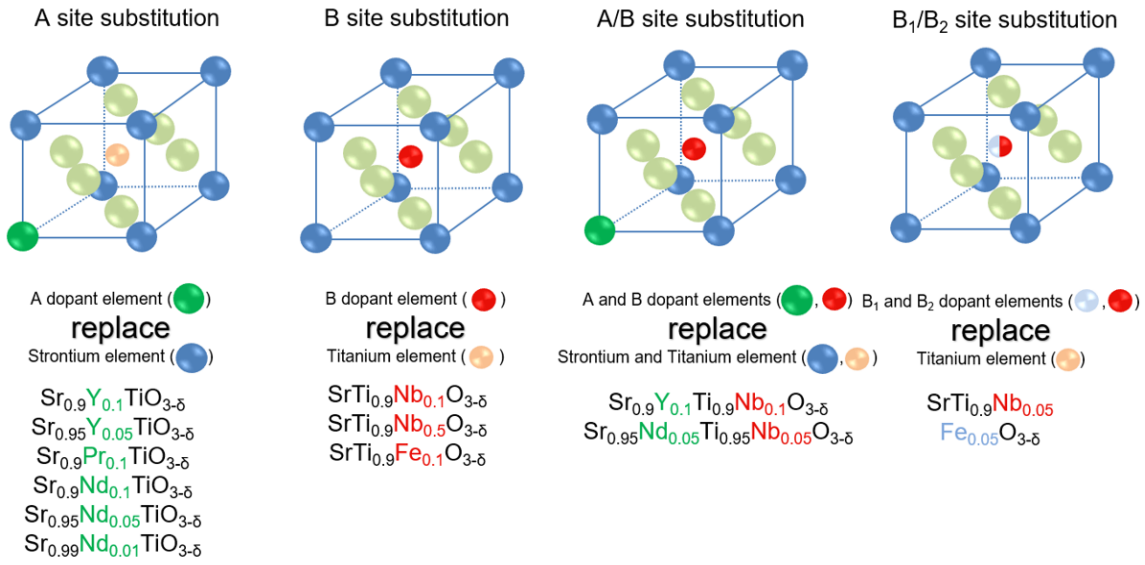

Figure 4.1: Summary of all the compositions synthesized during this PhD work

In this chapter, the first part is focused on the synthesis of n-doped and p-doped semiconductors based on strontium titanate as described in ***Figure 4.1***. A complete characterization of its structure and chemical composition is detailed. The main challenge here was to attest the successful doping with new elements in the lattice of strontium titanate, in either the A site meaning it substitutes a strontium atom, or the B site meaning it substitutes the titanium atom. Once the doping has been demonstrated, the powder has to be characterized for its electronic properties to confirm the heterovalent doping effect. This complex characterization is introduced in the second part where the processing of the nanoparticles synthesized using the supercritical method is achieved to produce dense pellets needed for four-probes measurement. The densification method is the Spark-Plasma Sintering (SPS) since it can limit the growth of nanoparticles. A last part is focused on the processing of the strontium titanate

synthesized by supercritical fluid into an electrode cell using the screen-printing method. The ink formulation as well as its deposition on different cells or substrates is presented.

1. Synthesis of Doped $SrTiO_3$

In Chapter 3, the synthesis of strontium titanate was achieved leading to monocrystalline nanoparticles with a mean size of about 20 nm and a deficiency on the strontium site, meaning the presence of vacancies on the A-sites. The availability of the acetylacetonate precursors for various elements and compatibility with the supercritical synthesis allows the development of doped strontium titanate. This part will refer to the composition that has been synthesized using the supercritical fluids synthesis and the characterization performed on the powder.

1.1 Selection of n and p doping elements of $SrTiO_3$

Doped variants of strontium titanate, with Y, Nb, Fe, Nd, Pr, were synthesized using a combination of acetylacetonate and isopropoxide precursors tailored for each element to fine-tune the perovskite structure. The selected precursors were dissolved in a supercritical ethanol/water mixture containing 0.29 mol.% ethanol, described before. The solubilized strontium precursor was introduced through the top injection line corresponding to the water line, while the titanium precursor was added and solubilized in the ethanol line represented by the left injection line as represented by ***Figure 2.4***. The concentrations of Sr^{2+}, Ti^{4+} and dopant precursors were set at 2×10^{-4} M at the mixing point before the reactor. The concentration of dopant(s) is adapted to the targeted atomic substitution rate. Conversely, the concentration of the substituted elements, either strontium or titanium, is adjusted. In order to predict the substituted site, the tolerance of ionic radii was considered. The reaction time was determined by the time required for the flow to pass through the reactors under supercritical conditions which is around 53 s. Upon obtaining the solutions, nanoparticles were recovered *via* centrifugation at 12,000 rpm (rotations per minute), followed by drying for 4 h at 80 °C in an oven to obtain dried powders suitable for characterization and further processing.

The ***Table 4.1*** summarizes the different compositions that were synthesized.

Table 4.1: List of the elements substituted with their ionic radius, the coordination number is considered twelvefold for the element doping in the A site and six-fold for the element doping in the B site

Elements substituted	Ionic radius (pm)	Site substitued	Composition
Y	122	A	$Sr_{1-x}Y_xTiO_{3-\delta}$
Pr	130	A	$Sr_{1-x}Pr_xTiO_{3-\delta}$
Nd	127	A	$Sr_{1-x}Nd_xTiO_{3-\delta}$
Nb	64	B	$SrTi_{1-x}Nb_xO_{3-\delta}$
Fe	61	B	$SrTi_{1-x}Fe_xO_{3-\delta}$

Alkoxides precursors were avoided due to critical stability issues, similar to those previously observed with strontium isopropoxide. Indeed, all the precursors were solubilized in the titanium solution since the ethanol media allowed obtaining a limpid solution. Out of all the dopants used, only the niobium was an isopropoxide precursor under a liquid form. As mentioned previously, this precursor must be handled in a glovebox to avoid any contamination from the ambient air. For reminder, the objective is to achieve a successful doping using the supercritical fluid synthesis developed with newly used acetylacetonate precursors. The following part justifies the choice of the dopants.

As already mentioned, the material can have its electronic properties enhanced by n-type or p-type doping. The electronic properties are based on the number of carriers and their mobility. The carriers are divided into two types, the electrons and the holes. Substituting the divalent strontium cation and/or the tetravalent titanium cation by an element with a different ionic configuration such as trivalent rare earth or pentavalent transition metal impacts the carrier number and nature. Using cations with a higher electron valence induces new electrons carrier type and increases the overall conductivity of the material. Conversely, using an element with lower electron valence induces the creation of positive holes which also increase the number of carriers leading to an increase of the conductivity.

In the case of the strontium titanate, the strontium A site has a twelvefold coordination which means there is twelve oxygen anions impacting its ionic radius. Regarding the titanium B site, it is in six-fold coordination. This explains the difference in ionic size for strontium (144 pm for CN=12) and titanium (60.5 pm for CN=6).

One of the most important features of the dopants is their ionic size. Thanks to the Shannon classification and the Goldschmidt tolerance factor, the elements selected for doping are predetermined on which site they are going to substitute. Since the substitution rate does not exceed more than 10% at. in our compositions and the difference in size between the dopant and the

substituted cation has to be small, we can predict that the tolerance should stay between 1 and 0.9 meaning that the structure keeps a cubic structure. Generally, rare earths are used to substitute the strontium site and transition metals are used to substitute the titanium site.

The yttrium-doped strontium titanate has been a material of interest for solid oxide fuel cells and more precisely the anode. In 2002, Hui *et al.* identified the property of mixed ionic / electronic conductivity under high temperature reducing conditions. $Sr_{1-3x/2}Y_xTiO_3$ with x=0.08 exhibited an electronic conductivity of 63 $S{\cdot}cm^{-1}$ at 800 °C and 10^{-19} atm oxygen pressure and an ionic conductivity of 6 x 10^{-3} $S{\cdot}cm^{-1}$ [301]. Another interesting study from Zhao *et al.* in 2009 showed the impact of A-site deficiency on the electronic conductivity of the strontium titanate. The material studied was $(Y_{0.08}Sr_{0.92})_{1-x}TiO_{3-\delta}$ with x varying from 0.01 to 0.05. The reported values under Ar/H_2 (5%) atmosphere at 800 °C for the electronic conductivity are around 60 $S{\cdot}cm^{-1}$ for x = 0.05 and 80 $S{\cdot}cm^{-1}$ for x = 0.01 showing that as the A site deficiency increases, the electronic conductivity decreases. However, the ionic conductivity increases as the A site deficiency increases. At 800 °C, the reported ionic conductivity for x = 0.01 is 0.005 $S{\cdot}cm^{-1}$ and 0.013 $S{\cdot}cm^{-1}$ for x=0.05 [215]. The most recent study (2018) by Singh *et al.* was on $Y_xSr_{1-x}TiO_{3-\delta}$ synthesized by citrate-nitrate auto-combustion route, with an yttrium rate going from 3% at. to 10% at. The electronic conductivity measurements showed the highest electrical conductivity for x = 0.08. However, an impurity of the pyrochlore phase $Y_2Ti_2O_7$ was detected when $x \geq 0.03$ [152]. Based on those results, using yttrium as dopants allows an increase of the electronic conductivity, it is the main reason why this dopant was chosen in the frame of this PhD. Moreover, a characteristic of $SrTiO_3$ obtained with the supercritical synthesis is a compound A-site deficiency. For reminder, the A site deficiency rate is at 20% at. for the strontium titanate synthesized using our method which 10% more than the previous strontium titanate prepared with strontium isopropoxide. This parameter should balance the properties of ionic and electronic conductivity.

The niobium-doped strontium titanate was also investigated as a potential material for application in solid oxide fuel cells. In 2008, Blennow *et al.* reported the electrical transport properties of Nb-doped $SrTiO_3$, more precisely $Sr_{0.94}Ti_{0.9}Nb_{0.1}O_3$. The reported value at 800 °C was 180 $S{\cdot}cm^{-1}$ under an atmosphere of 9 at. % H_2 in N_2. This study also showed the impact of the further increase of A-site deficiency rate which leads to a secondary phase not indexed in the study especially for the compound $Sr_{0.89}Ti_{0.9}Nb_{0.1}O_3$ [302]. It is also interesting to mention the study of Bochentyn *et al.* on the comparison of two composites which are $SrTi_{0.98}Nb_{0.02}O_{3-\delta}$-$CeO_2$ and $SrTi_{0.98}Nb_{0.02}O_{3-\delta}$-$O_3$-YSZ used in SOFC anode [303]. The study mentions that the conductivity of the composite is lower ($\geq$ 10 $S{\cdot}cm^{-1}$) than the one of pure $SrTi_{0.98}Nb_{0.02}O_{3-\delta}$ and is reported by Karczewski *et al.* in 2010 at 28 $S{\cdot}cm^{-1}$ at 800 °C [170]. However, the authors mention that it is sufficient for solid oxide fuel cells anode applications.

Iron doped strontium is also an interesting case for solid oxide fuel cells mostly as a cathode material. For example, in 2012, Molin *et al.* reported an electronic conductivity of 2 $S \cdot cm^{-1}$ at 800 °C for $SrTi_{1-x}Fe_xO_{3\pm\delta}$ with x=0.5 which is low compare to current used material but, as seen previously, would fit the anode application. The ionic conductivity is also reported with a value of 0.035 $S \cdot cm^{-1}$ at 800 °C for $SrTi_{0.5}Fe_{0.5}O_{3\pm\delta}$ and $SrTi_{0.65}Fe_{0.35}O_{3\pm\delta}$ [304]. As the opposite of yttrium and niobium, the amount of the atomic substitution rate is high. In order to balance the electronic and catalytic properties, co-doped compounds were investigated such as $Y_{0.08}Sr_{0.92}Ti_{1-x}Fe_xO_{3-\delta}$ with x=0, 0.2, 0.4 in yttria stabilized zirconia (YSZ) scaffolds by Sengodan *et al.* in 2013 [204]. The value reported for the electronic conductivity at 800 °C under H_2 is around 0.1 $S \cdot cm^{-1}$ and increasing the Fe content led to a slight decrease in conductivity.

No investigation on neodymium and praseodymium were considered as materials for solid oxide fuel cells. However, since these elements are trivalent ions, the substitution of the strontium element should lead to an enhancement of the electronic conductivity. In 2020, Lin *et al.* investigated the co-doped strontium titanate material with neodymium and dysprosium [305]. The value for the electronic conductivity measured for the compound $Sr_{0.8}Nd_{0.2}TiO_3$ is 850 $S \cdot cm^{-1}$ at 400 °C. However, secondary phases of pyrochlore $Nd_2Ti_2O_7$, mainly due to solid-state reaction, are observed showing the limit of the synthesis regarding the stoichiometry. Regarding the praseodymium doping impact, in 2013, Kovalevsky *et al.* reported an electronic conductivity of ~10 $S \cdot cm^{-1}$ for $Sr_{0.9}Pr_{0.1}TiO_{3-\delta}$ at 700 °C under reducing condition [306]. The main reasons why those dopants were identified for the oxidative coupling of methane are the following. Indeed, in 2019, Lim *et al.* provided a complete study by combining experimental and density functional theory on doped strontium titanate catalyst design [150]. Praseodymium and neodymium doped $SrTiO_3$ catalysts were found as the best option for OCM catalyst, for compounds such as $Sr_{0.8}Nd_{0.2}TiO_3$ and $Sr_{0.8}Pr_{0.2}TiO_3$. However, the study considered a successful doping of those large cations in the small B-sites, which is unlikely.

This concludes the part about the motivation of the choice of dopants. Whether in SOFC development, the enhancement of the electronic properties, their ability to perform OCM, limitations were still observed. The problem of phase purity often occurs for the solid-state reaction method and some interesting features such as the A site deficiency which is difficult to obtain using conventional synthesis method. This is where the solvothermal method by using supercritical continuous synthesis is an advantage. The next part will present the characteristics by XRD, TEM-EDS, ICP and Raman of the strontium titanate doped with yttrium and niobium.

1.2 Proof of concept: Doping A and B sites in $SrTiO_3$

To validate the success of doping (or substitution) in the A and B sites of strontium titanate using the supercritical solvothermal method, strontium titanate compositions doped with yttrium or niobium were synthesized with strontium acetylacetonate, titanium isopropoxide, niobium isopropoxide and yttrium acetylacetonate hydrate precursors. The successful substitution will be verified thanks to a structural characterization by XRD and the quality of the doping rate will be attested by coupling ICP-OES and EDS mapping. This part will provide an insightful structural and chemical study proving the supercritical solvothermal method is reliable and verified method to access at doped strontium titanate compositions.

The composition synthesized are $SrTiO_3$, $Sr_{0.9}Y_{0.1}TiO_{3-\delta}$, $Sr_{0.95}Y_{0.05}TiO_{3-\delta}$, $SrTi_{0.9}Nb_{0.1}O_{3-\delta}$, $SrTi_{0.95}Nb_{0.05}O_{3-\delta}$. These compositions were synthesized with the first reactor mentioned in Chapter 2 with assigned method involving a preheating. The lattice parameter of the undoped strontium titanate determined by Rietveld refinement is used as a reference value. It was expected that doping at the A-site by a smaller cation would affect the lattice parameter. A reduction in the ionic radius (r_Y=122 pm for CN=12) value would result in a shift of the PXRD signal towards higher angles, indicating a decrease in the lattice parameter, and *vice versa* if the B-site is doped with a larger cation (r_{Nb}=64 pm for CN=6). If such a shift is confirmed and no secondary phases are detected, it means the successful insertion/substitution with the doped element.

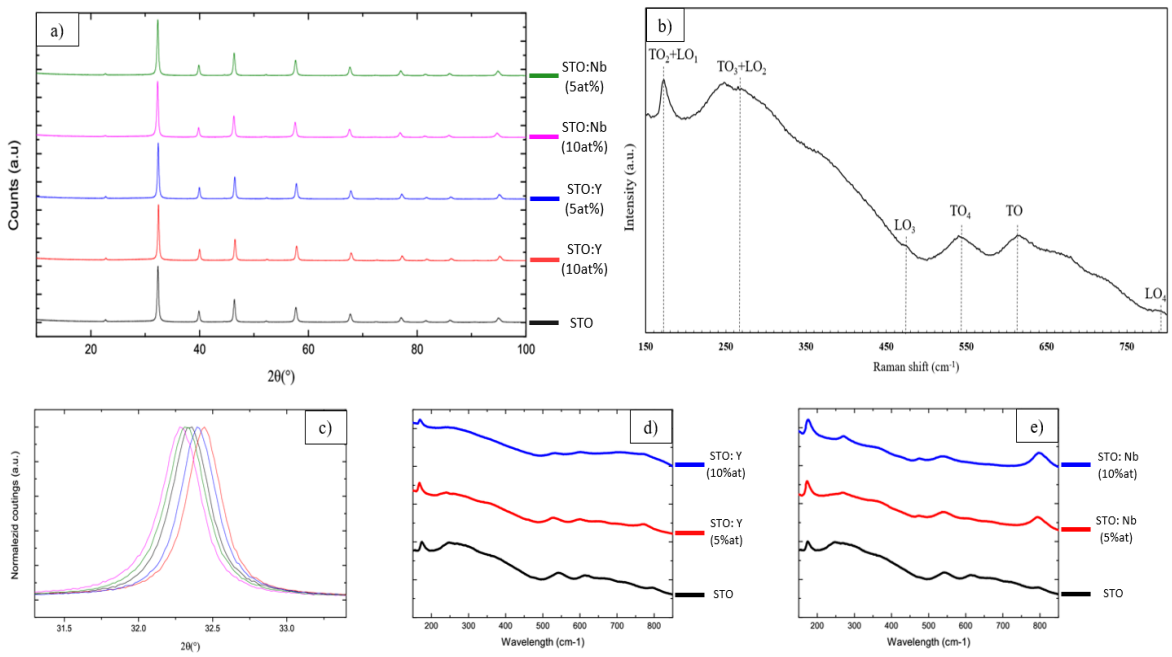

Figure 4.2: PXRD patterns of strontium titanate and A/B site doped strontium titanate (a). Raman signal of undoped strontium titanate (b). Zoom on the (1 1 0) peak of each strontium titanate (c). Raman signal of strontium titanate doped with yttrium (d)/ doped with niobium (e)

Figure 4.2 displays the PXRD and Raman signatures of both undoped and doped strontium titanate with yttrium or niobium with two different atomic rates. ***Figure 4.2***.a) illustrates the PXRD signals of each perovskite undoped and doped with yttrium and niobium at two atomic rates (5 at.% and 10 at.%).

The absence of secondary phases indicates the material purity. The cubic symmetry remains unaffected, indicating a Goldschmidt factor close to 1. It is inferred that yttrium occupies the A-site and niobium the B-site of the perovskite structure. A closer examination of the most intense peak of strontium titanate (1 1 0) highlights the observed peak shift in ***Figure 4.2***.c). Compared to the black curve representing the reference material, the blue and red patterns demonstrate a shift towards higher angles due to yttrium doping ($r_Y<r_{Sr}$), indicating a decrease in the lattice parameter. Conversely, the purple and green curves, corresponding to strontium titanate doped with niobium, show a peak shift with increasing niobium content towards lower angles, indicating a lattice expansion due to niobium larger ionic radius compared to titanium ($r_{Ti}<r_{Nb}$). Each synthesized composition was refined using the *FullProf* software. Appendix D.1 presents a comparative structural analysis, including the refined parameters and their estimated standard deviations. The refinements confirm the evolution of the lattice parameter. A reference value of 3.912 Å, determined from the XRD signal, is used. In the case of niobium substitution, an increase in the lattice parameter is observed, reaching 3.915 Å and 3.920 Å for 5 at.% and 10 at.% Nb substitution, respectively. Conversely, yttrium substitution leads to a decrease in the lattice parameter, with values of 3.907 Å and 3.905 Å, which correlates with the increasing Y substitution level. The doping can thus be confirmed based on PXRD characterization.

Raman spectra were also analyzed by comparing the different Raman signals of undoped and doped (yttrium and niobium) strontium titanate synthesized by supercritical continuous flow synthesis (***Figure 4.2***.b, d and e). The intensity counts were normalized to observe the doping impact on the different transversal and longitudinal modes. Regarding the doping with yttrium (***Figure 4.2***.d), the intensity of indexed modes decreased, including the TO_2+LO_1 and TO_4 modes. Conversely, in niobium-doped strontium titanate (***Figure 4.2***.e), the intensity of the TO_2+LO_1 mode increased, along with the LO_4 signal. These Raman signal modifications confirm a change in the compound microstructure, and the absence of new modes within the domain confirms the purity of doped strontium titanate.

The structural investigation confirmed the doping phenomenon thanks to the modification of some properties such as the lattice parameter or the impact on the phonon modes. The following part is focused on the quantification of the doping rate. The quantitative analysis of doped strontium titanate has been performed by energy dispersive spectroscopy measurements (EDS) using TEM. The objective

of the characterization is to investigate the homogeneity of the doping and the efficiency of the method.

ICP-OES analysis results are summarized in ***Table 4.2***. Undoped and doped strontium titanate as well as a commercial strontium titanate from SIGMA (<100 nm particle size), used as a reference, were mineralized for analysis. The purpose of mineralizing the commercial reference at the same time is to confirm the effectiveness of the mineralization process. It is supposed to give a ratio of Sr/Ti equal to one.

Table 4.2: ICP-OES results obtained on the compositions $Sr_{1-x}Y_xTiO_{3-\delta}$ and $SrTi_{1-x}Nb_xO_{3-\delta}$ synthesized using the first flow reactor

Composition	ICP results
$SrTiO_3$ (SIGMA)	$Sr_{0,99}TiO_3$
$SrTiO_3$	$Sr_{0,72}TiO_{3-\delta}$
$Sr_{0,9}Y_{0,1}TiO_{3-\delta}$	$Sr_{0.68}Y_{0.11}TiO_{3-\delta}$
$Sr_{0,95}Y_{0,05}TiO_{3-\delta}$	$Sr_{0.70}Y_{0.05}TiO_{3-\delta}$
$SrTi_{0,9}Nb_{0,1}O_{3-\delta}$	$Sr_{0.68}Ti_{0.78}Nb_{0.12}O_{3-\delta}$
$SrTi_{0,95}Nb_{0,05}O_{3-\delta}$	$Sr_{0.75}Ti_{0.91}Nb_{0.07}O_{3-\delta}$

Each experiment was replicated three times per sample to ensure a consistent average value and to validate the complete mineralization of the powder. The Sr/Ti ratio of the commercial powder gives a value close to 1 confirming the effective mineralization process. The reference powder for supercritical synthesis, which is the undoped strontium titanate, gives a Sr/Ti ratio of 0.72 which is within the range of ratio found in Chapter 3 for the composition synthesized with first reactor. This imbalance between the two elements has been hypothesized with two possibilities for this type of synthesis: (1) it has been observed before and was explained by the reaction of the strontium with organic compounds leading to the creation of strontium carbonate (attested in Chapter 3 as well) (2) Due to the combination of the aqueous media and the ionic nature of the Sr-O bonding, strontium content within the strontium titanate particles can be solubilized. However, we presume that the fast kinetic reaction in solvothermal medium allows stabilizing highly strontium deficient particles and so with a high amount of A-site vacancy. We confirm the STO: Y elemental composition $Sr_{0.68}Y_{0.11}TiO_{3-\delta}$ for STO (Y 10 at.%) and $Sr_{0.70}Y_{0.05}TiO_{3-\delta}$ for STO (Y 5 at.%). For STO: Nb, the elemental composition found is $Sr_{0.68}Ti_{0.78}Nb_{0.12}O_{3-\delta}$ for STO (Nb 10 at.%) and $Sr_{0.75}Ti_{0.91}Nb_{0.07}O_{3-\delta}$ for STO (Nb 5 at.%). Those results give a right and overall quantification of the doping elements in our material. The imbalance between the strontium content and the titanium content is still observed but the ratio is not impacted. It suggests that for the Y doped strontium titanate the dopant is inserted in the supposed existing strontium vacancy site instead of substituting strontium directly. This aligns with the previous observation using the Raman

spectroscopy. Regarding the B-site doped strontium titanate, we observe higher content and a supposed vacancy in titanium. Those gaps are considered as uncertainties linked to the instrumentation devices since the niobium content found is higher for the STO: Nb (10 at.%) and STO: Nb (5 at.%). Nonetheless, we confirm the presence of the doping element and doping rate of the perovskite synthesized.

In the next part, we investigate the homogeneity of each composition through an EDS spectroscopy mapping of each element except oxygen.

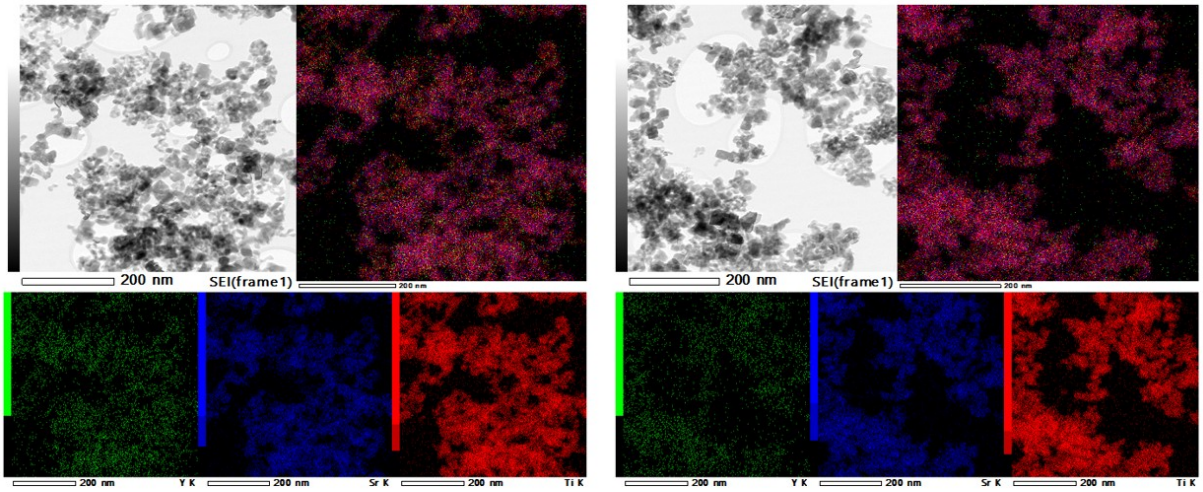

Element	(keV)	Mass%	Atom%
Ti K	4.508	43.3	58.4
Sr K	14.140	49.4	36.3
Y K	14.931	7.3	5.3
Total	-	100.0	100.0

Element	(keV)	Mass%	Atom%
Ti K	4.508	43.0	58.0
Sr K	14.140	53.3	39.3
Y K	14.931	3.7	2.7
Total	-	100.0	100.0

Figure 4.3: EDS-TEM of the strontium titanate composition doped with yttrium at 10 at.% (left) and 5 at.% (right) with a table quantifying the atomic percent of strontium, titanium and yttrium

Figure 4.3 corresponds to the EDS characterization of the STO: Y (10 at.%) on the left and STO: Y (5 at.%) with a TEM acquisition, a global mapping and a separated mapping of the different quantified elements. The titanium signal is in red, strontium in blue and yttrium in green. The bottom Table gives an atomic quantification of the studied composition. The TEM images confirm the nanosize of the particles. Regarding the different mappings, the homogeneity of the yttrium dopant is detected and confirmed. Based on the table, the value found for each element shows an imbalance between A and B cations populations, which has already been highlighted in Chapter 3 as an exclusive feature of the perovskite materials synthesized using the solvothermal supercritical method. The global A/B ratio of 0.68 and 0.72 shows that the overall A deficiency is around 32 at.% and 28 at.%, respectively for STO: Y (10 at.%) and STO: Y (5 at.%), which is almost similar as for pure $SrTiO_3$ synthesized on the first reactor based on the reference value given by ICP-OES. The proportion of Y within this overall A deficiency is

close to the targeted one. Based on the obtained values, the calculated yttrium content is 14.6 at.% in strontium titanate doped with 10 at.% yttrium and 6.8 at.% in strontium titanate doped with 5 at.% yttrium. The detection of yttrium content correlates with the previous PXRD observation explaining the decrease of the lattice size.

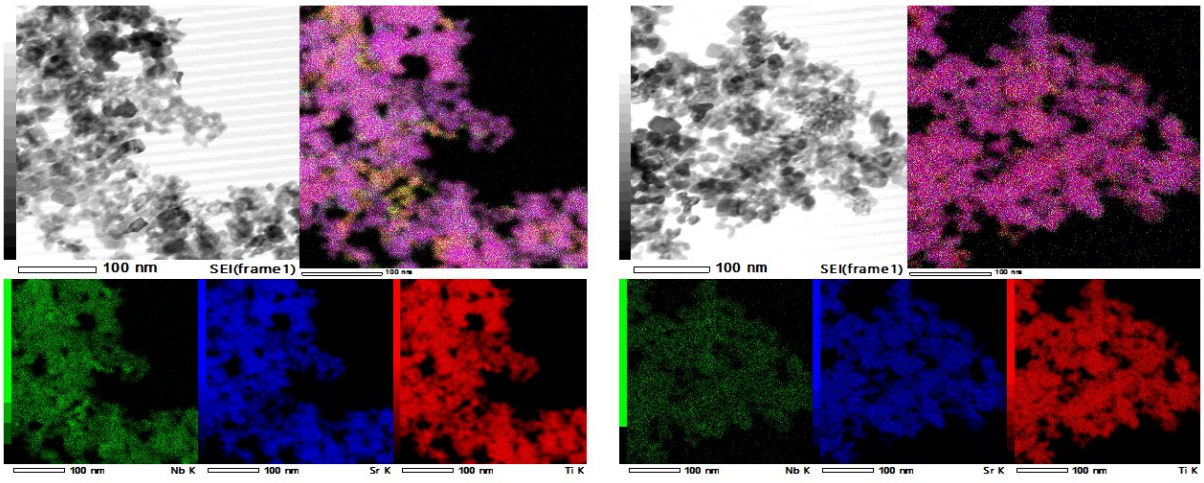

Element	(keV)	Mass%	Atom%
Ti K	4.508	35.2	50.1
Sr K	14.140	56.1	43.5
Nb K	16.581	8.7	6.4
Total	-	100.00	100.00

Element	(keV)	Mass%	Atom%
Ti K	4.508	37.9	52.9
Sr K	14.140	57.7	43.9
Nb K	16.581	4.4	3.2
Total	-	100.00	100.00

Figure 4.4: EDS-TEM of the strontium titanate composition doped with niobium at 10% at. (left) and 5% at. (right) with a Table quantifying the atomic percent of each strontium, titanium and niobium

Figure 4.4 shows the same kind of analysis for strontium titanate doped with niobium at 10 at.% (left) and 5 at.% (right). The observations are similar compared to ***Figure 4.3***. The TEM image confirms the nanosize of the particles. The homogeneity of the niobium content is confirmed although some very small clusters of strontium deficiency, represented on the mapping by a purple color contrast, can be observed for STO: Nb (10 at.%). However, they are not observable for STO: Nb (5 at.%). Based on the obtained values, the calculated niobium content is 12.7 at.% in strontium titanate doped with 10 at.% niobium and 5.9 at.% in strontium titanate doped with 5 at.% niobium. This overestimation was already observed for the previous composition with yttrium and is explained by the semi-quantitative feature of EDS analysis. Moreover, the content of strontium deficiency remains stable between the two compositions as the opposite of the titanium content which decreases as the niobium content increases meaning we successfully substituted titanium content by niobium. The A/B sites ratio is higher based on the reference value as well with 0.77 and 0.78 for STO: Nb (10 at.%) and STO: Nb (5 at.%), respectively.

To summarize, we observed on the EDS mapping the detection of the different elements, and so a global homogeneity between titanium and strontium and the detection and homogeneity of the doping element was attested. It is interesting to note that some subareas have less blue contrast, meaning that less strontium content is detected. The EDS realized in those areas showed an enhanced deficiency. This proves the existence another type of particles highly deficient in strontium content within the nanoparticles of strontium titanate. As mentioned before, the EDS-TEM characterization is defined as semi-quantitative since it only performs the quantification in a local area, it is not global. Conversely, the ICP-OES technics is the best method to quantify the atomic rate of an element since it is based on the mineralization on the whole sample. We used it to determine the content rate of strontium, titanium and dopant, here yttrium and niobium.

In summary, X-ray diffraction (XRD) analysis combined with Raman characterization revealed the influence of the dopant incorporation on lattice parameters, confirming alterations induced by the presence of additional elements. Furthermore, ICP-OES and confirmed the accurate quantification of each element, demonstrating the reliability of the supercritical flow synthesis in producing doped strontium titanate with adjustable atomic contents. HRTEM and EDS mapping provided insights into the nanoparticle morphology, consistent with previous studies on strontium titanate nanoparticle synthesis using acetylacetonate precursors. EDS mapping indicated a degree of homogeneity in dopant distribution, with almost similar elemental ratios observed; however, the doping rate of yttrium and niobium appeared higher than the aimed composition, potentially limited by semi quantitative nature of the characterization. Based on these results, we provide an approach to detect successful substitution and a proof of concept for the production of doped strontium titanate assisted by supercritical solvothermal synthesis which is a first in the state of art of nanoparticles synthesis using the supercritical method.

1.3 Development of doped optimized composition of $SrTiO_3$

Once substitution in strontium titanate was attested and the proof of concept verified, we moved toward dopant that presented an interest for electronic conductivity and oxidative coupling of methane catalysis reaction. In this part, we present different compositions of A-sites doped strontium titanate with rare earths (Y, Nd and Pr), B-sites doped strontium titanate with transition metals (Nb and Fe) and A/B codoped strontium titanate with Nd and Nb using isopropoxide and acetylacetonate precursors with the method described for the new reactor which has an optimized A/B ratio. The evidence of successful substitution is based on the evolution of the XRD signal. Appendix D.2 summarizes the structural and microstructural parameters of the strontium titanate-based samples

discussed in this section (excluding those with niobium substitution), as determined from signal refinement using the *FullProf* software.

1.3.1 A-site doped $SrTiO_3$

The following part presents the structural characterization of three new compositions of strontium titanates synthesized using the supercritical solvothermal method: 1 at.% and 5 at.% of neodymium and 10 at.% of praseodymium. The chemical composition of each A-site doped strontium titanate is characterized ICP-OES and EDS mapping is used on the new composition to attest the homogeneity of the new dopant used.

The lattice parameter of the undoped strontium titanate determined by Rietveld refinement served as a reference value (3.915 Å). As observed with the previous doping with yttrium, doping at the A-site with a smaller cation affects the lattice parameter. The ionic radius with a coordination number of twelve for neodymium and praseodymium is referred to in ***Table 4.1***. Again, the elements used have a smaller ionic radius compared to the ionic radius of strontium meaning that a reduction of the lattice parameter should happen. ***Figure 4.5*** shows the PXRD patterns of the undoped STO, STO: Nd (1 at.%) and STO: Nd (5 at.%). The signal of the peak (1 1 0) for each composition is compared and a TEM image of the corresponding nanoparticles is given.

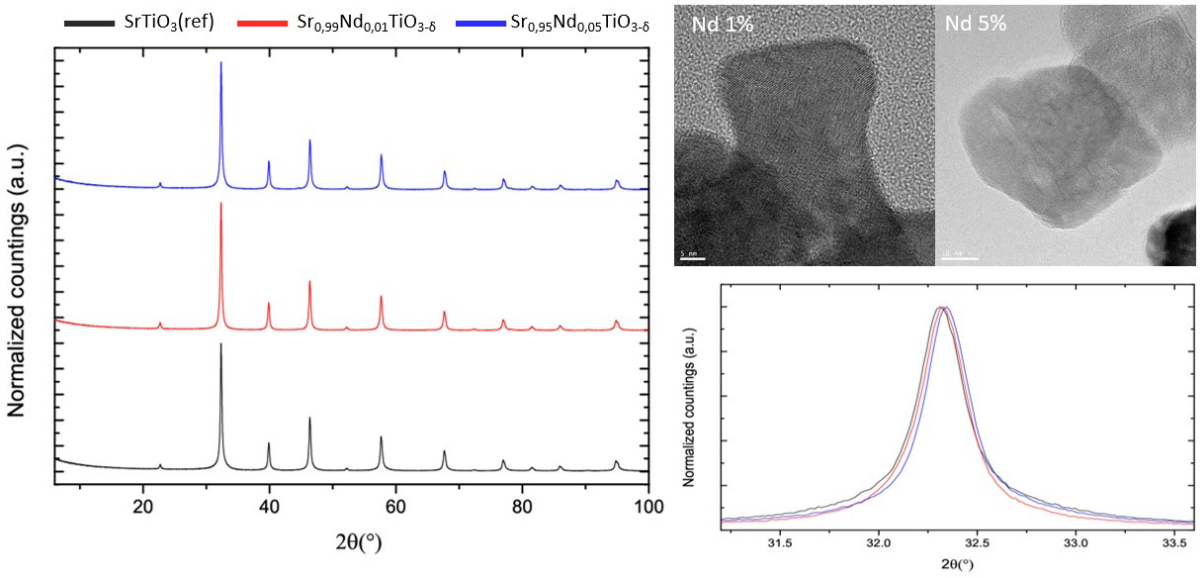

Figure 4.5: PXRD patterns of strontium titanate and A site doped with neodymium strontium titanate. Zoom on the (1 1 0) peak of each composition. TEM images of the crystallites of the different compositions

We observe very intense peak characteristics of the strontium titanate phase with no presence of the secondary phase. The TEM images show for both compositions (single-crystals) particles correlating with the defined peak observed on the PXRD patterns for substituted composition. A closer

examination of the most intense peak of strontium titanate (1 1 0) highlights the observed peak shift. The black curve corresponds to strontium titanate of reference, a progressive shift toward higher angle is observed for the red and blue curves corresponding to the substituted composition of strontium titanate. The gradual shift is linked to the substitution rates of the dopant element leading to a more important shift as the substitution rate increases. This is explained by the reduction of the lattice parameter due to the insertion of a smaller element since r_{Nd}= 127 pm and r_{Sr}= 144 pm. The same behavior was observed with yttrium, previously.

Figure 4.6 shows the same structural analysis as done in ***Figure 4.5***. The PXRD pattern recorded on the doped strontium with praseodymium corresponds to the red curve and it is compared with reference material in black. The TEM image of the particles is presented as well as a focus on the most intense peak of the overall signal.

The same observation is made regarding the purity and the crystallinity of the synthesized nanopowder. The success of the substitution is verified also since a shift toward higher angles is observed meaning the lattice size decrease. The Rietveld refinement of PXRD signal confirm this observation with a decrease from 3.914 Å to 3.910 Å.

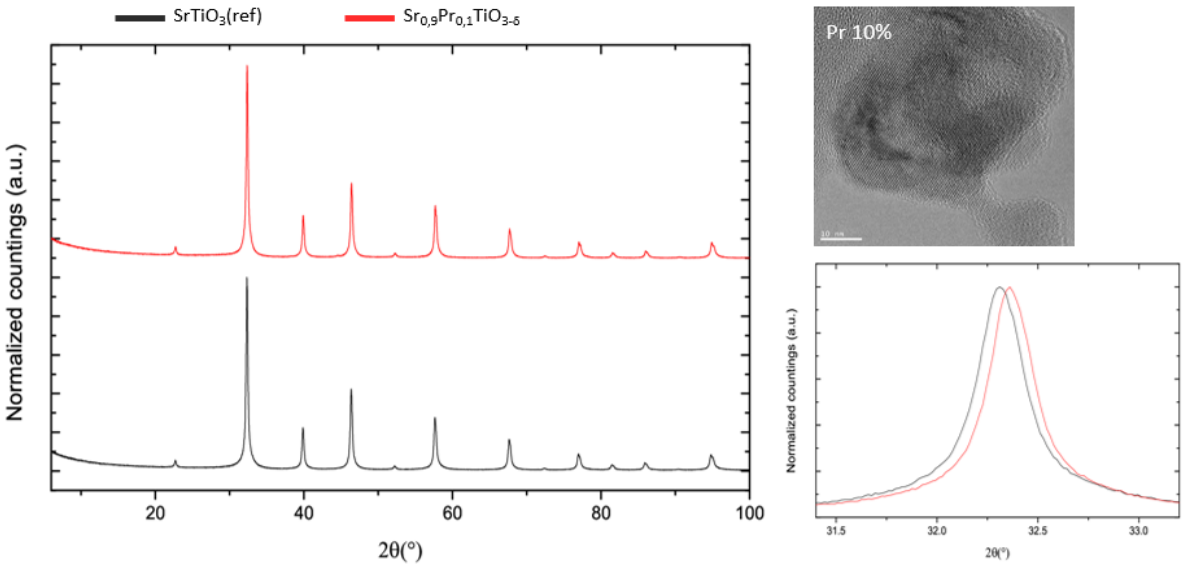

Figure 4.6: PXRD patterns of strontium titanate and A site doped with praseodymium strontium titanate. Zoom on the (1 1 0) peak of each strontium titanate. TEM image of a crystallite

To summarize, the microstructural characterization performed on the strontium titanate doped with rare earth showed in all cases a reduction of the lattice parameter because of the substitution of Sr with smaller ionic radius. We can move on to the elemental quantification of the different compositions to check the atomic substitution.

ICP-OES analyses were performed to determine the chemical composition of the investigated powders and the results are summarized on ***Table 4.3***. The Sr/Ti ratio of the commercial powder gives a value close to 1 confirming the mineralization process. The reference powder, which is the undoped strontium titanate synthesized in the present work gives a Sr/Ti of 0.79 which is within the range defined in Chapter 3 for the optimized method involving the new reactor.

Table 4.3: ICP-OES results of the composition $Sr_{1-x}Re_xTiO_{3-\delta}$ (Re: Y, Nd and Pr) synthesized using the second reactor

Composition	ICP results
$SrTiO_3$ (SIGMA)	$Sr_{0,98}TiO_3$
$SrTiO_3$	$Sr_{0,79}TiO_{3-\delta}$
$Sr_{0.9}Y_{0.1}TiO_{3-\delta}$	$Sr_{0,78}Y_{0,09}TiO_{3-\delta}$
$Sr_{0.95}Nd_{0.05}TiO_{3-\delta}$	$Sr_{0.80}Nd_{0.05}TiO_{3-\delta}$
$Sr_{0.99}Nd_{0.01}TiO_{3-\delta}$	$Sr_{0.82}Nd_{0.02}TiO_{3-\delta}$
$Sr_{0.9}Pr_{0.1}TiO_{3-\delta}$	$Sr_{0.76}Pr_{0.1}TiO_{3-\delta}$

The composition STO (Y 10 at.%) synthesized using the optimized reactor reveal a better balance of the A/B ratio (from 0.68 to 0.78) compare to the previous composition mentioned in the proof of concept. We confirm here the neodymium and praseodymium doping rate of the powder and calculate the composition of the powder, giving for STO: Nd an elemental composition $Sr_{0.80}Nd_{0.05}TiO_{3-\delta}$ for STO (Nd 5 at.%) and $Sr_{0.79}Nd_{0.02}TiO_{3-\delta}$ for STO (Nd 1 at.%). The elemental composition STO: Pr corresponds to $Sr_{0.76}Pr_{0.1}TiO_{3-\delta}$ for STO (Pr 10 at.%). Those results give a right and overall quantification of the doping elements in our material. The imbalance between the strontium and the titanium contents is still observed. We can even observe a slight increase on the A/B ratio going from 0.79 to 0.87 suggesting an insertion instead of a substitution. This aligns with the previous observation on the other composition. Nonetheless, we confirm the presence of the doping element and doping rate of the perovskite synthesized.

The following part is focused on the homogeneity of the new dopants. The homogeneity analysis of doped strontium titanate has been completed by energy dispersive spectroscopy measurements (EDS) using scanning TEM. The objective of the characterization is to have a proof that the powder contains the doped element and also to attest the homogeneity.

Figure 4.7 corresponds to the EDS characterization of the STO: Nd (5 at.%) on the left and STO: Nd (1 at.%) on the right with a TEM acquisition, a global mapping and a separated mapping of the different elements which have been quantified. The titanium signal is in red, strontium is in blue and neodymium

is in green. A table at bottom gives the atomic quantification. The TEM image confirms the nanosize of the particles.

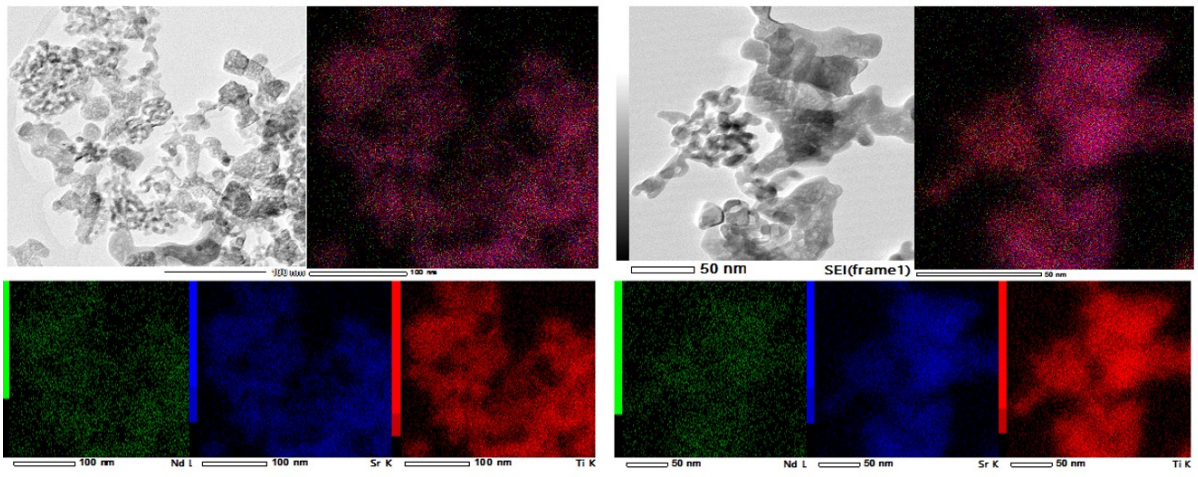

Element	(keV)	Mass%	Atom%
Ti K	4.508	38.9	54.8
Sr K	14.140	54.5	42.1
Nd L	5.229	6.6	3.1
Total	-	100.0	100.0

Element	(keV)	Mass%	Atom%
Ti K	4.508	40.9	56.0
Sr K	14.140	58.2	43.6
Nd L	5.229	0.9	0.4
Total	-	100.0	100.0

Figure 4.7: EDS-TEM of the strontium titanate composition doped with neodymium at 5% at. (left) and 1% at. (right) with a Table quantifying the atomic percent in each strontium, titanium and neodymium

Regarding the different mappings, the dispersive homogeneity of the neodymium dopant is detected. Based on the Table, the values found for each element show an imbalance between A and B cations populations in agreement with the previous part. It is observed that the neodymium value is lower than targeted but does not modify the A/B ratio. The lower value could be explained by the resolution of the apparatus. Also, increasing the content of neodymium leads to a slight decrease of the strontium content (larger than titanium) showing the substitution/insertion of neodymium in the A site of the perovskite which correlates with the previous observation on PXRD pattern.

Last notable observation is that the combination of neodymium and strontium contents gives the total value of A site atoms. This allows us to calculate the ratio of A site amount divided by the B site one, it reaches about 0.80, a value which is in the range of the A site deficiency determined in part “3.2 Toward an understanding of the origin of the defects” since those compositions have been synthesized in the second flow reactor after optimization.

Figure 4.8 corresponds to the EDS characterization of the STO: Pr (10 at.%) with a TEM acquisition, a global mapping and a separated mapping of the different quantified elements. The titanium signal is in red, strontium is in blue and praseodymium is in green. A table at the bottom gives an atomic quantification of the studied composition. The TEM image confirms the nanosize of the particles.

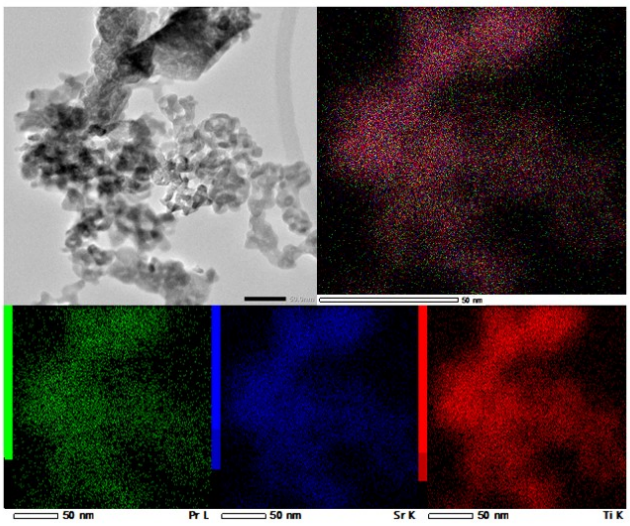

Element	(keV)	Mass%	Atom%
Ti K	4.508	38.2	54.7
Sr K	14.140	51.2	40.1
Pr L	5.033	10.6	5.2
Total	-	100.0	100.0

Figure 4.8: EDS-TEM of the strontium titanate composition doped with praseodymium at 10% at. with a Table quantifying the atomic percent in each strontium, titanium and praseodymium

Similar observations can be made from the result of EDS-TEM characterization for STO: Pr (10 at.%). Homogeneity of the dopant is verified. The content of praseodymium detected is equal to 13 at.% for STO: Pr (10 at.%) which is higher compared to the amount aimed, possibly explained by the resolution limit of the devices. A hypothesis would be that this praseodymium excess partially compensates the Sr vacancies. Nonetheless, the ratio A/B is similar to previous EDS characterizations showing the consistency of the supercritical solvothermal method to produce substituted composition. This quantitative study is then supplemented by ICP-OES measurement.

In summary, PXRD characterizations provides information such as the purity of the compound where no secondary phase is observed from the fresh powder out of the reactor. The particles are well crystallized based on the TEM pictures showing the atomic arrangement and PXRD pattern showing intense peaks relating to the strontium titanate phase. The Rietveld refinement shows a slight decrease of the lattice parameter which is amplified as the substitution rate increases. This correlates with the observation on the PXRD patterns showing a shift toward higher angle meaning the lattice decreases. The EDS and ICP characterizations allow to identify the presence and the amount of element inserted/ substituted in the compounds. The result in ICP suggests a possible insertion of A-site element since the deficiency is defined from the ICP results of the reference powder.

1.3.2 B-site doped $SrTiO_3$

As we saw previously, the supercritical solvothermal synthesis is reliable for the production of A-site doped strontium titanate but also for B-site doped strontium titanate. This next part present briefly the structural characterization of a n-doped strontium with niobium (10 at.%) and p-doped strontium titanate compound doped with iron (10 at.%).

Figure 4.9 represents the PXRD patterns of the reference sample and the sample doped with niobium at 10 at.%.

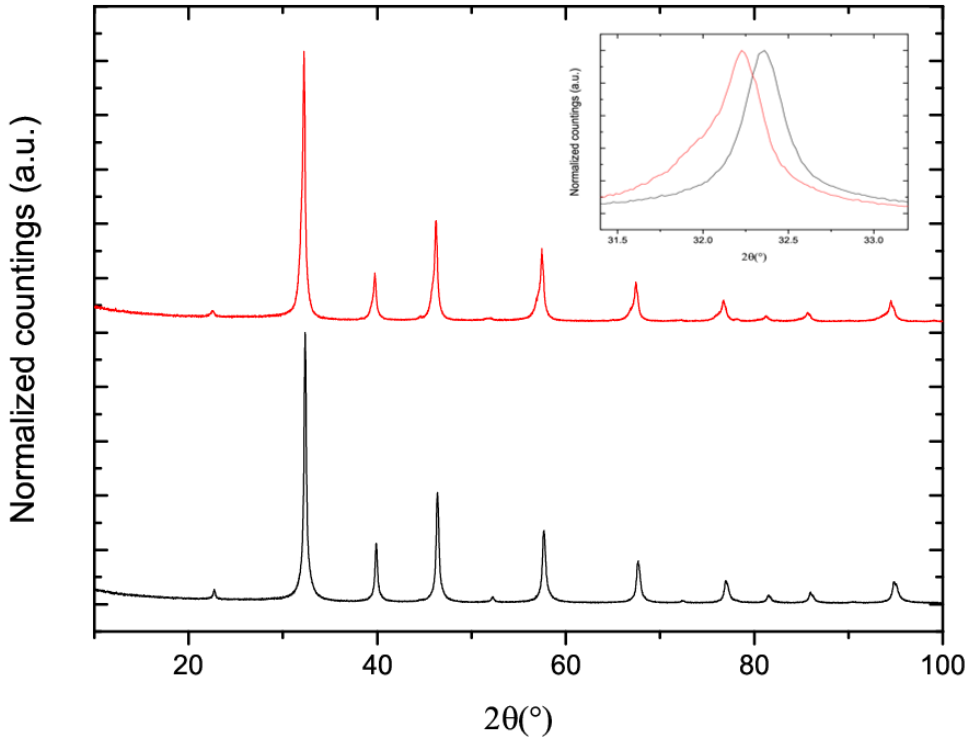

Figure 4.9: PXRD pattern of strontium titanate doped 10 at.% of niobium on B site (red curve). Zoom on the (1 1 0) peak of each strontium titanate

The black pattern represents the PXRD signal of the reference sample and the red pattern corresponds to the doped sample with niobium. The peaks in the patterns indicate a pure phase of strontium titanate and as what was observed before; the samples are crystalline and likely share a similar structure. In comparing the two signals, the peak of the red curve is slightly shifted relative to the black curve, as highlighted in the inset. The inset focuses on the peak (1 1 0) between 31.4° and 33.2°. A clear shift toward lower angle is observed meaning a lattice expansion which is explained by the substitution of the titanium element by the niobium element being a bigger cation. We confirm the successful insertion of the niobium element in the lattice. Also, the broadening of the red peak compare to the black peak imply that the crystallite size decreased. The Rietveld refinement of the STO: Nb (10 at.%)

confirms the expansion of the lattice with 3.925 Å and a decrease of the crystallite size down to 14 nm. This expansion can be either explained by the size-effect or the substitution rate higher than 10 at.% as showed by the ICP-OES which gives the real stoichiometry of the compound: $Sr_{0.88}Ti_{0.72}Nb_{0.15}O_{3-\delta}$. A content of 15 at.% of niobium is detected which is higher than the aimed composition. In any case we confirm the successful n-doping and the substitution of Ti^{4+} by Nb^{5+}. Further tests are needed in order to understand where this drastic decrease of the crystallite size originate from.

Figure 4.10 represents the PXRD patterns of the reference sample and the sample doped with iron at 10 at.%.

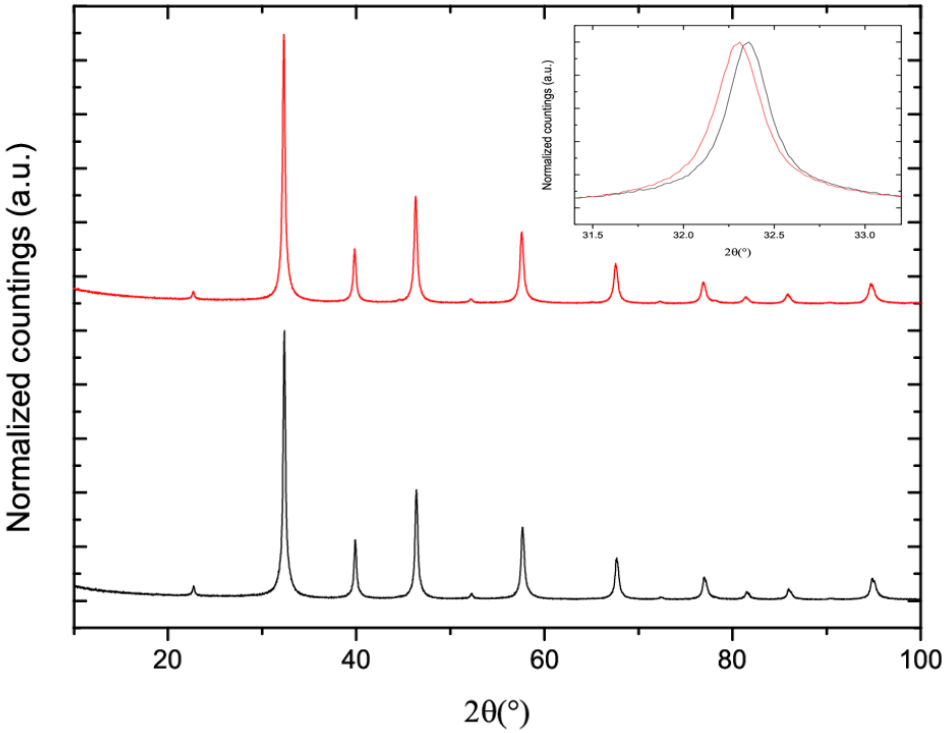

Figure 4.10: PXRD pattern of strontium titanate doped 10 at.% of iron on B site (red curve). Zoom on the (1 1 0) peak of each strontium titanate

The same characteristic observed in ***Figure 4.9*** are attested here. The shift toward lower angle for the doped compound highlighted in the inset attest a decrease of the lattice parameter. The Rietveld refinement of doped sample also confirmed an increase of the lattice parameter (3.919 Å). Based on these results, we confirm the successful development of p-doped strontium titanate by substituting the titanium element by a bigger iron cation. Based on the Shannon data, this expansion could be due to the replacing of Ti^{4+} by Fe^{3+} with high spin (64.5 pm).

To conclude on the development of A or B sites doped strontium titanate, we presented a method through the PXRD characterization to confirm the successful doping of a material by checking the

evolution of the lattice parameter. It is important also to consider the ionic radius of the elements substituting the corresponding site.

Another question we could consider is when the substituted element is located between the A or B sites. Let us consider the case where the composition doped with large size rare-earth such as neodymium (127 pm) would substitute titanium in the B site (60.5 pm). This would lead to an observable shift toward a lower angle on the PXRD pattern if we compare it with the reference material. Since it is not the case, we can conclude that the element manages to substitute on the A site. The other case to consider is doping with Fe which is supposed to substitute the B site. Since its radius is much smaller than Sr (144 pm versus 60.5 pm), such substitution would lead to a large decrease of the lattice parameter and thus to an upward shift of the diffraction line which is not observed. We conclude that Fe is substituting for Ti on the B site, in agreement with the literature.

1.3.3 A/B codoped $SrTiO_3$

This last part presents an exclusive composition that complete the study and flexibility of the supercritical solvothermal synthesis. This is a codoped composition on the A and B sites, $Sr_{0.95}Nd_{0.05}Ti_{0.95}Nb_{0.05}O_{3-\delta}$. A structural characterization and analysis quantification are presented for the codoped composition.

Figure 4.11 is the PXRD pattern of the codoped composition with a doping on the A-site with neodymium and on the B-site with niobium. The substitution rates chosen were 5 at.% of neodymium and 5 at.% of niobium.

The PXRD pattern and TEM image recorded on the codoped strontium titanate show the same characteristics as observed before. It is interesting to notice the direction of the shift because the lattice is doped with a smaller element on the A-site and a larger element on the B-site. Here, the shift goes toward the lower angle meaning the lattice parameter increases, it correlates with the value of the lattice parameter defined by the Rietveld refinement (3.921 Å). This means that the lattice is much more impacted by a modification of the size element in B-site than in the A-site. This structural characterization does not allow to prove the substitution of the element in the A site since only the increase lattice is characteristic of a successful B-site doping.

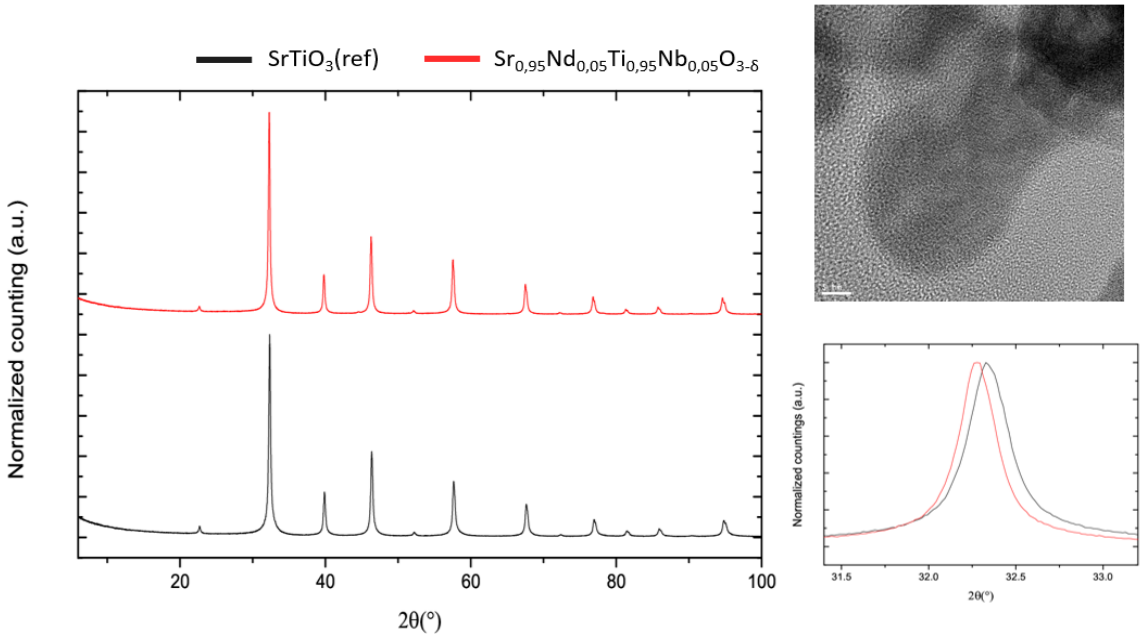

Figure 4.11: PXRD patterns of strontium titanate and A and B sites doped with neodymium and niobium. Zoom on the (1 1 0) peak of each strontium titanate. TEM image of a crystallite of the codoped material

This part presents the EDS characterization of the codoped compound which has been substituted on the A-site and the B-site. ***Figure 4.12*** presents the EDS results on the codoped composition with the overlay and the separate elements corresponding to each different color.

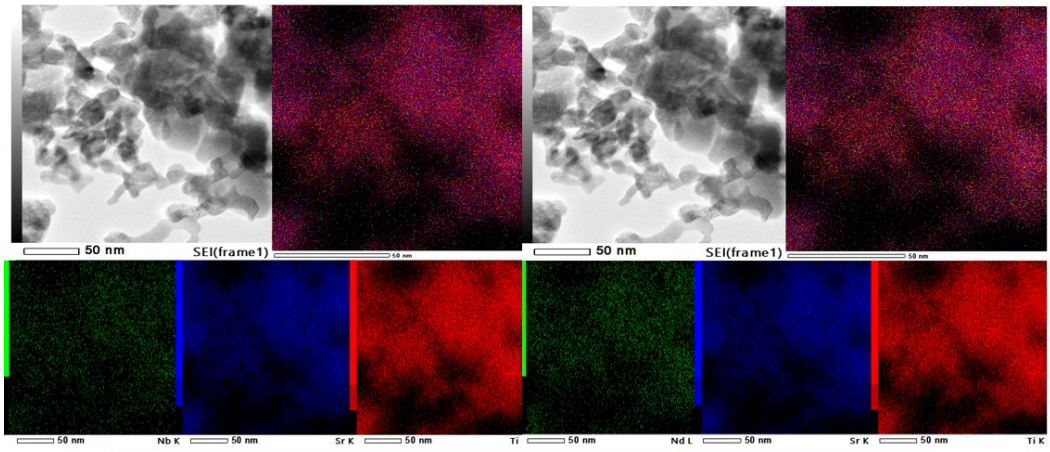

Element	(keV)	Mass%	Atom%
Ti K	4.508	40.8	56.6
Sr K	14.140	51.0	38.7
Nb K	16.581	3.5	2.5
Nd L	5.229	4.7	2.2
Total	-	100.00	100.00

Figure 4.12: EDS-TEM of the strontium titanate composition doped with neodymium and niobium at 5% at. each with a Table quantifying the atomic percent in strontium in blue, titanium in red and niobium in green (left) and neodymium in green also (right)

The dopants are both detected and no clusters of dopants are detected meaning a homogenous repartition of the neodymium and niobium elements. The contents determined are quite good with a content of neodymium equal to 5.5 at.% and niobium with 4.3 at.%. However, the ratio A/B decrease to 0.7 despite the optimized method.

The goal of synthesizing this codoped strontium titanate was to combine the benefits of both elements. As mentioned previously, neodymium is supposed to boost the reactivity of the material to perform the oxidative coupling of methane catalytic reaction while niobium is supposed to enhance the electronic conductivity of the material, both being properties required for the targeted application. The substitution rate was deliberately chosen to minimize the risk of secondary reactions as the number of reactants increased as it was observed with solid state reaction. At a total substitution level of 10 at.%, no secondary phases were detected.

1.4 Summary

This concludes the part on the synthesis of doped compositions of strontium titanate using the supercritical solvothermal method. To summarize, by combining structural characterization with XRD, TEM and Raman with elemental quantification and analysis using ICP-OES and EDS-TEM, we provided a complete study of the newly synthesized compounds.

- We establish a trend between the evolution of the lattice parameters and the successful substitution of the dopants elements and which site is substituted. The analysis gives a correct quantification of the dopant ant attests the strong imbalance between the A-site and the B-site.
- Combining Raman results and mostly ICP results show a possibility of an insertion phenomenon when the substituted sites are A due to the presence of many vacancy sites. However, the maximum filled sites so the closest ratio of A/B to one is 0.85 meaning that the stoichiometry of the compound is still imbalanced.
- Finally, we demonstrate the flexibility of the synthesis since it is easily adapted by mainly solubilizing the precursors in the right media. The ways to synthesize multiple types of compounds are either the substitution rate, the type of element and the possibility to produce codoped compounds.

2. Shaping of $SrTiO_3$ Powders

This part will present a first processing of the synthesized strontium titanate with doped and undoped compounds. A first part is detailed on the sintering of the nanopowders into dense pellets, the determination of the density and the post annealing treatment. Once the pellet reaches the right features, its resistivity is characterized using the four-probes method. From there we can verify and characterize the conductivity of the ceramic and attest the effect of substituting the material with n and p dopants.

2.1 Shaping of strontium titanate nanoparticles into dense pellets

2.1.1 Materials for pelletization

The powders used included three undoped strontium titanate variants and doped strontium titanate compositions with 5 at.% and 10 at.% of niobium, 1 at.% and 5 at.% of neodymium, 10 at.% of yttrium, 10 at% of iron, and a codoped compound containing 5 at.% neodymium and niobium. Additionally, two pellets composed of commercial strontium titanate sourced from Sigma Aldrich were used as reference. The characteristic of the powder has been described in the previous part.

2.1.2 Methodology

The powder underwent sintering *via* Spark Plasma Sintering to yield dense pellets. Approximately 350 mg of nanoparticles of varying compositions were loaded into a cylindrical carbon die with an inner diameter of 8 mm, without the use of any binder. To ensure optimal conductivity and homogeneous heating of the material, the powder was covered by a graphite foil. The entire sintering process was performed under vacuum conditions, fixing a sintering temperature of 1000 °C for a duration of 5 min, along with a uniaxial pressure of 100 MPa. One of the main concerns with this method is the atmosphere chosen to achieve sintering. Reported work at ICMCB showed that the processing of oxide-based nanoparticles containing titanium impacts the material defects due to the working atmosphere. It has been determined that the sintering under vacuum meaning low oxygen partial pressure atmosphere leads to the partial reduction of Ti^{4+} cations into Ti^{3+} resulting from the creation of oxygen vacancies and induces electronic conductivity in the sample. In order to correct that, the pellets, usually black after the treatment, were reoxidized thanks to a thermal annealing performed under air at 800 °C for 24 h. We can see the direct effect of the thermal treatment, the color of the pellet going from black to light grey. Also, one of the concerns was the possible occurrence of the secondary TiO_2 phase or other phases depending on which kinds of dopant were used.

2.2 Pellet characterization

2.2.1 Structural characterization of the pellet

The objective of this part is to see the impact of the sintering on the material. As a reminder from Chapter 3, the main limit of the undoped material is its thermal stability leading to the development of a secondary phase of titanium dioxide as the temperature increases. This feature was explained by combining TEM *in-situ* in temperature where two populations were identified with different sizes. The population with smaller grains tends to sinter itself with other particles leading to the formation of the supposed TiO_2 phase. Combined with EDS characterization, this population showed an imbalance between strontium and titanium that could be responsible for TiO_2 formation after the annealing treatment. Since SPS sintering imply higher temperature (1000°C) compared to screen-printing process (800°C), we have to verify that the optimization brought to the cation balance allow the material to hold higher temperature and limiting the secondary phase formation.

The goal of these characterizations is to verify the optimization brought and mentioned in Chapter 3 which are supposed to limit this formation of unwanted phases that could limit the possibility to characterize the material itself due to pollution.

Figure 4.13 presents the PXRD patterns of different undoped strontium titanate synthesized using the new optimized reactor. The PXRD patterns of each powder are given after the SPS treatment described previously. The Table on the left provides structural information such as the lattice parameter and crystallite size but most importantly the wt.% of the secondary phase

	Black	Red	Blue	Purple
Lattice (Å)	3,906	3,908	3,908	3,912
C.S. (nm)	42	37	38	35
wt% TiO_2	1,24	2,58	2,97	0

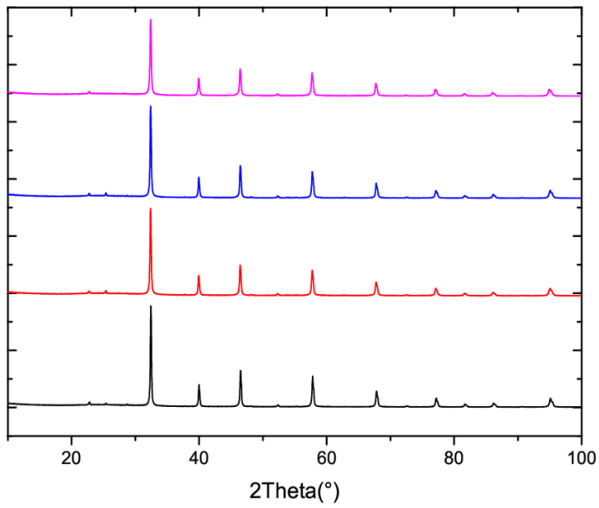

Figure 4.13: PXRD patterns of the different samples of strontium titanate after SPS treatment (right). Table of Characteristic of each powder (left)

From this result, we can conclude that the formation of the secondary phase goes from 0 to 3 wt.% for SPS sintered samples which is much less compared to standard sintering where the wt.% of TiO_2 could reach 16 wt.% which is too much for electronic conductivity measurements. Moreover, from the lattice parameter, we can deduce that the stoichiometry of the material is affected since the lattice parameter decreases compared to the reference value. However, despite a slight increase of the crystallite size, the nanosize is kept which was the main reason why this SPS process was chosen.

Another concern that was highlighted by this experiment is the risk to lose the totality of the dopant since as presented previously the stoichiometry of the material is modified. Some doped pellet indeed shows the formation of new phases such a pyrochlore $Y_2Ti_2O_7$ for yttrium-doped strontium titanate or ilmenite $FeTiO_3$ for iron-doped strontium titanate. However, the atomic percent deduced from Rietveld refinement did not exceed more than 5% wt. meaning the pellet was mainly constituted of strontium titanate.

To complete the study, three powder samples have been treated thermally at 1000 °C for 1 hour to observe the effect on the structure. The results are described on ***Figure 4.14*** where PXRD acquisitions were performed on the corresponding powders. The black pattern corresponds to the undoped strontium titanate, the blue pattern corresponds to strontium titanate doped with neodymium at 5 at.% and the red one corresponds to strontium titanate doped with praseodymium 10 at.%. A focus on the peak (1 1 0) is made in order to observe the shift. A Table at the bottom gives different structural characteristics of the powder.

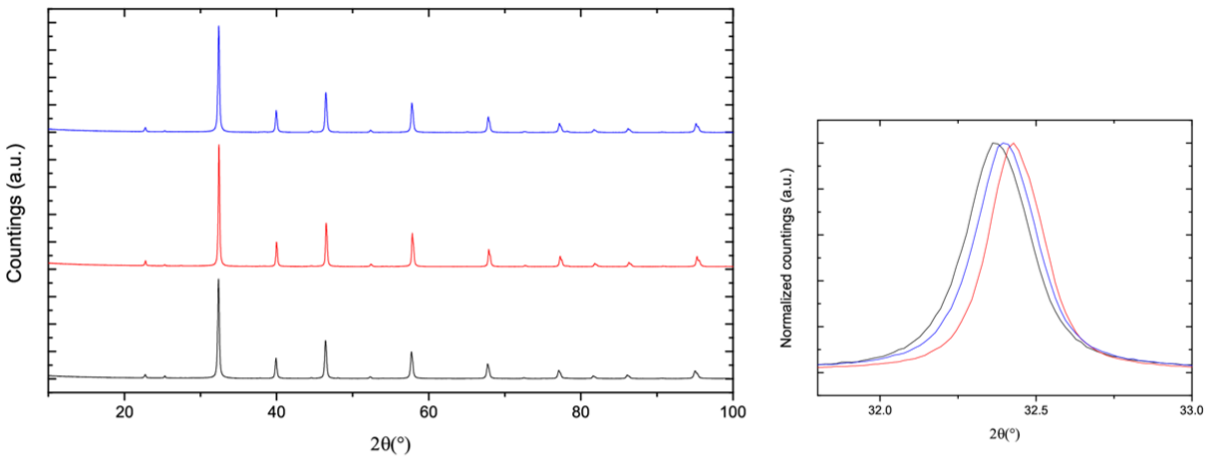

Samples	wt% $SrTiO_3$	wt% TiO_2	mol% $SrTiO_3$	mol% TiO_2	a parameter (Å)	Crystallites size (nm)
BLACK	98,09	1,91	96%	4%	3,909	32
RED	99,13	0,87	98%	2%	3,900	42
BLUE	99,26	0,74	98%	2%	3,905	35

Figure 4.14: PXRD patterns with a focus on the (1 1 0) peak and structural features of the different compositions determined by Rietveld refinement

The XRD patterns and mostly the shift toward higher angle shows the impact of the thermal treatment on the stoichiometry of the compound: TiO_2 is detected but the amount is very low (even lower for the doped compositions). The crystallite size increases as expected in this temperature range. More importantly, no secondary phase containing the dopant was detected for those compositions. Moreover, the lattice parameter change caused by doping remains stable even after thermal treatment. This means that the main difference between the two doped compounds and the undoped one is the presence of those smaller doping elements still inside the lattice.

To conclude on this study, we evidenced here that the SPS treatment would not affect the doping element inside the strontium titanate lattice since the lattice parameter reference of the undoped is lower compared to the rare-earth doped compound.

2.2.2 Determination of the pellet density

Subsequently, the resulting pellets were subjected to density measurements using the Archimedes method (cf Chapter 2, 3.2.3. Density measurement). The compacity of each pellet is larger than 96%, and are fitting with the features needed for the four-probes measurements. The selected compositions are gathered in ***Table 4.4***.

Table 4.4: Studied compositions of doped strontium titanate with the type of donor, the theoretical substitution rate and the site substituted

Element(s)	Donor type	Substitution rate (Theoric)	Site substitued
Nd^{3+}, Nb^{5+}	n	5% at. each	A and B
Nd^{3+}	n	5% at.	A
Nb^{5+}	n	10% at.	B
Nb^{5+}	n	5% at.	B
Y^{3+}	n	10% at.	A
Fe^{3+}	p	10% at.	B

The following part details the resistivity measurements results.

2.3 Electronic properties of doped $SrTiO_3$

Due to its high theoretical band gap value, $SrTiO_3$ is classified as a semiconductor with high resistivity. It is anticipated that the ceramics fabricated using commercial strontium titanate will demonstrate a substantial resistivity, expected to fall within the range of approximately 10^5 to 10^8 Ω·cm. A difference of colors can be observed between the pellet sintered using “supercritical” nanoparticle and “commercial” nanoparticles. The supercritical one is colored in grey and the commercial one is white

after the sintering treatment. The previous ICP-OES measurements showed that the main difference between those two compositions is the presence of strontium vacancies for the "supercritical" powder meaning that it has an impact on the material defect chemistry. The main result is the coloration arising from the titanium reduction.

This reduction led to the formation of oxygen vacancies inducing an electronic conductivity. We can predict that the electronic conductivity of "supercritical" ceramics will be higher than the commercial ones.

2.3.1 Electronic properties of commercial $SrTiO_3$

Figure 4.15 plots the resistivity measurements performed by four-probes method on the ceramic prepared with the commercial strontium titanate powder. The data are plotted as an Arrhenius law equation type, as described in Chapter 2 (cf 3.2.4. Electronic conductivity measurements). The y axis represents log(σ) while the x axis is 1000/T and a third axis at top translates the value of the x axis in the temperature in Kelvin.

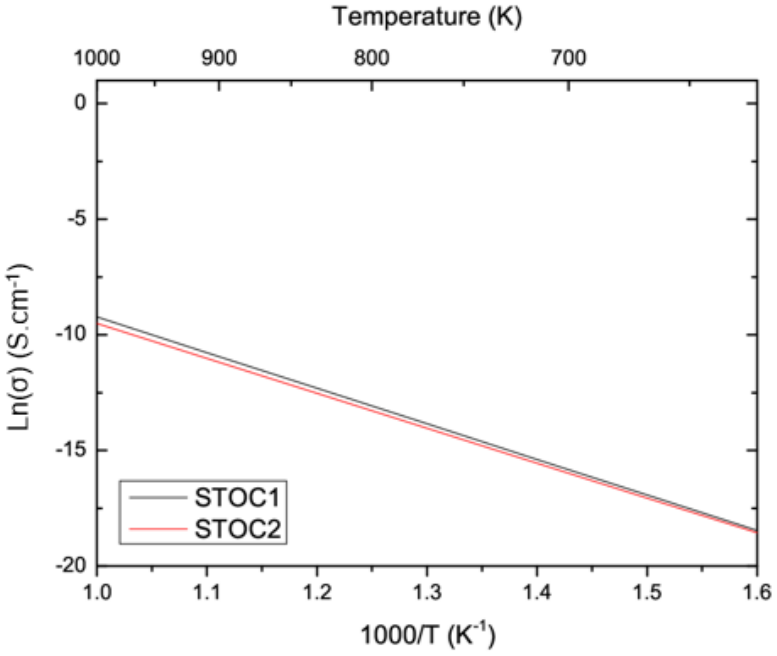

Figure 4.15: Electronic conductivity expressed as an Arrhenius law of SPS sintered pellet from commercial nanopowder of strontium titanate

STOC1 and STOC2 correspond to the ceramics prepared with commercial strontium titanate nanoparticles (SIGMA) and measured under argon (STOC1) and air (STOC2), respectively. As it can be observed in ***Figure 4.15***, the conductivity increases as the temperature increases, which is typical of semiconductor behavior. These ceramics exhibit a conductivity from ln(σ)=-18.47 ($\sigma = 9.51\times10^{-9}$ S·cm^{-1}) at 352 °C to ln(σ)=-9.23 ($\sigma = 9.81\times10^{-5}$ S·cm^{-1}) at 727 °C. We can also observe that the atmosphere has

no noticeable impact on the measurements. Those two .ill serve as the reference for the next measurements. Thanks to their electronic characteristics, we can determine the impact of the unique features exhibited by the nanopowder of strontium titanate synthesized with the new supercritical solvothermal method.

2.3.2 Electronic properties of $SrTiO_3$ synthesized by the supercritical solvothermal method

We performed the four-probes on different samples of strontium titanate named STO1 and STO2 shown in ***Figure 4.16***. They have the same structural characteristics as well as a small pollution of TiO_2 (2 at.%). Both samples have been measured under air and argon and the value of their resistivity is reported from 352 °C to 727 °C.

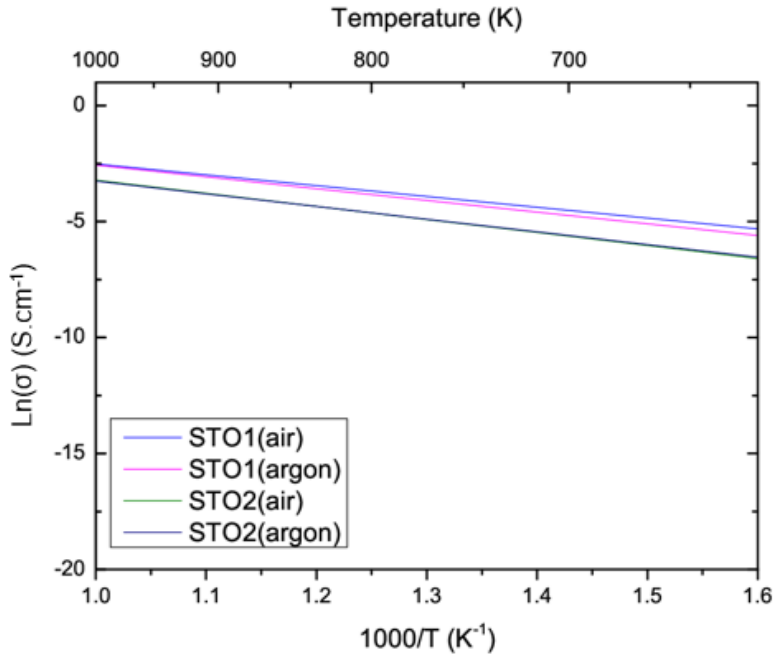

Figure 4.16: Electronic conductivity expressed as an Arrhenius law performed on ceramics prepared from nanopowders of strontium titanate

This second measurement performed on STO1, STO2 from powder synthesized using the supercritical solvothermal evidenced a higher conductivity compared to the ceramics made with the commercial powder, i.e. ln(σ)=-2.51 (σ =0.08 S·cm^{-1}) at 727 °C for STO1 and ln(σ)=-3.21 (σ =0.04 S·cm^{-1}) for STO2. The powder named STO1 exhibits a slightly higher conductivity than STO2 but the difference is not relevant and could be explained by the measurement resolution. Again, the impact between an oxidized and inert atmosphere is none and it is even more emphasized with the measurement of STO2 which shows no change at all. However, if we compare it to the electronic properties of the commercial strontium titanate, we see a drastic increase of the conductivity. This shows the significant impact of the synthesis method which is exclusive to the supercritical solvothermal method.

2.3.3 Electronic properties of $SrTiO_3$ substituted with dopants

The third part is dedicated to the electronic characterization of the doped strontium titanates synthesized by the supercritical solvothermal method. The compositions with their theoretical doping rate are STO: Nb 5%, STO: Nb 10%, STO: Y 10%, STO: Fe 10%, STO: Nd,Nb 5% and STO: Nd 5%. ***Figure 4.17*** presents the same feature as ***Figure 4.15*** and ***Figure 4.16***. The characterized ceramics are made with doped/substituted compositions of strontium titanate described earlier in the first part of this chapter. Their electronic conductivity has been characterized from 352 °C to 727 °C and the samples were measured under Ar. However, as shown previously the atmosphere does not impact the electronic properties of the samples.

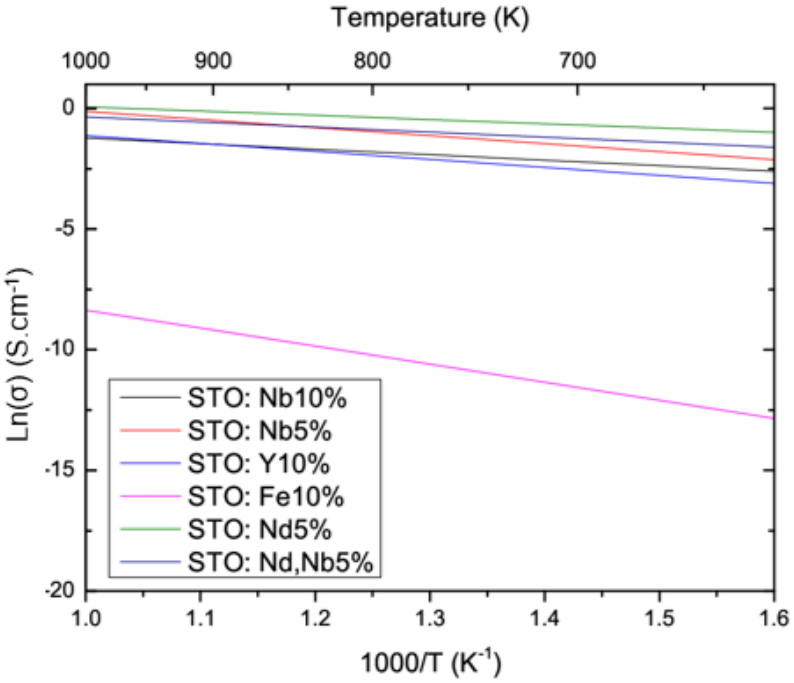

Figure 4.17: Electronic conductivity expressed as an Arrhenius law measured on ceramics prepared from powders synthesized by supercritical solvothermal method

Globally, the doped ceramics exhibited a higher conductivity in comparison with the undoped ones. The STO: Nb10% and STO: Y10% has a conductivity of σ =0.29 $S{\cdot}cm^{-1}$ and σ =0.33 $S{\cdot}cm^{-1}$ respectively at 727 °C. Higher conductivity is found for STO: Nb 5%: ln(σ) =-0.11 (σ =0.89 $S{\cdot}cm^{-1}$) at 727 °C and the codoped compound with STO: Nd,Nb 5%.with ln(σ)=-0.35 (σ =0.70 $S{\cdot}cm^{-1}$) at 727 °C. The highest value is measured for the composition STO: Nd 5% with ln(σ)= 0.07 (σ =1.07 $S{\cdot}cm^{-1}$) at 727 °C. The lowest conductivity is measured in STO: Fe 10% where the conductivity is even lower than the one of undoped strontium titanate but still higher than the commercial one with ln(σ) =-8.36 (σ =2.34×10^{-4} $S{\cdot}cm^{-1}$) at 727 °C. In this part, we show a decent upgrade of the electronic properties thanks to the

insertion/substitution phenomenon for n-dopant in opposition with p-dopant or iron substitution where the conductivity was greatly decreased.

We can compare those values to those from the literature mentioned at the beginning (1.1 Selection of n and p doping elements of $SrTiO_3$). Regarding the composition with yttrium, the conductivity is almost one hundred times lower than the reference value from Hui *et al.* and Zhao *et al.* (~60 $S \cdot cm^{-1}$ at 800 °C). Another change is the evolution of the conductivity with temperature. In the quoted reference the electronic conductivity decreases as the temperature increases according to a metallic behavior which is not the case for our compositions. Both of these papers synthesized the strontium titanate using the solid-state reaction. However, if we compare with Singh *et al.* the electronic conductivity of strontium titanate doped with yttrium (10 at.%) plotted log σ·T *vs*. 1000/T, our value is higher. It is also important to mention that the synthesis method used was citrate nitrate auto combustion. Regarding the niobium doping, in the case of Bennow *et al.*, the materials were prepared using glycine nitrate synthesis and the compound had a A-sites deficiency of 6 at.% and a substitution rate of 10 at.% of niobium element in B-sites leads to conductivity one thousand time higher compared to our result. This is also explained by the metallic behavior that was also obtain by Zhao *et al.* with yttrium doped strontium titanate. Karczewski *et al.* obtained a compound more conductive with 2 at.% of niobium by solid-state reaction and highlighted the impact of the annealing treatment where the electronic conductivity behavior is semiconductor for annealing temperature at 1200 °C and metallic for 1300 °C and 1400 °C under reductive atmosphere. The compound annealed at 1200 °C with ~2 $S \cdot cm^{-1}$ at 727 °C exhibit a conductivity value almost in the same range as our pellets. Also, a small amount of secondary phase of $Sr_2Nb_2O_7$ was detected. It is also noticeable in our measurement that substituting with more niobium content does not increase the electronic conductivity and suggests the opposite based on our results. In the case of a p-doping with iron, the value is lower than what is found in the literature, however we confirm the trend that iron doping is not as efficient as niobium or yttrium for the electronic conductivity enhancement. The neodymium-doped compound exhibits the highest conductivity among the studied samples, yet its value remains significantly lower than that reported by Lin *et al.* In their study, the compound demonstrated metallic behavior, a characteristic consistently observed in other studies when n-doping is successfully achieved.

This study concludes that supercritical nanoparticles of strontium titanate shaped into dense pellet by SPS demonstrated relatively high conductivity compared to the reference material one, though still lower than values reported in the literature. These discrepancies can largely be attributed to experimental parameters, such as the use of a reducing atmosphere, while the novelty here is the use of supercritical doped nanoparticles of strontium titanate for the first time. Notably, the nanoparticles

maintained their semiconducting behavior as the temperature increases. Further research is required to fully elucidate the intrinsic mechanisms underlying these observations.

2.3.4 Summary

To summarize this part, we presented the results on the conductivity determined from four probes measurements on three types of strontium titanate. Each type presented its own electronic characteristics such as the synthesis method, the structure properties and the stoichiometry.

As shown by EDS, the high temperature can impact the composition of the strontium titanate nanoparticles and leads to the creation of TiO_2 and even other phases depending on the element doped. The sintering by SPS under high temperature and pressure leads to the creation of impurities phases. The STO1, STO2 and STO3 shows the presence of 2 mol.% of TiO_2, while STO: Y 10% shows the presence of 2.5 mol.% of pyrochlore $Y_2Ti_2O_7$ and STO: Fe 10% shows a presence of 3 mol.% of Ilmenite. Nonetheless the impurities amount is low (below under 5 mol.%), and should not have impact on the four probes measurements.

Figure 4.18 sums-up the four-probes dc conductivity measurements performed on dense ceramics (sintered by SPS in vacuum and annealed at 800 °C under air) between 352 °C to 727 °C in air and argon atmosphere (depending on the sample) of the samples from the highest to the lowest one.

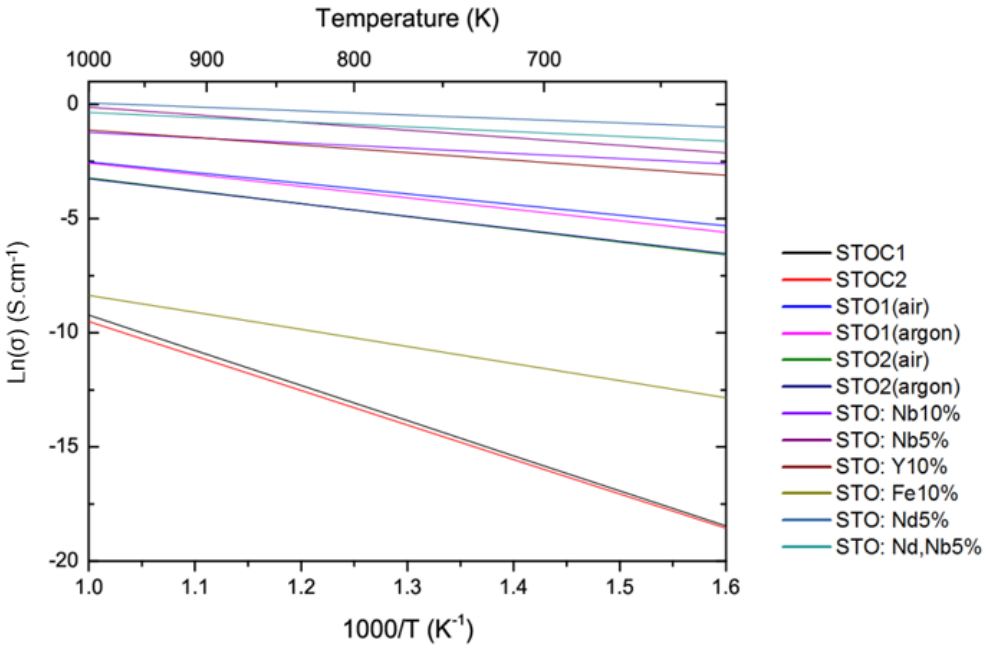

Figure 4.18: Electronic conductivity expressed as an Arrhenius law measured on ceramics prepared from nanopowders synthesized by supercritical solvothermal method for all the studied strontium titanate (doped / undoped)

A major difference between the electronic behavior of the dense pellets shaped from the commercial and the powders produced by supercritical solvothermal synthesis is the slope of the curve referring to activation energy value where the one of commercial strontium titanate is larger than the "supercritical" strontium titanate one. It means that the spacing between the conduction band and the valence band is larger for the reference compared to the synthesized nanopowder.

The ***Table 4.5*** summarized all the energy activation value found for each composition.

Table 4.5: Activation energy of the conductivity for each sample of strontium titanate.

Composition	σ at 1000K in $S.cm^{-1}$	Activation Energy (E_A) in eV
STOC1	9.81×10^{-5}	1.3
STOC2	7.42×10^{-5}	1.2
STO1(air)	0.08	0.4
STO1(argon)	0.05	0.4
STO2(air)	0.04	0.5
STO2(argon)	0.04	0.5
STO: Nb10%	0.29	0.2
STO: Nb5%	0.89	0.3
STO: Y10%	0.33	0.3
STO: Fe10%	2.34×10^{-4}	0.6
STO: Nd5%	1.07	0.1
STO: Nd5%Nb5%	0.70	0.2

As expected, the commercial strontium titanate has the highest E_A due to its chemical composition. This serves as a reference. The undoped composition of strontium titanate has less than two times the activation energy of the commercial strontium titanate. This was expected from the beginning due to the color of the ceramic. The commercial powder presented a white color after sintering and the synthesized powder presented a light gray color after sintering treatment and reoxidation. This also explains why its conductivity is larger since the band gap energy is reduced. To conclude, doping had the effect of enhancing conductivity by decreasing the activation energy. However, this was only observed for n-dopants, the p-dopant iron led to a drastic decrease of the electronic conductivity.

3. Shaping Synthesized $SrTiO_3$ Into Electrodes

This third part presents another type of shaping of the strontium titanate based-nanopowders. As mentioned in this work, screen-printing was the favored process to shape the anodes. The powders synthesized by the supercritical solvothermal synthesis were used. The screen-print paste was

formulated and the screen-printing apparatus was described in Chapter 2 (cf 3.1.2 Screen printing). The supported cells used were commercial Ni-YSZ/YSZ half-cell with a coating of GDC layer and YSZ cells with a GDC coating.

The following parts gather the structural characterizations using the different described cells. XRD acquisitions are presented as well as scanning electron microscopy to characterize the morphology of the deposition after screen-printing processing

3.1 Structure evolution of the developed electrodes

The freshly manufactured cell was characterized by XRD to analyze the different phases and confirm the general structure of the composite cell. ***Figure 4.19*** presents the XRD patterns recorded on the cell before and after deposition. The black curve represents the pattern of the composite cell including both yttria stabilized zirconia (YSZ) and gadolinium doped ceria (GDC) compounds prior to the deposition of strontium titanate nanoparticles. The red pattern represents the cell once the screen-printing process has been completed. The XRD patterns have been indexed with the available database and the JCPDS files are referenced.

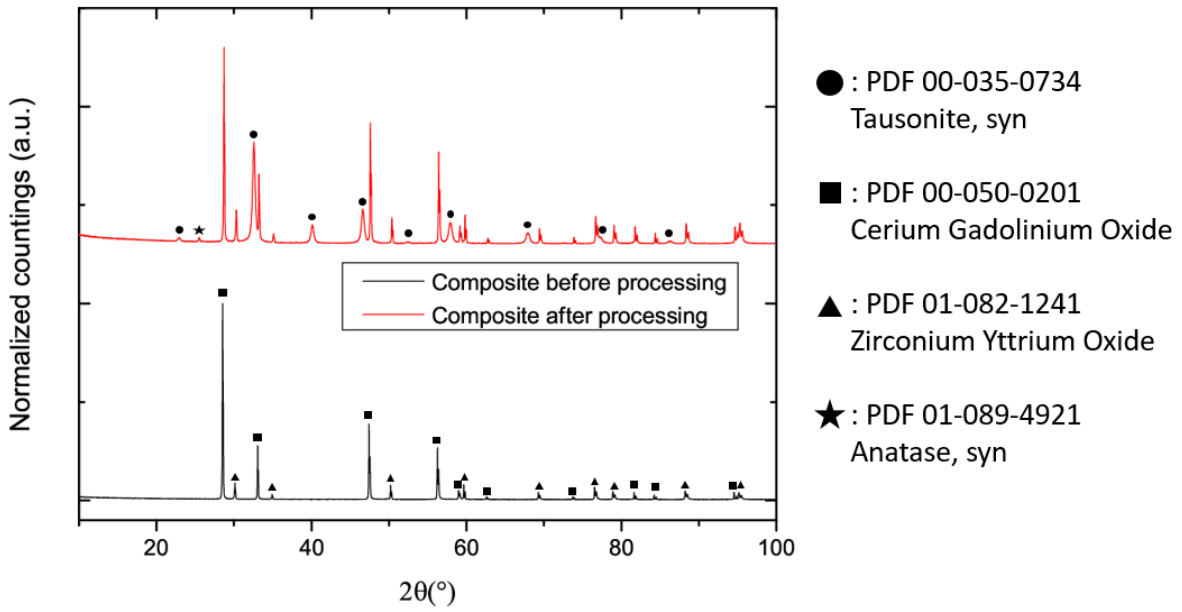

Figure 4.19: XRD patterns recorded on cells before screen-printing formulation and after. All the diffraction peaks of the composite material have been indexed using the available database

Based on the XRD process, we can observe that the support cell does not get impacted by the screen-printing process involving a thermal treatment at 800 °C at the end to harden mechanically the film. The deposition of strontium titanate was achieved and the phase is successfully indexed on the support. The peaks of strontium titanate are easily recognizable compared to the other ones detected

since they are more wide meaning that the crystallite size of strontium titanate is smaller. No additional phases are detected on the signal meaning that no oxides reacted with each other. However, a titanium dioxide phase is detected which is specific to the sample since the material has been thermally treated. Indeed, with the current process developed, we manage to produce a strontium titanate nanopowder that release no more than 5% at. of titanium dioxide at high temperature.

3.2 $SrTiO_3$ deposit characteristics

One of the purposes of the screen-printing protocol was the homogeneous deposition with a controlled thickness of the material. This following part presents a scanning electron microscopy (SEM) side picture of the prepared electrode. A back scattered electron picture is presented as well. The purpose of this characterization is to verify if the thickness, based on the ink-formulation, is correctly adjusted between 20 and 30 µm.

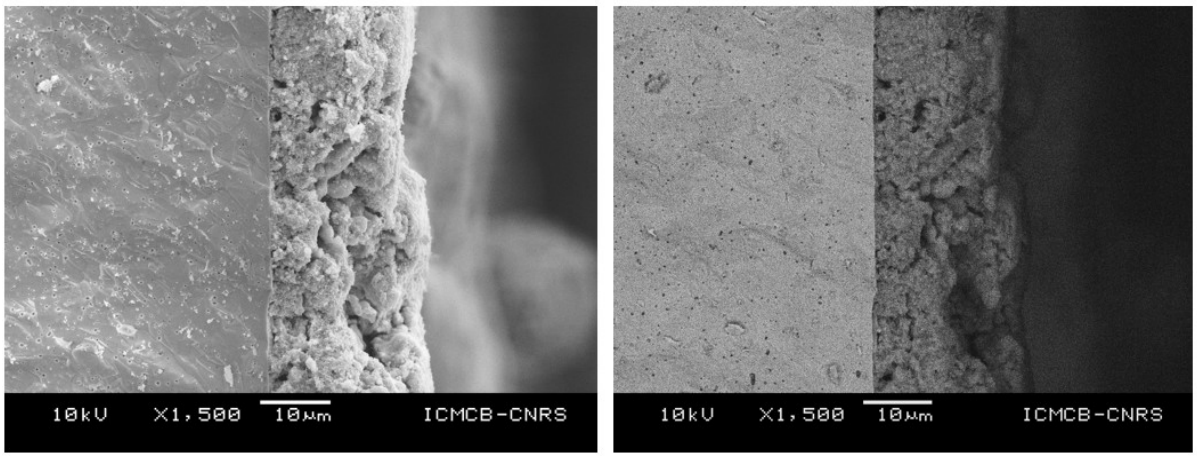

Figure 4.20: SEM (left) and BSE (right) on YSZ+STO substrate after thermal treatment at 800 °C

Figure 4.20 shows the picture of the support where strontium titanate-based nanopowder has been deposited. On the left part, we can see the SEM picture of the deposit with the yttria stabilized zirconia on the left side and strontium titanate deposit on the right. The two morphologies are clearly defined as the YSZ is very dense compared to the STO layer paste. No visible signs of reaction are observed at the electrolyte/anode interface meaning that both materials are stable at this temperature. On the right part, the BSE micrograph shows the two contrasts between the substrate and the deposit. YSZ being made with heavier elements, it appears more intensely compared to the strontium titanate deposit. The separation between the two morphologies is very clear and no other contrast signal is detected assuring that no other phase exists. Thanks to the clear delimitation and scale, the total thickness value is between 20 and 30 µm.

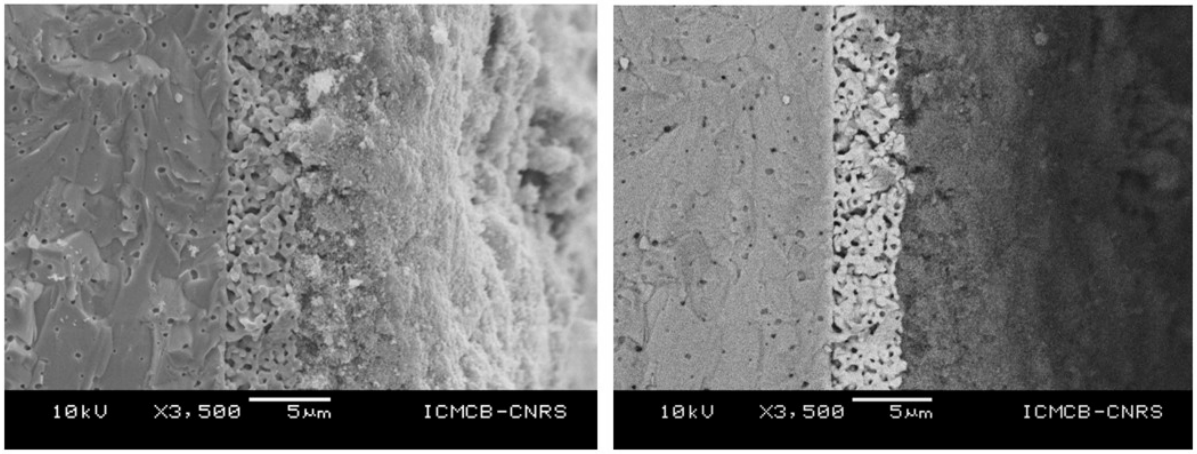

Figure 4.21: SEM (left) and BSE (right) on YSZ+GDC+STO substrate after thermal treatment at 800 °C

Figure 4.21 shows the same type of pictures as the previous Figure, except the support used, which is YSZ covered with gadolinium doped ceria (GDC) and strontium titanate. The thickness of strontium titanate has been reduced which is perhaps linked to the deposition on a porous surface. Nonetheless, the total thickness here corresponds to the deposition of GDC and the deposition of STO which is close to the required value.

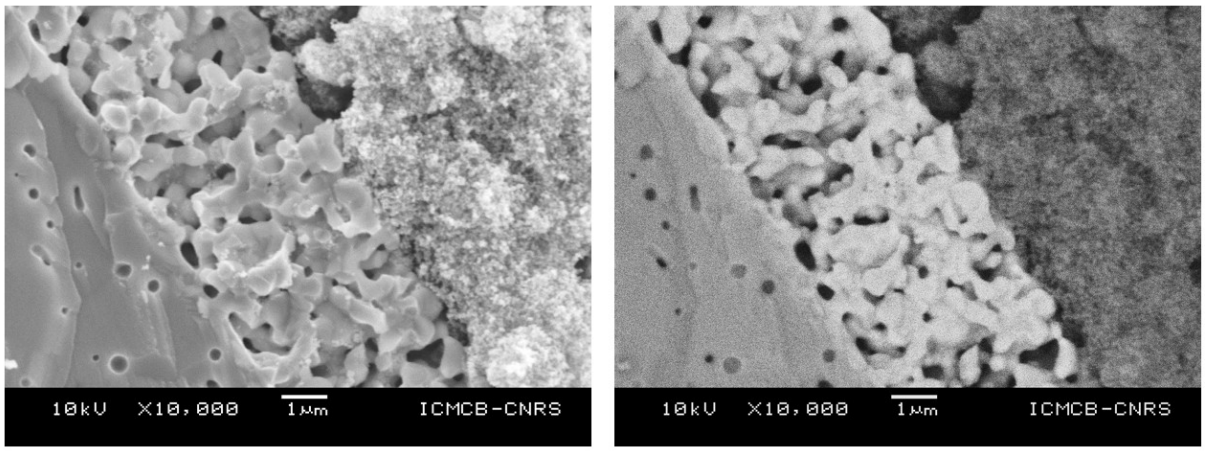

Figure 4.22: SEM (left) and BSE (right) on YSZ+GDC+STO substrate after thermal treatment at 800 °C with a bigger zoom

We can differentiate quite easily the different morphology of the material going from the left to right, the dense YSZ in light grey, the fibrous and porous morphology corresponding to the GDC and finally the strontium titanate with this agglomerated grain structure (***Figure 4.22***).

3.3 Summary

In this part, we presented the whole processing of strontium titanate based-nanopowders as electrodes. We successfully managed to produce strontium titanate paste that has been deposited on

the mentioned cells type. XRD and SEM showed the structural and morphology of the composite material.

- The microstructure of the composite cell is not impacted by the whole procedure since there is no new peaks to index on XRD patterns except a small amount of TiO_2, its origin is known and featured by the strontium titanate.
- We have characterized the total thickness and the morphology of the different materials. Their uniformity is as required.

The electrodes produced with this method were sent to the partners of the project to be electrochemically tested in the configuration of water EHT at Ni/YSZ cathode and OCM at the newly developed anode. This implies electrocatalytic tests of oxidative coupling of methane under polarization.

Conclusion of Chapter 4

This chapter details a method to identify the doping site of the strontium titanate in a perovskite structure and a method to synthesize different compositions of doped strontium titanate using the supercritical solvothermal synthesis in continuous flow in a water/ethanol mixture.

The structure of the nanopowders was characterized by XRD and Raman spectroscopy and the impacts of the doping were attested. The ICP and TEM EDS quantified the different elements composing the "supercritical" strontium titanate. It confirmed a homogeneous doping of the different elements. Nonetheless the presence of a unique imbalance between the strontium and titanium was observed.

A method to elaborate a dense ceramics of strontium titanate using spark plasma sintering followed by a reoxidation treatment was used. The Archimedes method was involved to determine the compacity of the ceramics. All the pellets exhibited a satisfactory density that allowed further physical characterizations.

The resistivity measurement by four-probes method showed that the "supercritical" strontium titanate has higher conductivity than the "commercial" strontium titanate. The n-type substituted composition (Y, Nd, Nb) has the highest conductivity. In comparison with the "commercial" strontium titanate, we managed to synthesize a material that is 1000 times more conductive than the original one. Moreover, this exclusive high A-site vacant oxide could only be obtained using the supercritical method.

A last part presented the shaping of the strontium titanate-based nanopowder into electrodes and more precisely within the framework of the project into an anode cell for high temperature electrolysis unit. The first step was the ink formulation with the nanoparticles and the screen-printing process were adapted to realize a deposition of the strontium titanate based-nanoparticles on the different substrates.

This chapter mainly focused on the exploitation of this new supercritical solvothermal method described in Chapter 3 to produce exclusive compositions of strontium titanate. Moreover, its processing to determine electronic properties and the production of an electrode was discussed. The following step would be to determine the ionic conductivity of the material.

General Conclusion

The increasing impact of greenhouse gases emissions from human activities and production has shifted research topics more and more toward innovative materials for renewable energy development. The purpose of the ANR project was to develop a unit of high temperature electrolysis to promote the power to gas (P2G) to power to chemical system. Based on the state of the art, the bottleneck need was determined as materials that exhibit mixed electronic ionic conductivity and catalytic activity to perform the oxidative coupling of methane in order to produce ethylene. To fulfill that goal, strontium titanate doped with rare earth elements and metal transition was the chosen material for this study. However, these specific mixed conductivity and catalytic activities require highly crystallized nanoparticles. It was then decided to move toward continuous flow synthesis under supercritical fluid conditions to achieve this crystalline nanosized materials. Also, the synthesis technic enabled a large production scale which was capital for the shaping of the nanoparticle in the framework of producing an electrode cell.

Throughout this research, the potential of supercritical fluid technology to address these challenges was demonstrated on the synthesis of strontium titanate undoped and doped and their elaboration for deposit and pellets. The impact of doping was attested with a characterization of the electronic conductivity.

Firstly, the synthesis and characterization of high-quality $SrTiO_3$ nanoparticles in supercritical fluids. Initial efforts focused on the formation of monocrystalline $SrTiO_3$ nanoparticles in supercritical fluids. We demonstrated for the first time in the state of the art of supercritical fluid synthesis the use of acetylacetonate precursors to produce nanoparticles of strontium titanate. Using standard *ex situ* characterization techniques (XRD, FTIR, Raman spectroscopy, HRTEM coupled with EDS spectroscopy, ICP-OES) we were able to thoroughly characterize the nanoparticle properties. PXRD and HRTEM confirmed their monocrystallinity, whereas EDS and ICP-OES confirmed an imbalance ratio between strontium and titanium that could be tuned by changing parameters such as the precursor type or the heating system.

Furthermore, we combined XRD and HRTEM with advanced *in situ* characterization to monitor in real time the behavior of strontium titanate nanoparticles as a function of the temperature. We managed to tune the A/B ratio between the strontium and titanium element and we observed that the non-desired TiO_2 formation during synthesis decreases as the A/B ratio tends toward the desired equilibrium value.

The process was then improved with the synthesis of doped composition of strontium titanate using various of elements. Doping on A and B sites was achieved and demonstrated through structural studies for the first time using supercritical fluids synthesis in continuous flow.

Secondly, the shaping and electrode cells production from $SrTiO_3$ nanoparticles. Once the synthesis work confirmed a production of strontium titanate material suitable for the incoming working environment such as high temperature, the nanoparticles were shaped into an ink formulation and molded in dense pellets. The ink formulation enabled a successful production of half-cell YSZ and complete-cell Ni-YSZ with a deposition thickness corresponding to 20 µm. This was achieved using the screen-printing process and to formulate terpineol-based slurry.

The cells were then sent to partner laboratories for further characterization. The production of dense pellets was achieved using spark-plasma sintering (SPS) with a satisfactory density (more than 96%) using nanoparticles of strontium titanate. The use of this technic contributed to a limitation on the crystallite size growth and optimized the size-effect of the material for the following advanced characterization.

Thirdly, the structure and doping effect investigation on synthesized $SrTiO_3$ compound. The process used for the acetylacetonate-based synthesis was adapted in order to produce extrinsic strontium titanate semiconductor nanoparticles. Acetylacetonate dopants were used since their compatibility with the supercritical fluids technology was previously demonstrated. Different rates of atomic substitution going from 1% to 10% with large panel of elements were achieved. We successfully demonstrated the possibility to insert/substitute n and p dopant from transition metals to rare-earth elements. The aimed substitution site was based on the Goldschmidt factor approach and verified by XRD analysis and EDS spectroscopy.

The compositions presented are the first of their kind identified among the supercritical fluids synthesis field. The previous SPS treatment enabled to produce samples that could be used for advanced characterization of the electronic properties of the intrinsic and extrinsic strontium titanate. By comparison with commercial strontium titanate material, the one we produced through supercritical synthesis in continuous flow is already presenting a higher conductivity. This increase was associated with the imbalanced strontium content that led to the creation of oxygen vacancies through electroneutrality equilibrium. The n-doped strontium titanate exhibited the best electronic conductivity reaching a value one-thousand-time superior to bare strontium titanate proving again the successful production of extrinsic strontium titanate semi-conductor.

The substitution involved introducing *n*-type donor atoms, specifically by replacing titanium with transition metals like niobium, or by replacing strontium with rare earth elements like neodymium. However, the p-doped strontium titanate exhibited an electronic conductivity lower than the intrinsic strontium titanate produced by supercritical fluid in continuous flow synthesis. Additionally, changes in the atmosphere between inert and oxidative conditions had no effect on the evolution of the electronic properties, nor did it impact the results from multiple measurement cycles.

Furthermore, adding another n-dopant did not increase the electronic conductivity. The activation energy of each composition was determined from the electronic measurement. One observation is that the strontium titanate compositions, produced by supercritical continuous flow synthesis, have their activation energy decreased compared to commercial strontium ones, highlighting an exclusive property obtained through this synthesis method.

To summarize, supercritical fluids synthesis in continuous flow was used to produce highly crystalline nanoparticles of undoped/doped strontium titanate using acetylacetonate precursors which are more accessible compared to isopropoxide precursors. We provided for the first time in the state of the art of nanoparticles synthesis under supercritical method, the electronic properties of doped strontium titanate. The nanosize crystallites ensured an optimized catalytic action thanks to increase in specific surface area. The high crystallinity also contributed to obtain the best electronic properties from the material. This work offers a promising new path for the synthesis of strontium titanate nanomaterials and production of extrinsic strontium titanate. Furthermore, this synthesis method could potentially be extended to perovskite synthesis, as long as the precursor is available. We also showed the adaptability of the nanoparticles synthesized with the possibility to prepare ink-formulation for electrode cell production by screen-printing process.

Perspectives

The perspective of this work is mainly based on the synthesis opportunity. Regarding the aimed properties for the project, the electronic conductivity has been confirmed by producing and characterizing an extrinsic strontium titanate semiconductor. The ionic conductivity of the material, to this date, has not been characterized yet, so no value could be provided and thus confirming the material being a mixed ionic electronic conductor. However, we made the assumption that the presence of oxygen vacancies (due to the cations content imbalance) should positively contribute to the optimization of the ionic conductivity. The intrinsic and extrinsic strontium titanate powders have been sent to partner laboratories for characterization thanks to an innovative set-up that enable powder measurement directly. Concerning the catalysis for the oxidative coupling of methane, the powders were sent to partners of the project for the measurement of their catalytic properties. The measured values were low compared to the value of the literature. In 2019, Lim *et al.* demonstrated the optimal doped strontium titanate composition, however no structural study was provided regarding the insertion of the element on the claimed site. Also, the strontium titanate material was synthesized using another method than the supercritical fluid technics. This highlights the main clue for the optimization of the OCM catalytic activity. The surface chemistry of the material has to be taken into account since it is favored by electrophilic lattice and strontium enrichment. Since the material presents an imbalance of strontium content, this could explain the drastic decrease of the catalytic properties for the OCM. This work presented different clues to optimize the A-site cations content by changing the type of precursor on the chemistry side or optimizing the temperature of the reactor on the engineering side. The synthesis of perovskite with a balanced composition, using supercritical fluids technology has been previously achieved by Ono *et al.* showing the possibility to obtain it with calcium strontium titanate oxide [264].

On the engineering improvements, a new reactor setup has been built, featuring an enhanced heating system and improved functionalities, including an upgraded cooling system and, most importantly, the possibility to monitor temperature in real time on multiple points within the reactor. Deep-insight studies can now be performed using this improved design to pinpoint important parameters that can affect the composition of the nanoparticle synthesis. The reactor is also split into three distinct parts which can be independently activated. This enables the possibility of studying the impact of the residence time, this type of modification leading to a decrease of the size but it could be completed by an ICP study of the composition to improve the A/B ratio. An interesting result shown in ***Figure P.1*** attests an important hint on the road to mastering the synthesis of pure strontium titanate. The XRD acquisition in black corresponds to the strontium titanate signal after SPS sintering, no presence of

secondary phase was detected. The red one confirms this observation even after a 1000 °C thermal treatment. The blue acquisition shows a possible clue to eliminate completely the formation of TiO_2 which could be related to the size of the crystallites. Indeed, the peaks are larger going toward higher angles and are characteristic of crystallite size being smaller. The measured value by Rietveld refinement is estimated as 14 nm which is 25% lower compared to the reference value found (between 19 and 23 nm).

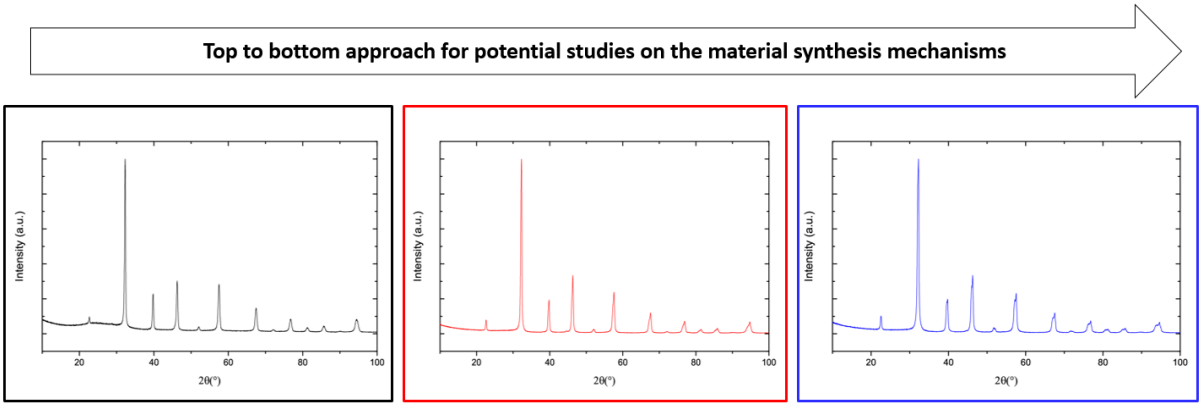

Figure P.1: Proposition of potential studies on the size effect of strontium titanate nanoparticles on the thermal stability of the material. The black XRD acquisition represent the strontium titanate after sintering process, the red one after 1000°C thermal treatment and the blue one after supercritical synthesis

The main highlight remains the versatility of the synthesis set-up for the production of extrinsic strontium titanate. The opportunities related to the synthesis of doped strontium titanate using the exclusive properties related to the supercritical synthesis are huge. Indeed, the specificities of strontium titanate rely on its tunable properties thanks to its perovskite structure. We showed previously in Chapter 1 a large panel of doped compositions synthesized using a different method. Every composition shows an effect on the properties that need to be tuned in order to suit the chosen application. The supercritical method with acetylacetonate precursors offers a solid base to synthesize a variety of extrinsic semiconductors and could even be extended to high-entropy alloys thanks to the flexibility of the method.

The strontium titanate and its large composition panel obtained thanks to doping or defect chemistry represent a wellspring of innovative applications related to energy, water treatment or biomedical that will serve for the mankind future in order to limit the environmental impact or serves the common good.

Appendix

Appendix A: List of the different applications of Strontium Titanate

Field-effect transistor:

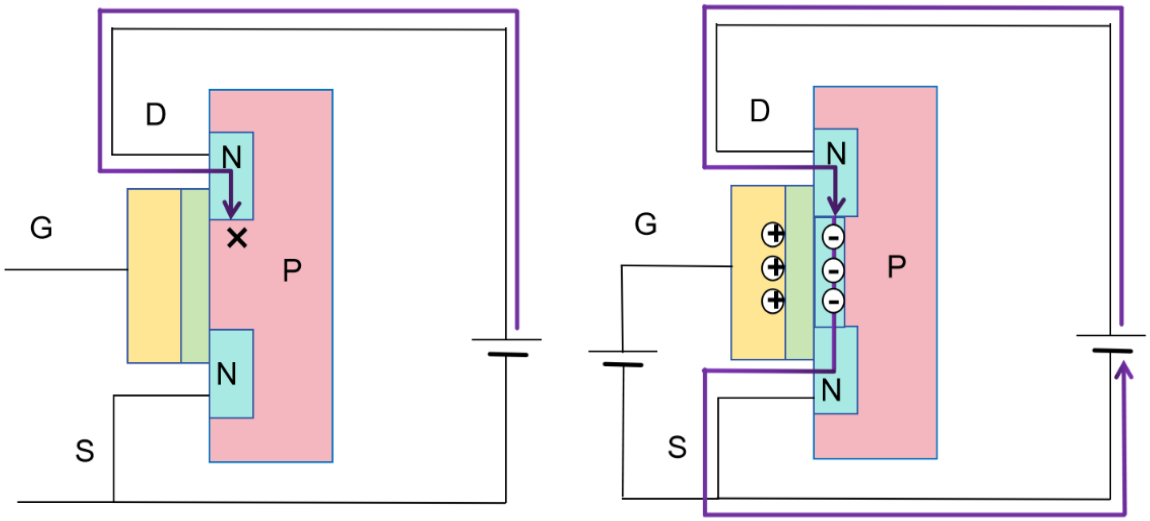

Appendix A.1: Working principle of field-effect transistor N-channel enhancement-mode MOSFET, cutoff state (left) and operating state (right) from Wang *et al.*

Solid oxide fuel cells:

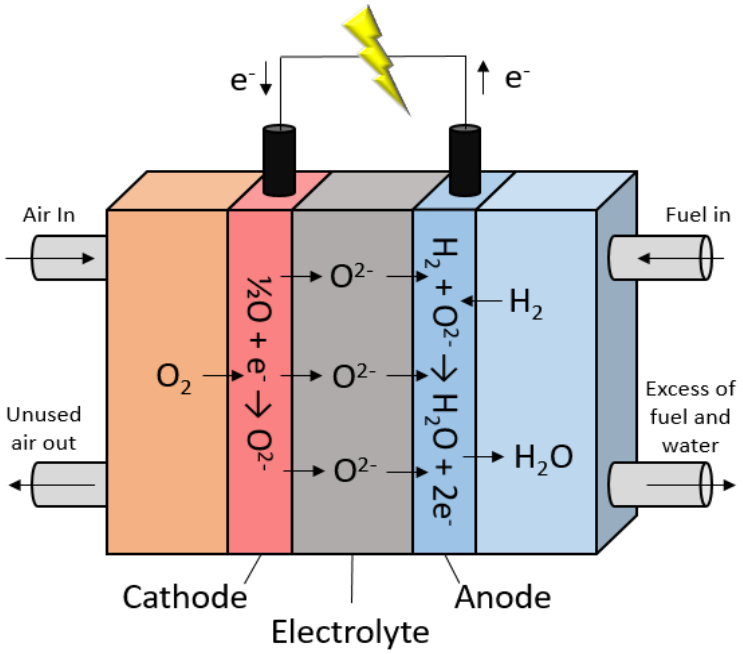

Appendix A.2: Solid oxide fuel cells and chemical mechanisms

Solar cell:

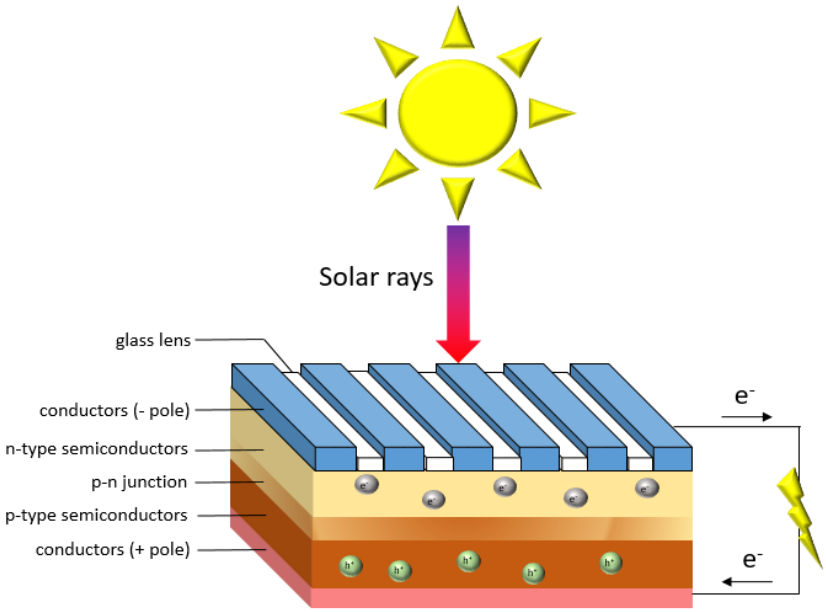

Hybrid Energy System:

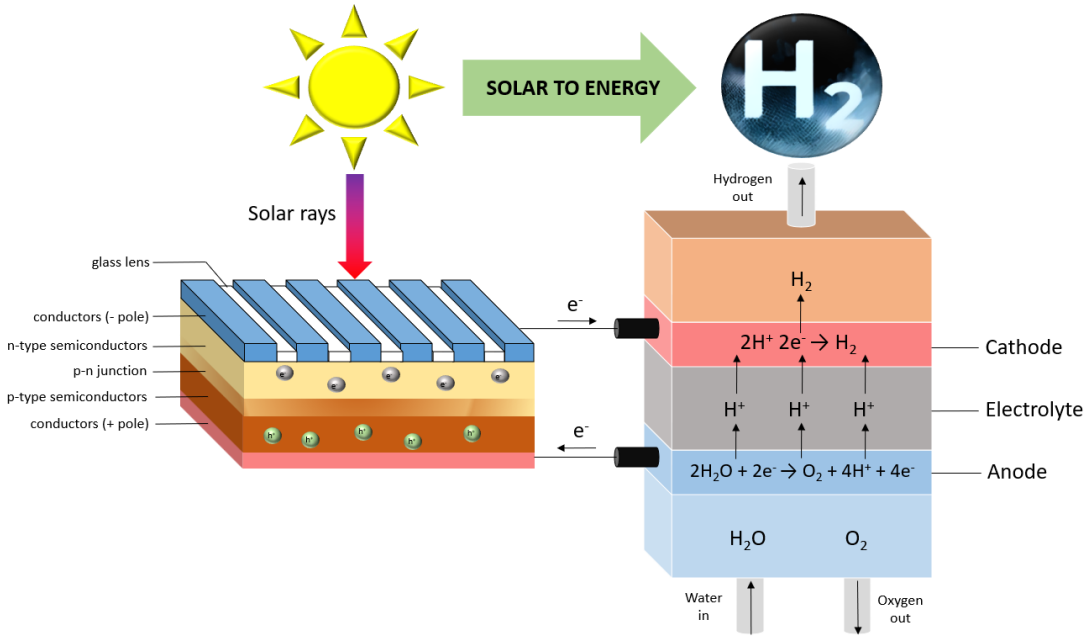

Appendix A. 3: Hybrid energy system combining solar cell and electrolysis to produce the direct conversion of solar ray into hydrogen

Lithium-ion batteries:

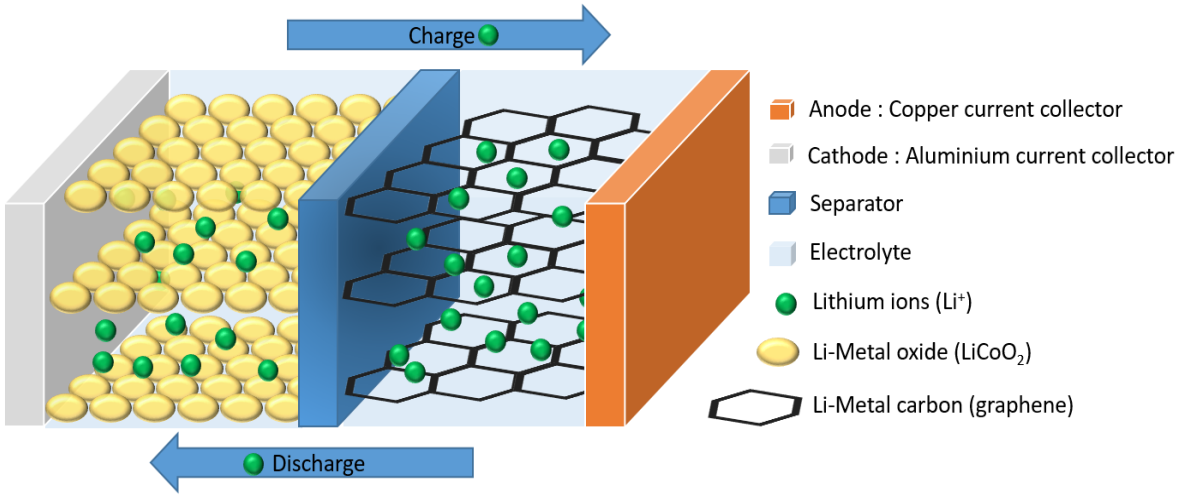

Appendix A.4: Composition and working principles of a Lithium-ion battery

Environmental remediation:

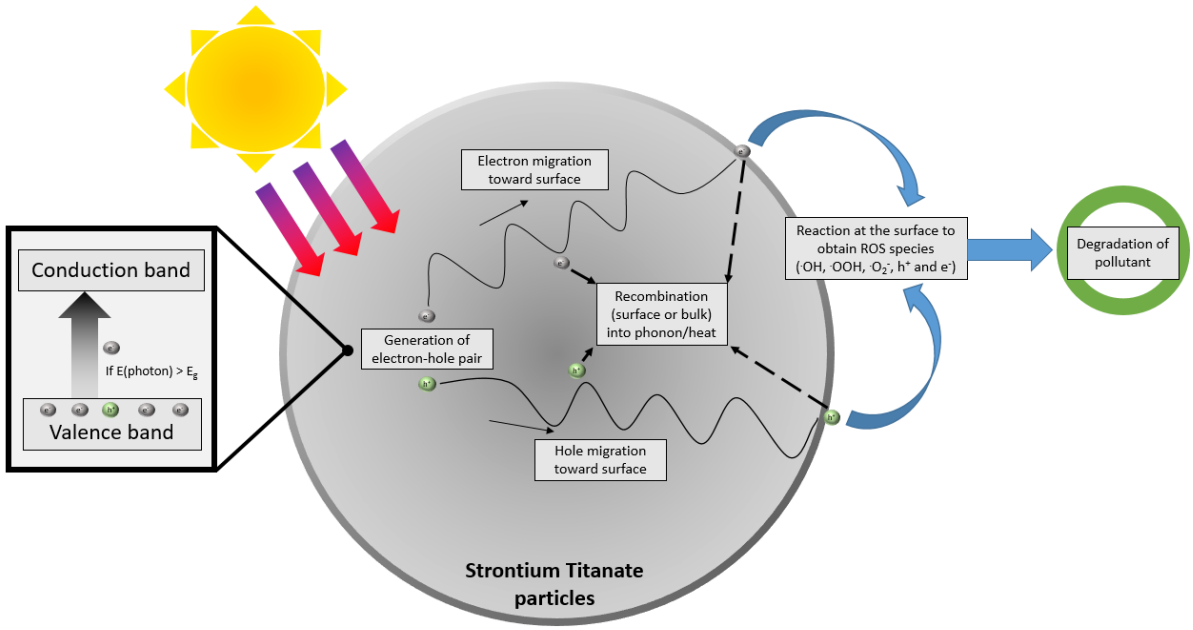

Appendix A.5: Application of strontium titanate for pollutant degradation and mechanism of the photocatalytic property, from solar rays to reactive oxidative species (inspired from Ren *et al.*)

Biomedical Applications:

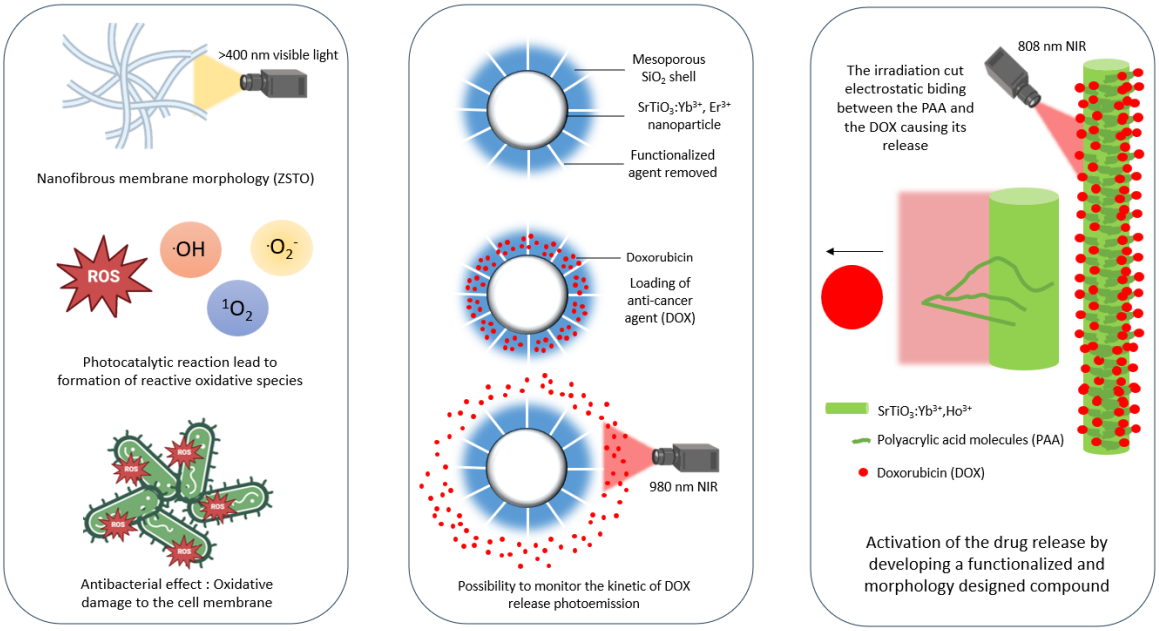

Appendix A.6: Applications relating to the antibacterial effect by photocatalytic activation using zirconium doped strontium titanate (ZSTO) nanofiber from Gao *et al.* (left)

Support for anti-cancer treatment molecules using nanoparticles of ytterbium, erbium doped strontium titanate with the possibility to monitor the kinetic of the release from Li *et al.* (middle)

Nanofiber of ytterbium, holmium doped strontium titanate functionalized with ligand and anti-cancer agents from Fu *et al.* (right)

Appendix B

Thermogravimetric Analysis of Strontium acetylacetonate:

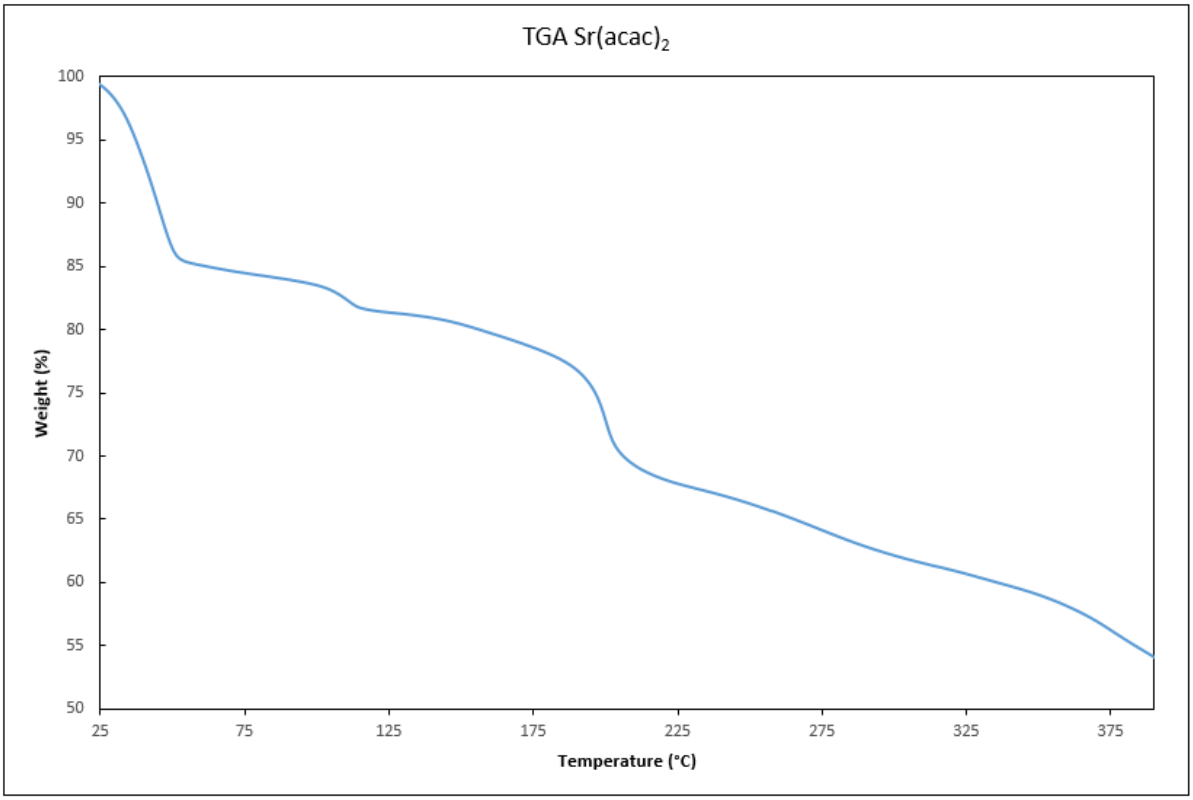

Appendix B: TGA of strontium acetylacetonate from SIGMA-ALDRICH from 25°C to 400°C

Appendix C

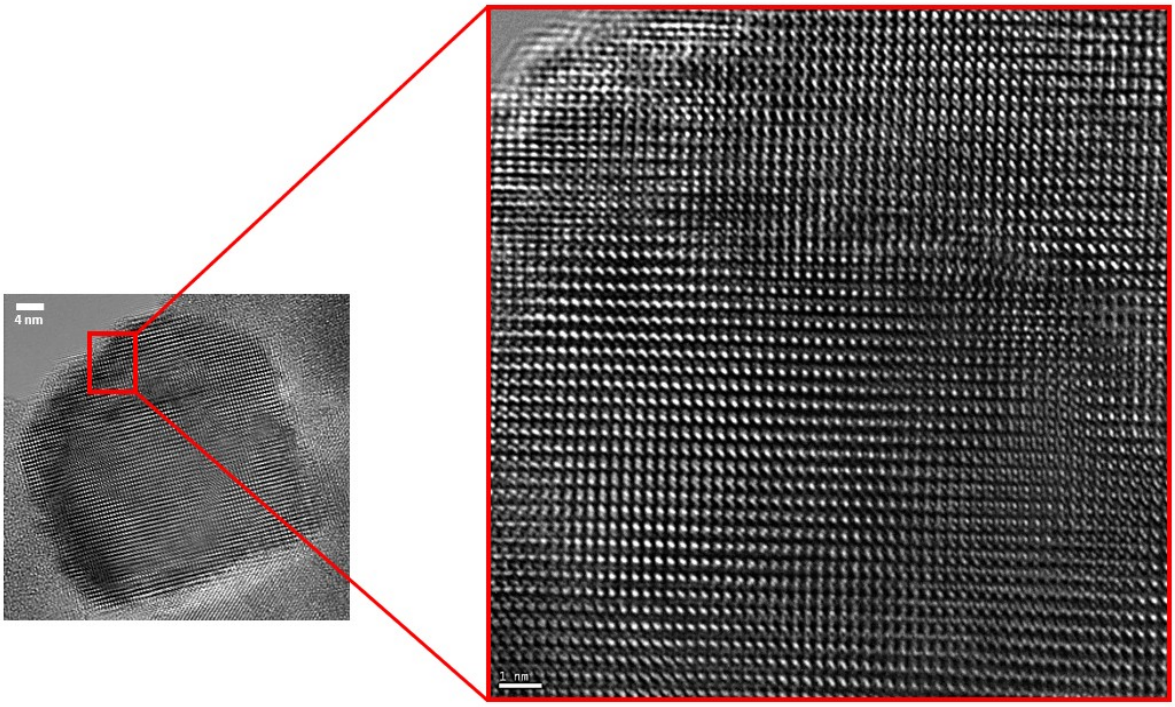

Appendix C: High-Resolution Transmission Electron Microscopy (HRTEM) Image of a Nanocrystal

The left panel represents a low-magnification HRTEM image showing the overall morphology of the nanocrystal. The crystal lattice fringes are visible, indicating a well-defined crystalline structure. The scale bar represents 4 nm.

The right panel (zoomed-in Area) represents the magnified view of the highlighted region, showing atomic-scale lattice fringes with high clarity. The periodic arrangement of atomic columns reflects the crystal's atomic structure. The scale bar represents 1 nm.

Appendix D

Parameters	$Sr_{0,72}TiO_{3-\delta}$	$Sr_{0,68}Y_{0,11}TiO_{3-\delta}$	$Sr_{0,70}Y_{0,05}TiO_{3-\delta}$	$Sr_{0,68}Ti_{0,78}Nb_{0,12}O_{3-\delta}$	$Sr_{0,75}Ti_{0,91}Nb_{0,07}O_{3-\delta}$
Space group	P m -3 m	P m -3 m	P m -3 m	P m -3 m	P m -3 m
Cell parameter (Å)	**3.91161**	**3.90526**	**3.90718**	**3.92046**	**3.91540**
$\sigma_{Cell\ parameter}$ (Å)	0.00003	0.00002	0.00002	0.00004	0.00003
Y	0.21193	0.19158	0.20007	0.23942	0.22027
σ_Y	0.00148	0.00123	0.00120	0.00228	0.00163
I_G	0.01490	0.01039	0.01054	0.01293	0.01573
σ_{I_G}	0.00039	0.00029	0.00030	0.00062	0.00044
Bragg R- factor	3.49	2.42	2.70	2.99	2.81
Rf –factor	1.69	1.23	1.38	1.86	1.65
Chi2	2.53	2.08	2.17	5.15	3.10
Cristallite size (Å)	**224.80**	**253,47**	**244.70**	**207.81**	**216.91**
$\sigma_{c.s}$	0.06	0.09	0.17	0.06	0.09

Appendix D.1: Structural and microstructural parameters of $SrTiO_3$-based samples for the proof of concept. This table presents a comparative analysis of various $SrTiO_3$-based perovskite compounds with partial substitution of Sr and Ti by Yttrium (Y) and Niobium (Nb), respectively. The following parameters are listed for each compound such as the cell parameter and the crystallite size as well as the estimated standard deviations for each parameter.

Parameters	$Sr_{0.79}TiO_{3-\delta}$	STO : 10%Fe	$Sr_{0.76}Pr_{0.10}TiO_{3-\delta}$	$Sr_{0.80}Nd_{0.05}TiO_{3-\delta}$	$Sr_{0.82}Nd_{0.02}TiO_{3-\delta}$	STO : 5%Nd 5%Nb
Space group	P m -3 m	P m -3 m	P m -3 m	P m -3 m	P m -3 m	P m -3 m
Cell parameter (Å)	**3.91378**	**3.91935**	**3.91091**	**3.91130**	**3.91265**	**3.92091**
$\sigma_{Cell\ parameter}$ (Å)	0.00005	0.00004	0.00004	0.00004	0.00003	0.00003
Y	0.30942	0.32790	0.27839	0.25996	0.25310	0.23169
σ_Y	0.00145	0.00123	0.00123	0.00104	0.00082	0.00086
Bragg R- factor	3.12	2.88	2.47	2.55	3.24	1.97
Rf –factor	1.79	1.57	1.65	1.49	1.73	1.27
Chi2	4.91	4.85	6.74	5.75	4.62	5.80
Cristallite size (Å)	**180.30**	**170,26**	**200.08**	**214.00**	**219.69**	**242.54**
$\sigma_{c.s}$	0.04	0.08	0.11	0.00	0.09	0.09

Appendix D.2: Structural and Microstructural Parameters of n and p substituted $SrTiO_3$-based samples. The following parameters are listed for each compound such as the cell parameter and the crystallite size as well as the estimated standard deviations for each parameter.

List of Abbreviations

ANR – Agence Nationale de la Recherche

BT – Barium Titanate

BST – Barium Strontium Titanate

CB – Conduction Band

CHEEC – Coupling Catalysis and High-Temperature Electrolysis for Ethylene from CO_2

CTE – Coefficient of Thermal Expansion

DFT – Density Functional Theory

EDS – Energy-Dispersive Spectroscopy

FTIR – Fourier Transform Infrared

GDC – Gadolinium-Doped Ceria

HPLC – High-Performance Liquid Chromatography

HRTEM – High-Resolution Transmission Electron Microscopy

HTE – High-Temperature Electrolysis

ICP – Inductively Coupled Plasma

ICPMS – Institut de physique et de chimie des matériaux de Strasbourg

ICP-OES – Inductively Coupled Plasma Optical Emission Spectroscopy

ICMCB – Institut de Chimie de la Matière Condensée de Bordeaux

IR – Infrared

LO – Longitudinal Optical

MEM – Maximum Entropy Method

METSA – Microscopie Électronique et Sonde Atomique

NMC 811 – Lithium Nickel Manganese Cobalt Oxide

OCM – Oxidative Coupling of Methane

P2G – Power-to-Gas

PLACAMAT – Plateforme Aquitaine de Caractérisation des Matériaux

PTFE – Polytetrafluoroethylene

PXRD – Powder X-ray Diffraction

ROS – Reactive Oxygen Species

SCF – Supercritical Fluid

SEM – Scanning Electron Microscopy

SHS – Supercritical Hydrothermal Synthesis

SOFCs – Solid Oxide Fuel Cells

SPS – Spark Plasma Sintering

STEM – Scanning Transmission Electron Microscopy

STO – Strontium Titanate

TEM – Transmission Electron Microscopy

TEM-EDS – Transmission Electron Microscopy with Energy-Dispersive Spectroscopy

TO – Transverse Optical

UV – Ultraviolet Radiation

VB – Valence Band

VLE – Vapor-Liquid Equilibrium

XPS – X-ray Photoelectron Spectroscopy

XRD – X-ray Diffraction

YSZ – Yttria-Stabilized Zirconia

Scientific contributions

First Author Articles:

“New solvothermal flow synthesis of strontium titanate nanoparticles based on the use of acetylacetonate precursors in water/ethanol mixture”. Journal of Supercritical Fluids, 2024, 213, pp.106353. ⟨10.1016/j.supflu.2024.106353⟩. Arnaud Dandre, Gilles Philippot, Mario Maglione, Jean-Marc. Bassat, Walid Baaziz, Ovidiu Ersen, Cyril Aymonier. ⟨hal-04680514⟩

Nth Author Articles:

“Investigation of the photochromism of WO3, TiO2, and composite WO3-TiO2 nanoparticles”. Inorganic Chemistry, 2024, 63 (21), pp.10079-10091. ⟨10.1021/acs.inorgchem.4c01379⟩. Ludovic Belhomme, Mathieu Duttine, Christine Labrugère, Emile Coicaud, Aline Rougier, Nicolas Penin, Arnaud Dandre, Serge Ravaine, Manuel Gaudon. ⟨hal-04596811⟩

“Cobalt-doped ZnO nanoparticles and PLD-deposited thin film forms: structure, optical properties and nature of magnetic anisotropy”. RSC Advances, 2024, 14 (38), pp.27622-27633. ⟨10.1039/d4ra05021e⟩. Najet Khlifi, Najib Ihzaz, Olivier Toulemonde, Arnaud Dandre, Christine Labrugère-Sarroste, Mohamed Nafti Bessadok, Mohamed Abdellah Lemine, Lassaad El Mir. ⟨hal-04699442⟩

First Author Conference:

“Innovative and flexible synthesis of Strontium Titanate nanoparticles with new composition in supercritical water/ethanol mixture”. 20th European Meeting on Supercritical Fluids, International Society for the Advancement of Supercritical Fluids; European Federation of Chemical Engineering; University of Maribor, May 2024, Maribor, Slovenia. pp.1-1. Arnaud Dandre, Gilles Philippot, Mario Maglione, Jean-Marc. Bassat, Cyril Aymonier. ⟨hal-04622300⟩

“Novel acetylacetonate precursors-based synthesis of Strontium Titanate nanoparticles in supercritical water/ethanol mixture”. 19th European Meeting on Supercritical Fluids - EMSF 2023, International Society for the Advancement of Supercritical Fluids, May 2023, Budapest, Hungary. Arnaud Dandre, Gilles Philippot, Mario Maglione, Jean-Marc. Bassat, Cyril Aymonier. ⟨hal-04701835⟩

Nth Author Conference:

“New supercritical flow synthesis of Ba1-xSrxTiO3 nanocrystals using acetylacetonate precursors for the development of dielectric composites”. 20th European Meeting on Supercritical Fluids, International Society for the Advancement of Supercritical Fluids; European Federation of Chemical Engineering; University of Maribor, May 2024, Maribor, Slovenia. pp.1-1. Dorian Adam, Arnaud Dandre, Mario Maglione, Cyril Aymonier, Gilles Philippot, Isabelle Bord-Makej. ⟨hal-04579236⟩

List of Figures

List of Figure Chapter 1:

Figure 1.1: Overall summary of strontium titanate possible applications (see Appendix A for details) 17
Figure 1.2: Unit cell of the perovskite structured strontium titanate made with the software VESTA (left). Plot of energies on the ionic model as a function of oxygen charge by Kahn *et al.* [49] (right) . 20
Figure 1.3: Evolution of the dielectric constant along the different crystallographic directions as a function of the temperature by Yang *et al.* [52] 21
Figure 1.4: Ti-O-Ti bond angles (left) and octahedral tilt and rotation angles (right) in $YTiO_3$ as a function of pressure from Loa *et al.* [69] (top)..... 24
Figure 1.5: Pressure dependence of the second order phonon modes and the first order phonon modes from Ishidate *et al.* [71] 25
Figure 1.6: Atom positions in cubic $SrTiO_3$ (a) and oxygen atoms displacement indicated by arrow in the tetragonal state (b) from Mattheiss *et al.* [72] 26
Figure 1.7: Thermal conductivity of strontium titanate as a function of the average grain size from Foley *et al.* [73] (left), the bulk value is represented by the straight line. Thermal conductivity of bulk single crystal strontium titanate as a function of temperature (1), lines (2) and (3) refer to strontium titanate thin film annealed at different temperatures from Yu *et al.* [75] (right) 27
Figure 1.8: Representation of the harmonic and anharmonic phonon with a 1D ball and spring model (left). Sketches of the three phonon scattering processes with decay and absorption respectively (right) from Wei *et al.* [87] 28
Figure 1.9: Thermal expansion coefficient of cubic perovskite and layered perovskite strontium titanate as a function of temperature from Lu *et al.* [92]..... 29
Figure 1.10: Temperature dependencies of unit-cell parameters of strontium borate from Filatov *et al.* [95]..... 30
Figure 1.11: Band structure of pristine strontium titanate (left) and optical absorption of pristine strontium titanate (right) from Hou *et al.* [106] 31
Figure 1.12: UV-Visible spectroscopy of pure strontium titanate and cerium doped strontium titanate (3 at.%) from Saravanan *et al.* [100] (left). Index of refraction of bulk strontium titanate from Trepakov *et al.* [109] (right) 32
Figure 1.13: The maximum entropy method (MEM) charge density distribution of strontium titanate at room temperature. Plane (001) (left) and plane (002) (right) from Ikeda *et al.* [118] (top) 33
Figure 1.14: Scheme of the potential upgrade of high temperature electrolysis unit from a power to gas process to a power to chemical achieving the conversion of methane into ethylene by OCM 35
Figure 1.15: Graphical abstract of Kim *et al.* [143] in a paper showing the different CH_4 conversion route based on the different selective oxygen species..... 36
Figure 1.16: Suggested surface reactions as depicted by Lim *et al.* [150]..... 37
Figure 1.17: Overview of the types of process and morphology that can be obtained with the sol gel method from Bokov *et al.* [223] 48
Figure 1.18: Scheme of the hydrothermal synthesis mechanism for strontium titanate from Zhang *et al.* [232] 51
Figure 1.19: Phase diagram of pure water with the information of its critical point (Tc= 374 °C and Pc= 22.1 MPa) from Serani *et al.* [240] 55
Figure 1.20: Proposition of the uptake phenomena and core-shell structure from the study of Yoko *et al.* [267] 59

Figure 1.21: Molar ratio of A-site ions (Ba+Sr) per B-site ion (Zr), obtained using different elements quantification analysis from Yoko *et al.* [268]..... 60
Figure 1.22: Sketch illustrating the particles growth $BaTiO_3$ and $Ba_{0.4}Sr_{0.6}TiO_3$ highlighting the effect of -OH defects amount using isopropoxide precursors in water/ethanol mixture from Philippot *et al.* [280] 61
Figure 1.23: Barium titanate nucleation and growth of TiO_2 seeds depending on the solvent properties based on the solubility of barium titanate (C*) and its energy interface (γ) from Yoko *et al.* [270] 62
Figure 1.24: TEM images and EDS mapping of $BaTiO_3$ particles with the molar ratio of A and B sites depending on their EtOH mol% media (A: 25% and B: 90%) from Yoko *et al.* [270] 62
Figure 1.25: XRD profiles of the PCSTO nanoparticles synthesized using hydrothermal synthesis at 400 °C with Ca+Sr/Ti = 0.85 annealed at (2) 600 °C, (3) 800 °C and (4) 1000 °C. from Hakuta *et al.* [272]. 63

List of Figure Chapter 2:

Figure 2.1: Picture of the original reactor built in 2004 with a side description of the different parts. The last project which was based on the use of this setup was about the synthesis of barium titanate 70
Figure 2.2: Scheme of the supercritical continuous solvothermal synthesis setup for the production of strontium titanate nanoparticles 70
Figure 2.3: Picture of the newly constructed twin reactors setup symbolized by two separated reactors connected to each pumping site located on the side of the setup 73
Figure 2.4: Scheme of the newly and improved set-up for the synthesis of doped and undoped strontium titanate nanoparticles 74
Figure 2.5: Summary of all the characterizations performed on the strontium titanate compound and their purpose 77
Figure 2.6: Scheme of the evolution of the processing of the nanomaterials throughout the different steps of deposition through screen-printing..... 83
Figure 2.7: Scheme of the overall functioning mechanism of the screen-printing device 85
Figure 2.8: Scheme of the principles and the different parts composing the SPS equipment 88
Figure 2.9: Scheme of the electrical resistivity measurement by four-point probe method with the inner probes (2&3) and outer probes (1&4) 90

List of Figure Chapter 3:

Figure 3.1: FullProf profile matching of $SrTiO_3$ (STO) PXRD pattern in the 20° to 130° 2Θ range confirming a lattice parameter of 3.911 Å and a mean crystallite size of 20 nm 98
Figure 3.2: PXRD acquisitions of strontium titanate synthesized by alkoxide (left) and acetylacetonate (right), comparative table of the results obtained from the pattern refinement..... 99
Figure 3.3: Indexed Raman spectrum of obtained $SrTiO_3$ nanoparticles..... 100
Figure 3.4: HRTEM analysis of the $SrTiO_3$ nanoparticles. a) Unzoomed TEM image of several particles, b) c) Close look on $SrTiO_3$ crystallites aggregation. d) Typical TEM image of several particles, e) high resolution image of a unique crystallite of $SrTiO_3$, f) Fast Fourrier Transform pattern of the image of the $SrTiO_3$ crystallite shown in e) 101
Figure 3.5: High-Resolution TEM Image showing crystalline structure of nanoparticles 102

Figure 3.6: EDS spectrum (bottom left) recorded in scanning TEM mode on several STO nanoparticles (image on top left) with corresponding elemental maps (top right: Sr/Ti relative map, Sr and Ti elemental maps) and the results of the quantification analysis (bottom right) 103
Figure 3.7: IR spectrum of strontium titanate nanosized powder synthesized in the continuous supercritical solvothermal process..... 105
Figure 3.8: In situ high temperature X-ray diffraction of $SrTiO_3$ with the evolution of the crystallites size on upper corner as a function of temperature 107
Figure 3.9: Evolution of the lattice parameter of $SrTiO_3$ as a function of the temperature during the heating (red) and cooling (blue) steps 108
Figure 3.10: Evolution of the linear thermal expansion of $SrTiO_3$ during the heating phase (top) and cooling (bottom) from the lattice parameter a where a_0 is the value at room temperature..... 109
Figure 3.11: In-situ high temperature TEM monitoring of an aggregate of STO nanoparticles. Images acquired at 150 °C under vacuum (a and b which corresponds to the red square), at 500 °C under air (c and d) and at 800 °C under air (e and f) 111
Figure 3.12: In-situ high temperature TEM monitoring of an aggregate of STO nanoparticles. Images acquired at 150 °C under vacuum (a), at 500 °C under air (b) and at 800 °C under air (c) 112
Figure 3.13: In-situ high temperature TEM monitoring of an aggregate of STO nanoparticles. The evolution shows the sintering of the smallest population into crystallized nanoparticles..... 113
Figure 3.14: TEM-EDS on the two populations of strontium titanate nanoparticles. The EDS result shows two different ratios of Sr/Ti..... 114
Figure 3.15: TEM-EDS on the two populations of strontium titanate nanoparticles. Same observations are verified 115
Figure 3.16: Molar percent of the $SrTiO_3$ and TiO_2 after thermal treatment of STO nanoparticles at 850 °C (left), the results were obtained from the PXRD pattern refinement and by ICP-OES (right). 117
Figure 3.17: High temperature in-situ XRD measurement of strontium titanate nanoparticles prepared using titanium isopropoxide precursor 119
Figure 3.18: Evolution of lattice parameter as a function of the annealing temperature of strontium titanate synthesized with a titanium precursor and table summarizing the data..... 120
Figure 3.19: Molar percent of the $SrTiO_3$ and TiO_2 after thermal treatment of STO nanoparticles synthesized using titanium precursor at 850 °C (left), the results were obtained from the XRD pattern refinement and by ICP-OES (right) 121
Figure 3.20: PXRD acquisition of the different powders synthesized using the new reactor as a function of the preheater temperature 122
Figure 3.21: PXRD pattern of synthesized strontium titanate using a different flow rate for the water, 6.4 $mL.min^{-1}$ being the reference, the table on the right summarized the lattice parameter value and the crystallite size (c.s) 123

List of Figure Chapter 4:

Figure 4.1: Summary of all the compositions synthesized during this PhD work..... 127
Figure 4.2: PXRD patterns of strontium titanate and A/B site doped strontium titanate (a). Raman signal of undoped strontium titanate (b). Zoom on the (1 1 0) peak of each strontium titanate (c). Raman signal of strontium titanate doped with yttrium (d)/ doped with niobium..... 132
Figure 4.3: EDS-TEM of the strontium titanate composition doped with yttrium at 10 at.% (left) and 5 at.% (right) with a table quantifying the atomic percent of strontium, titanium and yttrium. 135

Figure 4.4: EDS-TEM of the strontium titanate composition doped with niobium at 10% at. (left) and 5% at. (right) with a Table quantifying the atomic percent of each strontium, titanium and niobium 136
Figure 4.5: PXRD patterns of strontium titanate and A site doped with neodymium strontium titanate. Zoom on the (1 1 0) peak of each composition. TEM images of the crystallites of the different compositions 138
Figure 4.6: PXRD patterns of strontium titanate and A site doped with praseodymium strontium titanate. Zoom on the (1 1 0) peak of each strontium titanate. TEM image of a crystallite..... 139
Figure 4.7: EDS-TEM of the strontium titanate composition doped with neodymium at 5% at. (left) and 1% at. (right) with a Table quantifying the atomic percent in each strontium, titanium and neodymium 141
Figure 4.8: EDS-TEM of the strontium titanate composition doped with praseodymium at 10% at. with a Table quantifying the atomic percent in each strontium, titanium and praseodymium. 142
Figure 4.9: PXRD pattern of strontium titanate doped 10 at.% of niobium on B site (red curve). Zoom on the (1 1 0) peak of each strontium titanate 143
Figure 4.10: PXRD pattern of strontium titanate doped 10 at.% of iron on B site (red curve). Zoom on the (1 1 0) peak of each strontium titanate 144
Figure 4.11: PXRD patterns of strontium titanate and A and B sites doped with neodymium and niobium. Zoom on the (1 1 0) peak of each strontium titanate. TEM image of a crystallite of the codoped material 146
Figure 4.12: EDS-TEM of the strontium titanate composition doped with neodymium and niobium at 5% at. each with a Table quantifying the atomic percent in strontium in blue, titanium in red and niobium in green (left) and neodymium in green also (right) 146
Figure 4.13: PXRD patterns of the different samples of strontium titanate after SPS treatment (right). Table of Characteristic of each powder (left) 149
Figure 4.14: PXRD patterns with a focus on the (1 1 0) peak and structural features of the different compositions determined by Rietveld refinement 150
Figure 4.15: Electronic conductivity expressed as an Arrhenius law of SPS sintered pellet from commercial nanopowder of strontium titanate 152
Figure 4.16: Electronic conductivity expressed as an Arrhenius law performed on ceramics prepared from nanopowders of strontium titanate 153
Figure 4.17: Electronic conductivity expressed as an Arrhenius law measured on ceramics prepared from powders synthesized by supercritical solvothermal method 154
Figure 4.18: Electronic conductivity expressed as an Arrhenius law measured on ceramics prepared from nanopowders synthesized by supercritical solvothermal method for all the studied strontium titanate (doped / undoped). 156
Figure 4.19: XRD patterns recorded on cells before screen-printing formulation and after. All the diffraction peaks of the composite material have been indexed using the available database..... 158
Figure 4.20: SEM (left) and BSE (right) on YSZ+STO substrate after thermal treatment at 800°C. 159
Figure 4.21: SEM (left) and BSE (right) on YSZ+GDC+STO substrate after thermal treatment at 800 °C 160
Figure 4.22: SEM (left) and BSE (right) on YSZ+GDC+STO substrate after thermal treatment at 800 °C with a bigger zoom 160

List of Figure Perspective:

Figure P.1: Proposition of potential studies on the size effect of strontium titanate nanoparticles on the thermal stability of the material. The black XRD acquisition represent the strontium titanate after sintering process, the red one after 1000°C thermal treatment and the blue one after supercritical synthesis 169

List of Tables

List of Table Chapter 1:

Table 1.1: Perovskite structure at room temperature depending on the tolerance factors (τ) (1998, Carsten Schinzer) 23
Table 1.2: Summarized A-site doped strontium titanate 39
Table 1.3: Summarized B-site doped strontium titanate 41
Table 1.4: Summarized codoped strontium titanate 43
Table 1.5: Summary of strontium titanate properties synthesized using the solid-state reaction. 46
Table 1.6: Summary of strontium titanate properties synthesized using the sol gel method 49
Table 1.7: Summary of strontium titanate properties synthesized using the hydrothermal/solvothermal method 52
Table 1.8: Overview of the many ways to synthesized strontium titanate undoped and doped 54

List of Table Chapter 4:

Table 4.1: List of the elements substituted with their ionic radius, the coordination number is considered twelvefold for the element doping in the A site and six-fold for the element doping in the B site 129
Table 4.2: ICP-OES results obtained on the compositions $Sr_{1-x}Y_xTiO_{3-\delta}$ and $SrTi_{1-x}Nb_xO_{3-\delta}$ synthesized using the first flow reactor 134
Table 4.3: ICP-OES results of the composition $Sr_{1-x}Re_xTiO_{3-\delta}$ (Re: Y, Nd and Pr) synthesized using the second reactor 140
Table 4.4: Studied compositions of doped strontium titanate with the type of donor, the theoretical substitution rate and the site substituted 151
Table 4.5: Activation energy of the conductivity for each sample of strontium titanate 157

Bibliography

[1] IEA – International Energy Agency, IEA (2024). https://www.iea.org (accessed December 27, 2024).

[2] H.D. Megaw, Crystal structure of double oxides of the perovskite type, Proc. Phys. Soc. 58 (1946) 133. https://doi.org/10.1088/0959-5309/58/2/301.

[3] S. Yadav, S. Ghosh, Amorphous Strontium Titanate Film as Gate Dielectric for Higher Performance and Low Voltage Operation of Transparent and Flexible Organic Field Effect Transistor, ACS Appl. Mater. Interfaces 8 (2016) 10436–10442. https://doi.org/10.1021/acsami.6b02847.

[4] F. Pan, D. Olaya, J.C. Price, C.T. Rogers, Thin-film field-effect transistors based on La-doped SrTiO3 heterostructures, Appl. Phys. Lett. 84 (2004) 1573–1575. https://doi.org/10.1063/1.1651647.

[5] K. Shibuya, T. Ohnishi, M. Lippmaa, M. Kawasaki, H. Koinuma, Single crystal SrTiO3 field-effect transistor with an atomically flat amorphous CaHfO3 gate insulator, Appl. Phys. Lett. 85 (2004) 425–427. https://doi.org/10.1063/1.1773361.

[6] M. Abedi, Á. Szamosvölgyi, A. Sápi, Á. Kukovecz, Z. Kónya, T. Gyulavári, Z. Pap, Influence of Rapid Heat Treatment on the Photocatalytic Activity and Stability of Strontium Titanates against a Broad Range of Pollutants, Catalysts 13 (2023) 219. https://doi.org/10.3390/catal13020219.

[7] I.J. Peter, G. Vignesh, S. Vijaya, S. Anandan, K. Ramachandran, P. Nithiananthi, Enhancing the power conversion efficiency of SrTiO3/CdS/Bi2S3quantum dot based solar cell using phosphor, Appl. Surf. Sci. 494 (2019) 551–560. https://doi.org/10.1016/j.apsusc.2019.07.092.

[8] M. Cui, C. Qin, Y. Jiang, S. Zhang, C. Sun, M. Yuan, Y. Yang, Y. Liu, Tuning exciton dynamics by the dielectric confinement effect in quasi-two-dimensional perovskites, Photonics Res. 12 (2024) 563–570. https://doi.org/10.1364/PRJ.500205.

[9] D. Jennings, M.P. Zahler, D. Wang, Q. Ma, W. Deibert, M. Kindelmann, C. Kübel, S. Baumann, O. Guillon, J. Mayer, W. Rheinheimer, Grain boundary segregation in iron doped strontium titanate: From dilute to concentrated solid solutions, Acta Mater. 273 (2024) 119941. https://doi.org/10.1016/j.actamat.2024.119941.

[10] X. Xu, H. Li, X. Han, Y. Zheng, Enhancing electrochemical methane coupling in solid oxide cells by tuning oxygen species in the catalyst, J. Mater. Chem. A 12 (2024) 5115–5123. https://doi.org/10.1039/D3TA07648B.

[11] Y. Zhang, S.A. Horlick, E. Dogdibegovic, S.A. Barnett, Life Testing and Redox Cycling of Ni- and Ru-Doped Strontium Iron Titanate Exsolution Fuel Electrodes in Electrolyte-Supported Solid Oxide Cells, ECS Meet. Abstr. MA2023-01 (2023) 296. https://doi.org/10.1149/MA2023-0154296mtgabs.

[12] P. Guan, J. Min, S. Zhang, Y. Lu, T. Liang, L. Meng, Y. Yuan, Y. Zhou, F. Chen, L. Zhou, Z. Feng, C. Liu, Y. Hu, Z. Li, T. Wan, Y. Liu, J.N. Hart, D. Chu, Stabilizing High-Voltage Performance of Nickel-Rich Cathodes via Facile Solvothermally Synthesized Niobium-Doped Strontium Titanate, ACS Appl. Mater. Interfaces 16 (2024) 26167–26181. https://doi.org/10.1021/acsami.4c02691.

[13] P. Guan, J. Min, F. Chen, S. Zhang, Y. Zhu, C. Liu, Y. Hu, T. Wan, M. Li, Y. Liu, D. Su, J.N. Hart, Z. Li, D. Chu, Dual-modification of Ni-rich cathode materials through strontium titanate coating and thermal treatment, J. Colloid Interface Sci. 652 (2023) 1184–1196. https://doi.org/10.1016/j.jcis.2023.08.101.

[14] X. Xue, Z. Wang, S. He, L. Zhe, Z. Wu, C. Zheng, Y. Yang, H. Pan, Niobium-doped strontium titanate-coated lithium ion battery positive electrode material as well as synthesis method and application thereof, CN117976877A, 2024.

[15] B.L. Phoon, C.W. Lai, J.C. Juan, P.-L. Show, G.-T. Pan, Recent developments of strontium titanate for photocatalytic water splitting application, Int. J. Hydrog. Energy 44 (2019) 14316–14340. https://doi.org/10.1016/j.ijhydene.2019.01.166.

[16] R. Joy, S. Haridas, Strontuim titanate aided water splitting: An overview of current scenario, Int. J. Hydrog. Energy 46 (2021) 1879–1903. https://doi.org/10.1016/j.ijhydene.2020.10.148.

[17] K. Ikemiya, T. Takada, K. Domen, Photocatalyst for Water Decomposition, JP2023088059A, 2023.

[18] A. Jovanoski Kostić, N. Kanas, V. Rajić, A. Sharma, S.S. Bhattacharya, S. Armaković, M.M. Savanović, S.J. Armaković, Evaluation of Photocatalytic Performance of Nano-Sized Sr0.9La0.1TiO3 and Sr0.25Ca0.25Na0.25Pr0.25TiO3 Ceramic Powders for Water Purification, Nanomaterials 12 (2022) 4193. https://doi.org/10.3390/nano12234193.

[19] Y. Fu, C. Fang, Z. Ren, G. Xu, X. Li, G. Han, Constructing Implantable SrTiO3:Yb,Ho Nanofibers for NIR-Triggered and Optically Monitored Chemotherapy, Chem. – Eur. J. 23 (2017) 2423–2431. https://doi.org/10.1002/chem.201604956.

[20] Z. He, X.-Y. Sun, X. Gu, Electrospinning fabrication of SrTiO3:Er3+ nanofibers and their applications of upconversion properties, Ceram. Int. 43 (2017) 7378–7382. https://doi.org/10.1016/j.ceramint.2017.03.034.

[21] K.T. Jacob, G. Rajitha, Thermodynamic properties of strontium titanates: Sr2TiO4, Sr3Ti2O7, Sr4Ti3O10, and SrTiO3, J. Chem. Thermodyn. 43 (2011) 51–57. https://doi.org/10.1016/j.jct.2010.08.011.

[22] R.D. Shannon, Revised effective ionic radii and systematic studies of interatomic distances in halides and chalcogenides, Acta Crystallogr. A 32 (1976) 751–767. https://doi.org/10.1107/S0567739476001551.

[23] S. Piskunov, E. Heifets, R.I. Eglitis, G. Borstel, Bulk properties and electronic structure of SrTiO3, BaTiO3, PbTiO3 perovskites: an ab initio HF/DFT study, Comput. Mater. Sci. 29 (2004) 165–178. https://doi.org/10.1016/j.commatsci.2003.08.036.

[24] C. Chatzichristodoulou, P. Norby, P.V. Hendriksen, M.B. Mogensen, Size of oxide vacancies in fluorite and perovskite structured oxides, J. Electroceramics 34 (2015) 100–107. https://doi.org/10.1007/s10832-014-9916-2.

[25] N. Sharma, K. Hernadi, The Emerging Career of Strontium Titanates in Photocatalytic Applications: A Review, Catalysts 12 (2022) 1619. https://doi.org/10.3390/catal12121619.

[26] W. Hu, L. Li, G. Li, Y. Liu, R.L. Withers, Atomic-scale control of TiO6 octahedra through solution chemistry towards giant dielectric response, Sci. Rep. 4 (2014) 6582. https://doi.org/10.1038/srep06582.

[27] A. Jain, A. Somvanshi, Prashant, N. Ahmad, X-ray diffraction analysis of SrTiO3 nanoparticles by Williamson-Hall, size-strain plot and FullProf method, Mater. Today Proc. (2023). https://doi.org/10.1016/j.matpr.2023.03.166.

[28] I.M. Reaney, R. Ubic, Dielectric and structural characteristics of perovskites and related materials as a function of tolerance factor, Ferroelectrics 228 (1999) 23–38. https://doi.org/10.1080/00150199908226123.

[29] I.M. Reaney, E.L.C.E.L. Colla, N.S.N. Setter, Dielectric and Structural Characteristics of Ba- and Sr-based Complex Perovskites as a Function of Tolerance Factor, Jpn. J. Appl. Phys. 33 (1994) 3984. https://doi.org/10.1143/JJAP.33.3984.

[30] J.W. Bennett, I. Grinberg, A.M. Rappe, Effect of symmetry lowering on the dielectric response of BaZrO 3, Phys. Rev. B 73 (2006) 180102. https://doi.org/10.1103/PhysRevB.73.180102.

[31] A. Janotti, B. Jalan, S. Stemmer, C.G. Van de Walle, Effects of doping on the lattice parameter of SrTiO3, Appl. Phys. Lett. 100 (2012) 262104. https://doi.org/10.1063/1.4730998.

[32] T. Suzuki, M. Fujimoto, First-principles structural stability study of nonstoichiometry-related planar defects in SrTiO3 and BaTiO3, J. Appl. Phys. 89 (2001) 5622–5629. https://doi.org/10.1063/1.1362369.

[33] V.A. Trepakov, Z. Potůček, M.V. Makarova, A. Dejneka, P. Sazama, L. Jastrabik, Z. Bryknar, SrTiO3:Cr nanocrystalline powders: size effects and optical properties, J. Phys. Condens. Matter 21 (2009) 375303. https://doi.org/10.1088/0953-8984/21/37/375303.

[34] M. Bhakar, M. Garg, P. Bhardwaj, N.S. Mehta, G. Sheet, Laser-induced structural modulation and superconductivity in SrTiO3, Appl. Phys. Lett. 123 (2023) 052601. https://doi.org/10.1063/5.0156268.

[35] O.E. Kvyatkovskii, Quantum effects in incipient and low-temperature ferroelectrics (a review), Phys. Solid State 43 (2001) 1401–1419. https://doi.org/10.1134/1.1395075.

[36] T. Fix, Y. Zakaria, D. Stoeffler, D. Muller, A. Dinia, A. Slaoui, Sensitive Bandgap Reduction of SrTiO3 through Incorporation of Sulfur Using Ion Implantation, Sol. RRL 8 (2024) 2400237. https://doi.org/10.1002/solr.202400237.

[37] J. Fujisawa, T. Eda, M. Hanaya, Comparative study of conduction-band and valence-band edges of TiO2, SrTiO3, and BaTiO3 by ionization potential measurements, Chem. Phys. Lett. 685 (2017) 23–26. https://doi.org/10.1016/j.cplett.2017.07.031.

[38] I. Fareed, M. ul H. Farooq, M.D. Khan, Z. Ali, F.K. Butt, Band gap engineering of Strontium Titanate (SrTiO3) for improved photocatalytic activity and excellent bio-sensing aptitude, Mater. Sci. Semicond. Process. 177 (2024) 108327. https://doi.org/10.1016/j.mssp.2024.108327.

[39] D.J. Kok, K. Irmscher, M. Naumann, C. Guguschev, Z. Galazka, R. Uecker, Temperature-dependent optical absorption of SrTiO3, Phys. Status Solidi A 212 (2015) 1880–1887. https://doi.org/10.1002/pssa.201431836.

[40] I. Derkaoui, M. Achehboune, R.I. Eglitis, A.I. Popov, I. Boukhoubza, M.A. Basyooni-M. Kabatas, A. Rezzouk, Influence of the Hubbard U Correction on the Electronic Properties and Chemical Bands of the Cubic ($Pm3^{-}m$) Phase of SrTiO3 Using GGA/PBE and LDA/CA-PZ Approximations, Molecules 29 (2024) 3081. https://doi.org/10.3390/molecules29133081.

[41] K.C. Mishra, K.H. Johnson, P.C. Schmidt, A comparative study of the electronic structures of titanium dioxide and strontium titanate, J. Phys. Chem. Solids 54 (1993) 237–242. https://doi.org/10.1016/0022-3697(93)90315-I.

[42] W.F. Zhang, Z. Yin, M.S. Zhang, Study of photoluminescence and electronic states in nanophase strontium titanate, Appl. Phys. A 70 (2000) 93–96. https://doi.org/10.1007/s003390050018.

[43] M. Cardona, Optical Properties and Band Structure of SrTi O 3 and BaTi O 3, Phys. Rev. 140 (1965) A651–A655. https://doi.org/10.1103/PhysRev.140.A651.

[44] S. Ono, Y. Kumagai, Structural Properties of Two-Dimensional Strontium Titanate: A First-Principles Investigation, J. Phys. Soc. Jpn. 92 (2023) 114601. https://doi.org/10.7566/JPSJ.92.114601.

[45] M. Schneemann, A. Helbig, T. Kirchartz, R. Carius, U. Rau, Reverse biased electroluminescence spectroscopy of crystalline silicon solar cells with high spatial resolution, Phys. Status Solidi A 207 (2010) 2597–2600. https://doi.org/10.1002/pssa.201026309.

[46] C.E. Ekuma, M. Jarrell, J. Moreno, D. Bagayoko, First principle electronic, structural, elastic, and optical properties of strontium titanate, AIP Adv. 2 (2012) 012189. https://doi.org/10.1063/1.3700433.

[47] W. Luo, W. Duan, S.G. Louie, M.L. Cohen, Structural and electronic properties of n -doped and p -doped Sr Ti O 3, Phys. Rev. B 70 (2004) 214109. https://doi.org/10.1103/PhysRevB.70.214109.

[48] K. van Benthem, C. Elsässer, R.H. French, Bulk electronic structure of SrTiO3: Experiment and theory, J. Appl. Phys. 90 (2001) 6156–6164. https://doi.org/10.1063/1.1415766.

[49] A.H. Kahn, A.J. Leyendecker, Electronic Energy Bands in Strontium Titanate, Phys. Rev. 135 (1964) A1321–A1325. https://doi.org/10.1103/PhysRev.135.A1321.

[50] J. Nishiyama, K. Kanehara, H. Takeda, T. Tsurumi, T. Hoshina, Doping effect of Nb on ionic polarization of $SrTiO_3$, J. Ceram. Soc. Jpn. 127 (2019) 357–361. https://doi.org/10.2109/jcersj2.19031.

[51] V. Bilyk, K. Brekhov, A. Ovchinnikov, O. Chefonov, E. Mishina, Terahertz-induced polar state in quantum paraelectric SrTiO3, MRS Adv. 8 (2023) 943–946. https://doi.org/10.1557/s43580-023-00627-w.

[52] Z. Yang, D. Lee, J. Yue, J. Gabel, T.-L. Lee, R.D. James, S.A. Chambers, B. Jalan, Epitaxial SrTiO3 films with dielectric constants exceeding 25,000, Proc. Natl. Acad. Sci. 119 (2022) e2202189119. https://doi.org/10.1073/pnas.2202189119.

[53] Z.C. Zhao, M. Goryachev, J. Krupka, M.E. Tobar, Precision Multi-Mode Dielectric Characterization of a Crystalline Perovskite Enables Determination of the Temperature-Dependent Phase Transitions, IEEE Trans. Ultrason. Ferroelectr. Freq. Control 69 (2022) 423–429. https://doi.org/10.1109/TUFFC.2021.3108118.

[54] Y. Wang, S. Wang, X. Yu, L. Cao, M. Mao, H. Barzegar Bafrooei, Z. Lu, K. Song, D. Wang, Dramatic impact of raw chemicals on the electrical properties of SrTiO3 ceramics, Ceram. Int. (2024). https://doi.org/10.1016/j.ceramint.2024.02.218.

[55] S. Hameed, D. Pelc, Z.W. Anderson, A. Klein, R.J. Spieker, L. Yue, B. Das, J. Ramberger, M. Lukas, Y. Liu, M.J. Krogstad, R. Osborn, Y. Li, C. Leighton, R.M. Fernandes, M. Greven, Enhanced superconductivity and ferroelectric quantum criticality in plastically deformed strontium titanate, Nat. Mater. 21 (2022) 54–61. https://doi.org/10.1038/s41563-021-01102-3.

[56] R. Ranjan, R. Hackl, A. Chandra, E. Schmidbauer, D. Trots, H. Boysen, High-temperature relaxor ferroelectric behavior in Pr-doped $\mathrm{Sr}\mathrm{Ti}{\mathrm{O}}_{3}$, Phys. Rev. B 76 (2007) 224109. https://doi.org/10.1103/PhysRevB.76.224109.

[57] J. Liu, Y. Cao, Y.-L. Tang, Y.-L. Zhu, Y. Wang, N. Liu, M.-J. Zou, T.-T. Shi, F. Liu, F. Gong, Y.-P. Feng, X.-L. Ma, Room-Temperature Ferroelectricity of Paraelectric Oxides Tailored by Nano-Engineering, ACS Appl. Mater. Interfaces 15 (2023) 4226–4233. https://doi.org/10.1021/acsami.2c19944.

[58] E. Tosatti, R. Martoňák, Rotational melting in displacive quantum paraelectrics, Solid State Commun. 92 (1994) 167–180. https://doi.org/10.1016/0038-1098(94)90870-2.

[59] G. Geneste, J.-M. Kiat, Ground state of Ca-doped strontium titanate: Ferroelectricity versus polar nanoregions, Phys. Rev. B 77 (2008) 174101. https://doi.org/10.1103/PhysRevB.77.174101.

[60] S. Yun, X. Wang, B. Li, D. Xu, Dielectric properties Ca-substituted barium strontium titanate ferroelectric ceramics, Solid State Commun. 143 (2007) 461–465. https://doi.org/10.1016/j.ssc.2007.06.031.

[61] A. Ioachim, M.I. Toacsan, M.G. Banciu, L. Nedelcu, A. Dutu, S. Antohe, C. Berbecaru, L. Georgescu, G. Stoica, H.V. Alexandru, Transitions of barium strontium titanate ferroelectric ceramics for

different strontium content, Thin Solid Films 515 (2007) 6289–6293. https://doi.org/10.1016/j.tsf.2006.11.097.

[62] J. Qi, M. Cao, Y. Chen, Z. He, C. Tao, H. Hao, Z. Yao, H. Liu, Cerium doped strontium titanate with stable high permittivity and low dielectric loss, J. Alloys Compd. 772 (2019) 1105–1112. https://doi.org/10.1016/j.jallcom.2018.09.061.

[63] L.T. Li, T. Wang, X.H. Wang, J.C. Zhao, X. Li, Dielectric Characteristics of Doped Strontium Titanate within Broad Temperature Range, Key Eng. Mater. 336–338 (2007) 158–160. https://doi.org/10.4028/www.scientific.net/KEM.336-338.158.

[64] E. Padmini, K. Ramachandran, M. Muralidharan, Structural, optical, magnetic and dielectric properties of Dy-doped SrTiO3 nano ceramics, J. Mater. Sci. Mater. Electron. 29 (2018) 17078–17088. https://doi.org/10.1007/s10854-018-9804-7.

[65] K. Xue, L. Li, Colossal permittivity in Ta-doped SrTiO3 ceramics induced by interface effects and defect structure: An experimental and theoretical study, Ceram. Int. 49 (2023) 20388–20397. https://doi.org/10.1016/j.ceramint.2023.03.167.

[66] A. Tkach, O. Okhay, P.M. Vilarinho, A.L. Kholkin, High dielectric constant and tunability of strontium titanate ceramics modified by chromium doping, J. Phys. Condens. Matter 20 (2008) 415224. https://doi.org/10.1088/0953-8984/20/41/415224.

[67] A. Tkach, O. Okhay, I.M. Reaney, P.M. Vilarinho, Mechanical strain engineering of dielectric tunability in polycrystalline SrTiO3 thin films, J. Mater. Chem. C 6 (2018) 2467–2475. https://doi.org/10.1039/C8TC00414E.

[68] D. Kumar, A. David, A. Fouchet, A. Pautrat, J. Varignon, C.U. Jung, U. Lüders, B. Domengès, O. Copie, P. Ghosez, W. Prellier, Magnetism tailored by mechanical strain engineering in PrVO 3 thin films, Phys. Rev. B 99 (2019) 224405. https://doi.org/10.1103/PhysRevB.99.224405.

[69] I. Loa, X. Wang, K. Syassen, H. Roth, T. Lorenz, M. Hanfland, Y.-L. Mathis, Crystal structure and the Mott–Hubbard gap in YTiO3 at high pressure, J. Phys. Condens. Matter 19 (2007) 406223. https://doi.org/10.1088/0953-8984/19/40/406223.

[70] J. Zhao, N.L. Ross, D. Wang, R.J. Angel, High-pressure crystal structure of elastically isotropic CaTiO3 perovskite under hydrostatic and non-hydrostatic conditions, J. Phys. Condens. Matter 23 (2011) 455401. https://doi.org/10.1088/0953-8984/23/45/455401.

[71] T. Ishidate, T. Isonuma, Phase transition of SrTiO3 under high pressure, Ferroelectrics 137 (1992) 45–52. https://doi.org/10.1080/00150199208015936.

[72] L.F. Mattheiss, Effect of the 110°K Phase Transition on the SrTi O 3 Conduction Bands, Phys. Rev. B 6 (1972) 4740–4753. https://doi.org/10.1103/PhysRevB.6.4740.

[73] B.M. Foley, H.J. Brown-Shaklee, J.C. Duda, R. Cheaito, B.J. Gibbons, D. Medlin, J.F. Ihlefeld, P.E. Hopkins, Thermal conductivity of nano-grained SrTiO3 thin films, Appl. Phys. Lett. 101 (2012) 231908. https://doi.org/10.1063/1.4769448.

[74] R.S. Annam, S. Danayat, A. Nayal, F. Tarannum, M. Chrysler, J. Ngai, J. Jiang, A.J. Schmidt, J. Garg, Thickness dependent thermal conductivity of strontium titanate thin films on silicon substrate, J. Vac. Sci. Technol. A 42 (2024) 022707. https://doi.org/10.1116/6.0003320.

[75] C. Yu, M.L. Scullin, M. Huijben, R. Ramesh, A. Majumdar, Thermal conductivity reduction in oxygen-deficient strontium titanates, Appl. Phys. Lett. 92 (2008) 191911. https://doi.org/10.1063/1.2930679.

[76] K. Kato, M. Yamamoto, S. Ohta, H. Muta, K. Kurosaki, S. Yamanaka, H. Iwasaki, H. Ohta, K. Koumoto, The effect of Eu substitution on thermoelectric properties of SrTi0.8Nb0.2O3, J. Appl. Phys. 102 (2007) 116107. https://doi.org/10.1063/1.2822142.

[77] Y. Suemune, Thermal Conductivity of BaTiO3 and SrTiO3 from 4.5° to 300°K, J. Phys. Soc. Jpn. 20 (1965) 174–175. https://doi.org/10.1143/JPSJ.20.174.

[78] H. Ohta, K. Sugiura, K. Koumoto, Recent Progress in Oxide Thermoelectric Materials: p-Type Ca3Co4O9 and n-Type SrTiO3−, Inorg. Chem. 47 (2008) 8429–8436. https://doi.org/10.1021/ic800644x.

[79] J. He, Y. Xia, W. Lin, K. Pal, Y. Zhu, M.G. Kanatzidis, C. Wolverton, Exploring low lattice thermal conductivity materials using chemical bonding principles, (2021). https://doi.org/10.48550/arXiv.2107.04955.

[80] G. Guo, X. Yang, J. Carrete, W. Li, Revisiting the thermal conductivity of Si, Ge and diamond from first principles: roles of atomic mass and interatomic potential, J. Phys. Condens. Matter 33 (2021) 285702. https://doi.org/10.1088/1361-648X/abfd4e.

[81] T. Cheng, H. Zhao, L. Liu, J.-Y. Yang, Temperature-dependent in-plane thermal conductivity of SrTiO3 membranes enhanced by surface phonon polaritons, Int. J. Therm. Sci. 202 (2024) 109077. https://doi.org/10.1016/j.ijthermalsci.2024.109077.

[82] M. Tihtih, J.E.F.M. Ibrahim, M.A. Basyooni, R. En-nadir, W. Belaid, M.M. Abdelfattah, I. Hussainova, G. Pszota, I. Kocserha, Enhanced optical and thermal conductivity properties of barium titanate ceramic via strontium doping for thermo-optical applications, Opt. Quantum Electron. 55 (2023) 226. https://doi.org/10.1007/s11082-022-04516-8.

[83] M. Johanning, L. Porz, J. Dong, A. Nakamura, J.-F. Li, J. Rödel, Influence of dislocations on thermal conductivity of strontium titanate, Appl. Phys. Lett. 117 (2020) 021902. https://doi.org/10.1063/5.0010234.

[84] H. Yao, C. Chen, F. Cao, J. Mao, X. Liu, Q. Zhang, X. Lin, Anharmonicity of soft optical phonons as the origin of low lattice thermal conductivity in SrAgSb, Phys. Rev. B 108 (2023) 195206. https://doi.org/10.1103/PhysRevB.108.195206.

[85] D.-B. Zhang, T. Sun, R.M. Wentzcovitch, Phonon Quasiparticles and Anharmonic Free Energy in Complex Systems, Phys. Rev. Lett. 112 (2014) 058501. https://doi.org/10.1103/PhysRevLett.112.058501.

[86] L. Wang, Y.-N. Sun, Z.-H. Yao, Y. Chen, C. Wang, Anharmonicity in negative thermal expansion materials ZrW2O8 and ZrV2O7: Three-phonon interactions, Phys. Lett. A 517 (2024) 129667. https://doi.org/10.1016/j.physleta.2024.129667.

[87] B. Wei, Q. Sun, C. Li, J. Hong, Phonon anharmonicity: a pertinent review of recent progress and perspective, Sci. China Phys. Mech. Astron. 64 (2021) 117001. https://doi.org/10.1007/s11433-021-1748-7.

[88] J.P. Heremans, The anharmonicity blacksmith, Nat. Phys. 11 (2015) 990–991. https://doi.org/10.1038/nphys3542.

[89] S. Yamanaka, K. Kurosaki, T. Maekawa, T. Matsuda, S. Kobayashi, M. Uno, Thermochemical and thermophysical properties of alkaline-earth perovskites, J. Nucl. Mater. 344 (2005) 61–66. https://doi.org/10.1016/j.jnucmat.2005.04.017.

[90] B.H. Smith, W.C. Holler, M.D. Gross, Electrical properties and redox stability of tantalum-doped strontium titanate for SOFC anodes, Solid State Ion. 192 (2011) 383–386. https://doi.org/10.1016/j.ssi.2010.06.012.

[91] D. de Ligny, P. Richet, High-temperature heat capacity and thermal expansion of SrTiO3 and SrZrO3 perovskites, Phys. Rev. B 53 (1996) 3013–3022. https://doi.org/10.1103/PhysRevB.53.3013.

[92] Y. Lu, D. Jia, F. Gao, T. Hu, Z. Chen, First-principle calculations of the thermal properties of SrTiO3 and SrO(SrTiO3)n (*n*=1,2), Solid State Commun. 201 (2015) 25–30. https://doi.org/10.1016/j.ssc.2014.09.011.

[93] Z. Wang, M. Mori, T. Itoh, Thermal Expansion Properties of Sr1 − xLaxTiO3 (0 ⩽ x ⩽ 0.3) Perovskites in Oxidizing and Reducing Atmospheres, J. Electrochem. Soc. 157 (2010) B1783. https://doi.org/10.1149/1.3481458.

[94] R. Mittal, M.K. Gupta, S.L. Chaplot, Phonons and anomalous thermal expansion behaviour in crystalline solids, Prog. Mater. Sci. 92 (2018) 360–445. https://doi.org/10.1016/j.pmatsci.2017.10.002.

[95] S.K. Filatov, M.G. Krzhizhanovskaya, R.S. Bubnova, A.P. Shablinskii, O.L. Belousova, V.A. Firsova, Thermal expansion and structural complexity of strontium borates, Struct. Chem. 27 (2016) 1663–1671. https://doi.org/10.1007/s11224-016-0810-1.

[96] M. Rudenko, N. Gaponenko, V. Litvinov, A. Ermachikhin, E. Chubenko, V. Borisenko, N. Mukhin, Y. Radyush, A. Tumarkin, A. Gagarin, Structural Dependent Eu3+ Luminescence, Photoelectric and Hysteresis Effects in Porous Strontium Titanate, Materials 13 (2020) 5767. https://doi.org/10.3390/ma13245767.

[97] A. Raturi, P. Mittal, S. Choudhary, Density Functional Characterization of Electronic and Optical Properties of Strontium Titanate Under Doping and Strain for Optoelectronic Applications, IEEE Trans. Nanotechnol. 22 (2023) 481–489. https://doi.org/10.1109/TNANO.2023.3280083.

[98] H.J. Scheel, J.G. Bednorz, P. Dill, Crystal growth of strontium titanate SrTiO3, Ferroelectrics 13 (1976) 507–509. https://doi.org/10.1080/00150197608236653.

[99] V. Mishra, A. Sati, M.K. Warshi, A.B. Phatangare, S. Dhole, V.N. Bhoraskar, H. Ghosh, A. Sagdeo, V. Mishra, R. Kumar, P.R. Sagdeo, Effect of electron irradiation on the optical properties of SrTiO3: An experimental and theoretical investigations, Mater. Res. Express 5 (2018) 036210. https://doi.org/10.1088/2053-1591/aab6f5.

[100] G. Saravanan, K. Ramachandran, J. Gajendiran, E. Padmini, Effect of ceria concentration of Strontium titanate on the structural, optical, dielectric and electrical properties, Chem. Phys. Lett. 746 (2020) 137314. https://doi.org/10.1016/j.cplett.2020.137314.

[101] M. Siebenhofer, F. Baiutti, J. de Dios Sirvent, T.M. Huber, A. Viernstein, S. Smetaczek, C. Herzig, M.O. Liedke, M. Butterling, A. Wagner, E. Hirschmann, A. Limbeck, A. Tarancon, J. Fleig, M. Kubicek, Exploring point defects and trap states in undoped SrTiO3 single crystals, J. Eur. Ceram. Soc. 42 (2022) 1510–1521. https://doi.org/10.1016/j.jeurceramsoc.2021.10.010.

[102] X. Zhang, Y. Pu, L. Zhang, X. Lu, Y. Ning, J. Zhang, Y. Shang, Ultrahigh insulation resistivity potential under colossal permittivity SrTiO3 based ceramics via controlling oxygen backfill, J. Alloys Compd. 960 (2023) 170717. https://doi.org/10.1016/j.jallcom.2023.170717.

[103] H. Xie, Y. Pu, Y. Shang, Q. Pan, Y. Hao, L. Zhang, B. Wang, J. Qian, High resistivity under colossal permittivity SrTiO3 based ceramic via controlling ion diffusion, Ceram. Int. 50 (2024) 12672–12677. https://doi.org/10.1016/j.ceramint.2024.01.009.

[104] Y. Gao, Y. Masuda, K. Koumoto, Y. Gao, Y. Masuda, K. Koumoto, Band Gap Energy of $SrTiO_3$Thin Film Prepared by the Liquid Phase Deposition Method, J. Korean Ceram. Soc. 40 (n.d.) 213.

[105] M. Capizzi, A. Frova, Optical Gap of Strontium Titanate (Deviation from Urbach Tail Behavior), Phys. Rev. Lett. 25 (1970) 1298–1302. https://doi.org/10.1103/PhysRevLett.25.1298.

[106] Y.S. Hou, S. Ardo, R.Q. Wu, Hybrid density functional study of band gap engineering of SrTi O 3 photocatalyst via doping for water splitting, Phys. Rev. Mater. 5 (2021) 065801. https://doi.org/10.1103/PhysRevMaterials.5.065801.

[107] T. Ruf, M. Cardona, C.S.J. Pickles, R. Sussmann, Temperature dependence of the refractive index of diamond up to $925 \mathrm{K}$, Phys. Rev. B 62 (2000) 16578–16581. https://doi.org/10.1103/PhysRevB.62.16578.

[108] A. Frye, R.H. French, D.A. Bonnell, Optical Properties and Electronic Structure of Oxidized and Reduced Single-Crystal Strontium Titanate: Dedicated to Professor Dr. Dr. h. c. Manfred Rühle on the Occasion of his 65th Birthday, Z. Für Met. 94 (2003) 226–232. https://doi.org/10.3139/146.030226.

[109] V. Trepakov, A. Dejneka, P. Markovin, A. Lynnyk, L. Jastrabik, A 'soft electronic band' and the negative thermooptic effect in strontium titanate, New J. Phys. 11 (2009) 083024. https://doi.org/10.1088/1367-2630/11/8/083024.

[110] N. Talebi, Interaction of electron beams with optical nanostructures and metamaterials: from coherent photon sources towards shaping the wave function, J. Opt. 19 (2017) 103001. https://doi.org/10.1088/2040-8986/aa8041.

[111] G.A. Reider, Light–Matter Interaction, in: G.A. Reider (Ed.), Photonics Introd., Springer International Publishing, Cham, 2016: pp. 245–296. https://doi.org/10.1007/978-3-319-26076-1_6.

[112] A.N. Volobuev, S.V. Lukachev, A.P. Tolstonogov, I.V. Kolomin, Interaction of Photons with Electrons of a Metal during the Irradiation of Its Surface in Vector-Potential Space, J. Surf. Investig. X-Ray Synchrotron Neutron Tech. 13 (2019) 658–666. https://doi.org/10.1134/S102745101902040X.

[113] A. Slodczyk, Ph. Colomban, M. Pham-Thi, Role of the TiO6 octahedra on the ferroelectric and piezoelectric behaviour of the poled PbMg1⁄3Nb2⁄3O3–*x*PbTiO3 (PMN–PT) single crystal and textured ceramic, J. Phys. Chem. Solids 69 (2008) 2503–2513. https://doi.org/10.1016/j.jpcs.2008.05.004.

[114] E.A. Zhurova, V.G. Tsirelson, Electron density and energy density view on the atomic interactions in SrTiO3, Acta Crystallogr. B 58 (2002) 567–575. https://doi.org/10.1107/S0108768102009692.

[115] J.F. Wager, D.A. Keszler, Bonding and Tunneling, ACS Omega 8 (2023) 23182–23190. https://doi.org/10.1021/acsomega.3c02736.

[116] K. Fukushima, Comparison of Contributions to Interatomic Interactions Between Covalent and Ionic Bonds from Total Energy Calculations, in: T. Ishii, H. Wakita, K. Ogasawara, Y.-S. Kim (Eds.), DV-Xα Mol.-Orbital Calc. Method, Springer International Publishing, Cham, 2015: pp. 135–139. https://doi.org/10.1007/978-3-319-11185-8_5.

[117] Y. Rakita, T. Kirchartz, G. Hodes, D. Cahen, Type and Degree of Covalence: Empirical Derivation and Implications, (2019). https://doi.org/10.48550/arXiv.1907.03971.

[118] T. Ikeda, T. Kobayashi, M. Takata, T. Takayama, M. Sakata, Charge density distributions of strontium titanate obtained by the maximum entropy method, Solid State Ion. 108 (1998) 151–157. https://doi.org/10.1016/S0167-2738(98)00033-2.

[119] J. Friis, B. Jiang, J. Spence, K. Marthinsen, R. Holmestad, Extinction-free electron diffraction refinement of bonding in SrTiO3, Acta Crystallogr. A 60 (2004) 402–408. https://doi.org/10.1107/S010876730401726X.

[120] S.D. Bisarya, J. Shanker, Sizes and electronic polarizabilities of divalent ions in crystals, Pramana 2 (1974) 196–198. https://doi.org/10.1007/BF02847794.

[121] C.J.F. Böttcher, Computation of the radius and the polarizability of a number of ions, Recl. Trav. Chim. Pays-Bas 65 (1946) 19–38. https://doi.org/10.1002/recl.19460650105.

[122] P.W. Fowler, N.C. Pyper, A.D. Buckingham, In-crystal ionic polarizabilities derived by combining experimental and ab initio results, Proc. R. Soc. Lond. Math. Phys. Sci. 398 (1997) 377–393. https://doi.org/10.1098/rspa.1985.0040.

[123] H. Kakiuchida, K. Saito, A.J. Ikushima, Refractive Index, Density and Polarizability of Silica Glass with Various Fictive Temperatures, Jpn. J. Appl. Phys. 43 (2004) L743. https://doi.org/10.1143/JJAP.43.L743.

[124] M. Tyunina, N. Nepomniashchaia, V. Vetokhina, A. Dejneka, Optics of epitaxial strained strontium titanate films, Appl. Phys. Lett. 117 (2020) 082901. https://doi.org/10.1063/5.0021461.

[125] A.V. Kovalevsky, A.A. Yaremchenko, S. Populoh, A. Weidenkaff, J.R. Frade, Effect of A-Site Cation Deficiency on the Thermoelectric Performance of Donor-Substituted Strontium Titanate, J. Phys. Chem. C 118 (2014) 4596–4606. https://doi.org/10.1021/jp409872e.

[126] Y. Zhou, Q. Wen, Z. Ren, H. Xie, S. Tao, W. Zhou, Gadolinium-doped strontium titanate for high-efficiency electromagnetic interference shielding, J. Alloys Compd. 733 (2018) 33–39. https://doi.org/10.1016/j.jallcom.2017.10.289.

[127] L. Zhao, L. Fang, W. Dong, F. Zheng, M. Shen, T. Wu, Effect of charge compensation on the photoelectrochemical properties of Ho-doped SrTiO3 films, Appl. Phys. Lett. 102 (2013) 121905. https://doi.org/10.1063/1.4798829.

[128] T.D. McColm, J.T.S. Irvine, B site doped strontium titanate as a potential SOFC substrate, Ionics 7 (2001) 116–121. https://doi.org/10.1007/BF02375477.

[129] L.A. Dunyushkina, V.A. Gorbunov, A.A. Babkina, N.O. Esina, High-temperature electrical transport in Al-doped calcium and strontium titanates, Ionics 9 (2003) 67–70. https://doi.org/10.1007/BF02376539.

[130] J. Gerblinger, H. Meixner, Influence of dopants on the response time and the signals of lambda sensors based on thin films of strontium titanate, Sens. Actuators B Chem. 6 (1992) 231–235. https://doi.org/10.1016/0925-4005(92)80061-2.

[131] Y. Gao, Z. Lu, T.L. You, J. Wang, L. Xie, J. He, F. Ciucci, Energetics of Nanoparticle Exsolution from Perovskite Oxides, J. Phys. Chem. Lett. 9 (2018) 3772–3778. https://doi.org/10.1021/acs.jpclett.8b01380.

[132] M. Onoda, I. Goto, Correlation and phonon effects for the electronic transport and thermoelectric power factors in the metal–band-insulator crossover of perovskite-type titanates, J. Phys. Condens. Matter 21 (2009) 435603. https://doi.org/10.1088/0953-8984/21/43/435603.

[133] A. Murashkina, V. Maragou, D. Medvedev, V. Sergeeva, A. Demin, P. Tsiakaras, Single phase materials based on Co-doped SrTiO3 for mixed ionic-electronic conductors applications, J. Power Sources 210 (2012) 339–344. https://doi.org/10.1016/j.jpowsour.2012.02.066.

[134] R.R. Solís, J. Bedia, J.J. Rodríguez, C. Belver, A review on alkaline earth metal titanates for applications in photocatalytic water purification, Chem. Eng. J. 409 (2021) 128110. https://doi.org/10.1016/j.cej.2020.128110.

[135] G. Ren, H. Han, Y. Wang, S. Liu, J. Zhao, X. Meng, Z. Li, Recent Advances of Photocatalytic Application in Water Treatment: A Review, Nanomaterials 11 (2021) 1804. https://doi.org/10.3390/nano11071804.

[136] S.T. Sajjadian, K.-W.-A. Chee, R.A. Ejbarah, S.M. Hamidi, Y. Alissa, S. Sadeghi, Broadband and strong visible-light driven photocatalytic enhancement utilizing two-dimensional plasmonics of Au/Cu-modified SrTiO3 perovskite nanostructures, Optik 305 (2024) 171779. https://doi.org/10.1016/j.ijleo.2024.171779.

[137] M. Abd Elkodous, A.M. El-Khawaga, M.M. Abouelela, M.I.A. Abdel Maksoud, Cocatalyst loaded Al-SrTiO3 cubes for Congo red dye photo-degradation under wide range of light, Sci. Rep. 13 (2023) 6331. https://doi.org/10.1038/s41598-023-33249-1.

[138] S. Merrad, M. Abbas, R. Brahimi, M. Trari, Study of Congo Red removal from aqueous solution by using the deficient perovskite SrTiO3-δ under solar light, J. Mol. Struct. 1265 (2022) 133349. https://doi.org/10.1016/j.molstruc.2022.133349.

[139] Q. Jia, J. Liu, L. Zhong, Y. Li, D. Duan, Preparation of the regular polyhedral single-crystalline SrTiO3 particles with exposing different crystal facets, Mater. Lett. 288 (2021) 129338. https://doi.org/10.1016/j.matlet.2021.129338.

[140] M. Paszkiewicz-Gawron, E. Kowalska, M. Endo-Kimura, J. Zwara, A. Pancielejko, K. Wang, W. Lisowski, J. Łuczak, A. Zaleska-Medynska, E. Grabowska-Musiał, Stannates, titanates and tantalates modified with carbon and graphene quantum dots for enhancement of visible-light photocatalytic activity, Appl. Surf. Sci. 541 (2021) 148425. https://doi.org/10.1016/j.apsusc.2020.148425.

[141] H. Bai, X. Zan, J. Juay, D.D. Sun, Hierarchical heteroarchitectures functionalized membrane for high efficient water purification, J. Membr. Sci. 475 (2015) 245–251. https://doi.org/10.1016/j.memsci.2014.10.036.

[142] B. Thomas, L.K. Alexander, Nanoreactor based enhancement of photocatalysis with Co0.7Zn0.3Fe2O4@SrTiO3 core-shell nanocomposites, J. Alloys Compd. 788 (2019) 257–266. https://doi.org/10.1016/j.jallcom.2019.02.190.

[143] I. Kim, G. Lee, H.B. Na, J.-M. Ha, J.C. Jung, Selective oxygen species for the oxidative coupling of methane, Mol. Catal. 435 (2017) 13–23. https://doi.org/10.1016/j.mcat.2017.03.012.

[144] S. Alturkistani, H. Wang, R. Gautam, S.M. Sarathy, Importance of Process Variables and Their Optimization for Oxidative Coupling of Methane (OCM), ACS Omega 8 (2023) 21223–21236. https://doi.org/10.1021/acsomega.3c02350.

[145] H.N. Thanh, P.P.T. Mai, T.D. Thi, T.L. Minh, A comparative study on the catalytic activities of the SrTiO3 perovskite and oxide CuO-ZnO mixed oxides for the oxidative coupling of methane, Vietnam J. Catal. Adsorpt. 11 (2022) 114–121. https://doi.org/10.51316/jca.2022.060.

[146] L. Bai, F. Polo-Garzon, Z. Bao, S. Luo, B.M. Moskowitz, H. Tian, Z. Wu, Impact of Surface Composition of SrTiO3 Catalysts for Oxidative Coupling of Methane, ChemCatChem 11 (2019) 2107–2117. https://doi.org/10.1002/cctc.201900159.

[147] S. Pavlova, Y. Ivanova, S. Tsybulya, Y. Chesalov, A. Nartova, E. Suprun, L. Isupova, Sr2TiO4 Prepared Using Mechanochemical Activation: Influence of the Initial Compounds' Nature on Formation, Structural and Catalytic Properties in Oxidative Coupling of Methane, Catalysts 12 (2022) 929. https://doi.org/10.3390/catal12090929.

[148] K. Nomura, T. Hayakawa, K. Takehira, Y. Ujihira, Oxidative coupling of methane on perovskite oxides, (Ba,Ca)(Co,Fe)O3-δ, Appl. Catal. Gen. 101 (1993) 63–72. https://doi.org/10.1016/0926-860X(93)80138-G.

[149] D.V. Ivanov, L.A. Isupova, E.Yu. Gerasimov, L.S. Dovlitova, T.S. Glazneva, I.P. Prosvirin, Oxidative methane coupling over Mg, Al, Ca, Ba, Pb-promoted SrTiO3 and Sr2TiO4: Influence of surface composition and microstructure, Appl. Catal. Gen. 485 (2014) 10–19. https://doi.org/10.1016/j.apcata.2014.07.024.

[150] S. Lim, J.-W. Choi, D.J. Suh, K.H. Song, H.C. Ham, J.-M. Ha, Combined experimental and density functional theory (DFT) studies on the catalyst design for the oxidative coupling of methane, J. Catal. 375 (2019) 478–492. https://doi.org/10.1016/j.jcat.2019.04.008.

[151] P. Palani, D. Fasquelle, Dielectric properties and energy storage performance of lead-free strontium calcium titanate (Sr0.60Ca0.40)TiO3 thick films, Appl. Phys. A 130 (2024) 787. https://doi.org/10.1007/s00339-024-07938-1.

[152] S. Singh, P.A. Jha, S. Presto, M. Viviani, A.S.K. Sinha, S. Varma, P. Singh, Structural and electrical conduction behaviour of yttrium doped strontium titanate: anode material for SOFC application, J. Alloys Compd. 748 (2018) 637–644. https://doi.org/10.1016/j.jallcom.2018.03.170.

[153] E. Padmini, K. Ramachandran, Investigation on versatile behaviour of Cd doped SrTiO3 perovskite structured compounds, Solid State Commun. 302 (2019) 113716. https://doi.org/10.1016/j.ssc.2019.113716.

[154] C. Ang, Z. Yu, Effect of annealing on dielectric behavior and conduction transport of Bi doped SrTiO3, Appl. Phys. Lett. 88 (2006) 162902. https://doi.org/10.1063/1.2193655.

[155] K. Park, J.S. Son, S.I. Woo, K. Shin, M.-W. Oh, S.-D. Park, T. Hyeon, Colloidal synthesis and thermoelectric properties of La-doped SrTiO3 nanoparticles, J. Mater. Chem. A 2 (2014) 4217–4224. https://doi.org/10.1039/C3TA14699E.

[156] J.-Q. Zheng, Y.-J. Zhu, J.-S. Xu, B.-Q. Lu, C. Qi, F. Chen, J. Wu, Microwave-assisted rapid synthesis and photocatalytic activity of mesoporous Nd-doped SrTiO3 nanospheres and nanoplates, Mater. Lett. 100 (2013) 62–65. https://doi.org/10.1016/j.matlet.2013.02.107.

[157] D. Anand, K. Ramachandran, P. Sakthivel, M. Silambarasan, Investigations of crystallographic, magnetic, optical and photoluminescence nature of Sm2O3 doped SrTiO3 nanomaterials for LED, Ceram. Int. 50 (2024) 33590–33598. https://doi.org/10.1016/j.ceramint.2024.06.175.

[158] C. Stanciu, S. Hau, G. Stanciu, R. Trusca, B.S. Vasile, C. Tihon, Structural, microstructural characterization and luminescence spectroscopy of europium-doped strontium titanate prepared by the sol-gel method, Ceram. Int. (2023). https://doi.org/10.1016/j.ceramint.2023.09.054.

[159] M.V. Rudenko, V.S. Kortov, N.V. Gaponenko, A.V. Mudryi, S.V. Zvonarev, Photo- and cathodoluminescence of strontium titanate xerogel films doped with terbium ions, J. Surf. Investig. X-Ray Synchrotron Neutron Tech. 9 (2015) 1012–1015. https://doi.org/10.1134/S1027451015050407.

[160] Z. Potůček, A.P. Skvortsov, N.K. Poletaev, Z. Bryknar, L. Jastrabik, A. Dejneka, V.A. Trepakov, Optical spectroscopy of erbium-doped SrTiO3 crystals, J. Lumin. 154 (2014) 437–444. https://doi.org/10.1016/j.jlumin.2014.05.021.

[161] R. Kaur, A.K. Tyagi, Gadolinium and Thulium Doping to Perovskite Structured Strontium Titanates at Strontium and Titanium Sites, 38 (2022) 102–105. https://doi.org/10.13005/ojc/380112.

[162] G. López-Pacheco, R. López-Juárez, M.E. Villafuerte-Castrejón, C. Falcony, E. Barrera-Calva, F. González, Luminescence properties of Yb3+-doped SrTiO3: the significance of the oxygen–titanium charge transfer state on photon downshifting, Dalton Trans. 48 (2019) 11889–11896. https://doi.org/10.1039/C9DT01360A.

[163] Y.-X. Song, W.-Q. Ma, J.-J. Chen, J. Xu, Z.-Y. Mao, D.-J. Wang, Photocatalytic activity of perovskite SrTiO3 catalysts doped with variable rare earth ions, Rare Met. 40 (2021) 1077–1085. https://doi.org/10.1007/s12598-020-01674-0.

[164] M.C. Verbraeken, T. Ramos, K. Agersted, Q. Ma, C.D. Savaniu, B.R. Sudireddy, J.T.S. Irvine, P. Holtappels, F. Tietz, Modified strontium titanates: from defect chemistry to SOFC anodes, RSC Adv. 5 (2015) 1168–1180. https://doi.org/10.1039/C4RA09751C.

[165] T.-B. Chen, H. Rabiee, P. Yan, Z. Zhu, L. Ge, Enhancing the Ammonia Catalytic Decomposition of Lanthanum Strontium Titanate Nickel Perovskite Catalysts via a Balanced Cation Doping and

Deficiency Strategy, Energy Fuels 38 (2024) 5449–5456. https://doi.org/10.1021/acs.energyfuels.4c00345.

[166] C. Li, C. Huang, M. Zhu, S. Wang, A. Xu, X. Liu, X. Chen, S. Yan, B. Peng, J. Deng, X. Lei, Y. Shen, L. Liu, Defect engineering in rare-earth-doped SrTiO3 ceramics: Route to colossal capacitance material up to X9R capacitor standard, Mater. Today Commun. 39 (2024) 108680. https://doi.org/10.1016/j.mtcomm.2024.108680.

[167] Z. Shen, Y. Li, Q. Hu, W. Luo, Z. Wang, Dielectric properties of B–site charge balanced Dy–doped SrTiO3 ceramics for energy storage, J. Electroceramics 34 (2015) 236–240. https://doi.org/10.1007/s10832-014-9980-7.

[168] Z.-Y. Shen, Q.-G. Hu, Y.-M. Li, Z.-M. Wang, W.-Q. Luo, Y. Hong, Z.-X. Xie, R.-H. Liao, Structure and energy storage properties of Ti vacancies charge compensated Re2O3-doped SrTiO3 (Re = Pr, Nd, Gd) ceramics, J. Mater. Sci. Mater. Electron. 24 (2013) 3089–3094. https://doi.org/10.1007/s10854-013-1215-1.

[169] Structure and Dielectric Properties of Re_(0.02)Sr_(0.98)Ti_(0.995)O_3(Re=La,Sm,Er) Ceramic - CNKI, (n.d.). https://www.cnki.net/kcms/detail/11.2310.TQ.20130628.1051.001.html (accessed November 25, 2024).

[170] J. Karczewski, B. Riegel, M. Gazda, P. Jasinski, B. Kusz, Electrical and structural properties of Nb-doped SrTiO3 ceramics, J. Electroceramics 24 (2010) 326–330. https://doi.org/10.1007/s10832-009-9578-7.

[171] T. Fix, R. Bali, N. Stelmashenko, M.G. Blamire, Influence of the dopant concentration in In-doped SrTiO3 on the structural and transport properties, Solid State Commun. 146 (2008) 428–430. https://doi.org/10.1016/j.ssc.2008.03.019.

[172] S. Steinsvik, R. Bugge, J. Gjønnes, J. Taftø, T. Norby, THE DEFECT STRUCTUFE OF SrTi1−xFexO3−y (x = 0–0.8) INVESTIGATED BY ELECTRICAL CONDUCTIVITY MEASUREMENTS AND ELECTRON ENERGY LOSS SPECTROSCOPY (EELS), J. Phys. Chem. Solids 58 (1997) 969–976. https://doi.org/10.1016/S0022-3697(96)00200-4.

[173] L. Chen, S. Zhang, L. Wang, D. Xue, S. Yin, Photocatalytic activity of Zr:SrTiO3 under UV illumination, J. Cryst. Growth 311 (2009) 735–737. https://doi.org/10.1016/j.jcrysgro.2008.09.181.

[174] A.V. Kovalevsky, S. Populoh, S.G. Patrício, P. Thiel, M.C. Ferro, D.P. Fagg, J.R. Frade, A. Weidenkaff, Design of SrTiO3-Based Thermoelectrics by Tungsten Substitution, J. Phys. Chem. C 119 (2015) 4466–4478. https://doi.org/10.1021/jp510743h.

[175] F. Fang, J. Zhang, Z. Su, F. Xu, J. Li, K. Chang, Boost of solar water splitting on SrTiO3 by designing V-ions center for localizing defect charge to suppress deep trap, J. Catal. 425 (2023) 422–431. https://doi.org/10.1016/j.jcat.2023.06.011.

[176] P.C. Paul, A. Shah, L.R. Singh, Dr.M. Mahato, D.K. Mahato, Mn-Doped Srtio3 and Srtio3-Fe2o3 Composite Perovskites: Photocatalytic Dye Degradation and Supercapacitor Application, SSRN, 2023. https://doi.org/10.2139/ssrn.4333533.

[177] M. Lamhani, Z. Chchiyai, A. Elomrani, B. Manoun, A. Hasnaoui, Enhanced Photocatalytic Water Splitting of SrTiO3 Perovskite through Cobalt Doping: Experimental and Theoretical DFT Understanding, Inorg. Chem. 62 (2023) 13405–13418. https://doi.org/10.1021/acs.inorgchem.3c01758.

[178] Z. Li, G. Zhu, W. Zhang, L. Zhu, B. Cao, J. Gao, X. Shi, Y. Huang, P. Liu, M. Hojamberdiev, Dual-functional copper (Cu0/Cu2+)-modified SrTiO3-δ nanosheets with enhanced photothermal

catalytic performance for CO2 reduction and H2 evolution, Chem. Eng. J. 452 (2023) 139378. https://doi.org/10.1016/j.cej.2022.139378.

[179] F. Benlakhdar, M.A. Ghebouli, Z. Zerrougui, K. Bouferrache, Y. Slimani, B. Ghebouli, I. Bouchama, T. Chihi, M. Fatmi, S.A. Mouhammad, N. Algethami, S. Alomairy, Structural, elastic, mechanical and optoelectronic properties of zinc-doped SrTiO3 perovskite compounds, Mod. Phys. Lett. B (2023). https://doi.org/10.1142/S0217984923502007.

[180] H.A. Centurion, L.G. Rabelo, I. Rodriguez-Gutierrez, M.M. Ferrer, J. Bettini, H. Wender, L.M. Rossi, F.L. Souza, R.V. Gonçalves, Constructing Particulate p–n Heterojunction Mo:SrTiO3/NiO@Ni(OH)2 for Enhanced H2 Evolution under Simulated Solar Light, ACS Appl. Energy Mater. 5 (2022) 12727–12738. https://doi.org/10.1021/acsaem.2c02337.

[181] M. Matsumura, M. Hiramoto, H. Tsubomura, Photoelectrolysis of Water under Visible Light with Doped SrTiO3 Electrodes, J. Electrochem. Soc. 130 (1983) 326. https://doi.org/10.1149/1.2119704.

[182] A. Łącz, Ł. Łańcucki, R. Lach, B. Kamecki, E. Drożdż, Structural and electrical properties of Cr-doped SrTiO3 porous materials, Int. J. Hydrog. Energy 43 (2018) 8999–9005. https://doi.org/10.1016/j.ijhydene.2018.03.180.

[183] F. Nan, X. Qiu, L. Zhou, Z. Li, H. Liu, Preparation method of rhodium-doped strontium titanate inverse opal structure photoelectrode, CN115928139A, 2023.

[184] S.W. Bae, P.H. Borse, J.S. Lee, Dopant dependent band gap tailoring of hydrothermally prepared cubic SrTixM1−xO3 (M=Ru,Rh,Ir,Pt,Pd) nanoparticles as visible light photocatalysts, Appl. Phys. Lett. 92 (2008) 104107. https://doi.org/10.1063/1.2897300.

[185] L. Yan, M.R. Suchomel, C. Grygiel, H.J. Niu, S.R.C. McMitchell, J. Bacsa, J.H. Clark, M. Werner, P.R. Chalker, M.J. Rosseinsky, High permittivity SrHf0.5Ti0.5O3 films grown by pulsed laser deposition, Appl. Phys. Lett. 94 (2009) 232903. https://doi.org/10.1063/1.3151815.

[186] C.V. Nguyen, T.N.Q. Trang, H.Q. Pham, V.T.H. Thu, V.T.T. Ho, One-step heating hydrothermal of iridium-doped cubic perovskite strontium titanate towards hydrogen evolution, Mater. Lett. 282 (2021) 128686. https://doi.org/10.1016/j.matlet.2020.128686.

[187] R. Konta, T. Ishii, H. Kato, A. Kudo, Photocatalytic Activities of Noble Metal Ion Doped SrTiO3 under Visible Light Irradiation, J. Phys. Chem. B 108 (2004) 8992–8995. https://doi.org/10.1021/jp049556p.

[188] V. Subramanian, R.K. Roeder, E.E. Wolf, Synthesis and UV−Visible-Light Photoactivity of Noble-Metal−SrTiO3 Composites, Ind. Eng. Chem. Res. 45 (2006) 2187–2193. https://doi.org/10.1021/ie050693y.

[189] A.V. Kovalevsky, M.H. Aguirre, S. Populoh, S.G. Patrício, N.M. Ferreira, S.M. Mikhalev, D.P. Fagg, A. Weidenkaff, J.R. Frade, Designing strontium titanate-based thermoelectrics: insight into defect chemistry mechanisms, J. Mater. Chem. A 5 (2017) 3909–3922. https://doi.org/10.1039/C6TA09860F.

[190] J. Zhou, R. Li, J. Liu, Y. Shao, K. Cui, X. Li, B-site vacancy Fe-doped strontium titanate and preparation method thereof, CN110483036A, 2019.

[191] M.L. Weber, Y.J. Sohn, R. Dittmann, R. Waser, N.H. Menzler, O. Guillon, C. Lenser, S. Nemšák, F. Gunkel, Reversibility limitations of metal exsolution reactions in niobium and nickel co-doped strontium titanate, J. Mater. Chem. A 11 (2023) 17718–17727. https://doi.org/10.1039/D3TA02927A.

[192] J. Cavazzani, E. Squizzato, E. Brusamarello, A. Glisenti, Exsolution in La and Ni co-doped strontium titanate: a suitable anode for running SOFCs on ammonia as alternative fuel, E3S Web Conf. 334 (2022) 04008. https://doi.org/10.1051/e3sconf/202233404008.

[193] J. Pradhan, R.L. Nayak, M.P.K. Sahoo, A.K. Pattanaik, Activating and modulating ferroelectric and optical properties in La/Nd co-doped SrTiO3 ceramics, J. Alloys Compd. 876 (2021) 160131. https://doi.org/10.1016/j.jallcom.2021.160131.

[194] K. Shan, Z.-Z. Yi, X.-T. Yin, L. Cui, D. Dastan, H. Garmestani, F.M. Alamgir, Diffusion kinetics mechanism of oxygen ion in dense diffusion barrier limiting current oxygen sensors, J. Alloys Compd. 855 (2021) 157465. https://doi.org/10.1016/j.jallcom.2020.157465.

[195] W. Pan, M. Cao, H. Wang, A. Jan, H. Hao, Z. Yao, H. Liu, Giant dielectric response in (Nb + Zn) co-doped strontium titanate ceramics tailored by atmosphere, Scr. Mater. 170 (2019) 166–171. https://doi.org/10.1016/j.scriptamat.2019.05.034.

[196] B. Kamecki, T. Miruszewski, K. Górnicka, T. Klimczuk, J. Karczewski, Characterization methods of nickel nano-particles obtained by the ex-solution process on the surface of Pr, Ni-doped SrTiO3 perovskite ceramics, SN Appl. Sci. 1 (2019) 322. https://doi.org/10.1007/s42452-019-0317-7.

[197] V.-Q.-T. Hoang, T.-Q.-P. Phan, V. Senthilkumar, V.-T. Doan, Y.S. Kim, M.-V. Le, Enhanced photocatalytic activities of vandium and molybdenum co-doped strontium titanate under visible light, Int. J. Appl. Ceram. Technol. 16 (2019) 1651–1658. https://doi.org/10.1111/ijac.13248.

[198] M.L. Weber, Q. Ma, P. Meuffels, F.V.E. Hensling, C. Lenser, F. Gunkel, N.H. Menzler, R. Dittmann, R. Waser, O. Guillon, Development of Epitaxial Thin Film Model Electrodes for the Systematic Investigation of Metal Exsolution from MIEC Perovskite Oxides, ECS Trans. 91 (2019) 1783. https://doi.org/10.1149/09101.1783ecst.

[199] S. Usuki, K. Yamatoya, Y. Kawamura, Y. Yamaguchi, N. Suzuki, K. Katsumata, C. Terashima, A. Fujishima, A. Kudo, K. Nakata, Denaturation of Lysozyme with Visible-light-responsive Photocatalysts of Ground Rhodium-doped and Ground Rhodium-antimony-co-doped Strontium Titanate, J. Oleo Sci. 67 (2018) 1521–1533. https://doi.org/10.5650/jos.ess18155.

[200] Z. He, M. Cao, L. Zhou, L. Zhang, J. Xie, S. Zhang, J. Qi, H. Hao, Z. Yao, Z. Yu, H. Liu, Origin of low dielectric loss and giant dielectric response in (Nb+Al) co-doped strontium titanate, J. Am. Ceram. Soc. 101 (2018) 5089–5097. https://doi.org/10.1111/jace.15762.

[201] M. Lv, Y. Xie, Y. Wang, X. Sun, F. Wu, H. Chen, S. Wang, C. Shen, Z. Chen, S. Ni, G. Liu, X. Xu, Bismuth and chromium co-doped strontium titanates and their photocatalytic properties under visible light irradiation, Phys. Chem. Chem. Phys. 17 (2015) 26320–26329. https://doi.org/10.1039/C5CP03889H.

[202] B.R. Sudireddy, K. Agersted, Sintering and Electrical Characterization of La and Nb Co-doped SrTiO3 Electrode Materials for Solid Oxide Cell Applications, Fuel Cells 14 (2014) 961–965. https://doi.org/10.1002/fuce.201400017.

[203] L. Lu, M. Verbraeken, M. Cassidy, J.T.S. Irvine, A Solid Oxide Fuel Cell with Lanthanum and Calcium Co-Doped Strontium Titanate as Support, ECS Trans. 57 (2013) 1415. https://doi.org/10.1149/05701.1415ecst.

[204] S. Sengodan, J.S. Yoon, M.Y. Yoon, H.J. Hwang, J. Shin, G. Kim, Electrochemical Performance of YST Infiltrated and Fe Doped YST Infiltrated YSZ Anodes for IT-SOFC, ECS Electrochem. Lett. 2 (2013) F45. https://doi.org/10.1149/2.004306eel.

[205] S. Sharma, P. Tiwari, S. Basu, N. Kumari, Harnessing the electrocatalytic potential of *in-situ* exsolution of Ni nanoparticles on lanthanum and calcium co-doped strontium titanate for CO2

reduction in solid oxide electrolysis cells, J. Alloys Compd. 996 (2024) 174831. https://doi.org/10.1016/j.jallcom.2024.174831.

[206] B.L. Phoon, C.W. Lai, J.C. Juan, P. Show, W. Chen, A review of synthesis and morphology of $SrTiO_3$ for energy and other applications, Int. J. Energy Res. 43 (2019) 5151–5174. https://doi.org/10.1002/er.4505.

[207] E.A.R. Assirey, Perovskite synthesis, properties and their related biochemical and industrial application, Saudi Pharm. J. 27 (2019) 817–829. https://doi.org/10.1016/j.jsps.2019.05.003.

[208] E. Rocha-Rangel, J. Lopez Hernandez, J.A. Rodriguez-Garcia, A.-M. Eddie Nahúm, C. Calles-Arriaga, W.J. Pech-Rodríguez, J.A. Castillo-Robles, Dielectric properties of strontium titanate synthesized by means of solid state reactions activated mechanically, J. Ceram. Process. Res. 18 (2017) 590–593.

[209] Luo Shiyong, Zhang Jiayun, Wang ning, Kinetics of Strontium Titanate Formation from Solid State Reaction between Strontium Carbonate and Anatase, High Temp. Mater. Process. 26 (2007) 33–42. https://doi.org/10.1515/HTMP.2007.26.1.33.

[210] Diffusion-Key Role in Solid State Crystalline Material - A Review, Int. J. Sci. Res. Sci. Eng. Technol. 1 (2015) 486–489. https://doi.org/10.32628/IJSRSET118482.

[211] T. Moriga, S. Yabui, Y. Higashi, K.-I. Murai, Z.-W. Wang, M. Mori, A-SITE DEFICIENCY AND STRUCTURAL AND ELECTRICAL CHARACTERISTICS OF (Sr1-xREx)1-yTiO3 PEROVSKITES (RE=La, Nd and Sm), Int. J. Mod. Phys. Conf. Ser. 06 (2012) 85–90. https://doi.org/10.1142/S201019451200298X.

[212] M.H. El-Sadek, M.M. Farahat, H.H. Ali, Z.I. Zaki, Synthesis of SrTiO3 from celestite and rutile by mechanical activation assisted Solid-State reaction, Adv. Powder Technol. 33 (2022) 103548. https://doi.org/10.1016/j.apt.2022.103548.

[213] M. Dahan, L. Fadeev, H. Hayun, M. Gozin, Y. Gelbstein, B.A. Rosen, Influence of the La0.2Sr0.7Ti0.95Ni0.05O3 (LSTN) Synthesis Method on SOFC Anode Performance, Catalysts 14 (2024) 79. https://doi.org/10.3390/catal14010079.

[214] Z. Lou, P. Zhang, P. Chen, Z. Wei, J. Gou, J. Xu, C. Gong, F. Gao, Optimized thermoelectric performance driven by A-site deficient in SrLa0.1TiO3−/TiO2− composites, J. Am. Ceram. Soc. 107 (2024) 4717–4728. https://doi.org/10.1111/jace.19744.

[215] H. Zhao, F. Gao, X. Li, C. Zhang, Y. Zhao, Electrical properties of yttrium doped strontium titanate with A-site deficiency as potential anode materials for solid oxide fuel cells, Solid State Ion. 180 (2009) 193–197. https://doi.org/10.1016/j.ssi.2008.11.018.

[216] M. Mori, Z. Wang, T. Itoh, S. Yabui, K. Murai, T. Moriga, A-Site and B-Site Non-stoichiometry and Sintering Characteristics of (Sr1−xLax)1−yTi1−zO3 Perovskites, J. Fuel Cell Sci. Technol. 8 (2011) 051014. https://doi.org/10.1115/1.4003982.

[217] R.K. Ramanjeet Kaur, A.K.T. Anand K Tyagi, Sol Gel Synthesis and Characterization of Strontium Titanates, Orient. J. Chem. 38 (2022) 94–101. https://doi.org/10.13005/ojc/380111.

[218] Y. Ma, Z. Wu, H. Wang, G. Wang, Y. Zhang, P. Hu, Y. Li, D. Gao, H. Pu, B. Wang, X. Qi, Synthesis of nanocrystalline strontium titanate by a sol–gel assisted solid phase method and its formation mechanism and photocatalytic activity, CrystEngComm 21 (2019) 3982–3992. https://doi.org/10.1039/C9CE00495E.

[219] Y. Pei, Synthesis Of Nano-Porous Strontium Titanate Materials for Photocatalysis, Highlights Sci. Eng. Technol. 96 (2024) 220–226. https://doi.org/10.54097/m5a1kf92.

[220] P. Visuttipitukul, P. Sooksaen, N. Yongvanich, Sol-Gel Synthesis of SrTiO3 Nanoparticles Using Acetic Acid as a Chelating Agent, Ferroelectrics 457 (2013) 82–88. https://doi.org/10.1080/00150193.2013.848755.

[221] L.L. Hench, J.K. West, The sol-gel process, Chem. Rev. 90 (1990) 33–72. https://doi.org/10.1021/cr00099a003.

[222] U. Schubert, Chemistry and Fundamentals of the Sol–Gel Process, (n.d.). https://onlinelibrary.wiley.com/doi/10.1002/9783527670819.ch01 (accessed August 16, 2024).

[223] D. Bokov, A. Turki Jalil, S. Chupradit, W. Suksatan, M. Javed Ansari, I.H. Shewael, G.H. Valiev, E. Kianfar, Nanomaterial by Sol-Gel Method: Synthesis and Application, Adv. Mater. Sci. Eng. 2021 (2021) 5102014. https://doi.org/10.1155/2021/5102014.

[224] K. Shan, F. Zhai, Z. Yi, W. Liu, A-site and B-site co-doping strontium titanate mixed conductor material with A-site deficiency, CN106098137A, 2016.

[225] G. Chen, Y. Luo, Y. Gao, R. Guo, W. Ma, M. Liu, S. Geng, Chemical Compatibility of A-site Deficient La Substituted SrTiO3 Anode and Stabilized Zirconia Electrolyte, ECS Trans. 68 (2015) 1465. https://doi.org/10.1149/06801.1465ecst.

[226] Y. Zhang, L. Zhong, D. Duan, Single-step hydrothermal synthesis of strontium titanate nanoparticles from crystalline anatase titanium dioxide, Ceram. Int. 41 (2015) 13516–13524. https://doi.org/10.1016/j.ceramint.2015.07.145.

[227] B. Wang, A. Bian, F. Jia, J. Lan, H. Yang, K. Yan, L. Xie, H. Qiao, X. Chang, H. Lin, H. Zhang, Y. Huang, "Dual-functional" strontium titanate nanotubes designed based on fusion peptides simultaneously enhancing anti-infection and osseointegration, Biomater. Adv. 133 (2022) 112650. https://doi.org/10.1016/j.msec.2022.112650.

[228] G. Canu, V. Buscaglia, Hydrothermal synthesis of strontium titanate: thermodynamic considerations, morphology control and crystallisation mechanisms, CrystEngComm 19 (2017) 3867–3891. https://doi.org/10.1039/C7CE00834A.

[229] K.S. Kiran, R. Shashanka, S.V. Lokesh, Enhanced Photocatalytic Activity of Hydrothermally Synthesized Perovskite Strontium Titanate Nanocubes, Top. Catal. (2022). https://doi.org/10.1007/s11244-021-01558-2.

[230] X. Wei, G. Xu, Z. Ren, Y. Wang, G. Shen, G. Han, Synthesis and Characterization of Mesoporous SrTiO3 Spheres via a Poly Vinyl Alcohol-Assisted Hydrothermal Route, J. Am. Ceram. Soc. 91 (2008) 299–302. https://doi.org/10.1111/j.1551-2916.2007.02015.x.

[231] D. Chen, X. Jiao, M. Zhang, Hydrothermal synthesis of strontium titanate powders with nanometer size derived from different precursors, J. Eur. Ceram. Soc. 20 (2000) 1261–1265. https://doi.org/10.1016/S0955-2219(00)00003-0.

[232] S. Zhang, J. Liu, Y. Han, B. Chen, X. Li, Formation mechanisms of SrTiO3 nanoparticles under hydrothermal conditions, Mater. Sci. Eng. B 110 (2004) 11–17. https://doi.org/10.1016/j.mseb.2004.01.017.

[233] U.A. Joshi, J.S. Lee, Template-Free Hydrothermal Synthesis of Single-Crystalline Barium Titanate and Strontium Titanate Nanowires, Small 1 (2005) 1172–1176. https://doi.org/10.1002/smll.200500055.

[234] P. Guan, Y. Zhu, M. Li, T. Zeng, X. Li, R. Tian, N. Sharma, Z. Xu, T. Wan, L. Hu, Y. Liu, C. Cazorla, D. Chu, Enhancing cyclic and in-air stability of Ni-Rich cathodes through perovskite oxide surface coating, J. Colloid Interface Sci. 628 (2022) 407–418. https://doi.org/10.1016/j.jcis.2022.08.061.

[235] K.-L. Lim, J.-C. Sin, S.-M. Lam, H. Zeng, H. Lin, H. Li, L. Huang, J.-W. Lim, Controlled solvothermal synthesis of self-assembled SrTiO3 microstructures for expeditious solar-driven photocatalysis

dye effluents degradation, Environ. Res. 251 (2024) 118647. https://doi.org/10.1016/j.envres.2024.118647.

[236] K. Li, J. Zhu, F. Zhang, Morphology-controlled fabrication of Nb5+ doped SrTiO3 for promoting photocatalytic reduction of Cr(VI), Mol. Catal. 553 (2024) 113754. https://doi.org/10.1016/j.mcat.2023.113754.

[237] W. Zhang, L. Cao, W. Wang, G. Su, W. Liu, Synthesis, microstructure and dielectric properties of zirconium doped barium strontium titanate obtained by solvothermal method, J. Mater. Sci. Mater. Electron. 24 (2013) 2234–2239. https://doi.org/10.1007/s10854-013-1084-7.

[238] U. Sulaeman, S. Yin, T. Sato, Solvothermal synthesis of designed nonstoichiometric strontium titanate for efficient visible-light photocatalysis, Appl. Phys. Lett. 97 (2010) 103102. https://doi.org/10.1063/1.3486466.

[239] Q.-Q. Fu, H. Gu, J.-J. Xing, Z. Cao, J. Wang, Controlling the A-site deficiency and oxygen vacancies by donor-doping in pre-reductive-sintered thermoelectric SrTiO3 ceramics, Acta Mater. 229 (2022) 117785. https://doi.org/10.1016/j.actamat.2022.117785.

[240] A. Loppinet-Serani, C. Aymonier, F. Cansell, Supercritical water for environmental technologies, J. Chem. Technol. Biotechnol. 85 (2010) 583–589. https://doi.org/10.1002/jctb.2323.

[241] G. Philippot, C. Elissalde, M. Maglione, C. Aymonier, Supercritical fluid technology: A reliable process for high quality BaTiO3 based nanomaterials, Adv. Powder Technol. 25 (2014) 1415–1429. https://doi.org/10.1016/j.apt.2014.02.016.

[242] C. Aymonier, G. Philippot, A. Erriguible, S. Marre, Playing with chemistry in supercritical solvents and the associated technologies for advanced materials by design, J. Supercrit. Fluids 134 (2018) 184–196. https://doi.org/10.1016/j.supflu.2017.12.021.

[243] C. Aymonier, A. Loppinet-Serani, H. Reverón, Y. Garrabos, F. Cansell, Review of supercritical fluids in inorganic materials science, J. Supercrit. Fluids 38 (2006) 242–251. https://doi.org/10.1016/j.supflu.2006.03.019.

[244] T. Adschiri, A. Yoko, Supercritical fluids for nanotechnology, J. Supercrit. Fluids 134 (2018) 167–175. https://doi.org/10.1016/j.supflu.2017.12.033.

[245] F. Cansell, C. Aymonier, A. Loppinet-Serani, Review on materials science and supercritical fluids, Curr. Opin. Solid State Mater. Sci. 7 (2003) 331–340. https://doi.org/10.1016/j.cossms.2004.01.003.

[246] A. Auxéméry, G. Philippot, M.R. Suchomel, D. Testemale, C. Aymonier, Stabilization of Tetragonal Zirconia Nanocrystallites Using an Original Supercritical-Based Synthesis Route, Chem. Mater. 32 (2020) 8169–8181. https://doi.org/10.1021/acs.chemmater.0c01550.

[247] M.P. Tsang, G. Philippot, C. Aymonier, G. Sonnemann, Supercritical Fluid Flow Synthesis to Support Sustainable Production of Engineered Nanomaterials: Case Study of Titanium Dioxide, ACS Sustain. Chem. Eng. 6 (2018) 5142–5151. https://doi.org/10.1021/acssuschemeng.7b04800.

[248] E. Lester, P. Blood, J. Denyer, D. Giddings, B. Azzopardi, M. Poliakoff, Reaction engineering: The supercritical water hydrothermal synthesis of nano-particles, J. Supercrit. Fluids 37 (2006) 209–214. https://doi.org/10.1016/j.supflu.2005.08.011.

[249] T. Adschiri, K. Kanazawa, K. Arai, Rapid and Continuous Hydrothermal Crystallization of Metal Oxide Particles in Supercritical Water, J. Am. Ceram. Soc. 75 (1992) 1019–1022. https://doi.org/10.1111/j.1151-2916.1992.tb04179.x.

[250] T. Adschiri, K. Kanazawa, K. Arai, Crystalization of Metal Oxide Particle through Hydrolysis in Supercritical Water, in: World Congr. Chem. Eng., 1991.

[251] H. Hayashi, Y. Hakuta, Hydrothermal Synthesis of Metal Oxide Nanoparticles in Supercritical Water, Materials 3 (2010) 3794–3817. https://doi.org/10.3390/ma3073794.

[252] S. Ohara, T. Mousavand, M. Umetsu, S. Takami, T. Adschiri, Y. Kuroki, M. Takata, Hydrothermal synthesis of fine zinc oxide particles under supercritical conditions, Solid State Ion. 172 (2004) 261–264. https://doi.org/10.1016/j.ssi.2004.02.044.

[253] S. Ohara, T. Mousavand, T. Sasaki, M. Umetsu, T. Naka, T. Adschiri, Continuous production of fine zinc oxide nanorods by hydrothermal synthesis in supercritical water, J. Mater. Sci. 43 (2008) 2393–2396. https://doi.org/10.1007/s10853-007-1823-3.

[254] L. Liu, S. Wang, G. Jiang, H. Liu, J. Yang, Y. Li, Continuous supercritical hydrothermal synthesis of stabilized ZrO2 nanocomposites: Doping mechanism of typical metals and transition elements, Mater. Today Chem. 35 (2024) 101902. https://doi.org/10.1016/j.mtchem.2024.101902.

[255] L. Liu, S. Wang, B. Zhang, G. Jiang, J. Yang, Supercritical hydrothermal synthesis of nano-ZrO2: Influence of technological parameters and mechanism, J. Alloys Compd. 898 (2022) 162878. https://doi.org/10.1016/j.jallcom.2021.162878.

[256] Y. Hakuta, H. Takashima, M. Takesada, Hydrothermal synthesis of perovskite metal oxide nanoparticles in supercritical water, Ferroelectrics 539 (2019) 1–8. https://doi.org/10.1080/00150193.2019.1569999.

[257] P.W. Dunne, C.L. Starkey, A.S. Munn, S.V.Y. Tang, O. Luebben, I. Shvets, A.G. Ryder, Y. Casamayou-Boucau, L. Morrison, E.H. Lester, Bench- and pilot-scale continuous-flow hydrothermal production of barium strontium titanate nanopowders, Chem. Eng. J. 289 (2016) 433–441. https://doi.org/10.1016/j.cej.2015.12.056.

[258] Y. Denis, C. Elissalde, M.R. Suchomel, M. Gayot, F. Weill, C. Labrugère, L. Etienne, M. Vaudesca, N. Cam, U.-C. Chung, H. Reveron, J. Chevalier, T.H. de Beauvoir, C. Estournès, C. Aymonier, G. Goglio, G. Philippot, Continuous Flow Synthesis of Yttria-Stabilized-Zirconia Nanocrystals in Supercritical Solvothermal Conditions, Adv. Mater. Technol. 9 (2024) 2301474. https://doi.org/10.1002/admt.202301474.

[259] A. Auxéméry, B.B. Frias, E. Smal, K. Dziadek, G. Philippot, P. Legutko, M. Simonov, S. Thomas, A. Adamski, V. Sadykov, K. Parkhomenko, A.-C. Roger, C. Aymonier, Continuous supercritical solvothermal preparation of nanostructured ceria-zirconia as supports for dry methane reforming catalysts, J. Supercrit. Fluids 162 (2020) 104855. https://doi.org/10.1016/j.supflu.2020.104855.

[260] G. Philippot, K.M.Oe. Jensen, M. Christensen, C. Elissalde, M. Maglione, B.B. Iversen, C. Aymonier, Coupling in situ synchrotron radiation with ex situ spectroscopy characterizations to study the formation of Ba1- SrTiO3 nanoparticles in supercritical fluids, J. Supercrit. Fluids 87 (2014) 111–117. https://doi.org/10.1016/j.supflu.2013.12.009.

[261] K.-M. Choi, S.-H. Hong, D.-Y. Lim, J.-S. Nho, S.-B. Cho, Preparation of SrTiO3:Pr3+ phosphors using supercritical fluid method and its luminescence properties, J. Korean Ceram. Soc. 39 (2002) 1023–1027. https://doi.org/10.4191/kcers.2002.39.11.1023.

[262] H. Reverón, C. Elissalde, C. Aymonier, O. Bidault, M. Maglione, F. Cansell, Supercritical Fluid Route for Synthesizing Crystalline Barium Strontium Titanate Nanoparticles, J. Nanosci. Nanotechnol. 5 (2005) 1741–1744. https://doi.org/10.1166/jnn.2005.409.

[263] H. Reverón, C. Elissalde, C. Aymonier, C. Bousquet, M. Maglione, F. Cansell, Continuous supercritical synthesis and dielectric behaviour of the whole BST solid solution, Nanotechnology 17 (2006) 3527. https://doi.org/10.1088/0957-4484/17/14/028.

[264] T. Ono, K. Sue, D. Furuta, M. Aoki, Y. Hakuta, Y. Takebayashi, S. Yoda, T. Furuya, T. Sato, T. Hiaki, Continuous hydrothermal synthesis of Ca1−xSrxTiO3 solid-solution nanoparticles using a T-type micromixer, J. Supercrit. Fluids 85 (2014) 159–164. https://doi.org/10.1016/j.supflu.2013.11.010.

[265] T. Sasaki, A. Tanaka, M. Suzuki, M. Ajiri, Method for Producing Strontium Titanate Fine Particles and Strontium Titanate Fine Particles, JP2015151304A, 2015.

[266] M. Kim, S.-A. Hong, N. Shin, Y.H. Lee, Y. Shin, Synthesis of strontium titanate nanoparticles using supercritical water, Ceram. Int. 42 (2016) 17853–17857. https://doi.org/10.1016/j.ceramint.2016.08.120.

[267] A. Yoko, M. Akizuki, Y. Oshima, Formation mechanism of barium zirconate nanoparticles under supercritical hydrothermal synthesis, J. Nanoparticle Res. 16 (2014) 2330. https://doi.org/10.1007/s11051-014-2330-5.

[268] A. Yoko, M. Akizuki, N. Umezawa, T. Ohno, Y. Oshima, Growth of Ba1−xSrxZrO3 ($0 \leq x \leq 1$) nanoparticles in supercritical water, RSC Adv. 6 (2016) 67525–67533. https://doi.org/10.1039/C6RA12288D.

[269] A. Yoko, J. Wang, N. Umezawa, T. Ohno, Y. Oshima, A-Site Cation Bulk and Surface Diffusion in A-Site-Deficient BaZrO3 and SrZrO3 Perovskites, J. Phys. Chem. C 121 (2017) 12220–12229. https://doi.org/10.1021/acs.jpcc.7b02677.

[270] A. Yoko, H. Naito, G. Seong, T. Tomai, T. Adschiri, Nucleation and Coalescence of BaTiO3 Using a Continuous Flow Reactor with Water–Ethanol Mixed Solvents, J. Phys. Chem. C 125 (2021) 19489–19496. https://doi.org/10.1021/acs.jpcc.1c04914.

[271] K. Shan, Z.-Z. Yi, Synthesis and ionic-electronic conductivity of A-site deficient (Y, In) co-doped SrTiO3 as novel materials for mixed conductor, Scr. Mater. 107 (2015) 119–122. https://doi.org/10.1016/j.scriptamat.2015.06.001.

[272] Y. Hakuta, K. Sue, H. Takashima, Synthesis of praseodymium-ion-doped perovskite nanophosphor in supercritical water, Mater. Res. Express 5 (2018) 055034. https://doi.org/10.1088/2053-1591/aaa25a.

[273] H. Reverón, C. Aymonier, A. Loppinet-Serani, C. Elissalde, M. Maglione, F. Cansell, Single-step synthesis of well-crystallized and pure barium titanate nanoparticles in supercritical fluids, Nanotechnology 16 (2005) 1137. https://doi.org/10.1088/0957-4484/16/8/026.

[274] M. Tsang, G. Philippot, C. Aymonier, G. Sonnemann, Anticipatory life-cycle assessment of supercritical fluid synthesis of barium strontium titanate nanoparticles, Green Chem. 18 (2016) 4924–4933. https://doi.org/10.1039/C6GC00646A.

[275] C. Han, A. Yoko, A. Taufik, Wahyudiono, S. Ohara, T. Adschiri, Non-equilibrium Mn doping to CeO2 nanoparticles in continuous-flow hydrothermal synthesis, Chem. Eng. J. 496 (2024) 154022. https://doi.org/10.1016/j.cej.2024.154022.

[276] G. Philippot, Supercritical fluids synthesis of BaTiO3 based nanoparticles : study of the particles growth mechanisms, powder processing and ferroelectric properties, These de doctorat, Bordeaux, 2014. https://theses.fr/2014BORD0175 (accessed October 3, 2024).

[277] V.K. Dwivedi, A. Juyal, S. Mukhopadhyay, Colossal enhancement of electrical conductivity in Y2Ir2O7 nanoparticles, Mater. Res. Express 3 (2016) 115020. https://doi.org/10.1088/2053-1591/3/11/115020.

[278] R. Shahid, S. Murugavel, Particle size dependent confinement and lattice strain effects in LiFePO4, Phys. Chem. Chem. Phys. 15 (2013) 18809–18814. https://doi.org/10.1039/C3CP52953C.

[279] C. Elissalde, T. Hérisson de Beauvoir, U.-C. Chung, E. Martin, Y. Denis, J. de Landtsheer, M.R. Suchomel, G. Goglio, G. Philippot, C. Estournès, Densification of zirconia-based ceramics by non-conventional sintering processes and chemical pathways, Ceram. Int. 50 (2024) 37385–37394. https://doi.org/10.1016/j.ceramint.2024.06.155.

[280] G. Philippot, M. Albino, U.-C. Chung, M. Josse, C. Elissalde, M. Maglione, C. Aymonier, Continuous BaTi1−yZryO3 (0≤y≤1) nanocrystals synthesis in supercritical fluids for nanostructured lead-free ferroelectric ceramics, Mater. Des. 86 (2015) 354–360. https://doi.org/10.1016/j.matdes.2015.07.111.

[281] U.-C. Chung, C. Elissalde, M. Maglione, C. Estournès, M. Paté, J.P. Ganne, Low-losses, highly tunable Ba0.6Sr0.4TiO3/MgO composite, Appl. Phys. Lett. 92 (2008) 042902. https://doi.org/10.1063/1.2837621.

[282] C. Elissalde, M. Maglione, C. Estournès, Tailoring Dielectric Properties of Multilayer Composites Using Spark Plasma Sintering, J. Am. Ceram. Soc. 90 (2007) 973–976. https://doi.org/10.1111/j.1551-2916.2007.01485.x.

[283] M. Maglione, G. Philippot, D. Levasseur, S. Payan, C. Aymonier, C. Elissalde, Defect chemistry in ferroelectric perovskites: long standing issues and recent advances, Dalton Trans. 44 (2015) 13411–13418. https://doi.org/10.1039/C5DT01897H.

[284] E. Martin, U.C. Chung, M. Duttine, M.A. Dourges, G. Clermont, C. Labrugère, S. Fourcade, D. Michau, C. Estournès, T. Hérisson de Beauvoir, F. Mauvy, V. Jubera, M. Maglione, G. Goglio, C. Elissalde, Defect chemistry to trigger zirconia densification at low temperatures by Spark Plasma Sintering, Open Ceram. 17 (2024) 100518. https://doi.org/10.1016/j.oceram.2023.100518.

[285] R. Berthelot, B. Basly, S. Buffière, J. Majimel, G. Chevallier, A. Weibel, A. Veillère, L. Etienne, U.-C. Chung, G. Goglio, M. Maglione, C. Estournès, S. Mornet, C. Elissalde, From core–shell BaTiO 3 @MgO to nanostructured low dielectric loss ceramics by spark plasma sintering, J. Mater. Chem. C 2 (2014) 683–690. https://doi.org/10.1039/C3TC31990C.

[286] I. Saadeddin, B. Pecquenard, J.P. Manaud, R. Decourt, C. Labrugère, T. Buffeteau, G. Campet, Synthesis and characterization of single- and co-doped SnO2 thin films for optoelectronic applications, Appl. Surf. Sci. 253 (2007) 5240–5249. https://doi.org/10.1016/j.apsusc.2006.11.049.

[287] D.D.L. Chung, A critical review of electrical-resistance-based self-sensing in conductive cement-based materials, Carbon 203 (2023) 311–325. https://doi.org/10.1016/j.carbon.2022.11.076.

[288] E. Alleno, D. Bérardan, C. Byl, C. Candolfi, R. Daou, R. Decourt, E. Guilmeau, S. Hébert, J. Hejtmanek, B. Lenoir, P. Masschelein, V. Ohorodnichuk, M. Pollet, S. Populoh, D. Ravot, O. Rouleau, M. Soulier, Invited Article: A round robin test of the uncertainty on the measurement of the thermoelectric dimensionless figure of merit of Co0.97Ni0.03Sb3, Rev. Sci. Instrum. 86 (2015) 011301. https://doi.org/10.1063/1.4905250.

[289] M.B. Smith, K. Page, T. Siegrist, P.L. Redmond, E.C. Walter, R. Seshadri, L.E. Brus, M.L. Steigerwald, Crystal Structure and the Paraelectric-to-Ferroelectric Phase Transition of Nanoscale BaTiO3, J. Am. Chem. Soc. 130 (2008) 6955–6963. https://doi.org/10.1021/ja0758436.

[290] X.W. Wu, X.J. Liu, Negative pressure effects in strontium titanate nanoparticles, J. Lumin. 122–123 (2007) 869–872. https://doi.org/10.1016/j.jlumin.2006.01.312.

[291] C.T. Lee, M.S. Zhang, Z. Yin, W. Zhu, Structural and vibrational properties of BaxSr1−xTiO3 nanoparticles, J. Mater. Sci. 40 (2005) 1277–1279. https://doi.org/10.1007/s10853-005-6951-z.

[292] M.L. Moreira, V.M. Longo, W.Jr. Avansi, M.M. Ferrer, J. Andrés, V.R. Mastelaro, J.A. Varela, É. Longo, Quantum Mechanics Insight into the Microwave Nucleation of SrTiO3 Nanospheres, J. Phys. Chem. C 116 (2012) 24792–24808. https://doi.org/10.1021/jp306638r.

[293] V. Dwij, B.K. De, S. Tyagi, G. Sharma, V. Sathe, Fano resonance and relaxor behavior in Pr doped SrTiO3: A Raman spectroscopic investigation, Phys. B Condens. Matter 620 (2021) 413265. https://doi.org/10.1016/j.physb.2021.413265.

[294] Z. Wang, C. Li, H. Xie, Z. Zhang, W. Huang, S. Ke, L. Shu, Effect of Grain Size on Flexoelectricity, Phys. Rev. Appl. 18 (2022) 064017. https://doi.org/10.1103/PhysRevApplied.18.064017.

[295] G. Yang, J. Feng, W. Sun, N. Dai, M. Hou, X. Hao, J. Qiao, K. Sun, The characteristic of strontium-site deficient perovskites SrxFe1.5Mo0.5O6−δ (x = 1.9–2.0) as intermediate-temperature solid oxide fuel cell cathodes, J. Power Sources 268 (2014) 771–777. https://doi.org/10.1016/j.jpowsour.2014.06.129.

[296] V.V. Kharton, M.V. Patrakeev, E.V. Tsipis, M. Avdeev, E.N. Naumovich, P.V. Anikina, J.C. Waerenborgh, Oxygen nonstoichiometry, chemical expansion, mixed conductivity, and anodic behavior of Mo-substituted Sr3Fe2O7-δ, Solid State Ion. 181 (2010) 1052–1063. https://doi.org/10.1016/j.ssi.2010.06.004.

[297] O. Marina, Thermal, electrical, and electrocatalytical properties of lanthanum-doped strontium titanate, Solid State Ion. 149 (2002) 21–28. https://doi.org/10.1016/S0167-2738(02)00140-6.

[298] M. Sedlar, M. Sayer, Reactivity of titanium isopropoxide, zirconium propoxide and niobium ethoxide in the system of 2-methoxyethanol, 2,4-pentanedione and water, J. Sol-Gel Sci. Technol. 5 (1995) 27–40. https://doi.org/10.1007/BF00486708.

[299] V.G. Kessler, S. Gohil, S. Parola, Interaction of some divalent metal acetylacetonates with Al, Ti, Nb and Ta isopropoxides. Factors influencing the formation and stability of heterometallic alkoxide complexes, Dalton Trans. (2003) 544–550. https://doi.org/10.1039/B206662A.

[300] M. Krunks, I. Oja, K. Tõnsuaadu, M. Es-Souni, M. Gruselle, L. Niinistö, Thermoanalytical study of acetylacetonate-modified titanium(IV) isopropoxide as a precursor for TiO2 films, J. Therm. Anal. Calorim. 80 (2005) 483–488. https://doi.org/10.1007/s10973-005-0681-y.

[301] S. Hui, A. Petric, Electrical Properties of Yttrium-Doped Strontium Titanate under Reducing Conditions, J. Electrochem. Soc. 149 (2002) J1. https://doi.org/10.1149/1.1420706.

[302] P. Blennow, A. Hagen, K.K. Hansen, L.R. Wallenberg, M. Mogensen, Defect and electrical transport properties of Nb-doped SrTiO3, Solid State Ion. 179 (2008) 2047–2058. https://doi.org/10.1016/j.ssi.2008.06.023.

[303] B. Bochentyn, J. Karczewski, S. Molin, T. Klimczuk, M. Gazda, P. Jasinski, D.J. Safarik, B. Kusz, The comparison of SrTi0.98Nb0.02O3–δ-CeO2 and SrTi0.98Nb0.02O3–δ-YSZ composites for use in SOFC anodes, J. Electroceramics 28 (2012) 132–138. https://doi.org/10.1007/s10832-012-9693-8.

[304] S. Molin, W. Lewandowska-Iwaniak, B. Kusz, M. Gazda, P. Jasinski, Structural and electrical properties of Sr(Ti, Fe)O3-δ materials for SOFC cathodes, J. Electroceramics 28 (2012) 80–87. https://doi.org/10.1007/s10832-012-9683-x.

[305] J.-H. Lin, C.-S. Hwang, F.-R. Sie, Preparation and thermoelectric properties of Nd and Dy co-doped SrTiO3 bulk materials, Mater. Res. Bull. 122 (2020) 110650. https://doi.org/10.1016/j.materresbull.2019.110650.

[306] A.V. Kovalevsky, A.A. Yaremchenko, S. Populoh, A. Weidenkaff, J.R. Frade, Enhancement of thermoelectric performance in strontium titanate by praseodymium substitution, J. Appl. Phys. 113 (2013) 053704. https://doi.org/10.1063/1.4790307.

Introduction & Contextualisation

Le changement climatique est une préoccupation majeure qu'il faut prendre en compte afin de trouver des solutions pour réduire les risques environnementaux. Selon une étude de l'Agence Internationale de l'Énergie (AIE) publiée en mars 2024, un nouveau record a été atteint en 2023 avec 37,4 milliards de tonnes (Gt) d'émissions mondiales de CO_2. Il est également important de noter que 42 % des émissions mondiales de CO_2 sont dues à la production d'électricité. Pour citer une phrase importante de ce rapport : « *Les émissions ont augmenté en 2023, mais les énergies propres en limitent la croissance.* ».

Afin de réduire l'impact de la production d'électricité sur les émissions de CO_2, de nombreuses solutions sont développées, la plus connue étant l'utilisation des énergies renouvelables. Ces énergies reposent sur l'utilisation de ressources infinies telles que l'énergie solaire ou éolienne. Cependant, ces énergies présentent certains inconvénients par rapport aux méthodes conventionnelles ou à l'énergie fossile pour produire de l'électricité, notamment leur « flexibilité ». Leur production varie en fonction du moment de la journée ou de la période de l'année, ce qui accentue le problème d'un déséquilibre entre l'offre et la demande d'électricité. Pour résoudre ce problème, le stockage d'énergie est actuellement étudié. Parmi les solutions disponibles pour le stockage et la récupération d'électricité, la conversion d'électrons en produits chimiques représente l'une des solutions les plus adaptées, incluant l'électrolyse de l'eau ou du CO_2, ainsi que l'hydrogénation catalytique du CO_2 en méthane, appelée power-to-gas (P2G) ou, dans ce cas, power-to-methane.

Dans ce contexte, cette thèse s'inscrit dans le cadre du projet ANR CHEEC, pour « Couplage Catalyse et Electrolyse Haute Température pour l'Éthylène à partir de CO_2 ». L'innovation consiste à envisager le cas suivant : dans les systèmes conventionnels d'électrolyse haute température (HTE), l'oxygène produit pendant l'électrolyse est généralement rejeté. Le concept de CHEEC est d'utiliser cet oxygène comme réactif pour la conversion catalytique anodique du méthane en éthylène. Si ce procédé est réussi, il permettrait de transformer les unités HTE classiques fondées sur le « power-to-gas » en procédés « power-to-chemical », générant ainsi plus de valeur ajoutée que l'usage du méthane pour produire de l'électricité.

Deux propriétés physicochimiques critiques sont requises pour cette application : une haute efficacité catalytique pour le couplage oxydatif du méthane (OCM) et une conductivité mixte ionique-électronique robuste. Les composés d'oxydes à fort caractère basique, comme les oxydes à base de lanthane, sont connus pour posséder ces deux propriétés. En outre, puisque l'électrolyse à haute température (HTE) fonctionne aussi dans des conditions oxydantes, le matériau doit présenter une bonne stabilité thermique, ce qui rend les oxydes prometteurs et, plus récemment, des oxydes tel que le titanate de strontium.

Le titanate de strontium est un matériau suscitant un grand intérêt en raison de ses remarquables propriétés électriques, optiques et catalytiques, ainsi que de sa stabilité chimique. Sa structure cristalline de type pérovskite, qui permet divers dopages afin d'ajuster facilement ses propriétés, est au cœur de ce projet de doctorat. Ce matériau historique, connu depuis les années cinquante, a été utilisé dans de nombreuses applications électroniques, notamment comme supercondensateurs, grâce à ses propriétés diélectriques. Il est également utilisé aujourd'hui dans des applications liées à l'énergie, avec la découverte récente de titanate de strontium dopé pour les batteries lithium-ion, ou dans la dépollution environnementale, comme les systèmes de purification de l'eau basés sur ses propriétés photocatalytiques. Toujours dans le cadre des applications énergétiques, le titanate de strontium a fait l'objet de nombreuses recherches pour des unités d'électrolyse en combinaison avec des piles à combustible.

L'objectif de ce projet de doctorat est d'ajuster les propriétés électroniques du titanate de strontium afin qu'il présente une conductivité mixte ionique-électronique. Pour obtenir des particules de taille nanométrique, ce qui améliore les performances catalytiques du matériau, la synthèse en fluide supercritique en flux continu a été choisie.

Cette thèse de doctorat propose une nouvelle manière de synthétiser le titanate de strontium en utilisant les milieux fluides supercritiques en flux continu, avec la possibilité de produire des semi-conducteurs extrinsèques de titanate de strontium, une méthode encore inédite dans l'état de l'art sur le titanate de strontium et les fluides supercritiques.

Résumé du Chapitre 1

L'objectif principal de ce chapitre est de fournir une description la plus complète possible du titanate de strontium, incluant sa structure cristalline, ses propriétés physiques et ses méthodes de synthèse. Nous nous sommes d'abord concentrés sur les propriétés intrinsèques du titanate de strontium. La discussion a commencé par ses propriétés diélectriques, en mettant particulièrement en avant la constante diélectrique du matériau. Nous avons souligné l'importance de la structure atomique, qui peut être modifiée par différentes méthodes afin d'améliorer cette constante. Ensuite, nous avons exploré ses propriétés thermiques, avec une attention toute particulière portée à la conductivité thermique et au coefficient de dilatation thermique, où l'influence de la structure atomique a de nouveau été mise en évidence. Les propriétés thermiques ont été fortement corrélées aux propriétés électroniques du matériau, notamment dans le cadre des applications thermoélectriques. Étant donné que les propriétés électroniques sont étroitement liées à la structure de bande du matériau, nous avons également examiné ses propriétés optiques, en insistant sur l'indice de réfraction et la nature des liaisons atomiques au sein du matériau.

Ces propriétés sont intimement liées à la structure du matériau. Par conséquent, le dopage du composé avec de nouveaux éléments a été largement étudié dans le cadre de la structure pérovskite. Un tableau complet des dopants en site A et en site B a été présenté, mettant en évidence comment le dopage permet d'adapter le matériau pour atteindre des propriétés ciblées. Le concept de dopage hétérovalent a également été abordé, puisqu'il permet de combiner différents éléments pour des applications avancées. Les méthodes de synthèse de ces composés ont également été abordées, avec une discussion sur les défauts pouvant apparaître sur les sites A et B. En faisant varier les taux de dopage, nous avons mis en évidence les limites en compositions atteignables. Ensuite, nous avons présenté les propriétés catalytiques du matériau, en nous concentrant d'abord sur ses propriétés photocatalytiques globales, puis sur le couplage oxydatif du méthane.

Nous avons également passé en revue les différentes méthodes de synthèse du titanate de strontium, en commençant par la méthode la plus conventionnelle qui est la synthèse à l'état solide. Cette méthode permet d'obtenir une large gamme de compositions à partir de précurseurs accessibles, mais elle présente un coût énergétique élevé. De plus, la chimie des

défauts, notamment l'insertion de défauts ou de dopants de type n ou p, est limitée par le taux de dopage, car des taux plus élevés peuvent entraîner l'apparition d'impuretés. Pour répondre aux exigences des applications catalytiques, nous avons présenté des méthodes de synthèse permettant la taille nano du matériau, telles que la méthode sol-gel et les techniques haute pression comme les synthèses hydrothermale et solvothermale. Nous avons également exploré l'utilisation des technologies haute pression pour la synthèse de nanoparticules, avec une section consacrée à la synthèse supercritique.

Résumé du Chapitre 2

Dans ce chapitre, un aperçu est proposé sur les techniques et principes utilisés pour la production de nanoparticules de titanate de strontium pures et dopées, avec un accent particulier sur les méthodes de caractérisation, allant de l'analyse structurale à l'analyse élémentaire. Le traitement des nanopoudres, incluant la sérigraphie pour la fabrication d'une électrode et l'élaboration de céramiques denses, est abordé, ainsi que les outils utilisés pour leur caractérisation.

Ce chapitre présente les dispositifs supercritiques utilisés pour la synthèse de nanoparticules de titanate de strontium. Deux configurations sont abordées : la première, qui a servi de base pour la synthèse de ces nanoparticules et la validation de la chimie avec de nouveaux précurseurs, et une version améliorée. Cette version mise à jour a introduit des améliorations visant à rendre le système plus ergonomique, en particulier, en optimisant les procédés de chauffage et de refroidissement.

La deuxième section s'est concentrée sur les différentes méthodes de caractérisation utilisées pour les nanoparticules de titanate de strontium. Des techniques telles que la diffraction des rayons X (XRD), la spectroscopie Raman, la spectroscopie infrarouge à transformée de Fourier (FTIR), la microscopie électronique en transmission (TEM) et la spectroscopie photoélectronique X (XPS) ont été employées pour analyser en profondeur le matériau. Des caractérisations *in situ* avancées ont également été réalisées.

La dernière partie du chapitre a porté sur le traitement des poudres synthétisées pour leur transformation en électrodes et en pastilles denses. La fabrication des électrodes a impliqué plusieurs étapes, incluant la formulation d'une encre, la sérigraphie, puis un traitement

thermique, conduisant au dépôt réussi de nanoparticules de titanate de strontium. Ces nanoparticules ont été transformées en pastilles denses par SPS (Spark Plasma Sintering). Les propriétés électroniques de différentes compositions de titanate de strontium ont été mesurées à l'aide de la méthode des quatre pointes, dans le but de démontrer l'influence du dopage et son impact sur la conductivité.

Résumé du Chapitre 3

Ce chapitre présente les travaux réalisés sur la méthode solvothermale supercritique en flux continu pour la synthèse de nanoparticules de titanate de strontium en utilisant des précurseurs acétylacétonates. La structure du titanate de strontium a été étudiée à différentes échelles. Ce chapitre présente également une optimisation de la stœchiométrie du titanate de strontium. Enfin, les différentes améliorations apportées, tant sur les produits chimiques utilisés que sur les paramètres de synthèse liés au réacteur, ont permis de limiter drastiquement la formation d'impuretés à haute température.

Pour la première fois dans l'état de l'art de la synthèse supercritique, des précurseurs acétylacétonates de titane et de strontium ont été utilisés pour synthétiser du titanate de strontium. Les propriétés physicochimiques des particules produites, en mettant l'accent sur leur stabilité thermique, sont étudiées. L'utilisation de précurseurs acétylacétonates permet d'accéder à des matériaux présentant des propriétés physicochimiques inédites.

Des nanoparticules de $SrTiO_3$ avec une taille cristalline d'environ 20 nm ont été synthétisées avec succès. En plus de la structure cubique du $SrTiO_3$, la spectroscopie FTIR a révélé des fonctions de surface typiques des « wet process », tandis que la spectroscopie Raman a mis en évidence l'activation de modes non-centrosymétriques induits par des contributions non linéaires. D'après les mesures *in situ* de PXRD à haute température, les nanoparticules présentent une forme facettée et sont stables à des températures élevées. Cependant, en raison d'un déficit chimique en strontium, des phases de dioxyde de titane apparaissent à plus haute température. Des analyses *in situ* par HRTEM à haute température ont révélé l'existence de deux populations de particules, avec une meilleure stabilité des particules de plus grande taille après traitement thermique, ainsi qu'un frittage et une restructuration des plus petites, Les résultats de microscopie suggèrent également la possibilité d'une hétérogénéité chimique.

L'influence de paramètres externes tels que le débit, la température ou le type de précurseur de titane utilisé a permis d'améliorer la stabilité du matériau et de réduire le pourcentage atomique de TiO_2.

Résumé du Chapitre 4

Ce chapitre détaille une méthode permettant d'identifier le site de dopage du titanate de strontium dans une structure pérovskite, ainsi qu'une méthode pour synthétiser différentes compositions de titanate de strontium dopé en utilisant la synthèse solvothermale supercritique en flux continu dans un mélange eau/éthanol. La structure des nanopoudres a été caractérisée par diffraction des rayons X (XRD) et spectroscopie Raman, attestant des effets du dopage. Les analyses ICP et TEM-EDS ont permis de quantifier les différents éléments constituant le titanate de strontium « supercritique ». Elles ont confirmé un dopage homogène des divers éléments. Néanmoins, un déséquilibre unique entre le strontium et le titane a été observé.

La mesure de la résistivité par la méthode des quatre pointes a montré que le titanate de strontium « supercritique » présente une conductivité plus élevée que le titanate de strontium « commercial ». Les compositions dopées de type n (Y, Nd, Nb) affichent la conductivité la plus élevée. En comparaison avec le titanate de strontium « commercial », nous avons réussi à synthétiser un matériau mille fois plus conducteur que l'original. De plus, cet oxyde présentant une vacance exceptionnelle sur le site A n'a pu être obtenu que par la méthode supercritique.

Une dernière partie a présenté la mise en forme de la nanopoudre à base de titanate de strontium en électrodes, et plus précisément dans le cadre du projet, en cellule anode pour une unité d'électrolyse à haute température.

Conclusion & Perspectives

Premièrement, la synthèse et caractérisation de nanoparticules de $SrTiO_3$ de haute qualité en milieux fluides supercritiques. Les premiers travaux ont porté sur la formation de nanoparticules monocristallines de $SrTiO_3$ en milieux fluides supercritiques. Nous avons démontré, pour la première fois dans l'état de l'art de la synthèse en milieux fluides supercritiques, l'utilisation de précurseurs acétylacétonates pour produire des nanoparticules

de titanate de strontium. Grâce à des techniques de caractérisation *ex situ* standards (DRX, FTIR, spectroscopie Raman, HRTEM couplée à la spectroscopie EDS, ICP-OES), nous avons pu caractériser en profondeur les propriétés des nanoparticules. Les mesures PXRD et HRTEM ont confirmé leur monocrystallinité, tandis que l'EDS et l'ICP-OES ont révélé un déséquilibre entre les éléments strontium et titane, ajustable par modification du type de précurseur ou du système de chauffage. De plus, nous avons combiné la DRX et la HRTEM avec des techniques avancées de caractérisation *in situ* afin de suivre en temps réel le comportement des nanoparticules de titanate de strontium en fonction de la température. Nous sommes parvenus à ajuster le rapport A/B entre les éléments strontium et titane, et nous avons observé que la formation indésirable de TiO_2 pendant la synthèse diminue à mesure que le rapport A/B tend vers la valeur d'équilibre souhaitée. Le procédé a ensuite été amélioré avec la synthèse de compositions dopées de titanate de strontium utilisant différents éléments. Le dopage sur les sites A et B a été réalisé et démontré par des études structurales pour la première fois en utilisant la synthèse en milieux fluides supercritiques en flux continu.

Deuxièmement, la mise en forme et la production de cellules électrodes à partir de nanoparticules de $SrTiO_3$. Une fois la synthèse validée pour des matériaux adaptés à un environnement de fonctionnement à haute température, les nanoparticules ont été mises en forme sous forme d'encre puis moulées en pastilles denses. La formulation de l'encre a permis la production réussie de demi-cellules YSZ et de cellules complètes Ni-YSZ, avec une épaisseur de dépôt de 20 µm. Cette étape a été réalisée par sérigraphie en formulant une pâte à base de terpinéol. Les cellules ont ensuite été envoyées à des laboratoires partenaires pour une caractérisation complémentaire. La production de pastilles denses a été obtenue par frittage assisté par étincelles (SPS), avec une densité satisfaisante (>96 %) à partir de nanoparticules de titanate de strontium. L'utilisation de cette technique a permis de limiter la croissance des cristallites et d'optimiser l'effet de taille pour les caractérisations avancées suivantes.

Troisièmement, l'étude de la structure et de l'effet du dopage sur les composés $SrTiO_3$ synthétisés. Le procédé de synthèse basé sur les acétylacétonates a été adapté pour produire des nanoparticules semi-conductrices extrinsèques de titanate de strontium. Les dopants acétylacétonates ont été utilisés en raison de leur compatibilité avec la technologie des fluides supercritiques démontrée précédemment. Différents taux de substitution atomique allant de 1 % à 10 % ont été atteints avec une large gamme d'éléments. Nous avons démontré avec

succès la possibilité d'insérer des dopants de type n et p, des métaux de transition aux terres rares. Le site de substitution visé était basé sur l'approche du facteur de Goldschmidt et vérifié par analyses DRX et EDS.

Les compositions présentées sont les premières de leur genre identifiées dans le domaine de la synthèse en fluide supercritique. Le traitement SPS a permis d'obtenir des échantillons utilisables pour la caractérisation avancée des propriétés électroniques des titanates de strontium intrinsèques et extrinsèques. Comparé au titanate de strontium commercial, le matériau que nous avons produit par synthèse supercritique en flux continu montre déjà une conductivité supérieure. Cette augmentation est liée à un déséquilibre en strontium, induisant la création de lacunes en oxygène par équilibre électronucléaire. Le titanate de strontium dopé n a montré la meilleure conductivité électronique, atteignant une valeur mille fois supérieure à celle du titanate de strontium pur, prouvant ainsi la réussite de la synthèse d'un semi-conducteur extrinsèque.

Les perspectives de ce travail reposent principalement sur les opportunités de synthèse. Concernant les propriétés visées pour le projet, la conductivité électronique a été confirmée par la production et la caractérisation d'un semi-conducteur extrinsèque de titanate de strontium. La conductivité ionique du matériau n'a pas encore été caractérisée à ce jour, aucun chiffre ne pouvant être fourni pour confirmer sa nature de conducteur mixte ionique-électronique. Néanmoins, l'hypothèse a été faite que la présence de lacunes en oxygène (due au déséquilibre en cations) devrait contribuer positivement à l'optimisation de la conductivité ionique. Les poudres de titanate de strontium intrinsèques et extrinsèques ont été envoyées à des laboratoires partenaires pour caractérisation, grâce à un montage innovant permettant la mesure directe sur poudres. Concernant la catalyse du couplage oxydatif du méthane, les poudres ont été envoyées à des partenaires pour la mesure de leurs propriétés catalytiques. Les valeurs obtenues étaient faibles par rapport à la littérature. En 2019, Lim *et al.* ont présenté une composition dopée optimale de titanate de strontium, sans toutefois fournir d'étude structurale sur l'insertion du dopant. En outre, le matériau était synthétisé par une autre méthode que la technique supercritique. Cela met en évidence un élément central dans l'optimisation de l'activité catalytique en OCM. La chimie de surface du matériau doit être prise en compte, car elle est favorisée par un réseau électrophile et un enrichissement en strontium. Puisque le matériau présente un déséquilibre en strontium, cela pourrait expliquer

la diminution drastique des propriétés catalytiques pour l'OCM. Ce travail a présenté plusieurs pistes pour optimiser la teneur en cations du site A, soit par modification du type de précurseur (approche chimique), soit par optimisation de la température du réacteur (approche ingénierie). La synthèse de pérovskites équilibrées par technologie supercritique a déjà été obtenue avec du titanate de calcium-strontium.

Le point fort reste la polyvalence du procédé de synthèse pour la production de titanate de strontium extrinsèque**.** Les perspectives offertes par la synthèse de titanates dopés, grâce aux propriétés uniques de la méthode supercritique, sont immenses. Les spécificités du titanate de strontium reposent sur ses propriétés ajustables via sa structure pérovskite. Une large gamme de compositions dopées peut être synthétisée, chaque composition influant sur les propriétés à ajuster selon l'application. La méthode supercritique avec des précurseurs acétylacétonates offre une base solide pour produire une variété de semi-conducteurs extrinsèques, et pourrait même s'étendre aux alliages à haute entropie grâce à sa flexibilité.

Synthèse caractérisation et mise en forme de nanoparticules à base de $SrTiO_3$ en tant que matériaux d'anode EHT pour le couplage oxydant du méthane

Résumé : Le titanate de strontium ($SrTiO_3$) est un matériau d'un grand intérêt en raison de ses propriétés électriques, optiques et catalytiques remarquables, ainsi que de sa stabilité chimique. Sa structure cristalline de type pérovskite, qui autorise un certain nombre de dopages permettant d'ajuster facilement ses propriétés, est au cœur de son attrait. Parmi les méthodes de synthèse de $SrTiO_3$ dopé ou non dopé, la voie fluides supercritiques présente une alternative intéressante. En effet, dans le domaine de la science des matériaux, la voie fluides supercritiques a révolutionné la synthèse de nanoparticules, films minces et matériaux poreux. Cette méthode permet, au-delà d'élaborer des matériaux qui ne peuvent être obtenus avec des approches conventionnelles, d'obtenir une distribution uniforme des tailles de particules, une grande pureté et une cristallinité améliorée, des facteurs clés pour optimiser les performances des matériaux. Le titanate de strontium autorise le dopage sur les sites A (strontium) et B (titane). Les dopages les plus courants se font avec des terres rares sur le site du strontium ou des métaux de transition sur le site du titane. Le but du dopage est d'améliorer des propriétés spécifiques pour la photocatalyse, l'optique ou encore les propriétés diélectriques ou électroniques. Différents procédés de synthèse ont permis d'obtenir des compositions dopées de titanate de strontium, allant de la réaction à l'état solide aux méthodes plus avancées comme le sol-gel ou la synthèse hydrothermale. Cependant, la synthèse de titanate de strontium dopé par la voie fluides supercritiques n'a pas été rapportée, à l'exception de la solution solide complète entre le titanate de baryum et de strontium. Au cours de ces travaux de thèse, la synthèse de titanate de strontium par la voie fluides supercritiques en flux continu a été réalisée avec succès à l'aide de précurseurs du type alkoxydes et acétylacétonates. Une fois la synthèse validée, des compositions avec dopants ont été produites en substituant le strontium par des terres rares tel que le praséodyme et le titane par des métaux de transition comme le niobium, démontrant la flexibilité de cette méthode pour obtenir des matériaux dopés n ou p avec des taux atomiques précis allant d'un taux maximum de substitution de 10 at.% à 1 at.%, permettant d'améliorer les propriétés électroniques. De plus, ces propriétés électroniques ont été caractérisées pour évaluer l'impact du dopage. Les propriétés de conduction électronique ont ensuite été déterminées et ont démontré pour certaines compositions une conductivité 1 000 fois supérieure au titanate de strontium de base. Cette conductivité accrue permet au matériau d'être viable pour des applications d'électrodes dans divers dispositifs électrochimiques comme les électrolyseurs. Ces électrodes ont été élaborées par formulation des nanoparticules en encre et déposition sur support par sérigraphie. L'application finale envisagée pour ce matériau est l'utilisation comme anode dans un électrolyseur à haute température. Grâce à ses propriétés de conduction et sa taille nanométrique, ce matériau pourrait favoriser la réaction catalytique de couplage oxydant du méthane et promouvoir la conversion du méthane en éthylène.

Mots clés : Nanoparticules, Anode, $SrTiO_3$, Conducteurs mixtes, Catalyseurs, Fluides Supercritiques

---

Synthesis, characterization and shaping of nanoparticles based on $SrTiO_3$ as HTE anode materials for the oxidative coupling of methane

Abstract: Strontium titanate ($SrTiO_3$) is a material of great interest due to its remarkable electrical, optical, and catalytic properties, as well as its chemical stability. Its perovskite-type crystal structure, which allows for various dopings to easily adjust its properties, is central to its appeal. Among the synthesis methods for doped and undoped $SrTiO_3$, the supercritical fluid route presents an intriguing alternative. Indeed, in the field of materials science, the supercritical fluid route has revolutionized the synthesis of nanoparticles, thin films, and porous materials. This method not only enables the creation of materials that cannot be obtained through conventional approaches but also achieves a uniform particle size distribution, high purity, and improved crystallinity which is a key factor for optimizing material performance. Strontium titanate allows doping at both A-site (strontium) and B-site (titanium). The most common doping involves rare earth elements at the strontium site or transition metals at the titanium site. The goal of doping is to enhance specific properties for photocatalysis, optics, or dielectric and electronic characteristics. Various synthesis processes have yielded doped strontium titanate compositions, ranging from solid-state reactions to more advanced methods like sol-gel or hydrothermal synthesis. However, the synthesis of doped strontium titanate via the supercritical fluid route has not been reported, except for the complete solid solution between barium titanate and strontium titanate. In this thesis work, the synthesis of strontium titanate via the continuous-flow supercritical solvothermal method has been successfully achieved using alkoxide and acetylacetonate precursors. Once the synthesis was validated, compositions with dopants were produced by substituting strontium with rare earth elements such as praseodymium and titanium with transition metals like niobium, demonstrating the flexibility of this method to obtain n- or p-doped materials with precise atomic doping rates ranging from a maximum substitution rate of 10 at.% down to 1 at.%, thereby improving electronic properties. Additionally, these electronic properties were characterized to assess the impact of doping. The electronic conduction properties were then determined, revealing that for certain compositions, the conductivity was 1,000 times greater than that of the bare strontium titanate. This increased conductivity makes the material viable for electrode applications in various electrochemical devices, such as electrolyser. These electrodes were developed by formulating nanoparticles into ink and depositing them onto a substrate via screen printing. The final envisioned application for this material is as an anode in a high-temperature electrolyser. Due to its conductive properties and nanoscale size, this material could facilitate the catalytic oxidative coupling of methane and promote the conversion of methane to ethylene.

Keywords: Nanoparticles, Anode, $SrTiO_3$, Mixed conductors, Catalysts, Supercritical Fluids

---

Unité de recherche

ICMCB, Institut de Chimie de la Matière Condensée de Bordeaux, UMR 5026,

87 av Dr Albert Schweitzer, 33600 Pessac